Resolvent modeling of turbulent jets

Thesis by
Ethan Pickering

In Partial Fulfillment of the Requirements for the
Degree of
Doctorate of Philosophy

CALIFORNIA INSTITUTE OF TECHNOLOGY
Pasadena, California

2021
Defended February 4th, 2021

Ethan Pickering
ORCID: 0000-0002-4485-6359

ACKNOWLEDGEMENTS

I would like to dedicate this thesis to my high school math teacher, Troy DiFranco of Grafton, Ohio. Our high school had limited math courses, and when five students and myself had run out of courses for our senior year, Mr. DiFranco offered to learn Calculus B/C and teach us in the morning before school. Despite never teaching the material, having responsibilities as the head basketball coach, and raising three children, he would arrive an hour early at 6 a.m. to ensure we didn't go a year without learning math. Mr. DiFranco passed away unexpectedly at age 48 in 2019. I find it hard to believe that I would be here if it wasn't for Mr. DiFranco. His limitless capacity for selflessness and service continue to inspire.

Starting with the boss. Tim, I could not have asked for or imagined a better advisor. You have always genuinely cared about my development as a researcher and person, having spent countless hours either guiding or challenging my thought process. I know that it took a great deal of patience. I now recognize you tended to know the answers, but were patient enough to let me discover them myself. You have always seemed to know when to apply pressure, and remove it. To be honest, or just let things slide for the time being. Your versatility in approach has always held me in awe. Though, my favorite memories lie in middle ground with comments such as "OK. Maybe you are not as wrong as I thought you were... Still wrong though," or my all time favorite, "Hmmm. You know, it is incredibly impressive that you can do all of this without understanding any of the math." I may not understand all of the math yet, but with your help I have definitely learned some.

I also cannot thank my fellow Computational Flow Physics Group members both past and present enough: Phillipe Tosi, André Fernando de Castro da Silva, Kazuki Maeda, Ke Yu, Marcus Lee, Jean Sebastian Spratt, Ben Stevens, Liam Heidt, and Wei Ran. And those of the CFPG post doc union: George Rigas, Oliver Schmidt, Spencer Bryngelson, Benedikt Dorschner, Lennart Schneiders, Mauro Rodriguez, Gianmarco Mengdalo, and Shunxiang Cao, as well as our many visitors over the years, especially Francisco, Fabien, Ben, and Theresa. Their camaraderie and limitless ability to provide help, insight, and optimism made everyday in the office fulfilling and enjoyable. And a special shout out to the fellow jet-noise junkies George, Oliver, and Liam. The former two who took me in as a clueless grad student and helped me develop over my first two years. I hope I helped Liam as much as you two did, but he was far less clueless than I.

I would like to specifically thank a number of collaborators for their insights and help along the way: Aaron Towne, Peter Jordan, André Cavalieri, Petronio Nogueira, and Denis Sipp. Denis, I am specifically grateful for your assistance in teaching me the ins and outs of Lagrangian optimization.

I would have certainly thrown in the towel up during the insanity that was the first year class-load without the rest of my incoming MCE class and the specific companionship of Alex Choi and Connor McMahan. You both helped me in unbelievable ways during our first two years. And Connor, thanks for *literally*, and without question, always being there.

I'm grateful to my parents, Jay and Lill, who taught me the value of education and that honest, hard work opened up limitless opportunities for me, making this accomplishment possible. I would also like to thank my siblings, Jason, Rachel, and Tessa for always being there. To my entire family, I know moving across the country was not easy considering my poor communication abilities, but your patience and understanding have meant the world to me.

I'm thankful for the faithful care and support of my many friends and mentors from Sigma Chi, especially Mark Quiner, Kim Caldwell, Peter (PJ) Stephens, and Tim Sanderson. I would also like to thank the many softball teams that helped me destress on a nightly basis, from the Graduate Student Council, Jet Propulsion Laboratory, Glendale, Burbank, and Hollywood leagues, each helped make LA feel like home.

Last but not least, I would like to thank my thesis committee – Guillaume Blanquart, Beverley McKeon, and John Dabiri for serving in this capacity and for providing valuable feedback on this thesis.

ABSTRACT

Optimal control of turbulent flows requires a detailed prediction of the unsteady, three-dimensional turbulent structures that govern quantities of interest like noise, drag, and mixing efficiency. There is a need for physics-based, reduced-order models of turbulent structure for those cases where direct simulation of the flow would be computationally prohibitive. In this thesis, we explore *resolvent analysis* as a framework for such models. Based on a linearization about the turbulent mean flow field, the resolvent finds optimal (highest gain) forcing functions that give rise, through linear amplification mechanisms, to energetic coherent structures. The forcing functions represent the nonlinear interactions between the coherent structures as well as with background incoherent turbulence. While the high-gain structures capture many characteristics of the observed turbulent coherent structures in both wall-bounded and free-shear flows, closures for the forcing function are required to make these models predictive and thus utilize them for flow control.

In the first part of this thesis, we examine a linear model for the resolvent forcing by adapting the concept of a turbulent (eddy) viscosity from classical Reynolds-Averaged Navier–Stokes (RANS) turbulence modeling. We present a data-driven approach to identify an optimal eddy-viscosity field that best matches the resolvent prediction to the most energetic coherent structure educed via spectral proper orthogonal decomposition (SPOD) of data from high-fidelity simulations. We analyze the specific case of turbulent jets spanning a range of Mach numbers from subsonic to supersonic. We find the optimal eddy-viscosity field to be effective at matching both the shape and energy distribution of structures. More importantly, we find that calibrated eddy-viscosity fields predicted using standard eddy-viscosity models (utilizing only quantities available from RANS) yield results that are close to optimal.

We use the resulting resolvent model together with the high-fidelity data to investigate the full spectrum of amplification mechanisms and coherent structures present in turbulent jets. The addition of a turbulence model provides a clear separation between two established mechanisms in turbulent jets (Kelvin-Helmholtz and Orr) and leads to the identification of a third mechanism known as lift-up. Lift-up becomes the dominant mechanism at low-frequency limits for nonzero azimuthal wavenumbers, generating elongated, streaky structures. We find these streaks to be the most energetic structures in the jet, and that their presence has implications for altering

the mean flow and controlling noise.

Finally, we extend resolvent analysis to that of an acoustic analogy that relates the near-field forcing to the far-field acoustics 100 diameters from the nozzle. We again leverage high-fidelity data to produce an ensemble of realizations of the acoustic field and find that only a few resolvent modes are necessary for reconstruction. Ultimately, we find that a resolvent model based solely upon RANS quantities can reconstruct and predict the peak acoustic field at rank-1 to within 2 decibels for both the supersonic and transonic jets.

PUBLISHED CONTENT AND CONTRIBUTIONS

Pickering, E., G. Rigas, P. A. S. Nogueira, A. V. G. Cavalieri, O. T. Schmidt, and T. Colonius (2020). "Lift-up, Kelvin–Helmholtz and Orr mechanisms in turbulent jets". In: *Journal of Fluid Mechanics* 896 (2020), A2. DOI: 10.1017/jfm.2020.301.

Pickering, E., G. Rigas, O. T. Schmidt, D. Sipp, and T. Colonius (2020). "Optimal eddy viscosity for resolvent-based models of coherent structures in turbulent jets". In: *arXiv preprint arXiv:2005.10964* (2020).

Pickering, E., A. Towne, P. Jordan, and T. Colonius (2020). "Resolvent-based jet noise models: a projection approach". In: *AIAA Scitech 2020 Forum*. 2020, p. 0999. DOI: 10.2514/6.2020-0999.

Pickering, E., G. Rigas, D. Sipp, O. T. Schmidt, and T. Colonius (2019). "Eddy viscosity for resolvent-based jet noise models". In: *25th AIAA/CEAS Aeroacoustics Conference*. 2019, p. 2454. DOI: 10.2514/6.2019-2454.

For all of the above articles, the author performed the work, analyzed and interpreted the results, and was the principal writer of the journal articles. The first three listed articles are included as chapters in this thesis.

TABLE OF CONTENTS

LIST OF ILLUSTRATIONS

Number *Page*

LIST OF TABLES

Chapter 1

INTRODUCTION

1.1 Motivation

Optimal control of turbulent flows, from airfoils to wind-turbines to jet engines, remains a challenging and exciting area of research in fluid mechanics. Due to the complex and chaotic nature of turbulent flow, there exists no unique or repeatable time history for any general turbulent flow configuration (Karman, 1938; Hinze, 1959). Even so, the sensitivity of the equations to any external perturbations would render such an undertaking as moot (Bradshaw, 1972; Pope, 2001). This chaotic and, in many ways, unpredictable quality of turbulence presents a unique challenge for understanding and controlling the fundamental mechanisms of turbulence.

With recent advancements in computational power, time-averaged statistics of turbulent flows found via Reynolds-Averaged Navier–Stokes (RANS) simulations (Launder and Spalding, 1983), direct numerical simulation (DNS) (Moin and Mahesh, 1998), or large eddy simulation (LES) (Lesieur and Metais, 1996) have been found to provide data that agree with experiments of various flow configurations (e.g. jets, boundary layers). These are critical tools for furthering turbulence research, however, with each technique comes different limitations. RANS, the cheapest of the above, lacks universality and requires significant tuning for each new flow condition. DNS, while tremendously accurate, is prohibitively costly as it requires resolving scales of the flow down to the Kolmogorov length scale, and is intractable for nearly all complex or high-Reynolds number flows. LES presents a "compromise" as a much cheaper alternative to DNS and has emerged as an accurate tool for simulating turbulent flows and their associated noise for geometries relevant to full-scale aircraft (Brès and Lele, 2019). Yet, LES remains relatively expensive and, for engineers seeking control strategies, computing full parameter searches is not feasible. Further, even though simulations provide an immense amount of data, they are agnostic to the fundamental mechanisms active in the flow and thus lack a direct entry point for modifying the flow to alter engineering quantities of interest.

Although the chaotic nature of turbulence and the intractability of many computational tools would seem to spoil any hope for progress, reframing turbulence from a time-dependent quantity to a statistical one reveals that a great deal of order under-

pins turbulence. The "order" of turbulence that we are interested in characterizing in this thesis are known as *coherent structures*, meaning structures found to be present in turbulent flow for relatively long periods of time. These structures are of critical importance as they are a primary contributor to the transport of mass, momentum, and energy, and the radiation of acoustic waves in turbulence (Lumley, 1981). Some of the earliest observations of order among the fluctuating terms in turbulence are those of Mollo-Christensen (1967) and Crow and Champagne (1971), who found orderly structure in turbulent jets, and Brown and Roshko (1974) in planar mixing layers. Nearly 50 years later, a full understanding of the underlying mechanisms driving the generation and sustenance of coherent structures remains elusive, yet their connection to longstanding engineering problems such as jet acoustics (Jordan and Colonius, 2013) and drag in wall-bounded flows (Moarref and Jovanović, 2012; Jiménez, 2018; Toedtli, Luhar, and McKeon, 2019) has become increasingly apparent. Thus, there remains a clear need for reduced-order frameworks for modeling coherent structures and accurately predicting their associated statistics.

One attractive reduced-order framework is through an interpretation of turbulent flow via *resolvent analysis*. Proposed by McKeon and Sharma (2010), coherent structures are described as statistical features of turbulence, where nonlinear interactions are regarded as forcing terms to a linearized operator that amplifies them according to the turbulent mean flow. As a statistical approach to coherent structures in turbulence, the resolvent analysis is ideally suited for formulating data-driven approaches. Specifically, a data-eduction technique known as spectral proper orthogonal decomposition (SPOD), provides the observed analogue of resolvent analysis (Towne, Schmidt, and Colonius, 2018). In this thesis, we aim to couple these analyses by informing our approach to resolvent analysis with data educed via SPOD of high-fidelity data.

1.2 Resolvent analysis

Resolvent analysis (also called input/output analysis and frequency response analysis) has its roots in linear systems and control theory. The resolvent operator is derived from the linearized flow equations and constitutes a transfer function between inputs and outputs of interest. It has been used to study the linear response of flows to external body forces and perturbations (Trefethen et al., 1993; Farrell and Ioannou, 2001; Schmid, Henningson, and Jankowski, 2002; Jovanović and Bamieh, 2005; Bagheri et al., 2009; Sipp, Marquet, et al., 2010) and to forcing from the nonlinear terms in the Navier–Stokes equations (McKeon and Sharma, 2010; Sharma

and McKeon, 2013).

It is in the latter context of McKeon and Sharma (2010) that we focus our approach to resolvent analysis. The method can be derived by the partitioning of the Navier–Stokes equations into terms that are linear and nonlinear with respect to perturbations to the turbulent mean flow. This interpretation then relies on a singular value decomposition of the linearized compressible Navier–Stokes equations that *identifies* and *ranks* the optimal (highest gain) forcing functions that give rise, through linear amplification mechanisms, to energetic coherent structures in the near-field turbulence and far-field sound.

The most compelling quality of this approach for reduced-order modeling lies in the *ranking* of structures by their energetic gain, as it self-selects the most important coherent structures of the flow. Thus, the resolvent approach provides an attractive basis for reduced-order models as it naturally permits the use of a truncated set of the highest-gain modes as a basis for the output. Such an approach has led to several insights to fundamental mechanisms in turbulent flow (Jovanović, 2021), from canonical wall-bounded flows (Hwang and Cossu, 2010a; Hwang and Cossu, 2010b; McKeon and Sharma, 2010; Sharma and McKeon, 2013; Moarref, Sharma, et al., 2013) to free shear flows (Jeun, Nichols, and Jovanović, 2016; Schmidt et al., 2018).

However, closures for the forcing functions are necessary to make these models predictive. Recently, there have been a number of approaches coupling resolvent analysis with exact solutions to the Navier–Stokes equations or to observed data as discussed by McKeon (2017). In the former case, Sharma, Moarref, et al. (2016) showed that not only could exact invariant solutions of the Navier–Stokes equations for both pipe and channel flows be described through a truncated resolvent approximation, but they could also describe the nonlinear forcing at low rank. Building on this work, Rosenberg and McKeon (2019) closed the nonlinear terms by coupling resolvent analysis with a self-interaction feedback that iteratively produced a nearly neutrally stable and self-sustaining mean flow. Data-informed approaches are also of interest for estimating the nonlinear forcing and have come largely through designing optimizations that recover mean-flow statistics, as has been done by several authors (Moarref and Jovanović, 2012; Mantič-Lugo, Arratia, and Gallaire, 2014; Yim, Meliga, and Gallaire, 2019; Hwang and Eckhardt, 2020), or through knowledge of partial second-order statistics of the flow (Zare, Jovanović, and Georgiou, 2017; Illingworth, Monty, and Marusic, 2018; Towne, Lozano-Durán, and Yang, 2020).

A third approach for closure, which we study in detail in Chapter 2, is to adapt the concept of a turbulent (eddy) viscosity from classical Reynolds-Averaged Navier–Stokes (RANS) turbulence modeling. Motivation for augmenting our analysis with an eddy-viscosity model may be tied to concepts underlying the triple decomposition (Reynolds and Tiederman, 1967; Reynolds and Hussain, 1972), which identifies the Reynolds stresses as acting on the coherent fluctuations (from both the coherent and incoherent fluctuations). This approach is not novel, as many studies have applied eddy-viscosity models in the wall-bounded turbulence literature (Del Alamo and Jimenez, 2006; Cossu, Pujals, and Depardon, 2009; Pujals et al., 2009; Hwang and Cossu, 2010a), however, a quantitative assessment (with the exception of Morra et al. (2019)) of their effect on turbulent structures is lacking. Fortunately, recent connections between resolvent and SPOD provide the ideal measurement tool for investigating the potential for resolvent closures via eddy-viscosity models.

1.3 Turbulent jets and aeroacoustics

To present our approach for turbulence modeling, we investigate round, high-Reynolds number turbulent jets, a canonical free-shear flow configuration, at subsonic, transonic, and supersonic conditions. We develop our models with both the near hydrodynamic field and the far acoustic field. The latter is of particular importance to the jet community as jet noise is both a major community health hazard, with several non-auditory health effects (Stansfeld and Matheson, 2003), and a substantial issue for military personnel, as approximately $1 billion are spent per year by the U.S. Department of Veterans Affairs on hearing loss (Committee et al., 2009; Yankaskas, 2013).

The interpretation and modeling of coherent structures in turbulence have historically taken the form of instabilities of (typically steady) basic flows. In jet turbulence, Crighton and Gaster (1976) hypothesized that one could describe coherent structures as linear instabilities of the mean flow via a modal analysis. These analyses rendered instability modes reminiscent of observed structures, but limited computational abilities prevented global studies to investigate any discrepancies. In the interim of advancements in computational power, local studies were expanded upon with the parabolized stability equations (PSE), a marching method able to propagate local analyses downstream. Most times, the computed modes agreed well with data, such as Gudmundsson and Colonius (2011) who showed that PSE solutions for an experimentally measured jet mean flow yielded good predictions for the dominant frequency/azimuthal mode structures educed from a near-field caged mi-

crophone array. However, some discrepancies remained, and theoretical limitations in the PSE framework warranted alternative approaches. Further, once fully global studies were tractable, Garnaud et al. (2013a) found that global calculations were inadequate, with a stable eigenvalue spectrum and physically irrelevant eigenmode shapes, and that the characterization of instability mechanisms required transient (non-modal) growth.

Resolvent analysis permits this characterization, has been applied to jets by several authors (Garnaud et al., 2013b; Jeun, Nichols, and Jovanović, 2016; Semeraro, Lesshafft, et al., 2016; Schmidt et al., 2018; Lesshafft et al., 2019), and has lead to the characterization of two essentially different linear amplification mechanisms, one associated with the traditional, modal (parallel-flow) Kelvin-Helmholtz (KH) instability and the other as an Orr-type mechanism (also identified through PSE by Tissot, Lajús Jr, et al. (2017)). At those frequencies where the dominant singular value is significantly larger than the subdominant ones (which we refer to as low-rank behavior), the dominant modes are qualitatively similar to coherent modes extracted from data (Schmidt et al., 2018). However, when the response is not low rank, a non-trivial structure of the nonlinear forcing terms may lead to discrepancies between resolvent and observed modes. Thus, it is necessary to model the nonlinear forcing to attain resolvent analyses that are quantitatively predictive.

As described earlier, we approach closure of the nonlinear forcing by adapting the concept of an eddy-viscosity from RANS turbulence modeling. The unique feature to this approach is that the turbulence model directly alters the resolvent operator and therefore the associated resolvent basis. Considering SPOD provides the optimal basis of the observed flow, SPOD is an ideal target for assessing the ability of a classical turbulence model for closure. In the case that a perfect model could be found, the model would render a resolvent basis that matches SPOD, meaning that the resolvent and SPOD modes coincide. We therefore define a data-informed variational problem in Chapter 2 that seeks an optimal eddy-viscosity field that matches the most energetic SPOD mode with the first resolvent mode. We then show that we can achieve similar agreement using standard eddy-viscosity models, including one directly inferred from a corresponding Reynolds-Average Navier–Stokes (RANS) simulation.

This final observation, using low-cost mean-flow quantities from RANS, brings us back to our original motivation for performing resolvent analysis: a low-cost, reduced-order turbulence modeling framework. We now speculate about a complete

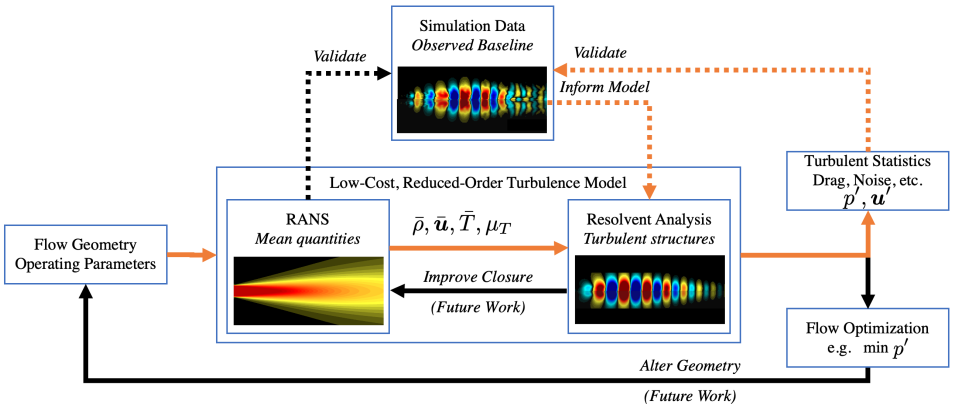

Figure 1.1: A conceptual turbulent flow design framework. The dotted lines indicate the use of only the baseline simulation (via LES) data for validation and for improving models. Once flow geometry and operating parameters are set, preliminary results are found via RANS and through an iterative analysis to ensure that solutions are self-consistent between solutions of the RANS equations and the turbulent structures found via resolvent analysis. Once converged, predictions of the fluctuating quantities may be made and optimizations can be posed via the resolvent for various engineering quantities through alterations to flow geometry. Those sections highlighted in orange are improved and addressed in this thesis.

framework for predicting turbulent quantities and tie components of this framework to efforts discussed in this thesis.

1.4 Towards fully predictive jet models and jet design

The overarching framework that this work seeks to improve, depicted in Figure 1.1, is one where we may couple RANS and resolvent analysis such that the fluctuating field is accurately predicted and ultimately controlled. The previous discussion has focused on the specific accuracy of resolvent analysis using data obtained via LES, however, to be computationally tractable, resolvent analysis must rely on cheaper strategies for obtaining the mean flow. Compared to LES, Reynolds Averaged Navier–Stokes (RANS) simulations are a much cheaper and simpler, albeit less accurate, modeling alternative. RANS simulations are orders of magnitude cheaper than LES and DNS, typically solved within minutes on standard laptops. However, RANS simulations are infamous for a lack of generality, the need to tune various coefficients within the governing equations, and their inability to predict the statistics of the fluctuating fields, such as the acoustic field.

For the case of the acoustic field, predictions have typically relied on the acoustic analogy (Lighthill, 1954). Similar to our approach via resolvent analysis, the analogy

takes the form of a linear operator acting on fluctuations driven by a source term, typically found via RANS for many current analogies. However, such approaches are indifferent to the development of the hydrodynamic structures and those structures' close connection to far-field sound propagation (Jordan and Colonius, 2013) and, as a result, have failed to produce universal models. As an example for our RANS-resolvent approach, and a proof of concept of those components highlighted in orange in Figure 1.1, we extend resolvent analysis to that of an acoustic analogy for predicting the acoustic field and perform calculations based solely on RANS quantities.

Finally, we note that this overarching framework subsumes, rather than replaces, traditional modeling frameworks and that this linear approach brings an opportunity to use several well-established strategies for imposing optimization upon the flow (Brandt et al., 2011; Mettot, Sipp, and Bézard, 2014; Toedtli, Luhar, and McKeon, 2019; Pickering, Rigas, Schmidt, et al., 2020). Thus, providing the means for a final feedback to the mean flow solver to shape the mean flow field by changing the geometry, which while outside this thesis, would provide a fully automated design. Current software packages could handle such shape optimization once cost functions for the far-field sound are determined.

1.5 Contributions and outline

In this thesis, we explore three different aspects of furthering resolvent models of jet turbulence: classical turbulence modeling for resolvent analysis, characterization of three amplification mechanisms, and prediction of jet noise.

In Chapter 2, we quantitatively test the extent to which a turbulence, or eddy-viscosity, model improves agreement between observed large-scale structures, educed via SPOD, and those computed from resolvent analysis. To find the optimal agreement via a turbulence model, we develop, in § 2.3, a data-informed optimization framework that identifies changes to the resolvent operator that lead to greater alignment with SPOD. We suggest that the eddy-viscosity approach acts as a proxy for modeling the effect of turbulence on large-scale structures, and in § 2.4 we find this approach provides substantial improvements in agreement (i.e. when compared to a baseline case that used a constant eddy-viscosity model corresponding to a value of $\mathrm{Re}_T = 3 \times 10^4$ (Schmidt et al., 2018)). By directly optimizing the eddy viscosity field to achieve the best alignment, we found alignments between resolvent and SPOD modes as high as 96% or improvements of over 10-fold from the baseline

alignment (i.e. 8% to 80%). Further, we find that the addition of an eddy-viscosity model to the resolvent operator highlights its effect on the different amplifications mechanisms in the turbulent jet, Orr-type, Kelvin-Helmholtz-type, and lift-up.

In § 2.7, we assess three additional eddy-viscosity models against the optimal eddy-viscosity field, which provides the upper bound for mode agreement. Of these models, we found that traditional eddy-viscosity models (e.g. RANS based) perform nearly as well as the optimal eddy-viscosity models in aligning the most energetic mode. The traditional models even outperformed the optimal model (i.e. optimal in the first mode) when considering the subdominant modes, giving the greatest diagonalization of the forcing CSD at $m = 0$, $St = 0.6$ (i.e. ability to model the effect of nonlinear forcing). Finally, we test the modeling potential of a RANS-inferred resolvent analysis over frequency, azimuthal wavenumber, and Mach number. We find the sensitivity to be weak, and that with a calibration of one constant, the approach provides significantly improved results for three turbulent jets over a substantial frequency range and azimuthal wavenumbers. Overall, these results show that "classical" eddy-viscosity models (RANS or a mean-flow consistent model) aid in estimating the impact of the Reynolds stresses for resolvent analysis.

In Chapter 3, we implement the eddy-viscosity augmented resolvent approach and find it sheds further light on the known amplification mechanisms (Kelvin-Helmholtz (KH) and Orr) and leads to the global identification of a third amplification mechanism, lift-up. In§ 3.3 we perform a global resolvent analysis at $St = 0$ and SPOD at $St \to 0$ for all three turbulent jets and find the presence of streamwise elongated structures, known as streaks. In§ 3.4, we expand the analysis to non-zero frequencies and multiple wavenumbers and discuss the interplay of the Kelvin-Helmholtz, Orr, and lift-up mechanisms in frequency-wavenumber space. We find that at moderate frequencies, KH becomes the globally dominant mechanism, and the Orr mechanism is active over all frequencies but plays a subdominant role at those frequencies and azimuthal wavenumbers where lift-up and KH are active. The behavior of the $m = 0$ response is unique, as axisymmetric streaks cannot exist; rather, the Orr response is dominant for low and high frequencies, with the KH response dominating over an intermediate-frequency regime centered on $St = 0.6$. For non-axisymmetric modes, the lift-up mechanism, and resulting streak response, is dominant as $St/m \to 0$, although with progressively higher wavenumber, lift-up responses are limited in spatial extent to nearer the nozzle exit. This latter observation is detailed in§ 3.5 as the analysis is truncated towards the nozzle, and we find that the azimuthal

wavenumber of dominant streak responses is inversely proportional to shear layer width and scales with $\sim 1/x$.

In Chapter 4 we extend resolvent analysis to that of an acoustic analogy relating the near-field forcing to both the near-field and far-field acoustics, the latter being 100 diameters from the nozzle. Leveraging the availability of a LES database, we examined resolvent-based reconstructions of the acoustic near- and far-field of round, turbulent $M_j = 1.5$ and $M_j = 0.9$ jets. We represented the forcing cross-spectral density matrix with a truncated set of resolvent modes and approximate the amplitudes of the modes with best-fit expansion coefficients of realizations from the LES acoustic field. In§ 4.4, we find that relatively low-rank models comprising as few as 1 resolvent mode can accurately reconstruct the acoustic field for the first two azimuthal modes for a $M_j = 1.5$ jet and the $m = 0$ azimuthal mode for the $M_j = 0.9$ jet, whereas about five modes were required for the higher azimuthal modes (i.e. $m = 2$ and $m = 1, 2$ for $M_j = 1.5$ and $M_j = 0.9$, respectively).

Based on the ability of the rank-1 reconstructions to describe much of the RMS energy, we investigated a simple model in§ 4.4 to collapse the forcing coefficients to one scaling function per wavenumber (and Mach number). We found that a power law representation, with only a scaling and a power value, suffices for describing the forcing coefficients for the optimal resolvent mode. Ultimately, we find that the rank-1 $m = 0$ resolvent models estimate the peak noise to within 2dB for both the $M_j = 1.5$ and $M_j = 0.9$ jets.

We then conclude in Chapter 5 with a summary of results and present a number of areas for future work.

Chapter 2

OPTIMAL EDDY VISCOSITY FOR RESOLVENT-BASED MODELS OF COHERENT STRUCTURES IN TURBULENT JETS

Under Review in the *Journal of Fluid Mechanics*

Chapter Abstract

Response modes computed via linear resolvent analysis of a turbulent mean-flow field have been shown to qualitatively capture characteristics of the observed turbulent coherent structures in both wall-bounded and free shear flows. To make such resolvent models predictive, the nonlinear forcing term must be closed. Strategies to do so include imposing self-consistent sets of triadic interactions, proposing various source models, or through turbulence modeling. For the latter, several investigators have proposed using the mean-field eddy viscosity acting linearly on the fluctuation field. In this study, a data-driven approach is taken to quantitatively improve linear resolvent models by deducing an optimal eddy-viscosity field that maximizes the projection of the dominant resolvent mode to the energy-optimal coherent structure educed using spectral proper orthogonal decomposition (SPOD) of data from high-fidelity simulations. We use large-eddy simulation databases for round isothermal jets at subsonic, transonic, and supersonic conditions and show that the optimal eddy viscosity substantially improves the agreement between resolvent and SPOD modes, reaching over 90% agreement at those frequencies where the jet exhibits a low-rank response. We then consider a fixed model for the eddy viscosity and show that with the calibration of a single constant, the results are generally close to the optimal one. In particular, the use of a standard Reynolds-Averaged- Navier–Stokes (RANS) eddy-viscosity resolvent model, with a single coefficient, provides substantial agreement between SPOD and resolvent modes for three turbulent jets and across the most energetic wavenumbers and frequencies.

2.1 Introduction

Resolvent analysis (also known as input/output analysis) determines a volumetric distribution of forcing in the frequency domain that gives rise, when acting in a time-invariant flow, to the most amplified linear response, typically measured in terms of its total kinetic energy. It is an important tool in stability and transition analysis (Trefethen et al., 1993; Farrell and Ioannou, 1993; Schmid, Henningson, and Jankowski, 2002; Jovanović and Bamieh, 2005), and has more recently been proposed as a reduced-order model of coherent structures in fully-developed turbulence (McKeon and Sharma, 2010; Hwang and Cossu, 2010b). In the latter context, resolvent analysis can be derived by partitioning the Navier–Stokes equations into terms that are linear and nonlinear with respect to perturbations. Such a rearrange-

ment of the equations is exact, and the equations may be explored without recourse to any further modeling. With varying degrees of formality, similar approaches were proposed in the past (Malkus, 1956; Michalke, 1971; Crighton and Gaster, 1976; Butler and Farrell, 1992), but increases in computer power that speed up the singular value decomposition (SVD) of the linear operator using direct LU decomposition (multi-frontal algorithms for sparse systems) have allowed a detailed characterization of the resolvent spectrum in several turbulent, canonical wall-bounded (Hwang and Cossu, 2010a; Hwang and Cossu, 2010b; McKeon and Sharma, 2010; Sharma and McKeon, 2013; Moarref, Sharma, et al., 2013) and free shear flows (Jeun, Nichols, and Jovanović, 2016; Schmidt et al., 2018).

At those frequencies where the dominant singular value is significantly larger than the subdominant ones (which we refer to as low-rank behavior), the dominant modes are qualitatively similar to coherent modes extracted from data (Schmidt et al., 2018). However, when the response is not low rank, a non-trivial structure of the nonlinear forcing terms may lead to discrepancies between resolvent and observed modes. Thus, it is necessary to model the nonlinear forcing to attain resolvent analyses that are quantitatively predictive. Previous studies have considered several approaches for modeling the nonlinear forcing in linear analyses. These include empirical models (Bechara et al., 1994; Tam and Auriault, 1999; Cavalieri, Jordan, Agarwal, et al., 2011; Cavalieri and Agarwal, 2014; Towne, Bres, and Lele, 2017), estimation given partial statistics of the response (Zare, Jovanović, and Georgiou, 2017; Towne, Lozano-Durán, and Yang, 2020; Martini et al., 2020), and/or the use of a turbulent, or eddy, viscosity. An eddy viscosity may be motivated by concepts underlying the triple decomposition (Reynolds and Tiederman, 1967; Reynolds and Hussain, 1972), which identifies the Reynolds stresses as acting on the coherent fluctuations (from both the coherent and incoherent fluctuations), even though the phase average used to define the coherent part of the turbulent-viscosity field is ambiguous in unforced turbulent flows. Many studies have applied eddy-viscosity models in the wall-bounded turbulence literature (Del Alamo and Jimenez, 2006; Cossu, Pujals, and Depardon, 2009; Pujals et al., 2009; Hwang and Cossu, 2010a; Hwang and Cossu, 2010b; Hwang, 2016; Vadarevu et al., 2019; Hwang and Eckhardt, 2020) either through implementation of the Cess (1958) model or by estimating the eddy-viscosity field via the Reynolds stresses and the mean shear rate of strain. Similarly, global stability analyses have applied eddy-viscosity models to identify and/or control forced or self-sustained resonances in transitional and turbulent flows (Crouch, Garbaruk, and Magidov, 2007; Meliga, Pujals, and Serre, 2012; Mettot,

Sipp, and Bézard, 2014; Sartor, Mettot, and Sipp, 2014; Semeraro, Jaunet, et al., 2016; Tammisola and Juniper, 2016; Rukes, Paschereit, and Oberleithner, 2016; Oberleithner, Paschereit, and Wygnanski, 2014). These studies implemented eddy viscosity on an ad hoc basis, citing improved qualitative agreement or improved integrated energy-densities.

In a more quantitative sense, eddy-viscosity enhanced linear models have also proven useful for assimilating known data to reconstruct observed energy spectra and mean-flow quantities. Moarref and Jovanović (2012) showed that a data-driven, white-in-time forcing could reproduce the DNS-based turbulent energy spectrum and, similarly, Illingworth, Monty, and Marusic (2018) could match DNS energy spectra using time-resolved velocity measurements. More recently, Towne, Lozano-Durán, and Yang (2020) showed that incorporating an eddy-viscosity model led to accurate estimates of space-time statistics using partially known data from DNS. Finally, Pickering, Towne, et al. (2020) used an eddy-viscosity enhanced resolvent model to reconstruct the large-eddy simulation (LES) acoustic field of transonic and supersonic turbulent jets at a significantly lower rank when compared to their non-eddy-viscosity enhanced computations. Other approaches have implemented eddy-viscosity fields to develop self-consistent models, such as Yim, Meliga, and Gallaire (2019) or Hwang and Eckhardt (2020), where the former study coupled a harmonically forced, quasi-linear resolvent analysis with RANS equations, citing eddy viscosity as a necessary link between the coherent and incoherent perturbation dynamics.

Although the utility of eddy-viscosity enhanced linear models for turbulent modeling and control has become increasingly apparent, a quantitative assessment of their effect on turbulent structures is lacking; even more, it is unclear which statistics turbulence models should seek to predict. One appealing target is modes educed by spectral proper orthogonal decomposition (SPOD), as these modes optimally reconstruct the turbulent kinetic energy and represent space-time coherent structures (Towne, Schmidt, and Colonius, 2018). In fact, the SPOD has a theoretical connection with resolvent analysis. Towne, Schmidt, and Colonius (2018) showed that if the resolvent forcing modes, at a given frequency and wavenumber, are mutually uncorrelated, then the resolvent response modes are identical to the SPOD modes. Likewise, discrepancies between the SPOD and resolvent modes imply correlated forcing modes.

Morra et al. (2019) applied a similar line of thinking by including an eddy viscosity in

their resolvent analysis of turbulent channel flow, showing that the resulting resolvent modes were in greater agreement with the SPOD modes educed from high-fidelity simulation data than resolvent analysis using only molecular viscosity. We extend this approach to turbulent jets, but consider a more general framework. The central question we ask is: how well can the inclusion of an eddy-viscosity model in the resolvent operator approximate the correlations of the forcing cross spectral density tensor? In this approach, an ideal model would render any remaining forcing as uncorrelated, meaning that the resolvent and SPOD modes coincide. We therefore define a data-informed variational problem that seeks an optimal eddy-viscosity field that maximizes the projection of the first SPOD mode on the first resolvent mode. We then show that we can achieve nearly optimal projections using standard eddy-viscosity models, including one directly inferred from a corresponding Reynolds-Average Navier–Stokes (RANS) simulation.

The work presented here is also relevant to a broader debate taking place regarding the interpretation of resolvent analysis. Since we can define the resolvent operator from the full nonlinear equations without introducing approximations or closures, it is attractive to proceed without introducing ad hoc models such as eddy viscosity, since we can still consider the framework *exact*. With a minor caveat (i.e. while exact, the resolvent decomposition is not necessarily unique as it can depend on the choice of dependent variables used to express the governing equations (Karban et al., 2020)), this implies that the forcing terms are *physically* interpretable (i.e. measurable) quantities. This perspective is, in our opinion, valuable, and may be pursued alongside efforts (such as the present work) aimed at empirically modeling the forcing. However, there is a subtlety that confounds the separation between "exact" and "modeled" resolvent analyses: namely, it may not be possible to compute, with meaningful accuracy, the exact resolvent modes in high Reynolds number flows, particularly when the mean flow is two- or three-dimensional. The fine-scale structure of the modes can require resolutions similar to DNS, and inversion of the resulting linear systems for singular value decomposition can be prohibitive. A survey of resolvent analyses conducted to date on multidimensional base flows shows that a variety of *regularizations* of the resolvent operator have been used to reduce the computational burden. By regularizations, we mean linear modifications to the operator that, whether through physical or numerical justification, provide results that are free from numerical artifacts or which more closely resemble observed quantities. These include the use of eddy-viscosity models (as discussed at length above), fourth-order numerical filters (Jeun, Nichols, and Jovanović, 2016),

case	M_j	Re_j	$\frac{p_0}{p_\infty}$	$\frac{T_0}{T_\infty}$	n_{cells}	$\Delta t a_\infty / D$	ΔSt
subsonic	0.4	4.5×10^5	1.117	1.03	15.9×10^6	0.2	0.049
transonic	0.9	1.01×10^6	1.7	1.15	15.9×10^6	0.2	0.022
supersonic	1.5	1.76×10^6	3.67	1.45	31×10^6	0.1	0.026

Table 2.1: Parameters, sampling rate, and frequency resolution for the LES.

effective Reynolds numbers (Schmidt et al., 2018), and linear damping (Yeh and Taira, 2019).

From a more general perspective, the present work also has a connection to the building of data-augmented turbulence models (Duraisamy, Iaccarino, and Xiao, 2019). Here, we specifically target the modeling of unsteady features (Wang et al., 2018; Maulik et al., 2019) and the optimal eddy-viscosity fields found, at each frequency-wavenumber pair, which are analogous to field-inversion steps (also based on variational data-assimilation methods, Foures et al. (2014) and Parish and Duraisamy (2016)) that assist Machine learning techniques in generating eddy-viscosity models from mean-flow quantities.

We organize the paper as follows. In § 2.2 we outline the governing equations, resolvent analysis, and SPOD. In § 2.3 we discuss the optimization framework developed to match, or align, SPOD and resolvent modes, and the specific eddy-viscosity models examined. § 2.4 provides the resulting resolvent mode shapes found via the four eddy-viscosity models and § 2.5 analyzes the associated optimal eddy-viscosity fields. In § 2.6 we show a favorable impact of the eddy-viscosity models on the subdominant resolvent modes and then conclude the analysis in § 2.7 by assessing the sensitivity of the RANS eddy-viscosity model. In this final section, we ultimately find a frequency independent RANS eddy-viscosity field that performs well for three turbulent jets (i.e. subsonic, transonic, and supersonic) and their most energetic frequencies ($St \in [0.05, 1]$) and azimuthal wavenumbers ($m \in \mathbb{N} \subset [0, 5]$).

2.2 Methods

The LES database, resolvent analysis, and SPOD were described in Schmidt et al. (2018) and Towne, Schmidt, and Colonius (2018). For brevity, we only recall the main details here.

Large Eddy Simulation database

The flow solver Charles was used to compute the LES databases, including subsonic (Mach 0.4), transonic (Mach 0.9), and supersonic (Mach 1.5) cases; Brès, Ham, et al. (2017) contains the details on the numerical method, meshing, and subgrid-models. Experiments conducted at PPRIME Institute, Poitiers, France were used to validate the Mach 0.4 and 0.9 jets (Brès, Jordan, et al., 2018). Table 2.1 provides a summary of parameters for the three jets considered. Parameters include the Reynolds number based on diameter $Re_j = \rho_j U_j D/\mu_j$ (where subscript j specifies the value at the centerline of the jet nozzle exit, ρ is density, μ is viscosity) and the Mach number, $M_j = U_j/a_j$, where a_j is the speed of sound. The simulated $M_j = 0.4$ jet corresponds to the experiments in Cavalieri, Rodríguez, et al. (2013), Jaunet, Jordan, and Cavalieri (2017), and Nogueira et al. (2019) with the same nozzle geometry and similar boundary-layer properties at the nozzle exit. Throughout the thesis, reported results are non-dimensionalized by the mean jet velocity U_j, jet diameter D, and dynamic pressure $\rho_j U_j^2$. We report frequencies in Strouhal number, $St = fD/U_j$, where f is the frequency.

Each database comprises 10,000 snapshots separated by $\Delta t a_\infty/D$, where a_∞ is the ambient speed of sound, and is interpolated onto a structured cylindrical grid $x, r, \theta \in [0, 30] \times [0, 6] \times [0, 2\pi]$, where x, r, θ are streamwise, radial, and azimuthal coordinates, respectively. Variables are reported by the vector

$$\boldsymbol{q} = [\rho, u_x, u_r, u_\theta, T]^T, \tag{2.1}$$

where u_x, u_r, u_θ are the three velocity components, and a standard Reynolds decomposition separates the vector into mean, $\bar{\boldsymbol{q}}$, and fluctuating, $\boldsymbol{q}'$, components

$$\boldsymbol{q}(x, r, \theta, t) = \bar{\boldsymbol{q}}(x, r) + \boldsymbol{q}'(x, r, \theta, t). \tag{2.2}$$

Resolvent analysis

We start with the nonlinear flow equations of the form

$$\frac{\partial \boldsymbol{q}}{\partial t} = \boldsymbol{F}(\boldsymbol{q}), \tag{2.3}$$

where $\boldsymbol{F}$ is the time-independent compressible Navier–Stokes operator (plus continuity and energy). Substituting Equation (2.2) for $\boldsymbol{q}$ and separating terms linear in state perturbations, $\boldsymbol{q}'$, to the left-hand side gives

$$\frac{\partial \boldsymbol{q}'}{\partial t} - \boldsymbol{A}(\bar{\boldsymbol{q}})\boldsymbol{q}' = \boldsymbol{f}(\bar{\boldsymbol{q}}, \boldsymbol{q}'), \tag{2.4}$$

where

$$\boldsymbol{A}(\bar{\boldsymbol{q}}) = \frac{\partial \boldsymbol{F}}{\partial \boldsymbol{q}}(\bar{\boldsymbol{q}}) \tag{2.5}$$

is the linearized flow operator (provided in Appendix A.2) and $\boldsymbol{f}$ contains the nonlinear terms and any additional external inputs (e.g. environmental noise or perturbations at the boundary).

For the round, statistically-stationary turbulent jets we consider, Equation (2.4) is Fourier transformed both temporally and azimuthally to the compact expression

$$(i\omega\mathbf{I} - \mathbf{A}_m)\boldsymbol{q}_{m,\omega} = \boldsymbol{f}_{m,\omega}, \tag{2.6}$$

where $\omega = 2\pi St$ is the frequency and m represents the azimuthal wavenumber. We can then rewrite Equation (2.6) by defining the resolvent operator, $\boldsymbol{R}_{\omega,m} = (i\omega\boldsymbol{I} - \boldsymbol{A}_m)^{-1}$,

$$\boldsymbol{q}_{m,\omega} = \boldsymbol{R}_{m,\omega}\boldsymbol{f}_{m,\omega}, \tag{2.7}$$

and introduce the compressible energy norm (Chu, 1965) via the matrix $\boldsymbol{W}$,

$$\langle \boldsymbol{q}_1, \boldsymbol{q}_2 \rangle_E = \int\int\int \boldsymbol{q}_1^* \mathrm{diag}\left(\frac{\bar{T}}{\gamma\bar{\rho}M^2}, \bar{\rho}, \bar{\rho}, \bar{\rho}, \frac{\bar{\rho}}{\gamma(\gamma-1)\bar{T}M^2}\right)\boldsymbol{q}_2 r\mathrm{d}r\mathrm{d}x\mathrm{d}\theta = \boldsymbol{q}_1^*\boldsymbol{W}\boldsymbol{q}_2, \tag{2.8}$$

to the forcing and response, where $\boldsymbol{W} = \boldsymbol{W}_f = \boldsymbol{W}_q$. The resolvent modes under this norm are then found by taking the singular value decomposition of the weighted resolvent operator,

$$\tilde{\boldsymbol{R}}_{m,\omega} = \boldsymbol{W}_q^{1/2}\boldsymbol{R}_{m,\omega}\boldsymbol{W}_f^{-1/2} = \tilde{\boldsymbol{U}}_{m,\omega}\boldsymbol{\Sigma}_{m,\omega}\tilde{\boldsymbol{V}}_{m,\omega}^*, \tag{2.9}$$

where the diagonal matrix $\boldsymbol{\Sigma}_{m,\omega}$ contains the ranked gains and the columns of $\boldsymbol{U}_{m,\omega} = \boldsymbol{W}_q^{-1/2}\tilde{\boldsymbol{U}}_{m,\omega}$ and $\boldsymbol{V}_{m,\omega} = \boldsymbol{W}_f^{-1/2}\tilde{\boldsymbol{V}}_{m,\omega}$ contain the response and forcing modes, respectively. These modes are orthonormal in the energy norm, Equation (2.8),

$$\boldsymbol{U}_{m,\omega}^*\boldsymbol{W}\boldsymbol{U}_{m,\omega} = \boldsymbol{V}_{m,\omega}^*\boldsymbol{W}\boldsymbol{V}_{m,\omega} = \boldsymbol{I}, \tag{2.10}$$

and recover the resolvent operator from Equation (2.7) as,

$$\boldsymbol{R}_{m,\omega} = \boldsymbol{U}_{m,\omega}\boldsymbol{\Sigma}_{m,\omega}\boldsymbol{V}_{m,\omega}^*\boldsymbol{W}. \tag{2.11}$$

For the resolvent analysis presented here, just as in Schmidt et al. (2018), the above equations are discretized in the streamwise and radial directions with fourth-order summation by parts, finite differences (Mattsson and Nordström, 2004), while the polar singularity is treated as in Mohseni and Colonius (2000) and non-reflecting boundary conditions are implemented at the domain boundaries.

Spectral Proper Orthogonal Decomposition

SPOD, similar to space-only proper orthogonal decomposition (POD) and originally shown by Lumley (1967) and Lumley (1970), determines an optimal (i.e. in terms of energy) set of orthogonal modes to describe a dataset, but unlike space-only POD, produces modes that express both spatial and temporal correlation in the data. Like dynamic mode decomposition, SPOD modes are computed at unique frequencies. However, through appropriate averaging, SPOD naturally ranks modes by energy and optimally accounts for the statistical variability of turbulent flows (Towne, Schmidt, and Colonius, 2018). Thus, the associated SPOD modes provide the ideal measurement tool to assess modes computed via resolvent analysis.

Decomposing the LES database $\boldsymbol{Q}$, where $\boldsymbol{Q}$ represents the temporal ensemble of perturbations ($\boldsymbol{q}'$) found by applying the standard Reynolds decomposition, in the azimuthal and temporal dimensions via the discrete Fourier transform gives the decomposed data matrices, $\hat{\boldsymbol{Q}}_{m,\omega}$. Multiplying the decomposed matrices, at a particular frequency and azimuthal wavenumber, by their complex conjugate give the cross-spectral density

$$\mathbf{S}_{m,\omega} = \hat{\boldsymbol{Q}}_{m,\omega}\hat{\boldsymbol{Q}}^{*}_{m,\omega}, \tag{2.12}$$

to which we solve the SPOD eigenvalue problem presented by Lumley (1967) and Lumley (1970)

$$\mathbf{S}_{m,\omega}\mathbf{W}\mathbf{\Psi}_{m,\omega} = \mathbf{\Psi}_{m,\omega}\mathbf{\Lambda}_{m,\omega}. \tag{2.13}$$

The SPOD modes form the columns of $\mathbf{\Psi}_{m,\omega}$, ranked by the diagonal matrix of eigenvalues $\mathbf{\Lambda}_{m,\omega} = \mathrm{diag}(\lambda_1, \lambda_2, ..., \lambda_N)$. The modes are orthonormal in the norm $\langle\cdot,\cdot\rangle_E$, and satisfy $\mathbf{\Psi}^{*}_{m,\omega}\boldsymbol{W}\mathbf{\Psi}_{m,\omega} = \boldsymbol{I}$. As a result, expansion of the cross-spectral density tensor gives,

$$\mathbf{S}_{m,\omega} = \mathbf{\Psi}_{m,\omega}\mathbf{\Lambda}_{m,\omega}\mathbf{\Psi}^{*}_{m,\omega}. \tag{2.14}$$

In this study, we perform all SPOD computations with a Hamming window and realization sizes of 256 snapshots with 50% overlap, resulting in 78 independent realizations.

To avoid ambiguity in referring to computed SPOD and resolvent modes, we use the following notation for the rest of the thesis. First, all computed modes, subscripts m, ω are dropped, but referenced when necessary in the text. Second, $\boldsymbol{\psi}_n$ represents the n-th most energetic SPOD mode, while $\boldsymbol{v}_n$ and $\boldsymbol{u}_n$ denote the resolvent forcing and response, respectively, that provide the n-th largest linear-amplification gain between $\boldsymbol{v}_n$ and $\boldsymbol{u}_n$. Finally, we use the notation $\boldsymbol{\psi}_1 : u_x$ when referring to specific components of each mode, as shown here with streamwise velocity.

Using SPOD to inform resolvent analysis

As SPOD provides the optimal description of the second order flow statistics, we wish to use this decomposition to inform our resolvent approach to match such statistics. The connection can be made through multiplication of Equation (2.7) by its complex conjugate and then applying the expectation operator to present the relation between the CSD tensors of the forcing and response through the resolvent operator,

$$\boldsymbol{S_{qq}} = \mathbb{E}[\boldsymbol{qq}^*] = \mathbb{E}[\boldsymbol{Rff}^*\boldsymbol{R}^*] = \boldsymbol{RS_{ff}R}^*. \tag{2.15}$$

If $\boldsymbol{q}$ is projected onto the SPOD modes and $\boldsymbol{f}$ is projected onto the input resolvent modes, $\boldsymbol{\beta} = \boldsymbol{V}^*\boldsymbol{W}\boldsymbol{f}$, where the vector $\boldsymbol{\beta}$ is the projection coefficients, then we may write

$$\boldsymbol{\Psi\Lambda\Psi}^* = \boldsymbol{U\Sigma S_{\beta\beta}\Sigma U}^*, \tag{2.16}$$

which highlights that if the forcing coefficients are uncorrelated ($\boldsymbol{S_{\beta\beta}} = \boldsymbol{\Lambda_\beta}$) then the resolvent modes would be equivalent to the SPOD modes (Towne, Schmidt, and Colonius, 2018). Conversely, when the resolvent and SPOD modes are not identical, which is the case in our study, the forcing coefficients are correlated and this correlation must be modeled.

Rather than pursuing a direct model of the forcing coefficients, we take an alternative perspective that asks whether a modified resolvent operator, $\boldsymbol{R}_T$, can match one or more of the dominant resolvent and SPOD modes. A trivial solution would be to define the operator by the SPOD expansion, i.e. $\boldsymbol{R}_T = \boldsymbol{\Psi}$, but this operator then corresponds to the (discretization of any) general (non-local) linear operator, rather than a specific partial differential equation (PDE). Instead, a practical model can be obtained by posing a modified PDE of the linearized governing equations with one or more unknown coefficients, and then finding the best choice of coefficients such that the resolvent and SPOD modes are optimally matched. We propose such an approach in the next section by exploiting an eddy-viscosity model, and develop an optimization procedure that fits the parameters to align one, or more, of the most dominant resolvent and SPOD modes.

To the extent that the modified resolvent operator achieves alignment of any one of its output modes with a specific SPOD mode, we may directly interpret the corresponding diagonal entry of $\boldsymbol{S_{\beta\beta}}$ as the forcing amplitude, λ_β, required to reproduce the SPOD mode amplitude λ, through the resolvent gain, σ^2. In other words,

$$\lambda_n = \sigma_n^2 \lambda_{\boldsymbol{\beta}_n} \quad \text{for any } n \text{ where} \quad \boldsymbol{u}_n = \boldsymbol{\psi}_n, \tag{2.17}$$

Turbulence model	$\boldsymbol{\mu}_T$ form	Parameter	Data	Abbreviation
Baseline*	$1/\mathrm{Re}_T = 3.\bar{3}\times10^{-5}$	–	–	Baseline
Optimal field	$\boldsymbol{\mu}_T(\boldsymbol{x})$	$\boldsymbol{\mu}_T(\boldsymbol{x})$	$\boldsymbol{\Psi}$	Opt. $\boldsymbol{\mu}_T$
Mean-flow consistent	$c\boldsymbol{\mu}_T(\boldsymbol{x})$	c	$\overline{\boldsymbol{q}}$	Mean $\boldsymbol{\mu}_T$
RANS	$c\overline{\rho}C_\mu k^2/\epsilon$	c	–	RANS $\boldsymbol{\mu}_T$
Turbulent Re	$1/\mathrm{Re}_T$	$1/\mathrm{Re}_T$	–	$\mathrm{Re}_{T,Opt}$

Table 2.2: Turbulence models investigated in this study. The baseline* case refers to the results of Schmidt et al. (2018).

independent of whether the other modes are aligned (as other modes are orthogonal).

2.3 Models considered

We now add an eddy-viscosity model to the linearized governing Equations (2.4). We follow the ad hoc model used in (amongst other references) Del Alamo and Jimenez (2006) and Hwang and Cossu (2010b), which is typically justified by extending eddy viscosity from its traditional use in modeling the mean Reynolds stresses to modeling the effect of the "background turbulence" on the coherent motion.

The perturbation equations including the eddy viscosity are, with the replacement $\mu \mapsto \mu_{\text{eff}} = \mu_j + \mu_T$, identical to the original linearized equations, provided one accounts for the (spatial) variability of μ_T (equations provided in Appendix A.2). There remains an unknown forcing that is the residual between the original forcing and the "coherent" part that is is modeled by the eddy viscosity. Unfortunately, the residual forcing no longer possesses its exact physical interpretation as the nonlinear interactions of resolved modes. However, the advantage is that the resulting response modes can significantly reduce the rank of the problem and lead to a residual forcing CSD that is tractable to model when compared to the forcing CSD of the exactly rearranged equations (Pickering, Towne, et al., 2020; Towne, Lozano-Durán, and Yang, 2020).

In what follows, we refer to the modified linear operator with $\mu_T \neq 0$ as $\boldsymbol{A}_T$ and note that the operator depends on the chosen field for μ_T, which, upon discretization becomes a vector $\boldsymbol{\mu}_T$. Since we assume that μ_T is steady and axisymmetric, the operators have a similar temporal/azimuthal Fourier transform that we denote $\boldsymbol{A}_{Tm}$.

We now consider four models for the eddy-viscosity field. The first model directly optimizes the eddy-viscosity field to maximize agreement between the dominant resolvent and SPOD modes. The second model fits an eddy viscosity to the LES mean flow by minimizing the residual in the steady RANS equations. The third

model uses an independently computed eddy-viscosity field from a RANS $k-\epsilon$ model. Finally, we consider a simpler constant eddy-viscosity model based solely upon a turbulent Reynolds number.

For brevity, we refer to the modes computed with the above eddy-viscosity models as EVRA (eddy-viscosity resolvent analysis) modes, while modes termed "baseline" refer to those computed by Schmidt et al. (2018). We chose this study as a reference for its extensive comparison of resolvent and SPOD modes across all three turbulent jets and many wavenumbers and frequencies. In the baseline study, they chose an effective Reynolds number of $\mathrm{Re}_T = 3 \times 10^4$, a value that is an order of magnitude smaller than the molecular Reynolds number, yet not consistent with the expected magnitude of an eddy viscosity (i.e. $\mathrm{Re}_T << 3 \times 10^4$) . Instead, we regard this intermediate value as a regularization of the resolvent operator. Table 2.2 summarizes the various models investigated.

For exploratory purposes, we find an eddy-viscosity field that best matches the (so modified) resolvent operator to the measured SPOD modes independently for each frequency and azimuthal mode. The purpose is to gauge the sensitivity of the eddy viscosity value needed to model the different frequencies and azimuthal modes, and should not be interpreted as a proposal for a frequency-dependent eddy viscosity.

Parenthetically, within the following optimization framework we can consider any turbulence model or regularization based on mean-flow quantities. A further example is given in Appendix A.1, where we consider a linear damping model recently proposed for resolvent analysis of unstable base flows (Yeh and Taira, 2019). In the Appendix, we find that the linear damping improves agreement, but the performance is generally inferior to the eddy-viscosity models. This is likely due to the monolithic damping effect over all regions and wavenumbers, whereas the eddy-viscosity methods directly addresses the effect of the Reynolds stresses both in regard to specific regions of the flow and the approach's ability to account for spatial gradients in the eddy-viscosity field.

Optimal eddy-viscosity field

Here we develop an optimization, computed independently for each frequency and azimuthal mode, that finds the eddy-viscosity field that is optimal (i.e. the upper bound) in matching the leading resolvent and SPOD modes. To find the analytical expression that determines the sensitivity of mode agreement to an eddy-viscosity field, we use a Lagrangian technique analogous to Brandt et al., 2011 that accounts

for the non-modal behavior of the resolvent operator. This technique couples constraints from the governing equations, resolvent analysis, a normalization, and a cost function (agreement of the leading SPOD and resolvent modes), into a Lagrangian functional for whose stationary point provides the desired maximum.

To build the Lagrangian functional, we begin with the forward Equation (2.6) and substitute $\boldsymbol{L}$ with $\boldsymbol{L}_T$, the linear operator that includes an eddy-viscosity model. The singular value/singular vector $(\boldsymbol{v}_1, \boldsymbol{u}_1, \sigma_1)$ as defined in (2.11) is a solution of both the forward Equation (2.6),

$$\boldsymbol{v}_1 = \boldsymbol{L}_T \boldsymbol{u}_1, \tag{2.18}$$

where $\boldsymbol{v}_1$ replaces $\boldsymbol{f}$ as the forcing and $\boldsymbol{u}_1$ replaces $\boldsymbol{q}$ as the associated response, and the resolvent eigenvalue problem,

$$\boldsymbol{W}\boldsymbol{u}_1 = \sigma_1^2 \boldsymbol{L}_T^* \boldsymbol{W} \boldsymbol{v}_1. \tag{2.19}$$

The above resolvent eigenvalue solution is found by taking the energy norm of Equation (2.7) and dividing by the forcing energy to give

$$\frac{\boldsymbol{u}_1^* \boldsymbol{W} \boldsymbol{u}_1}{\boldsymbol{v}_1^* \boldsymbol{W} \boldsymbol{v}_1} = \sigma_1^2 = \frac{\boldsymbol{v}_1^* \boldsymbol{R}_T^* \boldsymbol{W} \boldsymbol{R}_T \boldsymbol{v}_1}{\boldsymbol{v}_1^* \boldsymbol{W} \boldsymbol{v}_1}. \tag{2.20}$$

Rearranging and eliminating $\boldsymbol{v}_n^*$ we arrive at

$$\boldsymbol{R}_T^* \boldsymbol{W} \boldsymbol{R}_T \boldsymbol{v}_1 = \sigma_1^2 \boldsymbol{W} \boldsymbol{v}_1, \tag{2.21}$$

where replacing $\boldsymbol{R}_T \boldsymbol{v}_1$ with $\boldsymbol{u}_1$ and multiplying both sides by $\boldsymbol{R}_T^{-*} = \boldsymbol{L}_T^*$ recovers Equation (2.19). Finally,we define a normalization constraint via,

$$\langle \boldsymbol{u}_1, \boldsymbol{u}_1 \rangle_E = \boldsymbol{u}_1^* \boldsymbol{W} \boldsymbol{u}_1 = 1. \tag{2.22}$$

The last component of the Lagrangian functional is the cost function,

$$\mathcal{J} = \boldsymbol{u}_1^* \boldsymbol{W} \boldsymbol{\psi}_1 \boldsymbol{\psi}_1^* \boldsymbol{W} \boldsymbol{u}_1 - l^2 \boldsymbol{\mu}_T^* \boldsymbol{M} \boldsymbol{\mu}_T, \tag{2.23}$$

where the first term, representing the primary objective, measures the squared projection, what we term the alignment or agreement, between the dominant SPOD mode, $\boldsymbol{\psi}_1$, and the first resolvent mode, $\boldsymbol{u}_1$. The alignment measure, $\boldsymbol{u}_1^* \boldsymbol{W} \boldsymbol{\psi}_1$, is squared to ensure the cost function is real. For brevity, we denote the outer product of the dominant SPOD mode as $\boldsymbol{\Psi}_1 = \boldsymbol{\psi}_1 \boldsymbol{\psi}_1^* = \boldsymbol{\Psi}_1^*$. The cost function may also

consider multiple resolvent/SPOD modes by considering a (weighted if desired) sum of the squared alignment terms.

The second term, $-l^2\boldsymbol{\mu}_T^*\boldsymbol{M}\boldsymbol{\mu}_T$, is a Tikhonov regularization that penalizes values of $\boldsymbol{\mu}_T$ that do not affect the alignment (high values of $\boldsymbol{\mu}_T$ diminish the value of $\mathcal{J}$), with $\boldsymbol{M}$ representing the cylindrical quadrature weights of the grid. As done in standard regularization methods, the value of l^2 is chosen high enough to remove the values of $\boldsymbol{\mu}_T$ in insensitive regions, but also sufficiently small to not interfere with the primary objective (Hansen and O'Leary, 1993). This penalization is effective at minimizing the eddy viscosity in non-turbulent regions of the flow such as the far field. A substantial range of l^2 values (i.e. multiple orders of magnitude) removes negligible regions of the eddy-viscosity field from the initial field without an observable drop in the primary objective, alignment between $\boldsymbol{u}_1$ and $\boldsymbol{\psi}_1$.

We now formally construct the Lagrangian functional to include the cost function (2.23), forward Equation (2.18), the resolvent eigenvalue problem (2.19), and the normalization constraint (2.22) to give,

$$\begin{aligned}\mathcal{L} = {} & \boldsymbol{u}_1^*\boldsymbol{W}\boldsymbol{\Psi}_1\boldsymbol{W}\boldsymbol{u}_1 - l^2\boldsymbol{\mu}_T^*\boldsymbol{M}\boldsymbol{\mu}_T \\ & - \tilde{\boldsymbol{u}}_1^*(\boldsymbol{L}_T\boldsymbol{u}_1 - \boldsymbol{v}_1) - \tilde{\boldsymbol{v}}_1^*(\boldsymbol{W}\boldsymbol{u}_1 - \sigma_1^2\boldsymbol{L}_T^*\boldsymbol{W}\boldsymbol{v}_1) - \tilde{\sigma}_1(\boldsymbol{u}_1^*\boldsymbol{W}\boldsymbol{u}_1 - 1) + c.c.,\end{aligned} \tag{2.24}$$

where $(\tilde{\boldsymbol{u}}_1, \tilde{\boldsymbol{v}}_1, \tilde{\sigma}_1)$ are Lagrange multipliers and $\tilde{\sigma}_1$ is real-valued as the corresponding constraint is real). This results in a functional that depends on seven variables,

$$\mathcal{L}([\boldsymbol{u}_1, \boldsymbol{v}_1, \sigma_1], [\tilde{\boldsymbol{u}}_1, \tilde{\boldsymbol{v}}_1, \tilde{\sigma}_1], \boldsymbol{\mu}_T). \tag{2.25}$$

We can find the maximum of the cost function by finding the stationary point of the entire functional (i.e. where variations with respect to each variable are zero). Stationarity with respect to the Lagrange multipliers yields the state equations, which are by definition satisfied, while stationarity with respect to the state variables yields:

$$\frac{\partial\mathcal{L}}{\partial\boldsymbol{u}_1}\delta\boldsymbol{u}_1 = (2\boldsymbol{W}\boldsymbol{\Psi}_1\boldsymbol{W}\boldsymbol{u}_1 - \boldsymbol{L}_T^*\tilde{\boldsymbol{u}}_1 - \boldsymbol{W}\tilde{\boldsymbol{v}}_1 - 2\tilde{\sigma}_1\boldsymbol{W}\boldsymbol{u}_1)^*\delta\boldsymbol{u}_1 \quad = 0 \tag{2.26}$$

$$\frac{\partial\mathcal{L}}{\partial\boldsymbol{v}_1}\delta\boldsymbol{v}_1 = (\tilde{\boldsymbol{u}}_1 + \sigma_1^2\boldsymbol{W}\boldsymbol{L}_T\tilde{\boldsymbol{v}}_1)^*\delta\boldsymbol{v}_1 \quad = 0 \tag{2.27}$$

$$\frac{\partial\mathcal{L}}{\partial\sigma_1}\delta\sigma_1 = (\tilde{\boldsymbol{v}}_1^*\boldsymbol{L}_T^*\boldsymbol{W}\boldsymbol{v}_1)^*\delta\sigma_1 \quad = 0, \tag{2.28}$$

and the condition in the last equation may be simplified into $\tilde{\boldsymbol{v}}_1^*\boldsymbol{L}_T^*\boldsymbol{W}\boldsymbol{v}_1 = \tilde{\boldsymbol{v}}_1^*\boldsymbol{W}\boldsymbol{u}_1$ using Equation (2.19). The stationary point is subsequently met by constructing the

Algorithm 1 Optimization

1: Initialize. Choose an initial eddy-viscosity/turbulence model and target SPOD mode.
2: **while** $d\mathcal{J}/d\boldsymbol{\mu}_T \neq \mathbf{0}$ **do**
3: Compute the EVRA mode(s).
4: Solve for the Lagrange multipliers.
5: Calculate the update direction, $d\mathcal{J}/d\boldsymbol{\mu}_T$.
6: Determine the optimal value of the step α by repeated evaluation of the cost functional along the steepest ascent direction.
7: **end while**

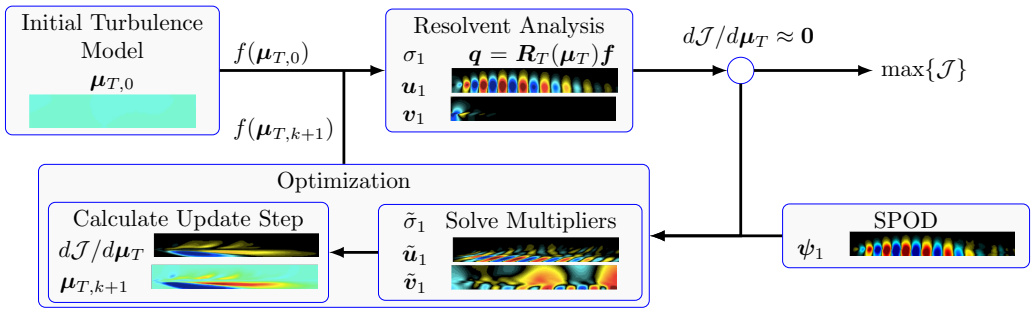

Figure 2.1: Schematic of the optimization framework for determining the optimal eddy-viscosity field that maximizes the alignment/agreement between computed resolvent modes, $\boldsymbol{u}_1$, and educed SPOD modes, $\boldsymbol{\psi_1}$. Included graphics are from implementation of the full-field eddy-viscosity model at $St = 0.6$, $m = 0$, and $M_j = 0.4$.

following system of equations and solving for the Lagrange multipliers:

$$\begin{bmatrix} -\boldsymbol{L}_T^* & -\boldsymbol{W} & -2\boldsymbol{W}\boldsymbol{u}_1 \\ \boldsymbol{W}^{-1} & \boldsymbol{L}_T\sigma_1^2 & 0 \\ 0 & \boldsymbol{u}_1^*\boldsymbol{W} & 0 \end{bmatrix} \begin{bmatrix} \tilde{\boldsymbol{u}}_1 \\ \tilde{\boldsymbol{v}}_1 \\ \tilde{\sigma}_1 \end{bmatrix} = \begin{bmatrix} -2\boldsymbol{W}\boldsymbol{\Psi}_1\boldsymbol{W}\boldsymbol{u}_1 \\ 0 \\ 0 \end{bmatrix}. \tag{2.29}$$

The upper left 2×2 block is degenerate due to the state Equations (2.18) and (2.19) (the couple, $\tilde{\boldsymbol{u}}_1 = \boldsymbol{W}\boldsymbol{v}_1$ and $\tilde{\boldsymbol{v}}_1 = -\sigma_1^{-2}\boldsymbol{u}_1$, is in the null-space of this block) and the third column and line regularizes this system. Combining the three equations, one can show that $\tilde{\sigma}_1 = \boldsymbol{u}_1^*\boldsymbol{W}\boldsymbol{\Psi}_1\boldsymbol{W}\boldsymbol{u}_1$, proving that $\tilde{\sigma}_1$ is a real value.

A final variation is taken with respect to the eddy-viscosity, $\boldsymbol{\mu}_T$ (which may be a scalar or vector quantity), providing the direction of gradient ascent for the eddy-viscosity field,

$$\frac{\partial \mathcal{L}}{\partial \boldsymbol{\mu}_T}\delta\boldsymbol{\mu}_T = -\tilde{\boldsymbol{u}}_1^*\left(\frac{\partial \boldsymbol{L}_T}{\partial \boldsymbol{\mu}_T}\delta\boldsymbol{\mu}_T\right)\boldsymbol{u}_1 + \sigma_1^2\tilde{\boldsymbol{v}}_1^*\left(\frac{\partial \boldsymbol{L}_T^*}{\partial \boldsymbol{\mu}_T}\delta\boldsymbol{\mu}_T\right)\boldsymbol{W}\boldsymbol{v}_1 - 2l^2\boldsymbol{\mu}_T^*\boldsymbol{M}\delta\boldsymbol{\mu}_T + c.c \tag{2.30}$$

$$= \left(\frac{d\mathcal{J}}{d\boldsymbol{\mu}_T}\right)^* \boldsymbol{M}\delta\boldsymbol{\mu}_T. \tag{2.31}$$

The gradient at the k^{th} grid point is then:

$$\left.\frac{d\mathcal{J}}{d\boldsymbol{\mu}_T}\right|_k = \boldsymbol{M}_{km}^{-1}\left(-\boldsymbol{u}_{1,j}^{*}\boldsymbol{L}_{m,ij}^{*}\tilde{\boldsymbol{u}}_{1,i} + \sigma_1^2\boldsymbol{W}_{lj}\boldsymbol{v}_{1,l}^{*}\boldsymbol{L}_{m,ji}\tilde{\boldsymbol{v}}_{1,i}\right) - 2l^2\boldsymbol{\mu}_{T,k} + c.c, \quad (2.32)$$

where $\boldsymbol{L}_{m,ij} = \lim_{\epsilon\to 0}\frac{\boldsymbol{L}_{T+\epsilon\,\delta\mu_m,ij}-\boldsymbol{L}_{T,ij}}{\epsilon}$, $\delta\boldsymbol{\mu}_m$ being a null vector except at the m^{th} position where it is equal to 1. This tensor may be obtained either through automatic differentiation of $\boldsymbol{L}_T$ with respect to $\boldsymbol{\mu}_T$ or by finite differences. Full storage of such tensors is not an issue when finite differences, finite volumes, or finite elements are used for the spatial discretization as the resulting tensors are extremely sparse.

The updated optimization parameter is then:

$$\boldsymbol{\mu}_T^{(k+1)} = \boldsymbol{\mu}_T^{(k)} + \alpha\frac{d\mathcal{J}}{d\boldsymbol{\mu}_T}, \quad (2.33)$$

where k is the iteration number and α is a step size determined through a root finding algorithm or a line search. If multiple SPOD/resolvent modes are considered for the optimization, then one has to solve Equation (2.29) for each couple $[\boldsymbol{\Psi}_n, (\boldsymbol{v}_n, \boldsymbol{u}_n, \sigma_n)]$, and the total gradient $\frac{d\mathcal{J}}{d\boldsymbol{\mu}_T}$ is the sum of each individual gradient, while the line search for α is performed considering the full cost functional. Although considering multiple modes is theoretically straightforward (and we present one example in § 2.6), there are two practical issues. Each additional mode brings further complexity to the gradient, increasing computation time, and the quality of SPOD modes, $\boldsymbol{\Psi}_n$, become increasingly noisy with n, thus rendering gains via the optimization as marginal. We discuss the latter issue in more detail throughout the chapter. Figure 2.1 presents a schematic of the above optimization framework, including graphical examples from the optimal eddy-viscosity field case at $St = 0.6$, $m = 0$, and $M_j = 0.4$.

For some cases, the optimization step imparts a region of negative effective viscosity (i.e. $-\mu_T > \mu_j$) presenting a challenge in both the physical interpretation and the numerical stability of the resolvent operator. However, negative *eddy* viscosity is not a unique concept to the algorithm presented. Literature surrounding eddy-viscosity models used in RANS and LES, where the eddy and effective viscosities are identical, attribute physical interpretations of negative eddy-viscosity to backscattering of turbulent energy, which, in many simulations, results in unstable simulations (Ghosal et al., 1995). Common treatment of a negative eddy viscosity has included filtering operations, ensemble averaging in homogeneous directions, and ad hoc clipping of the eddy-viscosity field (Vreman, 2004), while inferences of the eddy-viscosity field

via a Boussinesq approximation of data are often regularized to remove negative regions (e.g. Semeraro, Lesshafft, et al., 2016). Here, we similarly elect to remove any negative effective viscosity using a simple clipping strategy by setting any negative regions to the molecular value. Although a reduction of effective viscosity below the molecular viscosity is theoretically possible, we found that permitting the optimization to do so either led to numerical instabilities or negligible improvements in alignment.

The topology of the proposed cost function is complex, as $\boldsymbol{\mu}_T$ involves many degrees of freedom, and our optimizer may return a local rather than global maximum. Therefore, a complete assessment of the sensitivity of initial conditions or demonstration of a global maximum is intractable, but the relative insensitivity of the results to initial guesses and the fact that no other considered method outperforms the full optimization (shown later in Figure 2.4) provides confidence in the robustness of the maxima achieved. For all of the results presented here, we use the optimal constant eddy-viscosity field results (introduced in § 2.3) as the initial condition for the full-field optimizations.

Finally, the above optimization is derived considering the full (perturbation) state as the output. The formulation is similar if the input and output spaces are restricted, as shown in Appendix A.3. Such an extension is of particular use for experiments, or coarse simulations, where observed data may be sparse.

Mean-flow consistent eddy-viscosity model

For many experimental and numerical datasets, including the LES databases used here, an eddy-viscosity field is absent. We circumvent this issue by finding the eddy-viscosity field that minimizes the error to which the mean flow satisfies the (zero frequency and axisymetric wavenumber) linearized Navier–Stokes equations, supplemented with an eddy-viscosity model, provided in Appendix A.2. To do so, we find an eddy-viscosity field that minimizes the residual $\overline{\boldsymbol{f}}$ given by

$$\boldsymbol{L}_T\overline{\boldsymbol{q}} = \overline{\boldsymbol{f}}. \tag{2.34}$$

Thus we define the cost function,

$$\mathcal{J} = -\overline{\boldsymbol{f}}^*\boldsymbol{W}\overline{\boldsymbol{f}}, \tag{2.35}$$

and develop a Lagrangian functional with the forward equation as the only additional constraint to give

$$\mathcal{L} = -\overline{\boldsymbol{f}}^*\boldsymbol{W}\overline{\boldsymbol{f}} - \tilde{\boldsymbol{u}}^*(\boldsymbol{L}_T\overline{\boldsymbol{q}} - \overline{\boldsymbol{f}}). \tag{2.36}$$

Variations with respect to the residual are

$$\frac{\partial \mathcal{L}}{\partial \overline{\boldsymbol{f}}}\delta\overline{\boldsymbol{f}} = (-2\boldsymbol{W}\overline{\boldsymbol{f}} + \tilde{\boldsymbol{u}})^*\delta\overline{\boldsymbol{f}} = 0, \tag{2.37}$$

and we may directly solve for the Lagrange multipliers as,

$$\tilde{\boldsymbol{u}} = -2\boldsymbol{W}\overline{\boldsymbol{f}}. \tag{2.38}$$

Then by taking variations with respect to the eddy-viscosity field gives,

$$\frac{\partial \mathcal{L}}{\partial \boldsymbol{\mu}_T}\delta\boldsymbol{\mu}_T = -2(\boldsymbol{W}\overline{\boldsymbol{f}})^*\left(\frac{\partial \boldsymbol{L}_T}{\partial \boldsymbol{\mu}_T}\delta\boldsymbol{\mu}_T\right)\overline{\boldsymbol{q}}. \tag{2.39}$$

Similar to Equation (2.32), we obtain the update step:

$$\left.\frac{d\mathcal{J}}{d\boldsymbol{\mu}_T}\right|_k = -2\boldsymbol{M}^{-1}_{km}\overline{\boldsymbol{q}}_j\boldsymbol{L}_{m,ij}\boldsymbol{W}_{il}\overline{\boldsymbol{f}}_l, \tag{2.40}$$

and find the field via a line search. These steps are described in greater detail in the preceding subsection § 2.3. Figure 2.2 (a) provides the eddy-viscosity field that optimally minimizes the residual of the mean-flow solution. The associated residual field for this model reduced errors to approximately 10% of the original residual field, with the exception where the shear layer is thin near the nozzle. The thin shear-layer region improved by only $\approx 50\%$, but as shown later in the chapter, modes in this region are generally less sensitive to the eddy-viscosity field.

We refer to this model as the mean-flow consistent eddy-viscosity model and we optimally tune this field at each frequency by introducing the coefficient, c, $\boldsymbol{\mu}_T = c\boldsymbol{\mu}_{T,Mean}$. Our interest in the value of c is not to propose a functional of its frequency dependence (or assign to it a physical meaning), but to measure and observe the overall variation and help determine whether a frequency independent coefficient might suffice.

RANS-based eddy-viscosity field

We compute steady-state RANS solutions for each case to assess the applicability of the associated eddy-viscosity field for resolvent analysis. For simplicity, we perform the RANS computations in Fluent. The 2D axisymmetric grid extends 40 diameters in the streamwise directions and 20 diameters in the radial direction with grid spacing mirroring that of the interpolated LES grid scaled to be four times finer, giving 3×10^5 grid points. We set the inlet boundary conditions to the base-flow profile from the LES simulations and use the standard 2-equation $k - \epsilon$

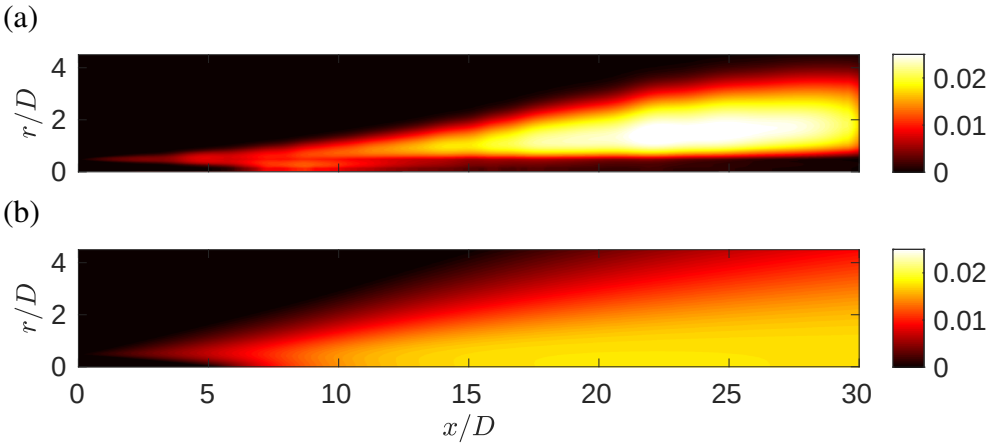

Figure 2.2: (a) Mean-flow consistent eddy-viscosity model computed at zero frequency and azimuthal wavenumber. (b) Eddy-viscosity field computed via a RANS simulation for the $M_j = 0.4$ jet, $c = 1$.

model (Launder and Spalding, 1983) for turbulence modeling. Coefficients used for the model are variants of those suggested by Thies and Tam (1996), with turbulent viscosity coefficient $C_\mu = 0.0874$, dissipation transport coefficients $C_{\epsilon 1} = 1.4$ and $C_{\epsilon 2} = 2.02$, turbulent Prandtl numbers for kinetic energy $\sigma_k = 0.324$ and dissipation $\sigma_\epsilon = 0.377$, and the turbulent Prandtl number $Pr_T = 0.422$. However, the standard $\kappa - \epsilon$ model provided in ANSYS does not incorporate the Pope (1978) and Sarkar et al. (1991) correction terms used in Thies and Tam (1996), requiring a calibration of the mean-flow quantities by introducing a scaling constant a to $C_\mu = 0.0874/a$, $\sigma_K = 0.324/a$, and $\sigma_\epsilon = 0.377/a$.

RANS mean-flow quantities closely match those of the LES for each of the three turbulent jets using values for a of 1.2, 1.3, and 1.575, for $M_j = 0.4$, 0.9, and 1.5, respectively. While tuning of the constant a to match LES is not in the spirit of obtaining a universal RANS model, we do so here to give the RANS-generated eddy-viscosity field the best chance at being consistent with the LES results from which the SPOD modes were educed. For a full assessment of the accuracy of RANS predictions for turbulent jets, we refer the reader to Thies and Tam (1996) and Georgiadis, Yoder, and Engblom (2006).

Figure 2.2 (b) presents the RANS-predicted eddy-viscosity field for the $M_j = 0.4$ jet, and Figure 2.3 shows near identical agreement with the mean LES streamwise flow. We observe similar agreement in radial velocity, density, and turbulent kinetic energy, and also find close agreement for the $M_j = 0.9$ and 1.5 jets; we do not show these results for brevity. For determination of the optimal RANS-based eddy-

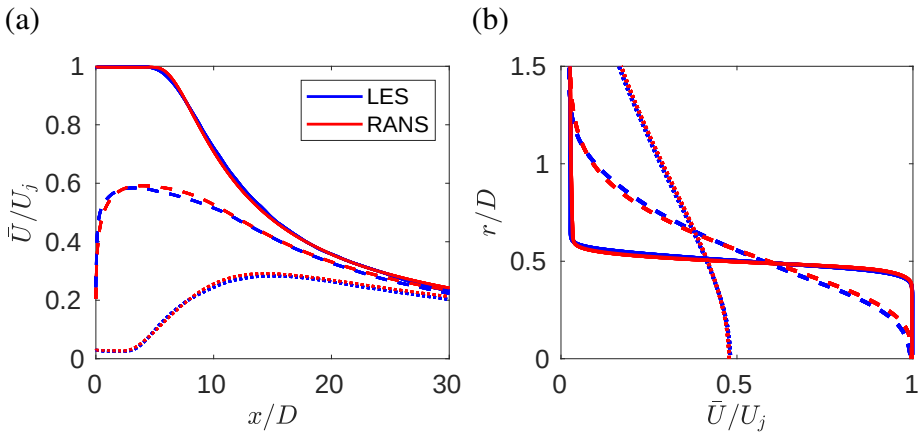

Figure 2.3: Mean-flow profiles of both the $M_j = 0.4$ LES and RANS, where the RANS simulation was tuned to best match the LES mean flow. (a) presents the streamwise mean velocity at three radial locations, $r/D =$ — 0.25, - - - 0.5, ····· 1, versus streamwise distance from the nozzle, while (b) gives the streamwise mean velocity at three streamwise locations, $x/D =$ — 0.5, - - - 5, ····· 10, versus radial distance.

viscosity field at each frequency, we take the computed eddy-viscosity fields,

$$\boldsymbol{\mu}_{T,RANS} = \overline{\rho} C_\mu \frac{k^2}{\epsilon}, \tag{2.41}$$

and introduce the coefficient, c, $\boldsymbol{\mu}_T = c\boldsymbol{\mu}_{T,RANS}$ (just as in § 2.3). This final relation underscores the difference between the traditional use of eddy viscosity with RANS and ours via resolvent analysis. In the former context, eddy viscosity accounts for *all* perturbations, while in resolvent analysis, the eddy viscosity is intended to model the effect of nonlinear, triadic interactions and the background turbulence on the linear structures. Thus, a coefficient of $c < 1$, for resolvent analysis, presents an eddy viscosity that omits a fraction of the overall eddy-viscosity field. As will be shown, we find all optimal values for c to be less than unity. This interpretation may also be applied to the mean-flow consistent eddy-viscosity field presented in the previous sub-section.

Constant eddy-viscosity field

Finally, we consider a simple, constant eddy viscosity, $\boldsymbol{\mu}_T = 1/\mathrm{Re}_T$. We primarily investigate this model because of its use in many turbulent jet studies that used a Reynolds number based either upon the molecular viscosity (Jeun, Nichols, and Jovanović, 2016; Lesshafft et al., 2019), on the order of $10^5 - 10^6$, or through an effective turbulent viscosity (Garnaud et al., 2013b; Schmidt et al., 2018), on the order of $10^3 - 10^4$. These, quite different, choices inevitably provided discrepan-

cies in amplification gains and mode shapes across each study, particularly at low frequencies (i.e. $St < 0.3$ for $m = 0$) – showing that the Reynolds stresses have a substantial impact on resolvent analyses of turbulent jets. Here, we find the optimal Re_T at each frequency and azimuthal mode number by a line search.

2.4 Optimal SPOD and resolvent mode alignment

In this section, we present modes predicted by the various EVRA models presented in the previous section. We focus on the axisymmetric disturbances, $m = 0$, for the $M_j = 0.4$ jet, and report results for other azimuthal modes and jet Mach numbers in section 2.7. We performed optimizations over the frequency range $St \in [0.05, 1]$, resulting in the alignment coefficients displayed in Figure 2.4, with alignment defined as $|\boldsymbol{\psi}_1^* \boldsymbol{W} \boldsymbol{u}_1|$. This metric not only represents how similar the spatial structures, represented as complex eigenfunctions, are between the dominant resolvent and SPOD modes, but also measures the similarity in distribution of energy amongst the five state variables. A value of 1 signifies perfect agreement, giving both identical agreement in structure and distribution of energy in the state variables. Typically, in this metric, values of approximately 0.4 or greater show qualitative agreement, whereas values less than 0.4 have little visual similarity.

Figure 2.4 (a) shows that throughout the frequency range considered, the alignments improve considerably from the baseline case (constant eddy viscosity with $\mathrm{Re}_T = 3 \times 10^4$). The alignment is best for $St > 0.3$, which corresponds to the frequencies where the jet has a strong, low-rank Kelvin-Helmholtz (KH) response (Schmidt et al., 2018), as highlighted by Figure 2.4 (b), presenting the spectra of the first five SPOD modes and their 95% confidence interval. For this region, $St > 0.3$, the baseline case gives reasonable (> 75% alignment) results, nonetheless, the eddy-viscosity models still improve the modes to nearly perfect alignment. At lower frequencies, $St \leq 0.3$, we find the most dramatic increase in alignments, from approximately 10% to 80%. These substantial improvements, at $St \leq 0.3$, coincide with a change of mode type, from KH to Orr (Schmidt et al., 2018), a viscous, non-modal instability mechanism sensitive to Reynolds number (with rapidly increasing amplification as Reynolds number increases), that dominates the non-optimized, low-frequency and subdominant regions of the resolvent spectrum for the $M_j = 0.4$ jet. We also find that the optimal eddy-viscosity field provides the greatest alignment among the models, which is at least suggestive that the optimization achieved a global maximum.

Surprisingly, the other eddy-viscosity models produce alignments close to the op-

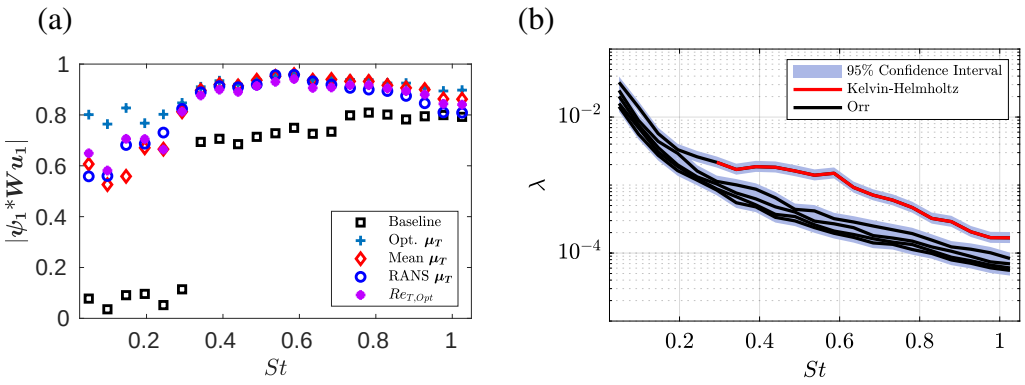

Figure 2.4: (a) Optimal alignments for all methods investigated including the baseline case, $\mathrm{Re}_T = 3 \times 10^4$. (b) SPOD eigenvalue spectra of the first five modes for $m = 0$, including the 95% confidence intervals and the modes associated with the Kelvin-Helmholtz and Orr mechanisms.

timal eddy-viscosity field. The constant eddy-viscosity is nearly optimal at lower frequencies (Orr-type modes), whereas the RANS and optimal mean-flow eddy-viscosity models are more nearly optimal at higher ones. We stress that in the optimal mean-flow, RANS, and constant $\boldsymbol{\mu}_T$ models, a different optimal value of the coefficient (i.e. c and Re_T) is used at each frequency. We defer a discussion of the sensitivity of these coefficients to § 2.7.

Starting with the lowest frequency, $St = 0.05$, we now investigate the mode shapes associated with the improved resolvent alignments achieved with the optimized eddy-viscosity models. Figure 2.5 displays the real part of the fluctuating field for all state variables for the dominant SPOD and resolvent modes, comparing resolvent results using both the optimal eddy-viscosity field and the baseline case with constant $\mathrm{Re}_T = 3 \times 10^4$. It is immediately apparent that the optimal eddy-viscosity resolvent mode can closely match the observed mode shapes from SPOD for all variables (including the correct distribution of energy), while the baseline resolvent mode bears little resemblance to the SPOD modes for any of the variables.

Despite the increased alignment, there remains an obvious mismatch in u'_θ between the SPOD and resolvent modes, highlighting a statistical limitation to our approach. For the axisymmetric wavenumber, $m = 0$, perturbations in the azimuthal velocity must be zero. Both resolvent models meet this constraint, however, the SPOD mode does not. One should then view the nonzero component in the SPOD mode as a statistical error. Compared to the streamwise velocity, u'_θ is about five times smaller in magnitude, and lacks the coherent wavepacket structure of the other variables. The corresponding u'_θ contribution in the projection coefficient $|\boldsymbol{\psi}_1^* \boldsymbol{W} \boldsymbol{\psi}_1|$ is ≈ 0.08,

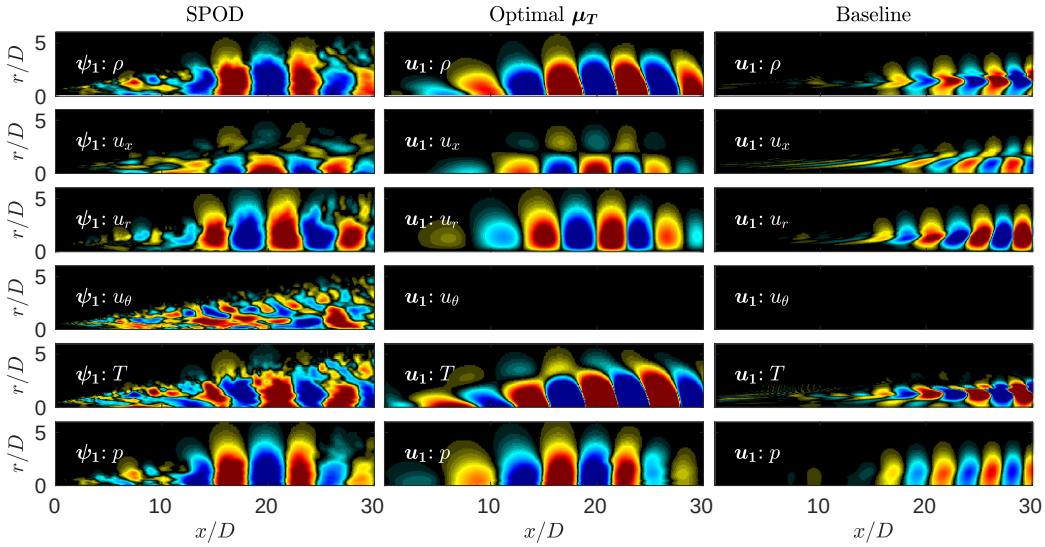

Figure 2.5: Real component of the fluctuating response state variables, $\boldsymbol{q}' = [\rho, u_x, u_r, u_\theta, T]$, and pressure, p, at $St = 0.05$, $m = 0$. The columns display SPOD ($\boldsymbol{\psi}_1$), optimal eddy viscosity ($\boldsymbol{u}_1$), and baseline ($\boldsymbol{u}_1$) modes from left to right, respectively. Contours (■■■) are given by $\pm 0.5||\boldsymbol{\psi}_1 : \cdot||_\infty$ of the SPOD mode, where $\cdot$ is the fluctuating variable in question (with $||\boldsymbol{\psi}_1 : \cdot||_\infty$ values: $[\rho, u_x, u_r, u_\theta, T, p] = [2.8, 198.6, 46.0, 37.2, 1.2, 10.4] \times 10^{-3}$).

bounding the physical maximum of the optimization to $|\boldsymbol{\psi}_1^* \boldsymbol{W} \boldsymbol{u}_1| \leq 0.92$ without considering additional error in the other variables. We link these statistical errors to the weak low-rank behavior with this frequency, where there is little eigenvalue separation between the dominant and subdominant modes (Schmidt et al., 2018). We may then view the projection-coefficient value of 0.08 as a kind of error bar on the alignments produced by the optimal eddy-viscosity field, as it is attempting to align to a mode shape that is (at this frequency) in error by as much as about 10%.

The pressure field, a quantity of particular interest for jet noise, provides a relatively simple representative mode shape for each case. We proceed by visualizing only the fluctuating pressure component for the rest of the study, however, the projection coefficients, $|\boldsymbol{\psi}_1^* \boldsymbol{W} \boldsymbol{u}_1|$, account for the full state results. Further, for all response pressure modes presented, we see similar trends and improvements in all flow variables similar to Figure 2.5.

Figure 2.6 shows the pressure modes at two low frequencies, $St = 0.05$ and 0.2, and compares the results for all considered eddy-viscosity models. The top row shows the dominant SPOD mode from the LES, the second row gives the dominant resolvent mode for the baseline case, and the remaining rows provide the four

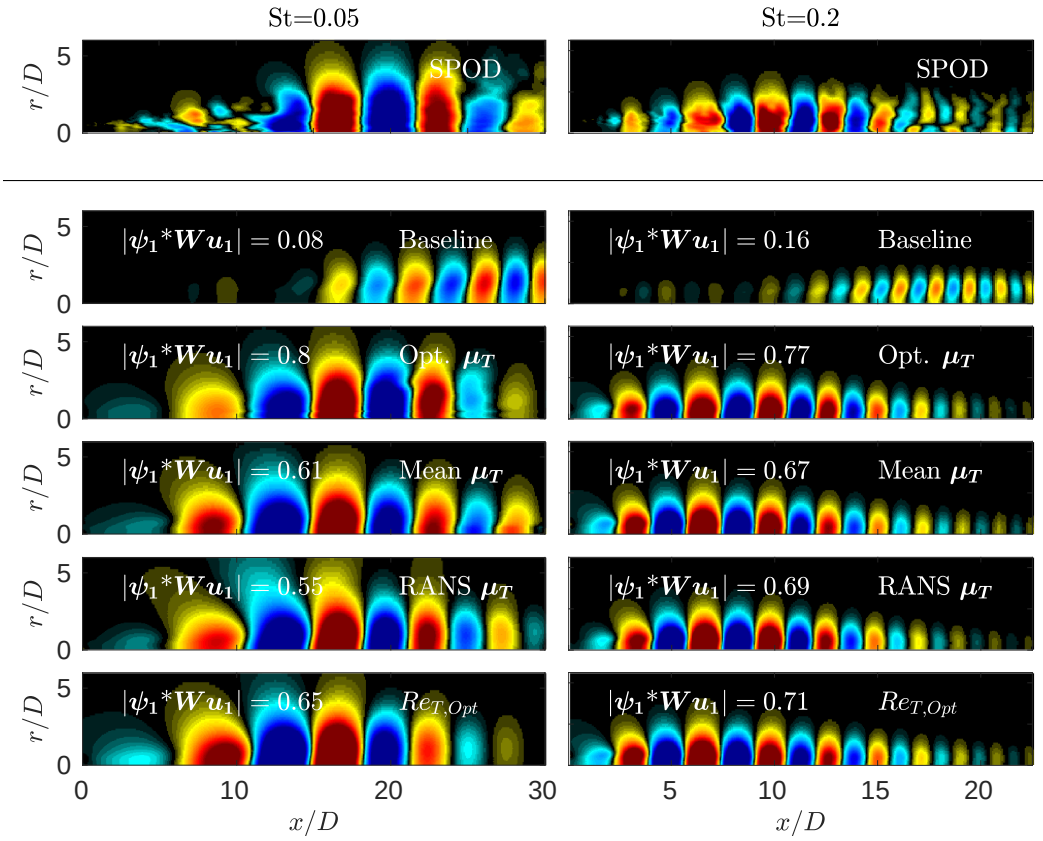

Figure 2.6: Real component of the response pressure fluctuations (■■■, $\pm 0.5||\psi_1 : p||_\infty$) for $St = 0.05$ and $St = 0.2$ in the left and right columns, respectively. Row 1 presents the dominant SPOD mode for which the optimization seeks to match. The following rows present results for the baseline, optimal eddy-viscosity field, mean-flow consistent model, RANS eddy-viscosity model, and the optimal turbulent Reynolds number.

optimized models. At low frequencies, the baseline resolvent analysis cannot capture the observed mode shapes, while the optimized eddy-viscosity models have much better alignment with SPOD. The EVRA models increase the projection coefficients by as much as 10-fold and display a wavepacket structure consistent with the SPOD mode. Orr-type modes dominate the low-frequency (i.e. $St < 0.3$) baseline resolvent spectrum (Schmidt et al., 2018), and we see that the eddy viscosity attenuates these modes in favor of a KH-like response that peaks further upstream, consistent with the observed SPOD modes.

Proceeding to higher frequencies, Figure 2.7 displays the dominant fluctuating pressure modes for SPOD and the five EVRA models for $St = 0.6$ and 1. The baseline projection coefficients are already high for these frequencies, but are fur-

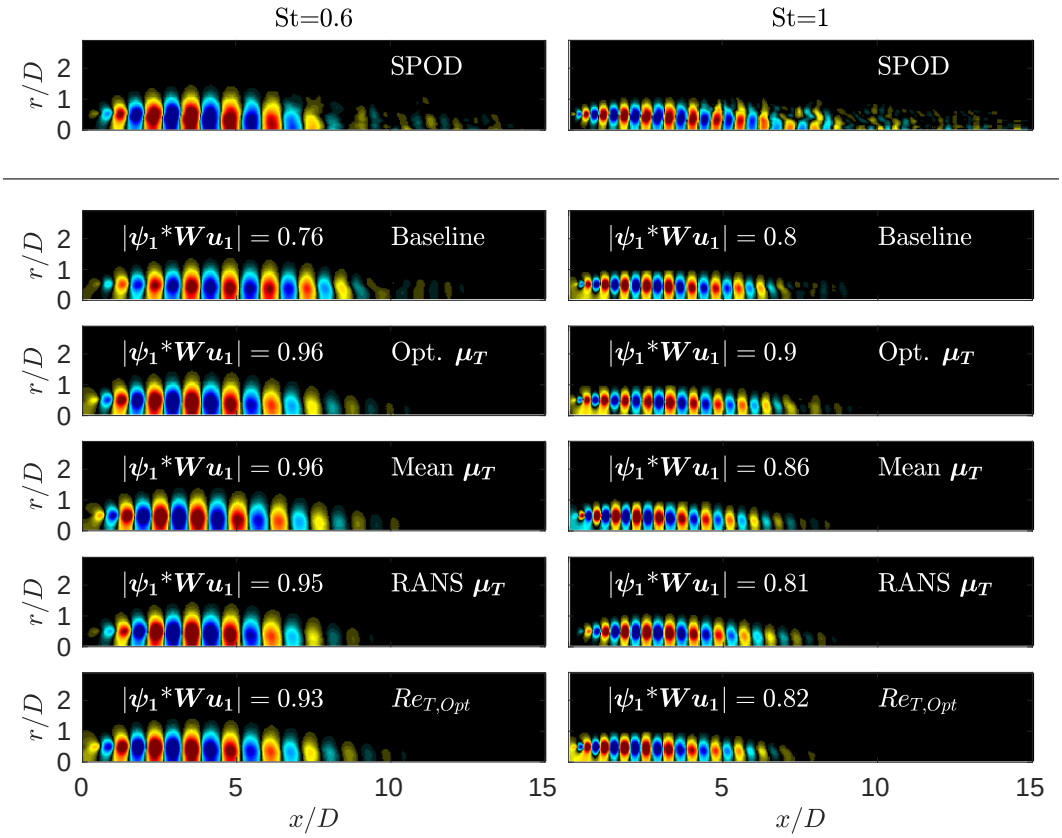

Figure 2.7: Real component of the response pressure fluctuations for $St = 0.6$ and $St = 1$ in the left and right columns, respectively. Rows present the equivalent methods as described in Figure 2.6.

ther increased with the eddy-viscosity models, reaching 96% for the optimal eddy viscosity. Here the differences in the mode shapes are subtle, with the streamwise extent of the modes shortening from the baseline case to better match the SPOD at both frequencies. At these higher frequencies, the jet response is a clear, low-rank KH wavepacket (a modal, inviscid stability mechanism), and it is thus unsurprising that the results are relatively insensitive to the precise eddy-viscosity model. However, the improved alignment is a product of the non-zero eddy-viscosity field, showing that a turbulence model is still important.

For $St = 1$, the optimized projection coefficient is falling compared to the $St = 0.6$ case. This is due to the emergence of Orr-type modes with similar energy as the KH modes. When performing SPOD in limited domains near the nozzle exit, the modal, low-rank KH response continues to dominate at much higher frequencies in the near nozzle region (Sasaki et al., 2017), but when considering the global response, the

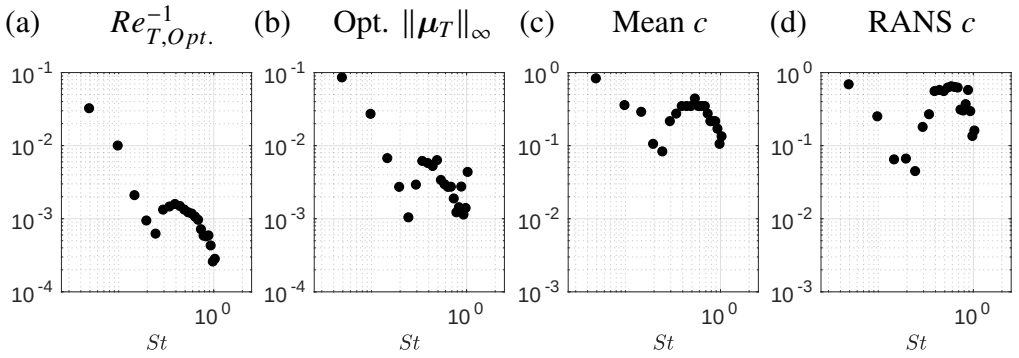

Figure 2.8: The optimal parameters across $St \in [0.05, 1]$ for (a) the optimal constant field $1/\mathrm{Re}_T$, (b) optimal eddy-viscosity field model, (c) the mean-flow consistent model, and (d) the optimal RANS model. The optimal eddy-viscosity field parameter shown is the maximum value of the field at each frequency, $\|\boldsymbol{\mu}_T\|_\infty$, while the latter two models present the optimal coefficient c. The associated alignments for each model/parameter are shown in Figure 2.4.

KH response becomes inferior, in energy, to the Orr response, which peaks further downstream.

2.5 Analysis of the optimized eddy-viscosity fields

The previous section shows that the EVRA approach results in substantial alignment of the dominant resolvent and SPOD modes. In this section, we examine the optimal parameters associated with the eddy-viscosity fields to investigate *how* the eddy viscosity improved the alignment and to identify potential universalities in modeling coefficients.

Structure of the eddy-viscosity fields

For the constant eddy viscosity, RANS-based, and mean-flow consistent eddy-viscosity fields, the optimization is over a single value, and we plot the optimal values as a function of frequency (still for $m = 0$) in Figure 2.8 (a,c,d) and the maximum value of the optimal field in 2.8 (b). We investigated several other metrics for the optimal field and each metric provided similar trends and therefore, we chose $\|\boldsymbol{\mu}_T\|_\infty$, as it gave the most intuitive comparison against the other scalar quantities. For all models, the frequency dependence of the values is similar, with three regions of interest: $St \in [0.05, 0.3]$, $St =\in [0.3, 0.8]$, and $St \in [0.8, 1]$.

In the low frequency region, the baseline jet response comprises of spatially extensive Orr-type modes that have a strong Reynolds number dependence, requiring a relatively larger eddy viscosity to damp them. For $St = 0.05$ the ratio of the molecu-

lar Reynolds number to the optimal effective Reynolds number is $\mu_j/\boldsymbol{\mu}_T \approx 13,500$, a four order-of-magnitude difference when compared to the molecular viscosity.

In the moderate frequency regime, where the baseline spectrum transitions from the broadband, viscous Orr mechanism to the low-rank, inviscid KH mechanism, eddy viscosity becomes less important, and we expect (confirming below, in § 2.7) insensitivity to the overall value based on the relatively favorable alignment achieved in the baseline case. As frequency increases, the responses transition back to a mix of KH and Orr-type waves, with a progression towards broadband, viscous Orr modes at higher frequency.

At these higher frequencies, we see that the low-frequency dependence on inverse effective Reynolds number resumes, similar to low the frequencies. Interestingly, this trend shows that at higher frequencies $\mathrm{Re}_T \rightarrow Re_j$ such that the effect of eddy viscosity "turns-off" as frequency increases and the associated wavepacket wavelength becomes small (i.e. approaching finer-scale turbulence), as expected on physical grounds.

Similar trends are observed for the mean-flow consistent and RANS eddy-viscosity coefficients. For both eddy-viscosity fields, c is less than unity and only varies from 0.7 to 0.1 with a few exceptions. These values suggest that the optimal eddy-viscosity model is a fraction of the total RANS or mean-flow consistent eddy-viscosity models that integrate all perturbations.

For the full-field eddy-viscosity optimization, we stress that its primary purpose is to determine what may be an upper bound for how well *any* eddy-viscosity model could perform. Given that the alignments between the resolvent and SPOD modes were not significantly higher for the optimized scheme than for the modeled eddy-viscosity approaches (with optimal parameters), the detailed eddy-viscosity fields are of lesser importance. Still, some aspects of the physics, such as the spatial locations where Reynolds stresses become important for each frequency, are apparent in the optimized fields. Figure 2.9 presents the optimized fields for two selected Strouhal numbers, comparing them to both the RANS and mean-flow consistent eddy-viscosity fields scaled by their optimal coefficient c at each frequency. In addition, the dominant resolvent mode, computed with the displayed optimal-eddy-viscosity field, is shown for comparison with the eddy-viscosity fields. The contours for the eddy-viscosity fields are set from 0 to the maximum value of the $St = 0.6$ optimal eddy-viscosity field.

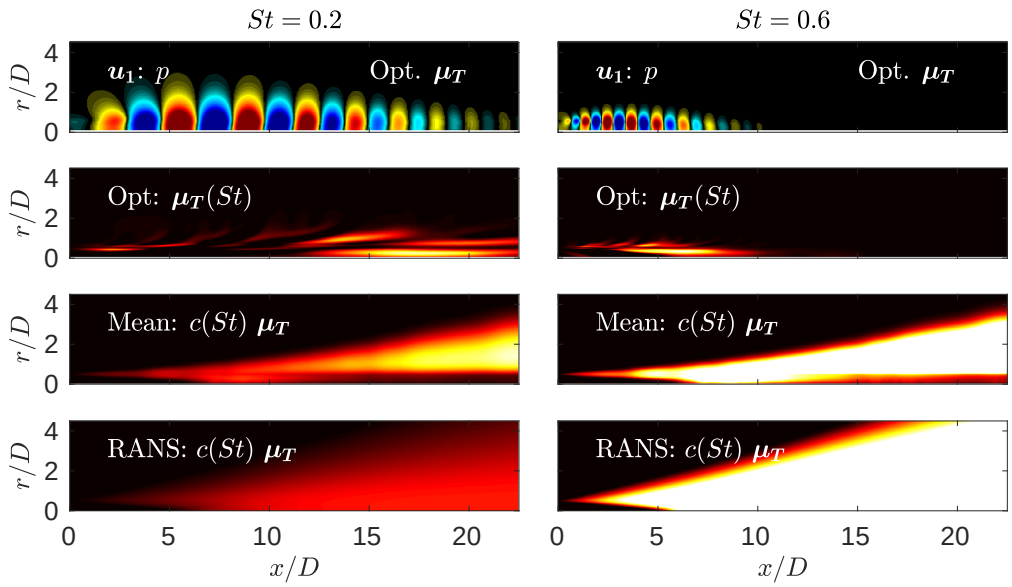

Figure 2.9: Comparisons of the optimal eddy-viscosity fields (i.e. full-field optimal, mean-flow consistent, and RANS) and the associated dominant resolvent mode found via the optimization for $St = 0.2$ and 0.6. Contours for all six eddy-viscosity fields are set from 0 to 3×10^{-3}.

Overall, both frequencies present optimal eddy-viscosity fields that are complex, unsurprising given the ability of the optimization to choose any eddy-viscosity field, constrained only by the structure of the equations and positivity. The optimal eddy-viscosity fields pinpoint the locations where linear structures break down (i.e. where nonlinearities/Reynolds stresses become important) and inform what features an eddy-viscosity model must include. In both cases, the optimization removes viscosity from the potential core (i.e. the interior region of the jet relative to the critical layer), when compared to the initial guess, while increasing the turbulent viscosity just outside of the critical layer. The increase in eddy-viscosity is most often observed just downstream of the peak amplitude of the wavepacket, coinciding with each wavepacket's decay downstream.

Although not entirely clear from Figure 2.9, these findings are reasonably consistent with each of the modeled eddy-viscosity fields when restricting the view to the region where the resolvent/SPOD mode has significant amplitude. We can see that both the RANS and mean-flow consistent eddy-viscosity fields present similar features as the optimal field, explaining the ability of each model to achieve nearly optimal results. We will show in the following section how such features also explain the ability of the RANS and mean-flow consistent models to predict the subdominant

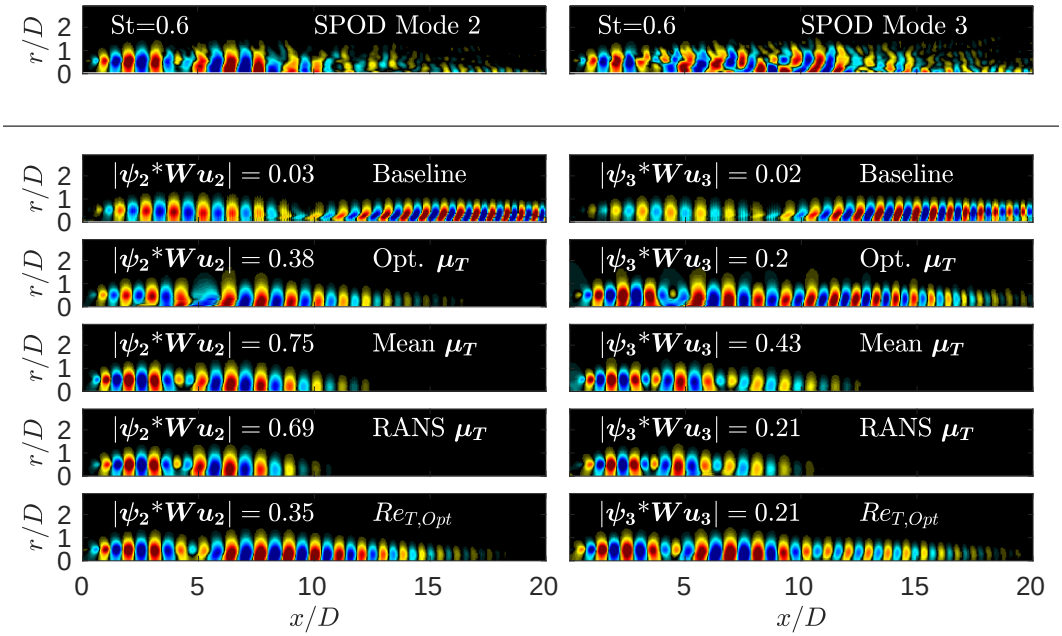

Figure 2.10: Subdominant modes 2 and 3 at $St = 0.6, m = 0$ in the left and right columns respectively for SPOD, baseline, and all EVRA models.

modes, which require further turbulence modeling downstream.

2.6 Alignment of subdominant modes

Although the optimization presented only aligns the dominant SPOD and resolvent modes, subdominant modes are also of interest, particularly as they are necessary to reconstruct flow statistics in the near field and are relevant for modeling coherence decay associated with the "jittering of wavepackets" to produce sound (Cavalieri, Jordan, Agarwal, et al., 2011). In this section we seek to answer two questions: whether alignment with only the dominant mode substantially alters the alignment of the subdominant modes and the effect of expanding the optimization to subdominant modes. We first assess the former case using the optimal parameters for each method. We show the computed subdominant modes in Figure 2.10 for modes 2 and 3 for the $St = 0.6$, $m = 0$ frequency-wavenumber pair.

Comparing the second mode to the baseline case ($\mathrm{Re}_T = 3 \times 10^4$), we find that all EVRA models give significantly improved alignments, reaching ≈70% for the RANS and mean-flow consistent models. Both the RANS and mean-flow consistent models are superior to the optimal eddy-viscosity field, which is only fitted to align the dominant mode. The RANS and mean-field models are also superior for the

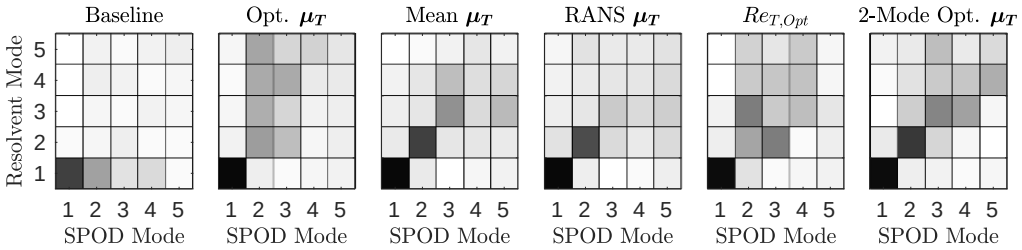

Figure 2.11: Projections of the first five SPOD modes into the first five resolvent modes computed for all EVRA models at $St = 0.6, m = 0$, including the 2-mode optimization shown in Figure 2.12.

third, fourth, and fifth modes (the latter two not shown for brevity), but with an alignment that falls off with increasing mode number.

To observe how well the optimization of the first SPOD mode models the forcing statistics (i.e. diagonalizes the forcing CSD $\boldsymbol{S_{ff}}$), we compare projections of the first five SPOD modes with the first five modes from each eddy-viscosity method (including a 2-mode optimization described next) in Figure 2.11. The plots show that the EVRA models, in particular the RANS and mean-flow consistent models, are superior at diagonalizing the CSD when compared to the baseline case.

Although the optimal eddy-viscosity field, aligned only with the dominant SPOD mode, shows improvements in the subdominant modes, we can extend the optimization to align an arbitrary number of subdominant modes and achieve alignment superior to any eddy-viscosity model. However, convergence issues with increasing SPOD mode number suggest that optimizing for many modes (e.g. $n > 5$) would have marginal returns. For this study, we present only the optimization of both the first and second modes at $St = 0.6$, $m = 0$ to show the generality of the optimization framework and the physical implications of the associated eddy-viscosity field for the subdominant modes.

Figure 2.12 presents the aligned resolvent mode via the optimization and the associated eddy-viscosity field for the first subdominant mode. By including the second SPOD mode, the optimization can achieve an alignment of 77%, superior to any of the other eddy-viscosity models, without altering the alignment of the dominant mode, 96%. We also observe that the remaining subdominant modes also increase in their projections, as shown in Figure 2.11. This observation is likely linked to the difference in mechanisms of the dominant and subdominant modes at $St = 0.6$, $m = 0$. The dominant mode is KH-type, while the subdominant modes are of

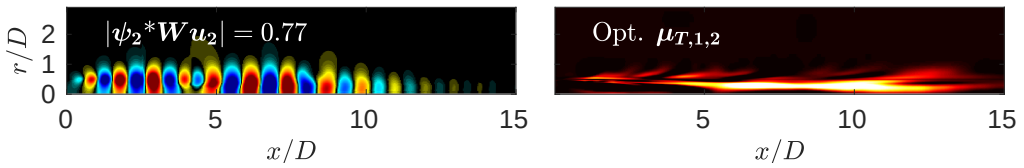

Figure 2.12: The second subdominant mode at $St = 0.6$ and the associated eddy-viscosity field that provides the optimal alignment for both modes. The contour for the eddy-viscosity field is set to the same value as those shown in Figure 2.9 from 0 to 3×10^{-3}.

Orr-type. By aligning just the first Orr-type mode, we observe improved alignments for the entire family of Orr modes, conversely, alignment of only the KH mode does not substantially improve Orr modes.

The increase in alignment results from additional eddy-viscosity located downstream of the 1-mode, KH-type field, $\boldsymbol{\mu}_{T,1}$, shown in Figure 2.9. The second mode imposes a need for further eddy-viscosity acting further downstream and towards the centerline, as representative of the Orr-mechanism at $m = 0$ for turbulent jets (Pickering, Rigas, Nogueira, et al., 2020). We find that this additional downstream eddy-viscosity, present in both the RANS and mean-flow consistent models, is responsible for the increased subdominant mode alignment. Considering the simpler RANS (and mean-flow) model also shows similar downstream structure, we investigate its merit for a predictive model in the next section.

2.7 Towards a predictive EVRA model for turbulent jets

Through the previous sections, we have shown that both the RANS and mean-flow consistent eddy-viscosity models perform well across Strouhal numbers from 0.05 to 1 at $m = 0$, provided the overall constant associated with their application to the disturbance fields is optimal (at each frequency and azimuthal mode number). In this section, we consider the sensitivity of the results regarding the choice of a frequency (and wavenumber) independent constant, and show that over a range of frequencies and azimuthal mode numbers, alignments are relatively insensitive to the choice of a constant, such that a single, universal value may be acceptable. While both RANS and mean-flow consistent models both performed well with optimal coefficients, we focus only on the RANS $k - \epsilon$ model, as it is better regarded as universal across a range of flows. We then apply EVRA-RANS to the $M_j = 0.4$ jet using a single constant to six azimuthal wavenumbers, $m = 0 - 5$, and find substantially improved predictions when compared to the baseline. We also find similar observations when using the same EVRA-RANS model for both the transonic and supersonic jets.

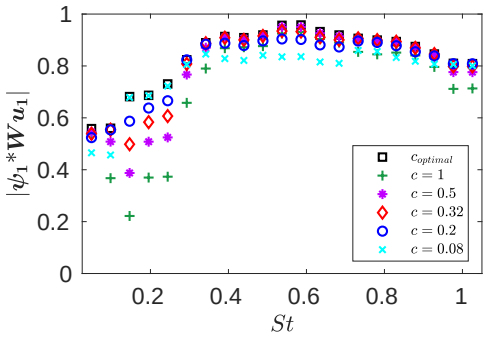

Figure 2.13: Alignments across all Strouhal numbers for the RANS eddy-viscosity model coefficients compared with the optimal RANS coefficient at each frequency. The RANS coefficients are $c = [1, 0.5, 0.32, 0.2, 0.08]$.

Finally, we present the effect of the eddy viscosity on the resolvent spectra.

Frequency and azimuthal mode sensitivity

The optimal RANS coefficients (Figure 2.8) ranged from $c = 0.7 - 0.004$, with a relatively constant region, $c = 0.5$, for moderate frequencies and, considering the fully optimized eddy-viscosity field produced only marginally improved alignments for most cases, the results may not be sensitive to the precise constant. We test this hypothesis for the RANS model across a range of frequencies with proposed "universal" values of constant $c = [1, 0.5, 0.32, 0.2, 0.08]$. We plot the resulting alignments versus frequency in Figure 2.13. With little compromise, compared to the optimal constant for each frequency, a single constant of $c = 0.2$ provides significant alignment across all frequencies up to $St = 1$. Although not shown for brevity, we found similar observations using $c = 0.08 - 1$ for all three Mach numbers and six azimuthal wavenumbers. In these cases, not only did $c = 0.2$ give the best overall alignment, but the alignments were comparably insensitive to the value of c chosen over this range.

We do not present a rigorous justification for the value of $c = 0.2$, however, c may have a connection with LES eddy-viscosity modeling. If we compare the empirical coefficients used in this RANS eddy-viscosity analysis, cC_μ, to the square of the Smagorinsky coefficient, C_s^2, used for SGS eddy-viscosity fields in LES (Smagorinsky, 1963), we can find that the value of $c = 0.2$ lies within the bounds of wall-bounded and isotropic turbulence. Setting equal the products of each set of coefficients, we find $c = C_s^2/C_\mu$. Then using the $M_j = 0.4$ RANS coefficient, $C_\mu = 0.073$, and the commonly used range of C_s, 0.1 for wall-bounded flows and

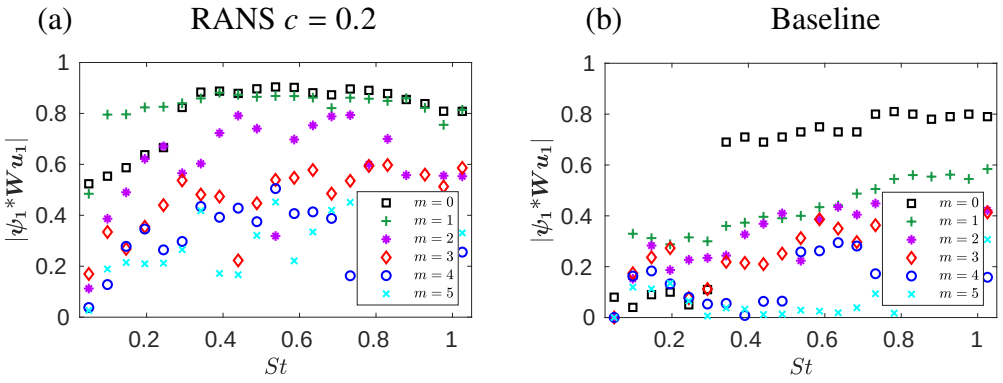

Figure 2.14: Alignments for frequencies, $St \in [0.05, 1]$, and azimuthal wavenumbers, $m = 0 - 5$, for the (a) RANS eddy-viscosity model using $c = 0.2$ and the (b) baseline, constant eddy-viscosity case (i.e. $\mathrm{Re}_T = 3 \times 10^4$).

0.18 for isotropic turbulence (Zhiyin, 2015), we find that $c = [0.14 - 0.45]$ (ranges for the $M_j = 0.9, 1.5$ jet are $c = [0.15 - 0.48], [0.17 - 0.57]$, respectively). This range approximately corresponds to the acceptable values found in Figure 2.13.

For nonzero azimuthal modes, Figure 2.14 presents the alignment of the EVRA-RANS model with SPOD using $c = 0.2$ and the baseline case for $m = 0 - 5$. The EVRA-RANS model substantially increases the alignments for all nonzero wavenumbers. The results for $m = 1$ are particularly encouraging, with a uniform, 80% alignment across all frequencies. Azimuthal modes greater than 1 result in poorer alignment, albeit much improved compared to the baseline case, especially when $m > 2$.

Expanding to nonzero azimuthal wavenumbers, the eddy-viscosity field also affects a third mechanism observed in the global SPOD spectrum (as $St \to 0$), the lift-up mechanism (Pickering, Rigas, Nogueira, et al., 2020). Similar to the Orr mechanism, the lift-up mechanism arises from triadic nonlinear interactions in the flow (Hamilton, Kim, and Waleffe, 1995; Sharma and McKeon, 2013; Giovanetti, Sung, and Hwang, 2017; Cho, Hwang, and Choi, 2018), identifying it as a likely benefactor to an EVRA approach. Figure 2.14 supports this claim, showing significant improvements at low frequencies for nonzero wavenumbers. These observations also agree with Pickering, Rigas, Nogueira, et al. (2020), who showed that resolvent modes related to streaks required an eddy-viscosity model (using the TKE model reported by Pickering, Rigas, Sipp, et al. (2019) with $c = 0.0065$). They also observed that, in turbulent jets, the spatial extent of resolvent modes increase as frequency decreases and that without an eddy-viscosity, modes extend indefinitely

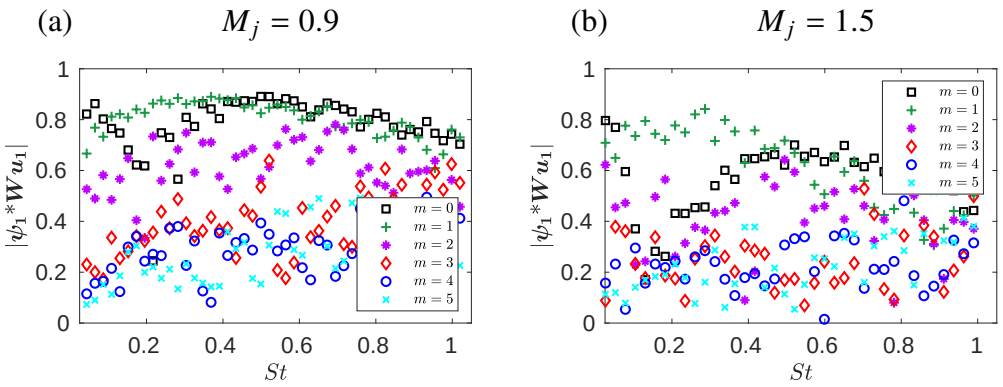

Figure 2.15: Alignments using the RANS eddy-viscosity model with coefficient $c = 0.2$ across Strouhal numbers $St \in [0.05, 1]$ and azimuthal wavenumbers $m = 0 - 5$ for the (a) $M_j = 0.9$ and (b) 1.5 jets.

downstream for $St = 0$. This is analogous to theory surrounding streaks where the lift-up mechanism presents a rapid spatial growth of streamwise streaks until viscous dissipation becomes dominant and the structures decay (Hultgren and Gustavsson, 1981). Considering the significant improvements between alignments for low-frequency and nonzero wavenumbers, we find the lift-up mechanism to also be sensitive to an eddy-viscosity model.

Transonic and supersonic turbulent jets

We now generalize the RANS-EVRA model performance for both $M_j = 0.9$ and 1.5 turbulent jets using $c = 0.2$. Figure 2.15 provides the alignments across frequencies and azimuthal wavenumbers for each. The transonic jet gives substantial agreement for $m = 0$ and $m = 1$ at about 80% for much of the frequency range, while $m = 2$ gives alignments of 60%, on average. For the supersonic jet, the agreement is not as favorable, however, much improved from the $\mathrm{Re}_T = 3 \times 10^4$ alignments (not shown here for brevity).

The RANS eddy-viscosity model increases many of the alignments, however, poor alignments remain, and these alignments appear to correspond to SPOD spectra without large energy separation. As shown earlier in Figure 2.4, EVRA and SPOD modes aligned best when there exists large eigenvalue separation between the first and second SPOD mode. We find similar behavior here for all cases. Figure 2.16 presents the SPOD spectra of the first five modes across all six azimuthal wavenumbers and three turbulent jets, with their associated 95% confidence intervals in light blue. A handful of the spectra show a clear separation between mode energies, such as those between the first and second mode for $M_j = 0.4$, $m = 0$

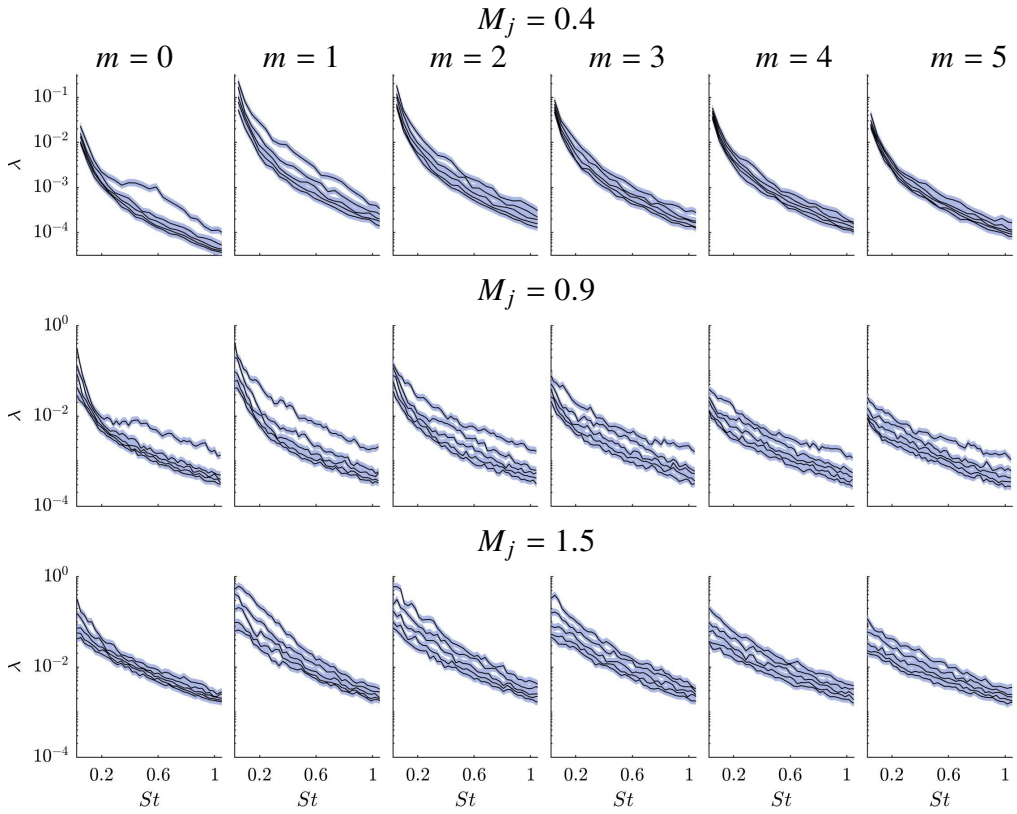

Figure 2.16: Spectra, and their associated 95% confidence interval in light blue, of the first five SPOD modes for azimuthal wavenumbers $m = 0 - 5$ from left to right and the subsonic, transonic, and supersonic jets from top to bottom, respectively.

and 1, for $M_j = 0.9$, $m = 0$ and 1 (and higher frequencies for $m = 2 - 5$), and for $M_j = 1.5$, $m = 1$. In each case where there is large eigenvalue separation, we find, from Figures 2.14 and 2.15, significantly greater agreement in projection coefficients between the resolvent and SPOD modes, while finding poor projections for cases without clear separation in eigenvalues. We also observe this for the subdominant modes investigated in the $M_j = 0.4$, $m = 0$ case in § 2.6.

These observations point to a limitation to our method when comparing EVRA modes with SPOD modes. For the SPOD modes without clear eigenvalue separation, the eigenvalues themselves fall within the uncertainty bands (i.e. 95% confidence interval) of the other modes. The eigenvectors corresponding to these eigenvalues are expected to have, at best, similar uncertainty levels. Thus, without more data, it is not possible to attribute the lack of agreement to a failure of the EVRA ansatz.

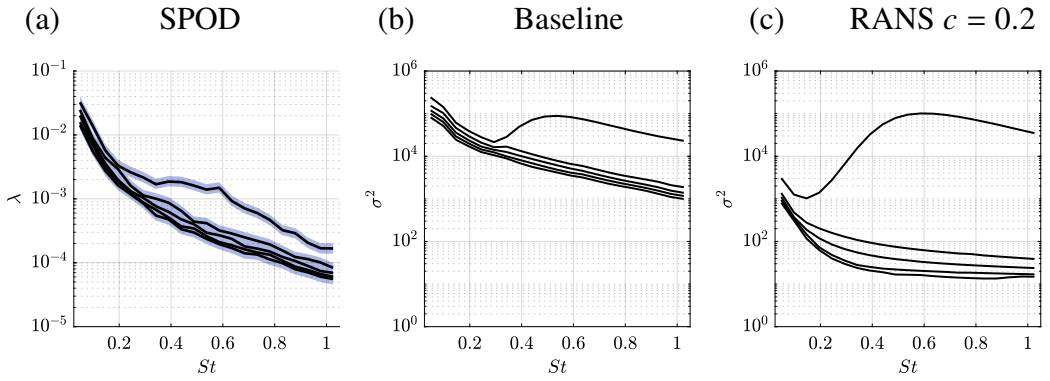

Figure 2.17: Spectra of first five (a) SPOD, (b) baseline resolvent, and (c) the RANS eddy-viscosity model resolvent modes at $m = 0$ for $St \in [0.05, 1]$.

Singular values

We return to the $m = 0$, $St \in [0.05, 1]$ case to assess the EVRA-RANS $c = 0.2$ model's effect on the singular values and compare them to the baseline case and the SPOD eigenvalues. Figure 2.17 provides the spectra of the first five modes for SPOD (accompanied by a shaded region providing the 95% confidence interval of the eigenvalues), the baseline resolvent model, and the RANS-EVRA model (using $c = 0.2$) for $m = 0$. Comparing the resolvent spectra to the SPOD spectra, we immediately see that the separation between λ (i.e. the ratio between λ_n/λ_{n+1}) and σ^2 of either resolvent models does not compare favorably. In fact, the RANS-EVRA spectrum has increased its energetic separation when compared to the baseline case.

This behavior may be linked to multiple (in this case two for $m = 0$) distinct mechanisms represented in the flow, the KH and Orr-mechanisms. As detailed earlier, the inclusion of an eddy-viscosity model presents a substantial effect on the Orr modes, significantly reducing the streamwise extent of each mode, while the KH modes are relatively unchanged. We observe an analogous effect here in Figure 2.17 where the singular values related to the Orr mechanism decrease substantially, pulling away from the unaffected singular values of the KH mechanism, resulting in a much larger separation between singular values than is observed between the SPOD eigenvalues. This sensitivity of Orr modes to an eddy-viscosity was also observed in Schmidt et al. (2018) at $St = 0.6, m = 0$ when adjusting Re_T, finding that the squared singular values of the subdominant Orr modes scaled as $\mathrm{Re}_T^{1.2}$. We observe the same effect using the RANS eddy-viscosity model, interestingly (and perhaps unsurprising given the preceding discussions), Figure 2.17 (c) provides similar values as those reported by Schmidt et al. (2018) at $St = 0.6, m = 0$ when using $\mathrm{Re}_T = 10^3$.

Figure 2.17 (a) and (c) also show that the forcing amplitudes, λ_β, are not uniform in turbulent jets, contrary to a customary assumption used in resolvent analysis where $\mathbf{\Lambda}_\beta = \alpha \boldsymbol{I}$, with α as an arbitrary constant (Morra et al., 2019; Lesshafft et al., 2019; Hwang and Eckhardt, 2020). Focusing on only the first and second resolvent and SPOD modes for $St = 0.6$ and $m = 0$, where mode alignments are 95% and 69%, respectively (the optimal-field case increases the latter value to 77% without appreciably changing the singular value), we may assume that the diagonal components of the forcing, $\lambda_{\beta,1}$ and $\lambda_{\beta,2}$, account for nearly all the energetic contributions by these two modes. As shown by Equation (2.17), this assumption allows for a one-to-one comparison between the first two SPOD eigenvalues, resolvent singular values, and forcing amplitudes (i.e. $\lambda_{\beta,n} = \lambda_n \sigma_n^{-2}$ for $n = 1, 2$). If the customary assumption of uniform forcing is applied, $\mathbf{\Lambda}_\beta = \alpha \boldsymbol{I}$, then $\alpha = \lambda_1 \sigma_1^{-2} = \lambda_2 \sigma_2^{-2}$ or, alternatively, $\lambda_1/\lambda_2 = \sigma_1^2/\sigma_2^2$, and Figure 2.17 shows this cannot be true. Therefore, unless the SPOD and resolvent spectra are equivalent, we must model or estimate the non-trivial forcing amplitudes.

The sizeable difference between the singular values reflects the forcing of different mechanisms at significantly different amplitudes in the flow. Pickering, Rigas, Nogueira, et al. (2020) showed that there are three distinct spatial regions that lead to the most efficient amplification of the KH, Orr, and the lift-up mechanisms. They found that regions localized near the nozzle where perturbations are smaller, associate with KH-type responses, while regions downstream and near the end of the potential core where perturbations are significantly larger, support Orr-type responses. Considering these observations, a logical next step in completing a resolvent-based turbulence model is to tie the forcing amplitude of different modes to the turbulence intensities in the respective regions that force them.

2.8 Conclusions

We developed a data-informed optimization that quantitatively tested the extent to which an eddy-viscosity model improves the alignment (i.e. agreement) between observed large-scale structures, educed via SPOD, and those computed from resolvent analysis. This eddy-viscosity approach acts as a proxy for modeling the effect of turbulence on large-scale structures, and we found this approach provides substantial improvements in agreement (i.e. when compared to a baseline case that used a constant eddy-viscosity model corresponding to a value of $\mathrm{Re}_T = 3\times10^4$). By directly optimizing the eddy viscosity field to achieve the best alignment, we found alignments between resolvent and SPOD modes as high as 96% or improvements of

over ten-fold from the baseline alignment (i.e. 8% to 80%).

Across the frequencies and wavenumbers considered, the addition of an eddy-viscosity model to the resolvent operator highlighted its effect on the different amplifications mechanisms in the turbulent jet: Orr-type, KH-type, and lift-up. Although eddy-viscosity models improved modes related to the KH-type mode, we found KH modes to be rather insensitive to the eddy-viscosity field, a result expected from the inviscid nature of the inflectional KH instability. For resolvent modes associated with the Orr and lift-up mechanisms, known to arise from nonlinear interactions, we found significant sensitivity. Resolvent modes computed without a sufficient eddy-viscosity model were visually unrecognizable from their SPOD counterpart, while those computed with an eddy-viscosity model aligned to nearly 80%.

The optimal eddy-viscosity field also provided an upper bound for mode agreement, providing a benchmark to assess three additional eddy-viscosity models. Of these models, we found that traditional eddy-viscosity models (e.g. RANS based) perform nearly as well as the optimal eddy-viscosity models in aligning the most energetic mode. The traditional models even outperformed the optimal model (i.e. optimal in the first mode) when considering the subdominant modes, giving the greatest diagonalization of the forcing CSD at $m = 0$, $St = 0.6$ (i.e. ability to model the effect of nonlinear forcing), leading to a more efficient resolvent basis for describing turbulent jets.

Finally, we tested the modeling potential of a RANS-inferred EVRA through a sensitivity analysis and observed its performance over frequency, azimuthal wavenumber, and Mach number. We found the sensitivity of the RANS-based EVRA model's calibration constant, c, to be weak, giving similar agreement for coefficients ranging over an order of magnitude. We found that the coefficients resulting in similar agreement fell within a range of values that may have a connection to the Smagorinsky coefficient for sub-grid scale modeling of eddy viscosity in LES. Choosing a frequency-independent RANS-EVRA model (i.e. $c = 0.2$), we tested its performance across six azimuthal frequencies and three turbulent jets, spanning subsonic, transonic, and supersonic regimes. For the first three azimuthal wavenumbers (i.e. $m = 0 - 2$), we observed substantially increased alignments for all three turbulent jets and across Strouhal numbers $St \in [0.05, 1]$. Overall, these results show that "classical" eddy-viscosity models (RANS or a mean-flow consistent model) aid in estimating the impact of the Reynolds stresses for resolvent analysis.

While the present data-driven analysis points to the efficacy of relatively simple eddy-viscosity-based models for modeling the effect of nonlinear forcing and providing a more efficient resolvent basis, there remains a need for refinements to this approach and careful comparison and consideration of alternative formulations.

Acknowledgments

This research was supported by a grant from the Office of Naval Research (grant No. N00014-16-1-2445) with Dr. Steven Martens as program manager. E.P. was supported by the Department of Defense (DoD) through the National Defense Science & Engineering Graduate Fellowship (NDSEG) Program. The LES study was performed at Cascade Technologies, with support from ONR and NAVAIR SBIR project, under the supervision of Dr. John T. Spyropoulos. The main LES calculations were carried out on DoD HPC systems in ERDC DSRC.

Chapter 3

LIFT-UP, KELVIN-HELMHOLTZ, AND ORR MECHANISMS IN TURBULENT JETS

Published in the *Journal of Fluid Mechanics*, August 2020

Chapter Abstract

Three amplification mechanisms present in turbulent jets, namely lift-up, Kelvin-Helmholtz, and Orr, are characterized via global resolvent analysis and spectral proper orthogonal decomposition (SPOD) over a range of Mach numbers. The lift-up mechanism was recently identified in turbulent jets via local analysis by Nogueira et al. (*J. Fluid Mech.*, vol. 873, 2019, pp. 211–237) at low Strouhal number (St) and non-zero azimuthal wavenumbers (m). In these limits, a global SPOD analysis of data from high-fidelity simulations reveals streamwise vortices and streaks similar to those found in turbulent wall-bounded flows. These structures are in qualitative agreement with the global resolvent analysis, which shows that they are a response to upstream forcing of streamwise vorticity near the nozzle exit. Analysis of mode shapes, component-wise amplitudes, and sensitivity analysis distinguishes the three mechanisms and the regions of frequency-wavenumber space where each dominates, finding lift-up to be dominant as $St/m \to 0$. Finally, SPOD and resolvent analyses of localized regions show that the lift-up mechanism is present throughout the jet, with a dominant azimuthal wavenumber inversely proportional to streamwise distance from the nozzle, with streaks of azimuthal wavenumber exceeding five near the nozzle, and wavenumbers one and two most energetic far downstream of the potential core.

3.1 Introduction

Coherent structures in turbulence are responsible for the transport of mass, momentum, and energy, and the radiation of acoustic waves. Early observations of Mollo-Christensen (1967) and Crow and Champagne (1971) found orderly structure in turbulent jets and Brown and Roshko (1974) in planar mixing layers. Almost fifty years later, a full understanding of the underlying mechanisms driving the generation and sustenance of coherent structures remains elusive, yet their connection to longstanding engineering problems such as jet acoustics (Jordan and Colonius, 2013) and drag in wall-bounded flows (Jiménez, 2018) has become increasingly clear.

The interpretation and modeling of coherent structures in turbulence have historically taken the form of instabilities of (typically steady) basic flows. In jet turbulence, Crighton and Gaster (1976) hypothesized that coherent structures could be described as linear instabilities of the mean flow via a modal analysis. Since

that time, researchers have computed modal and non-modal mechanisms in jets with varying degrees of generality. Earlier work focused on parabolized stability equations (PSE), and Gudmundsson and Colonius (2011) showed that PSE solutions for an experimentally measured jet mean flow yielded good predictions for the dominant frequency/azimuthal mode structures educed from a near-field caged microphone array. However, in fully global studies, Garnaud et al. (2013a) yield a stable spectrum (for jets that are not too highly heated), and the characterization of instability mechanisms required transient (non-modal) growth. Resolvent analysis, by contrast, characterizes linear amplification of disturbances in the frequency domain, and is therefore easier to relate experimental mechanisms in both transitional and turbulent flows. McKeon and Sharma (2010) proposed a resolvent interpretation for the turbulent case, where nonlinear interactions are regarded as forcing terms to a linearized operator that amplifies them according to the turbulent mean flow. Resolvent analysis of a variety of jet mean flows has been reported in the literature (Garnaud et al., 2013b; Jeun, Nichols, and Jovanović, 2016; Semeraro, Lesshafft, et al., 2016; Schmidt et al., 2018; Lesshafft et al., 2019) and has shown two essentially different linear amplification mechanisms, one associated with the traditional, modal (parallel-flow) Kelvin-Helmholtz (KH) instability and the other as an Orr-type mechanism, also identified through PSE by Tissot, Lajús Jr, et al. (2017).

The KH mechanism has long been invoked to describe coherent structures in both transitional and turbulent planar shear layers and jets. Strictly speaking, the mechanism itself is not defined outside of the context of parallel/quasi-parallel laminar shear layers, where, in the spatial stability theory, KH is an unstable modal solution with an associated spatial growth rate. For jets, the solution is typically a convective instability, and, under spreading of the flow, an initially growing wave (at a fixed frequency) will eventually become neutral and decay (Crighton and Gaster, 1976). For the axisymmetric azimuthal wavenumber, $m = 0$, the resulting wavepacket has a nearly constant phase speed $c_{ph} \approx 0.8$ (for Strouhal number, $St \in [0.3, 1]$) (Michalke, 1984; Malik and Chang, 1997; Schmidt et al., 2018), a phase change in streamwise velocity over the critical layer (Cavalieri, Rodríguez, et al., 2013), and is coincident with what has been termed the preferred mode of the jet (most amplified mode to external forcing) between Strouhal numbers $\approx 0.3 - 1$ (Morris, 1976; Ho and Huerre, 1984; Tam and Hu, 1989; Gudmundsson and Colonius, 2011; Garnaud et al., 2013b; Rodríguez et al., 2015; Semeraro, Lesshafft, et al., 2016; Schmidt et al., 2018; Lesshafft et al., 2019). According to the parallel theory and its

quasi-parallel extensions, the mode is unstable at low frequencies but with a growth rate that goes to zero faster than the frequency. In more recent global stability (Nichols and Lele, 2011) and resolvent analyses (Garnaud et al., 2013b; Semeraro, Lesshafft, et al., 2016; Jeun, Nichols, and Jovanović, 2016; Schmidt et al., 2018; Lesshafft et al., 2019), the optimal resolvent response has been related to the KH mechanism from $St \in [0.3, 1]$, possessing similar characteristics described above through quasi-parallel analysis. Each of these resolvent studies found the KH response, triggered by optimal forcing localized to the initial shear layer (i.e. the lip line ($r/D = 0.5$) at the nozzle exit), to exhibit high gain, as well as significant gain separation between the optimal and sub-optimal modes, suggesting an intrinsic mechanism reminiscent of a parallel-flow modal instability. At low frequencies, the gain separation diminished, and Schmidt et al. (2018) explicitly tracked the KH mode for $St < 0.3$, finding the KH mode fell into the sub-optimal gains of the resolvent spectrum and was overtaken by another family of resolvent response modes governed by the Orr mechanism.

What we term the Orr mechanism, by contrast with KH, is, in the context of the response of jets, a relatively recent observation based on either non-modal parallel-flow or global analysis (Garnaud et al., 2013b; Semeraro, Lesshafft, et al., 2016; Tissot, Lajús Jr, et al., 2017; Tissot, Zhang, et al., 2017; Schmidt et al., 2018; Lesshafft et al., 2019). The characteristics of the Orr mechanism are similar to what has been observed in non-modal analyses of wall-bounded flows (Farrell, 1988; Dergham, Sipp, and Robinet, 2013; Sipp and Marquet, 2013; Jiménez, 2018). The Orr wavepacket has a phase speed of $c_{ph} \approx 0.4$ (Schmidt et al., 2018) (at low frequencies, $St < 0.3$) and is forced (or most efficiently initialized) by structures oriented at 45 degrees against the direction of mean shear, while the response structure that appears downstream is oriented at 45 degrees along the direction of mean shear. Structures are thus tilted by the mean shear, with algebraic amplitude growth of velocity fluctuations in this process (Jiménez, 2013). Schmidt et al. (2018) showed that modes with these characteristics were the dominant global resolvent modes in the jet at high frequencies (i.e. $St > 2$), for all m. For $m = 0$, at low frequencies (i.e. $St < 0.3$ and mentioned above) the Orr mechanism appears again as the dominant mode as the gain associated with the KH mode becomes small and falls below the gains of Orr responses.

However, these previous global resolvent computations neglected the lowest-frequency region of the spectrum, owing largely to computational difficulties, i.e. the large

spatial domains required. Recently, Nogueira et al. (2019) presented evidence, both through spectral proper orthogonal decomposition (SPOD) of particle image velocimetry data and a locally parallel resolvent analysis, that a third and uniquely distinct mechanism is at play in the low-frequency region of the spectrum, namely the lift-up mechanism.

The lift-up mechanism (Ellingsen and Palm, 1975) and the associated coherent structures, streaks, have long been understood as an important mechanism in wall-bounded flows (see review by Brandt (2014) and references therein). Parallel to the history of mechanism identification in jet flows, the lift-up mechanism and its interplay with the Tollmien-Schlichting and Orr mechanisms has been systematically described, first through observations (Kline et al., 1967; Klebanoff, 1971; Kim, Kline, and Reynolds, 1971), then local analyses (Moffatt, 1965; Ellingsen and Palm, 1975; Landahl, 1980), followed by transient growth (Butler and Farrell, 1992; Farrell and Ioannou, 1993), and most recently resolvent analysis (Hwang and Cossu, 2010a; Marant and Cossu, 2018; Abreu et al., 2019). The salient properties of the lift-up mechanism include streamwise vortices (rolls with streamwise vorticity) that lift up low-speed fluid from the wall (and push high-speed fluid toward the wall) until viscous dissipation becomes important. The associated optimal forcing takes the form of streamwise rolls (cross-stream forcing components) which result in growth of both streamwise response rolls and the streamwise velocity component (streaks). Although research surrounding streaks is most closely tied with wall-bounded flows, it is known that the wall is not necessary for the lift-up mechanism to persist (Jiménez and Pinelli, 1999; Mizuno and Jiménez, 2013; Chantry, Tuckerman, and Barkley, 2016).

Around the same time that the identification and recognition of the lift-up mechanism was being studied in wall-bounded flows, so too were the implications of streamwise vortices in free shear flows, in particular, the plane free shear layer. The earliest theoretical evidence of streaks in the plane free shear layer likely belongs to Benney and Lin (1960) and Benney (1961), who studied secondary instabilities of the flow in the form of weakly nonlinear interactions between two-dimensional and three-dimensional waves. They found streamwise vortices to be responsible for alternate steepening and flattening of the velocity profile, associated with the presence of streaks. Miksad (1972) first observed this behavior, followed by the observations of Konrad (1976), Breidenthal (1978), Bernal, Breidenthal, et al. (1979), Bernal (1981), Breidenthal (1981), and Bernal and Roshko (1986), along with numerical

visualizations of Jimenez, Cogollos, and Bernal (1985), Metcalfe et al. (1987), and Rogers and Moser (1992).

Advancing the original theoretical work of Benney and Lin, Widnall, Bliss, and Tsai (1974) and Pierrehumbert and Widnall (1982) made explicit the connection of streamwise vortices and streaks through secondary instability of the plane free shear layer. Introducing KH-like vortices into the flow and increasing their amplitude produced three-dimensional modes that became unstable, leading to streamwise vortex generation along with streaks. Further three-dimensional, secondary-flow theory came via the approximate dynamical models of Lin (1981), Lin and Corcos (1984), and Neu (1984) who assumed generation of streamwise vorticity occurs in the braid regions by the strain field of two adjacent spanwise structures, resulting in streamwise streaks. A comprehensive review of the early works on secondary instability and streaks in plane shear flow can be found in Ho and Huerre (1984).

Although the plane shear layer is a general case of the free shear layer, explicit connections of jet flow to streamwise vortices and streaks did not receive such detailed attention during the same time period. Bradshaw, Ferriss, and Johnson (1964) identified elongated structures, albeit in the transitional region. Their visualizations provided evidence of "mixing jet" structures present in the flow, inclined in the $x - r$ plane, and forced through radial/azimuthal components leading to streamwise momentum transfer. They also postulated, similar to boundary-layer transition, that the highly energetic structures were essential for breakdown to turbulence. Later works by Becker and Massaro (1968), Browand and Laufer (1975), Yule (1978), Dimotakis, Miake-Lye, and Papantoniou (1983), and Agüí and Hesselink (1988) all observed streamwise vortices in jet flow, but questions remained, where does the instability originate and by what means does it grow?

Two works, one numerical (Martin and Meiburg, 1991) and one experimental (Liepmann and Gharib, 1992), sought to address the above questions. Martin and Meiburg (1991) showed how the strain field and radial shear were instrumental in the creation and evolution of streamwise vortices in the braid region. While Liepmann and Gharib (1992), through the use of digital image particle velocimetry on a transitional round jet, identified streamwise vortices and again connected them to highly strained regions between vortex rings (i.e. the braid region), finding that the streamwise vortices have a fundamental effect on the dynamics and statistical properties of the flow. Of particular note, they also found strong streamwise vortices persisted in the fully turbulent region of their flow, even when the energy of azimuthal rollers, necessary

for further vortex generation, diminished. Regardless of this final observation, both studies supported the stability theory of Pierrehumbert and Widnall (1982) and the collapse of the braid region into vortices by Lin and Corcos (1984) and Neu (1984), however, they each brought forth questions regarding additional tertiary instabilities resulting from their observations, increasing analysis complexity. The resolvent framework presented here seeks to eliminate the need for continued secondary and tertiary stability analyses.

In more recent work, Citriniti and George (2000) identified streamwise vortices using a 138 hot-wire array located 3 diameters downstream of a turbulent round jet to identify, through SPOD, structures. Their structures contained both streamwise vorticity (i.e. rolls) and streamwise velocity (i.e. streaks), with peak energies at $m = 4$. Jung, Gamard, and George (2004), expanding the above experiment, found that the most energetic, non-zero azimuthal wavenumber scaled inversely to downstream location. Other experiments investigating streamwise vortices in high Reynolds number jets, exiting from both transitional and turbulent boundary layers, found that interactions between strong streamwise vortices and weak axisymmetric vortices may generate further streamwise vortices (Davoust, Jacquin, and Leclaire, 2012; Kantharaju et al., 2020). As the importance of streamwise vortices to the overall dynamics became increasing apparent, various techniques such as chevrons (Bridges, Wernet, and Brown, 2003; Saiyed, Mikkelsen, and Bridges, 2003; Bridges and Brown, 2004; Violato and Scarano, 2011) and microjets (Arakeri et al., 2003; Greska et al., 2005; Alkislar, Krothapalli, and Butler, 2007; Yang et al., 2016) were implemented to impact the near-field turbulence for far-field noise reduction. In these cases, the addition of chevrons and microjets directly imprint strong streamwise vortices and velocity variations upon the mean of each flow case. However, not all configurations led to reductions in noise, motivating further theoretical understanding of streamwise vortices in jets.

Only recent work on non-modal instability provided direct theoretical evidence of the lift-up mechanism in round jets. Boronin, Healey, and Sazhin (2013) performed local transient growth analyses on liquid, laminar jets of Reynolds number 1,000 and found lift-up to be responsible for optimal growth. Jimenez-Gonzalez and Brancher (2017) extended this approach considering the influence of jet aspect ratio, Reynolds number, and azimuthal wavenumber on lift-up. Similar results were found by Garnaud et al. (2013a) using a global transient analysis, for both incompressible laminar and turbulent jets, however, they noted there was no firm evidence of lift-up

effects at the present time and did not investigate the zero-frequency limit in their companion resolvent study (Garnaud et al., 2013b).

Although it is clear that lift-up is present in laminar, transitional, and, in a more limited sense, turbulent jets at high Reynolds number, a direct quantitative comparison between globally observed and computed structures is lacking. Resolvent analysis and SPOD provide a statistical connection between structures observed in turbulent flow to those computed through linear-amplification theory (Towne, Schmidt, and Colonius, 2018).

In this paper, we use these tools to study characteristics of the lift-up mechanism, expanding upon the work of Nogueira et al. (2019). The jets we consider are fully turbulent at high Reynolds numbers and are issued from nozzles consisting of a fully turbulent boundary layer. We demonstrate the presence and energetic importance of the lift-up mechanism over subsonic to supersonic regimes, and characterize, as a function of frequency and azimuthal mode number, the interplay between the (now three) mechanisms (KH, Orr, lift-up). We show that previously described experimental (Liepmann, 1991; Paschereit et al., 1992; Liepmann and Gharib, 1992; Arnette, Samimy, and Elliott, 1993; Citriniti and George, 2000; Jung, Gamard, and George, 2004; Alkislar, Krothapalli, and Butler, 2007; Cavalieri, Rodríguez, et al., 2013) and numerical (Martin and Meiburg, 1991; Caraballo et al., 2003; Freund and Colonius, 2009) observations result from the lift-up mechanism, yet do not reject the potential origin of streamwise vortices through secondary instabilities of the flow (Widnall, Bliss, and Tsai, 1974; Pierrehumbert and Widnall, 1982; Lin and Corcos, 1984; Neu, 1984). In this work, resolvent analysis provides the key statistical link between response modes observed in the SPOD spectrum and their underlying resolvent forcing modes, shedding light on the most active linear-amplification mechanisms throughout the frequency-wavenumber space.

The chapter is organized as follows. In § 3.2 we describe the resolvent and SPOD methodology and discuss the large eddy simulation (LES) databases used to educe coherent structures. In § 3.3 we introduce a collection of snapshots from the LES of a Mach 0.4 jet showing streaky characteristics. In § 3.3 we present the dominant energies and gains computed using SPOD and resolvent analysis respectively. In § 3.3 SPOD results approaching Strouhal number $St \to 0$ and resolvent analysis at $St = 0$ are shown, identifying streaks and the direct presence of the lift-up mechanism in turbulent jets. We then compare SPOD and resolvent modes in § 3.4 at non-zero azimuthal wavenumbers and frequencies from $St = 0.6$ to $St \to 0$ and

case	M_j	Re_j	$\frac{p_0}{p_\infty}$	$\frac{T_0}{T_\infty}$	n_{cells}	$\Delta t a_\infty / D$	ΔSt
subsonic	0.4	4.5×10^5	1.117	1.03	15.9×10^6	0.2	0.049
transonic	0.9	1.01×10^6	1.7	1.15	15.9×10^6	0.2	0.022
supersonic	1.5	1.76×10^6	3.67	1.45	31×10^6	0.1	0.026

Table 3.1: Parameters, sampling rate, and frequency resolution for the LES.

present a sensitivity analysis delineating the various mechanisms pertaining to KH, Orr, and lift-up, while also suggesting a mechanism map of the most amplified response mechanism throughout the frequency-wavenumber space of turbulent jets. We then conclude the chapter in § 3.5 addressing the presence of streaks throughout the domain, both near and far from the nozzle.

3.2 Methods

The LES database, resolvent analysis and SPOD were described in Schmidt et al. (2018) and Towne, Schmidt, and Colonius (2018). For brevity, we recall the main details here.

Large Eddy Simulation database

The LES databases, including subsonic (Mach 0.4), transonic (Mach 0.9), and supersonic (Mach 1.5) cases, were computed using the flow solver Charles; details on the numerical method, meshing, and subgrid models can be found in Brès, Ham, et al. (2017). The simulations were validated with experiments conducted at PPRIME Institute, Poitiers, France for the Mach 0.4 and 0.9 jets (Brès, Jordan, et al., 2018). A summary of parameters for the three jets considered is provided in Table 3.1. These include the Reynolds number based on diameter $Re_j = \rho_j U_j D / \mu_j$ (where subscript j indicates the value at the center of the jet, ρ is density, μ is viscosity) and the Mach number, $M_j = U_j / a_j$, where a_j is the speed of sound at the nozzle exit. The simulated $M_j = 0.4$ jet corresponds to the experiments in Cavalieri, Rodríguez, et al. (2013), Jaunet, Jordan, and Cavalieri (2017), and Nogueira et al. (2019) with the same nozzle geometry and similar boundary-layer properties at the nozzle exit. Throughout the thesis, reported results are non-dimensionalized by the mean jet velocity U_j and jet diameter D; pressure is made non-dimensional using $\rho_j U_j^2$. Frequencies are reported in Strouhal number, $St = fD/U_j$, where f is the frequency.

Each database consists of 10,000 snapshots separated by $\Delta t a_\infty / D$, where a_∞ is the ambient speed of sound, and interpolated onto a structured cylindrical grid

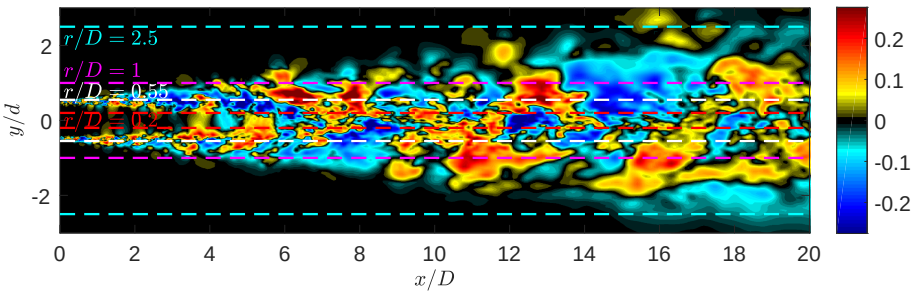

Figure 3.1: LES snapshot of fluctuating streamwise velocity in a plane through the $M_j = 0.4$ jet centerline. The lines show the areas of interest plotted in Figure 3.3.

$x, r, \theta \in [0, 30] \times [0, 6] \times [0, 2\pi]$, where x, r, θ are streamwise, radial, and azimuthal coordinates, respectively. Variables are reported by the vector

$$\boldsymbol{q} = [\rho, u_x, u_r, u_\theta, T]^T, \tag{3.1}$$

where u_x, u_r, u_θ are the three velocity components, T is temperature, and a standard Reynolds decomposition separates the vector into mean, $\bar{\boldsymbol{q}}$, and fluctuating, $\boldsymbol{q}'$, components

$$\boldsymbol{q}(x, r, \theta, t) = \bar{\boldsymbol{q}}(x, r) + \boldsymbol{q}'(x, r, \theta, t). \tag{3.2}$$

Figure 3.1 displays one snapshot of the streamwise velocity component in a plane through the $M_j = 0.4$ jet centerline.

Spectral Proper Orthogonal Decomposition

SPOD is implemented to determine a set of orthogonal space-time correlated modes that optimally describe the turbulent flow statistics (Towne, Schmidt, and Colonius, 2018). To perform SPOD we decompose each LES database, $\boldsymbol{Q}$, where columns of $\boldsymbol{Q}$ are temporal snapshots of the state vector $\boldsymbol{q}$, in the azimuthal and temporal dimensions via discrete Fourier transforms to give, $\boldsymbol{Q}_{m,\omega}$. The azimuthal decomposition is performed over 128 azimuthal grid points, allowing for valid transforms of up to $m = 64$, however we only report results using up to $m \approx 30$ with most of the analysis at low azimuthal wavenumbers, $m \leq 5$. The temporal transforms require the dataset to be segmented into sequences $\boldsymbol{Q} = [\boldsymbol{q}^{(1)}\boldsymbol{q}^{(2)}...\boldsymbol{q}^{(n_{\text{freq}})}]$ where each segment (or block) contains n_{freq} instantaneous snapshots (including

overlap), with a periodic Hanning window employed over each block to prevent spectral leakage. Applying the temporal and azimuthal Fourier transforms gives $\hat{\boldsymbol{Q}}^{(l)}_{m,\omega_k} = [\hat{\boldsymbol{q}}^{(l)}_{m,\omega_1}\hat{\boldsymbol{q}}^{(l)}_{m,\omega_2}...\hat{\boldsymbol{q}}^{l}_{m,\omega_{n_{\text{freq}}}}]$, where $\hat{\boldsymbol{q}}^{l}_{m,\omega_k}$ is the l-th realization of the transform at the k-th frequency. The cross-spectral density tensor at a given frequency $\omega_k = 2\pi St$ and azimuthal wavenumber m is then given by

$$\mathbf{S}_{m,\omega_k} = \hat{\boldsymbol{Q}}_{m,\omega_k}\hat{\boldsymbol{Q}}^{*}_{m,\omega_k} \tag{3.3}$$

and the SPOD eigenvalue problem presented by Lumley (1967) and Lumley (1970) can be solved

$$\mathbf{S}_{m,\omega_k}\mathbf{W}\mathbf{\Psi}_{m,\omega_k} = \mathbf{\Psi}_{m,\omega_k}\mathbf{\Lambda}_{m,\omega_k}. \tag{3.4}$$

The SPOD modes are represented by the columns of $\mathbf{\Psi}_{m,\omega_k}$ and are ranked by the diagonal matrix of eigenvalues $\mathbf{\Lambda}_{m,\omega_k} = \text{diag}(\lambda_1, \lambda_2, ..., \lambda_N)$. The modes are orthonormal in the norm $\boldsymbol{W}$, representing the compressible energy norm of Chu (1965)

$$\langle \boldsymbol{q}_1, \boldsymbol{q}_2 \rangle_E = \int\int\int \boldsymbol{q}_1^{*}\text{diag}\left(\frac{\bar{T}}{\gamma\bar{\rho}M^2}, \bar{\rho}, \bar{\rho}, \bar{\rho}, \frac{\bar{\rho}}{\gamma(\gamma-1)\bar{T}M^2}\right)\boldsymbol{q}_2 r\,dr\,dx\,d\theta \tag{3.5}$$

and satisfy $\mathbf{\Psi}^{*}_{m,\omega_k}\boldsymbol{W}\mathbf{\Psi}_{m,\omega_k} = \boldsymbol{I}$.

Given that SPOD is a discrete method for educing turbulent coherent structures, challenges persist for approaching the limit of $St \to 0$. We must strike a balance between snapshots per block (frequency resolution) and the number of blocks (convergence) when performing SPOD. When considering $St \in [0.2, 1]$ for the $M_j = 0.4$ jet, Schmidt et al. (2018) used block sizes of 256 snapshots with 50 % overlap (resulting in 78 blocks), and we use these same parameters in § 3.3. However, to uncover stationary-in-time structures such as streaks, increases in frequency resolution, and therefore block sizes, are necessary in the limit of $St \to 0$. For the global SPOD analysis presented, and after experimentation with block sizes (256, 512, 1024, 2048) and overlap (50%, 75%), we use 1024 snapshots with 75% overlap (36 blocks) to attain the required frequency resolution, yet maintain convergence with sufficient blocks as $St \to 0$ in § 3.3. We also note that the use of 2048 snapshots per block produced almost identical SPOD modes as using 1024 snapshots, albeit with a greater uncertainty as we reduced the block ensemble to 16 blocks.

Resolvent analysis

For the round, statistically stationary, turbulent jets we consider, the compressible Navier–Stokes, energy, and continuity equations are linearized through a standard

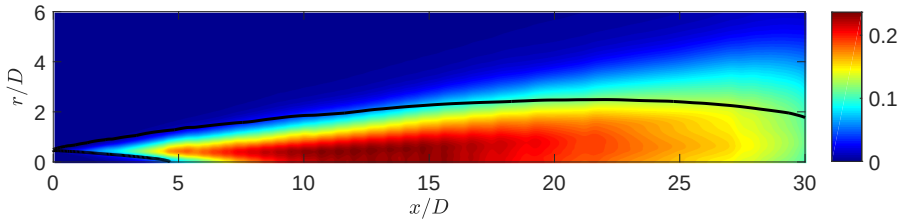

Figure 3.2: Resolvent eddy-viscosity field using the turbulent kinetic energy model, $\mu_T = \bar{\rho} c k^{1/2} l_m$, with $c = 1$. The black lines denote the region of $> 10\%$ maximum TKE which defines the length scale, l_m.

Reynolds decomposition, and Fourier transformed both temporally and azimuthally to the compact expression,

$$(i\omega \mathbf{I} - \mathbf{A}_m)\boldsymbol{q}_{m,\omega} = \boldsymbol{f}_{m,\omega}. \tag{3.6}$$

Here, $\mathbf{A}_m$ is the discretized linear operator considering the mean field as the base flow, $\boldsymbol{q} = [\rho', u_x', u_r', u_\theta', T']$ is the state vector, and $\boldsymbol{f}$ constitutes the forcing in each variable.

The influence of viscosity on the linear operator, $\boldsymbol{A}_m$, was previously (Schmidt et al., 2018) based on a spatially uniform Reynolds number using an altered molecular viscosity. However, recent resolvent analyses for turbulent jets (Pickering, Rigas, Sipp, et al., 2019) and channel flows (Morra et al., 2019), have shown substantial improvement in SPOD-resolvent correspondence by using a mean-flow eddy-viscosity model on the fluctuations. We proceed here by including an eddy-viscosity model based upon the turbulent kinetic energy (TKE) suggested for turbulent jets by Pickering, Rigas, Sipp, et al. (2019). This model was primarily chosen due to its simplicity and availability of the corresponding quantities from the LES database. The model takes the form

$$\mu_T = \bar{\rho} c k^{1/2} l_m, \tag{3.7}$$

where c is a scaling constant, k is the mean-flow turbulent kinetic energy, and l_m is a chosen length scale representative of the mean shear layer thickness; l_m is chosen as the width of the shear layer where the turbulent kinetic energy is more than 10% of its maximum value at each streamwise location, and the scaling constant $c = 0.0065$ is used considering the favourable SPOD-resolvent alignments previously shown for $m = 0$ and $St = 0.05 - 1$. The eddy-viscosity field implemented in this analysis is shown in Figure 3.2, note that the field is shown when $c = 1$.

With the inclusion of an eddy-viscosity model, the forward operator becomes $(i\omega \boldsymbol{I} - \boldsymbol{A}_m - \boldsymbol{A}_{m,T}(\mu_T))$, where $\boldsymbol{A}_{m,T}(\mu_T)$ only possesses terms that include μ_T (equations for $\boldsymbol{A}_{m,T}(\mu_T)$ are included in Pickering, Rigas, Sipp, et al. (2019)). The streamwise plane is discretized using fourth-order finite difference operators satisfying a summation by parts rule developed by Mattsson and Nordström (2004), the polar singularity is treated as in Mohseni and Colonius (2000), and non-reflecting boundary conditions are implemented at the domain boundaries.

We can rewrite Equation 3.6 by defining the resolvent operator, $\boldsymbol{R}_{\omega,m} = (i\omega \boldsymbol{I} - \boldsymbol{A}_m - \boldsymbol{A}_{m,T}(\mu_T))^{-1}$,

$$\boldsymbol{q}_{m,\omega} = \boldsymbol{R}_{m,\omega} \boldsymbol{f}_{m,\omega}, \tag{3.8}$$

and introducing the compressible energy norm (Chu, 1965) via the matrix $\boldsymbol{W}$ to the forcing and response, where $\boldsymbol{W} = \boldsymbol{W}_f = \boldsymbol{W}_q$, gives the weighted resolvent operator, $\hat{\boldsymbol{R}}_{m,\omega}$,

$$\hat{\boldsymbol{R}}_{m,\omega} = \boldsymbol{W}_q^{1/2} \boldsymbol{R}_{m,\omega} \boldsymbol{W}_f^{-1/2}. \tag{3.9}$$

Taking the singular value decomposition of the weighted resolvent operator gives

$$\hat{\boldsymbol{R}}_{m,\omega} = \hat{\boldsymbol{U}}_{m,\omega} \boldsymbol{\Sigma} \hat{\boldsymbol{V}}^*_{m,\omega} \tag{3.10}$$

where the optimal response and forcing modes are contained in the columns of $\boldsymbol{U}_{m,\omega} = \boldsymbol{W}_y^{-1/2} \hat{\boldsymbol{U}}_{m,\omega}$, with $\boldsymbol{U}_{m,\omega} = [\boldsymbol{u}^1_{m,\omega}, \boldsymbol{u}^2_{m,\omega}, ..., \boldsymbol{u}^N_{m,\omega}]$, $\boldsymbol{V}_{m,\omega} = \boldsymbol{W}_f^{-1/2} \hat{\boldsymbol{V}}_{m,\omega}$, with $\boldsymbol{V}_{m,\omega} = [\boldsymbol{v}^1_{m,\omega}, \boldsymbol{v}^2_{m,\omega}, ..., \boldsymbol{v}^N_{m,\omega}]$, respectively, while $\boldsymbol{\Sigma} = \mathrm{diag}(\sigma_1, \sigma_2, ..., \sigma_N)$ are the ranked gains.

To avoid ambiguity in referring to computed SPOD and resolvent modes, the following notation is used in the remainder of the thesis: $\boldsymbol{\psi}_n$ represents the n-th most energetic SPOD mode, while $\boldsymbol{v}_n$ and $\boldsymbol{u}_n$ denote the resolvent forcing and response, respectively, that provide the n-th largest linear-amplification gain between $\boldsymbol{v}_n$ and $\boldsymbol{u}_n$. In this paper, we only consider the optimal, or dominant, modes such that n is unity. Additionally, when referring to specific components of each mode, such as streamwise velocity, the notation $\boldsymbol{\psi}_1 : u_x$ is used. Finally, for all computed modes subscripts m, ω are dropped, but referenced when necessary in the text.

Resolvent-based sensitivity analysis

A structural sensitivity analysis (Qadri and Schmid, 2017) is applied to reveal regions of the flow where small perturbations to the operator have the largest effect on the resolvent gain. The component-wise sensitivity tensor is defined as the

component-wise product of the forcing and response modes,

$$S_{i,j} = \sigma^2 Re((\boldsymbol{v}_1 : i) \circ (\boldsymbol{u}_1 : j)^*), \tag{3.11}$$

where subscripts i, j denote the i-th or j-th component of the forcing or response, and $\circ$ denotes component-wise multiplication, giving the spatial sensitivity for each i, j forcing-response combination to the gain, σ. The sensitivity is calculated for the three forcing and response velocities of the momentum equation, presenting a 3×3 sensitivity tensor.

3.3 Lift-up mechanism & streaks

The lift-up mechanism, and the associated streaks, were first described by Moffatt (1965) and Ellingsen and Palm (1975), where low-energy vortices "lift-up" streamwise momentum of the basic flow and generate high-energy streaks. This simple description continues to provide an intuitive and accurate description in line with modern analyses. Here, we extend findings on non-modal growth of streaks in jets (Boronin, Healey, and Sazhin, 2013; Garnaud et al., 2013a; Jimenez-Gonzalez and Brancher, 2017; Nogueira et al., 2019) and compare our findings to wall-bounded optimal forcing studies of Hwang and Cossu (2010a) and Monokrousos et al. (2010), as well as the transient growth analysis of planar mixing layers by Arratia, Caulfield, and Chomaz (2013).

There are three salient characteristics that we use to identify the lift-up mechanism in the SPOD and resolvent results. First, the optimal forcing structures take the form of cross-stream vortices while the response assumes a highly amplified streamwise velocity structure. Second, the structures are elongated in the streamwise coordinate and are most amplified as their wavelength lengthens (i.e. represented in wall-bounded flows as a streamwise wavenumber of 0, and in the jet as $St = 0$). Third, streaks are azimuthally non-uniform (spanwise non-uniform in planar flows), i.e. they do not occur at $m = 0$.

For the remainder of this chapter, we report results for the $M_j = 0.4$ turbulent jet. Similar analyses are provided for both the $M_j = 0.9, 1.5$ jets in Appendix B.1.

LES visualization

Previous SPOD and resolvent analyses of turbulent jets (Schmidt et al., 2018) showed that the energy of the most amplified mode increases for non-zero azimuthal wavenumber as $St \to 0$. Considering significant energy is found at low frequencies, we expect to find elongated, streak-like structures to be visually present in the LES

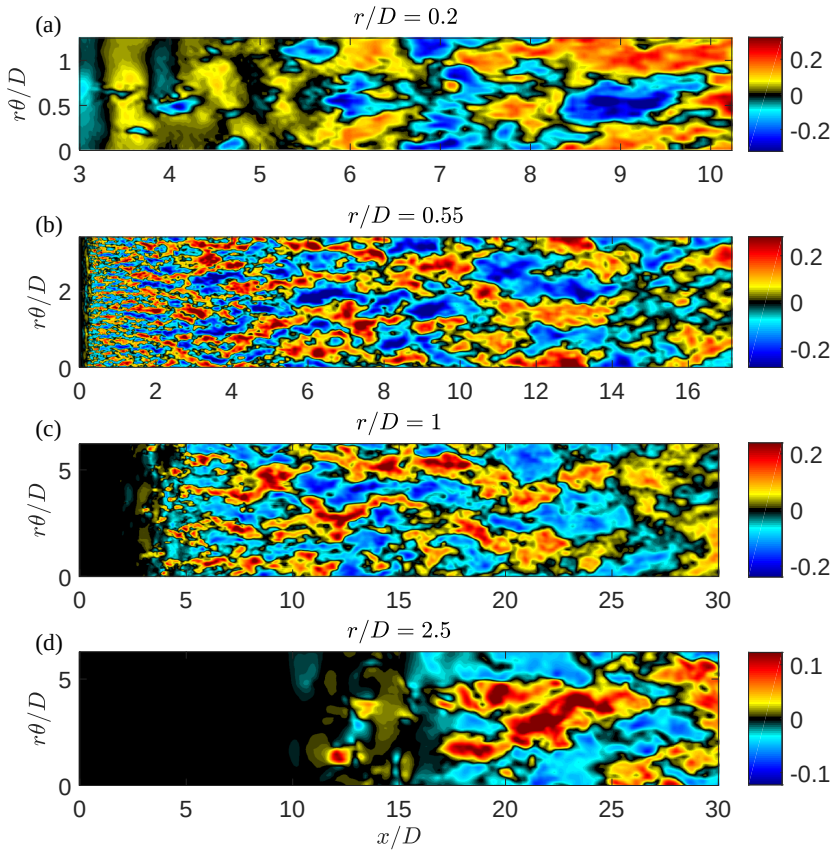

Figure 3.3: Instantaneous LES snapshots of streamwise fluctuating velocity, u'_x, taken at radial locations $r/D = 0.2, 0.55, 1, 2.5$ (a-d) with the y-axis representing the unwrapped surface $r\theta/D$. Only $2/5$ of the $r/D = 2.5$ surface is shown in the last plot.

snapshots. Instantaneous snapshots of fluctuating streamwise velocity, u'_x, are shown on four unwrapped cylindrical surfaces at $r/D = 0.2, 0.55, 1$, and 2.5 (denoted in Figure 3.1) in Figure 3.3. The Figures are plotted with the circumferential location of the unwrapped surface, $r\theta/D$, as the y-axis to maintain the physical aspect ratio of the data. Note that the plots are therefore increasingly zoomed into the near nozzle region as the radial position is decreased.

These instantaneous visualizations bear a resemblance to streaky structures found in plane shear flows, wall-bounded flows, and most recently the visualization of the present flow by Nogueira et al. (2019) invoking Taylor's hypothesis. We see elongated structures at each radial location taking forms analogous to Konrad (1976) and Bernal and Roshko (1986) in plane shear flow, turbulent boundary layers (Swearingen and Blackwelder, 1987; Hutchins and Marusic, 2007; Eitel-Amor, Örlü, and Schlatter, 2014), channel flow (Monty et al., 2007), and pipe flow (Hellström, Sinha,

and Smits, 2011). The Figures also show, more subtly, the presence of KH rollers. Beginning with radial surface $r/D = 0.2$ in Figure 3.3 (a) we attain a viewpoint from within the potential core, showing both KH rollers and streaky structures. From $x/D = [3, 6]$ structures appear to have a dominant $r\theta/D$ dimension and are likely to be associated with KH $m = 0, 1$ instabilities (i.e. KH rollers and non-streaky) extending throughout the potential core. However, at $x/D \approx 6$, where the potential core ends, the turbulent kinetic energy increases and streamwise-elongated (i.e. x/D dominated) structures begin to appear; they become more pronounced further downstream. For the radial surface $r/D = 0.55$ (b), we see streaky structures of smaller scale close to the nozzle and larger scale further downstream. These are similar to the structures visualized by Nogueira et al. (2019) at this radial location. The structures also meander as they propagate downstream, a quality also observed in turbulent boundary-layer flows by Hutchins and Marusic (2007). Comparable behavior is seen for both $r/D = 1$ (c) and 2.5 (d).

SPOD and resolvent analysis

SPOD and resolvent analyses were performed over a range of frequencies and azimuthal wavenumbers. Figure 3.4 (a) shows the SPOD ($E^{SPOD}_{m,St} \equiv \lambda_{m,St}$) energies and (b) resolvent ($E^{resolvent}_{m,St} \equiv \sigma^2_{m,St}$) amplifications of the leading mode. In Figure 3.4 (c,d), for SPOD and resolvent respectively, we perform a supplementary step to highlight the relative contribution of each azimuthal wavenumber at a particular frequency. The data presented in (a,b) are normalized at each frequency with the sum of energy over all azimuthal wavenumbers ($E_{m,St}/\sum_m E_{m,St} \times 100$) and plotted in the $St - m$ plane. We note that the gains have been normalized in the bottom row (c,d) as a means of visualizing the data, as it is otherwise difficult to identify behavior occurring at different frequencies as the gain drops off rapidly with increasing frequency. Both plots in Figure 3.4 (c,d) highlight the dominant wavenumbers at each frequency and facilitate the identification of different mechanisms. The contour maps (c,d) are interpolated for non-integer wavenumbers despite their discrete nature in azimuthal wavenumber, m. This representation was chosen as we found it easier to visually interpret the trends, and to more readily compare them to spanwise-streamwise wavenumber contours familiar to boundary-layer (Monokrousos et al., 2010) or plane shear (Arratia, Caulfield, and Chomaz, 2013) flows where wavenumbers are continuous. For reference, the semi-discrete representation of Figure 3.4 is provided in Appendix B.2.

There is a qualitative agreement between the SPOD energy and resolvent gain.

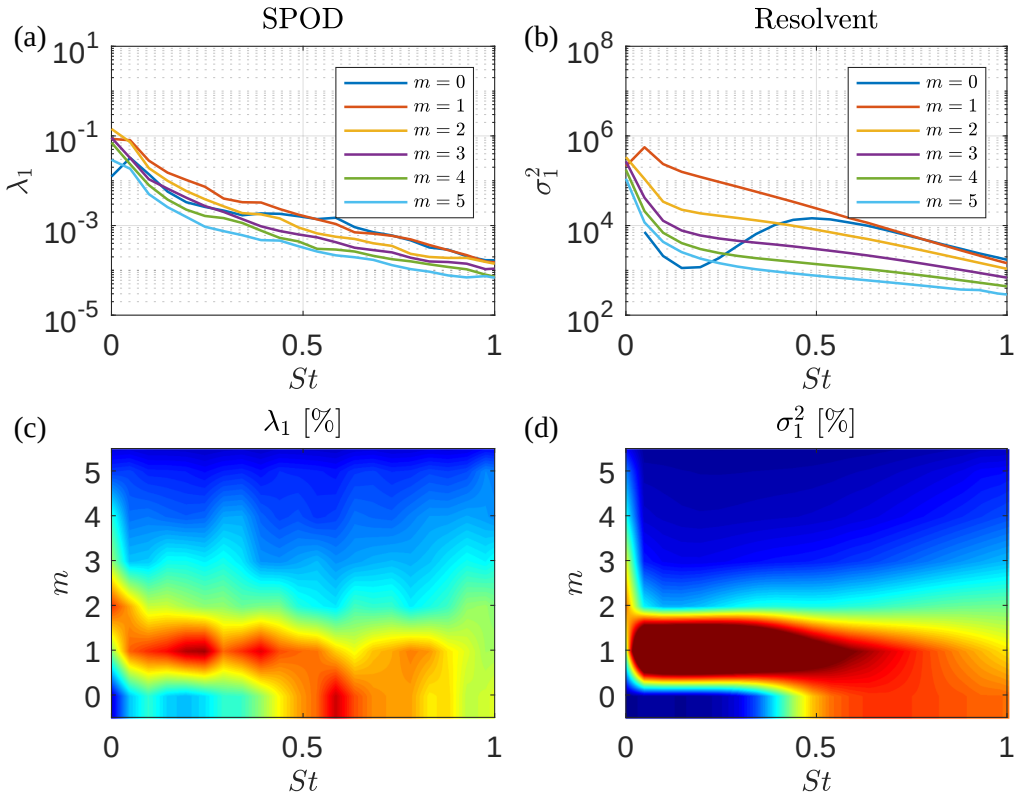

Figure 3.4: Energy of the most amplified mode from SPOD (left) and resolvent (right) analyses. The top row displays the energies (a) and gains (b) for the first six azimuthal wavenumbers. The bottom row (c,d) recasts the above plots (a,b) as a percentage of the sum of energy at each azimuthal wavenumber with contours ranging from 0-40%.

Here, we focus on Figure 3.4 (c,d) and note three regions in $St - m$ space: i) The energetic region near $St = 0.6$ at low azimuthal wavenumbers (particularly $m = 0$) is associated with the KH mechanism (Garnaud et al., 2013b; Semeraro, Lesshafft, et al., 2016; Schmidt et al., 2018; Lesshafft et al., 2019); ii) at low frequencies, meaning $St \to 0$, and $m = 0$ the dominant mode switches from the KH to the Orr mechanism for $St < 0.3$ (Schmidt et al., 2018) as the growth of the KH mechanism diminishes; iii) at low frequencies and non-zero azimuthal wavenumbers (mainly $m = 1$ and $m = 2$), a second energetic region is observed. This region comprises the lift-up mechanism that is described more fully in what follows. These frequency-wavenumber contour plots present trends similar to those obtained for laminar plane shear (Arratia, Caulfield, and Chomaz, 2013) and laminar boundary layers (Monokrousos et al., 2010), where the lift-up mechanism dominates

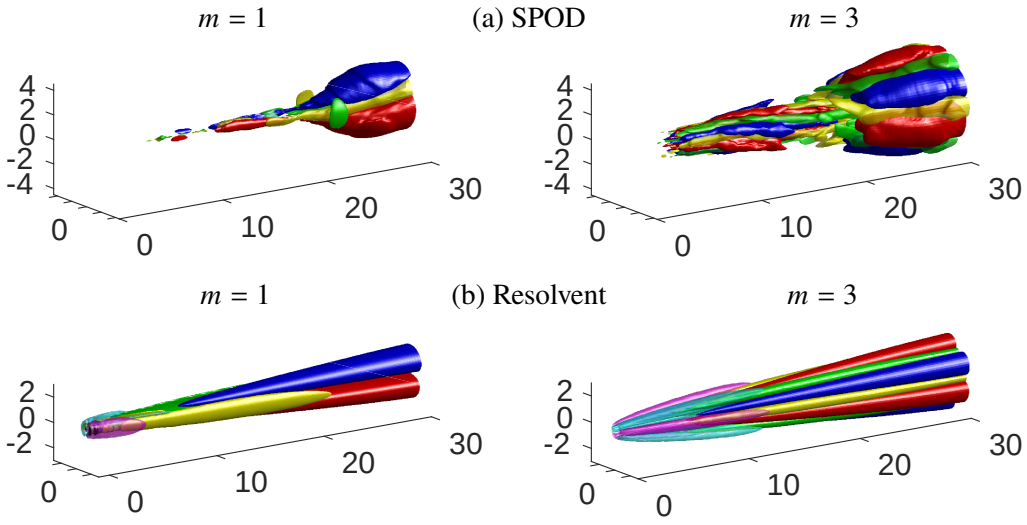

Figure 3.5: Streaks computed via SPOD and resolvent analyses for $m = 1$ and 3. (a) Most energetic SPOD mode at $St \to 0$ for $m = 1$ (left) and $m = 3$ (right). Isosurfaces of streamwise velocity ($\boldsymbol{\psi_1} : u_x$, red, blue) and streamwise vorticity ($\boldsymbol{\psi_1} : \omega_x$, yellow, green), both at ±25% of their maximum value. (b) Global resolvent forcing and response for $m = 1$ (left) and $m = 3$, (right) at $St = 0$. The streamwise forcing vorticity, $\boldsymbol{v_1} : \omega_x$ is shown in magenta-cyan with isosurfaces $\pm 0.05\|\boldsymbol{v_1} : \omega_x\|_\infty$ for $m = 1$ and $\pm 0.15\|\boldsymbol{v_1} : \omega_x\|_\infty$ for $m = 3$. Streamwise response vorticity, $\boldsymbol{u_1} : \omega_x$, is shown in yellow-green with isosurfaces $\pm 0.5\|\boldsymbol{u_1} : \omega_x\|_\infty$, and streamwise response velocity, $\boldsymbol{u_1} : u_x$, is shown in red-blue with isosurfaces $\pm 0.25\|\boldsymbol{u_1} : u_x\|_\infty$.

as streamwise wavenumbers approach 0 (i.e. streamwise uniform), or as frequency approaches zero for jet flows as documented by local analyses in laminar (Boronin, Healey, and Sazhin, 2013; Jimenez-Gonzalez and Brancher, 2017) and turbulent jets (Nogueira et al., 2019). For non-zero azimuthal wavenumbers, where the lift-up mechanism may be permitted due to its three-dimensional characteristics, $m = 1$ provides the largest energy across all frequencies, save $m = 2$ at $St \approx 0$, followed by a gradual reduction for higher azimuthal wavenumbers.

Global characteristics of streaks

The SPOD modes for $St \to 0$ are shown in Figure 3.5. The streaks are visualized in physical space by inverse (azimuthal) Fourier transforming the SPOD mode for a given azimuthal wavenumber. For $m = 1$, a well-defined streak ($\boldsymbol{\psi_1} : u_x$, red-blue isosurfaces) is observed throughout the domain starting at approximately the end of the potential core. In the $m = 3$ plot, streaks are seen upstream and downstream of the potential core, however, at approximately $x/D = [15, 20]$, the streaks are

less dominant and appear to slightly rotate. The slight rotation is likely an artefact of imperfect SPOD convergence at $St \rightarrow 0$, as approaching zero frequency still includes small, but non-zero, frequencies. Interestingly, the slight rotation of these modes is rather similar to energetic POD modes found by Freund and Colonius (2009).

Further evidence that these structures are due to the lift-up mechanism is shown by the yellow-green isosurfaces of streamwise vorticity, $\boldsymbol{\psi_1} : \omega_x$, included in Figure 3.5. The presence of streamwise vorticity, or rolls, and their particular location, situated precisely between positive and negative streamwise velocity contours, is indicative of the lift-up mechanism. The observation of such streamwise vortices in jets has previously been reported by a number of authors, including Bradshaw, Ferriss, and Johnson (1964), Liepmann (1991), Martin and Meiburg (1991), Paschereit et al. (1992), Liepmann and Gharib (1992), Arnette, Samimy, and Elliott (1993), Alkislar, Krothapalli, and Butler (2007), Citriniti and George (2000), and Jung, Gamard, and George (2004), and Caraballo et al. (2003), among others, each noting the significant impact these vortices imposed upon the mean flow and the accompanying streaks.

Performing resolvent analysis for $m = 1, 3$ at $St = 0$ provides a detailed understanding of the forcing mechanisms which give rise to the observed behavior of the SPOD modes. In Figure 3.5 (b) we see the canonical lift-up progression. The optimal forcing acts on the cross-stream components upstream at the nozzle, with associated streamwise vorticity $\boldsymbol{v_1} : \omega_x$ (magenta-cyan isosurfaces), in order to optimally generate rolls, $\boldsymbol{u_1} : \omega_x$. The rolls, in turn, give rise to streamwise velocity responses, $\boldsymbol{u_1} : u_x$, i.e. streaks. This connection, between these two response structures, has generally been interpreted as lift-up in jets, while the lift-up mechanism we describe refers to the input-output nature of both optimal forcing and response. Further, the responses in both streamwise vorticity and velocity shown by the SPOD modes in Figure 3.5 (a) agree quite well with the resolvent findings for both azimuthal wavenumbers.

Although the three-dimensional (3-D) representation of Figure 3.5 (b) presents many of the salient characteristics of the lift-up mechanism, a 2-D cut at $x/D = 5$ shown in Figure 3.6 highlights the radial and azimuthal velocity components of forcing and response rolls with respect to streaks. In Figure 3.6 (a) the forcing velocity vectors show the lifting of high-/low-speed fluid from the center/outer jet inducing positive/negative streaks, respectively. These mode shape qualities show agreement with previous local analyses of non-modal growth in laminar (Boronin, Healey, and

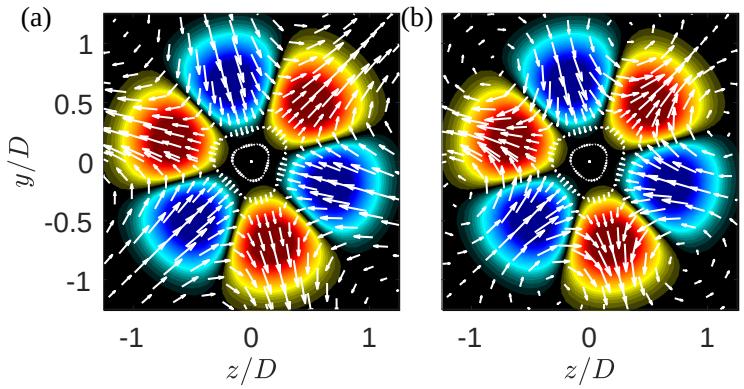

Figure 3.6: Cross plane at $x/D = 5$ of rolls and streaks at $m = 3$ computed via resolvent in Figure 3.5. The red-blue contours present streaks with values set at $\pm 0.75 \|\boldsymbol{u_1} : u_x(x/D = 5)\|_\infty$. The overlaid vectors represent the forcing rolls in (a) and response rolls in (b).

Sazhin, 2013; Jimenez-Gonzalez and Brancher, 2017) and turbulent jets (Nogueira et al., 2019). More precisely, the forcing rolls show strong radial velocities coincident with maximum streamwise response for both azimuthal wavenumbers, while strictly azimuthal velocities are located exactly between positive and negative streaks. This latter observation (i.e. location of azimuthal velocities) has implications for results found via the resolvent sensitivity analysis and will be discussed further in § 3.4. Additionally, the forcing rolls give rise to response rolls shown in Figure 3.6 (b) presenting similar velocity characteristics as the forcing vectors, however, the response vectors show the vortices are centered near the jet, a quality not shared with the forcing vectors.

To ensure the visualized streamwise components in Figure 3.5 are the dominant variables, we present component-wise amplitudes of each variable. Figure 3.7 shows quantitative comparisons of the compressible energy inner product computed at each streamwise position between SPOD ($St \to 0$) and resolvent ($St = 0$), for $m = 1, 3$. We emphasize that the full compressible energy inner product of the five variables over the streamwise direction is unity by construction. The curves from SPOD (dotted) and resolvent (solid) are trend-wise similar, with noise in the SPOD results due to statistical convergence issues. The streamwise velocity response (i.e. streaks) is clearly the dominant response variable throughout the domain for both the resolvent and SPOD analyses. For the forcing terms, the radial and azimuthal velocities dominate throughout the domain by two orders of magnitude and correspond to the streamwise vorticity (i.e. rolls). Together, the forcing and response amplitudes confirm SPOD and resolvent modes computed at $St = 0$ are

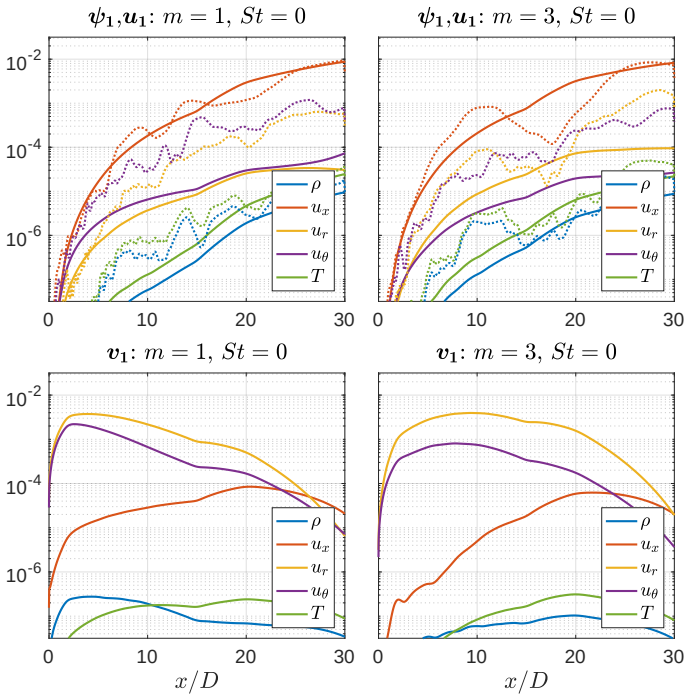

Figure 3.7: Component-wise amplitude curves in the streamwise direction of the streaks for $St = 0$ and $m = 1$ and 3. Optimal response (top) and forcing (bottom) amplitudes from resolvent (solid) and SPOD (dotted) analyses as a function of streamwise coordinate from the nozzle exit.

dominated by the lift-up mechanism.

The generation of streaks through the lift-up mechanism is also observed for the transonic, $M_j = 0.9$, and supersonic, $M_j = 1.5$ cases, showing similar trends. SPOD and resolvent analysis results for both jets, providing even clearer agreement, are shown in Appendix B.1.

3.4 Interplay of lift-up, Kelvin-Helmholtz, and Orr mechanisms

We now discuss the interplay between the three jet mechanisms in the frequency-wavenumber space.

However, before proceeding, we emphasize that distinct characteristics of each mechanism generally refer to the *response*, as, for example, the optimal forcings for both KH and Orr wavepackets are similar. Garnaud et al. (2013b) found that the KH preferred jet mode could be more efficiently excited through the Orr mechanism in the pipe upstream of the jet, thus combining algebraic spatial growth in the pipe with the downstream exponential growth associated with KH. This is analogous to the triggering of Tollmien-Schlichting waves via the Orr forcing structures in boundary

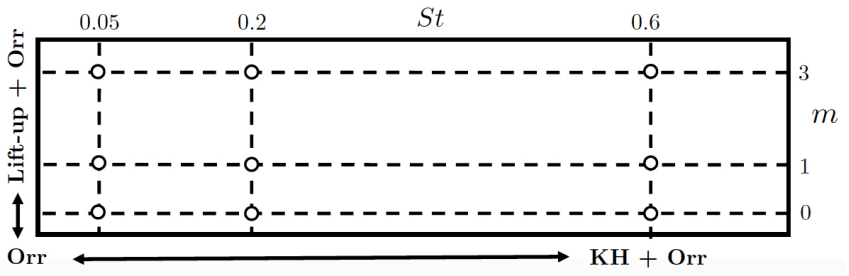

Figure 3.8: A cartoon mechanism map highlighting the know regions of active mechanisms along the $m = 0$ and $St = 0$ axes. The locations of the circles mirror the placement of the subsequent SPOD and resolvent analyses and denote their location in the frequency-wavenumber plane.

layers (Åkervik et al., 2008). In a similar vein, the Orr mechanism has also been (for small, but non-zero streamwise wavenumbers) observed to accompany the lift-up mechanism in both the plane shear layer (Arratia, Caulfield, and Chomaz, 2013) and wall-bounded flows (Hack and Moin, 2017). Therefore, in this analysis we note that the Orr mechanism will likely be present throughout the frequency-wavenumber space considered. The question we seek to address here is which mechanism is dominant in energy/amplification (i.e. SPOD/resolvent analyses). In most cases, we will find that lift-up (discussed next) or KH are the dominant mechanism, however, when both mechanisms are suppressed, the Orr mechanism becomes dominant by default.

Based on previous KH and Orr studies discussed in the introduction and results of the prior section on lift-up, we hypothesize regions of dominance between the mechanisms as a function of frequency and azimuthal mode number in Figure 3.8. This map will be filled in and clarified in the remainder of this section. The Orr mechanism would be present over all frequencies and wavenumbers, but only dominant where the lift-up and KH are not strongly amplified. Lift-up would dominate at $St \to 0$ (but is absent for $m = 0$), whereas KH would dominate over a range of intermediate frequencies.

To fill in the map, we plot in Figure 3.9 the streamwise velocity of the dominant SPOD (a) and resolvent forcing/response (b/c) at the 9 frequency-wavenumber pairs depicted in Figure 3.8. For these same frequency-wavenumber pairs, Figure 3.10 shows the radially integrated amplitudes for all response flow variables (in both SPOD and resolvent), whereas Figure 3.11 shows the radially integrated amplitudes of the forcing flow variables. Finally, the sensitivity of the resolvent gains for selected cases is shown in Figure 3.12.

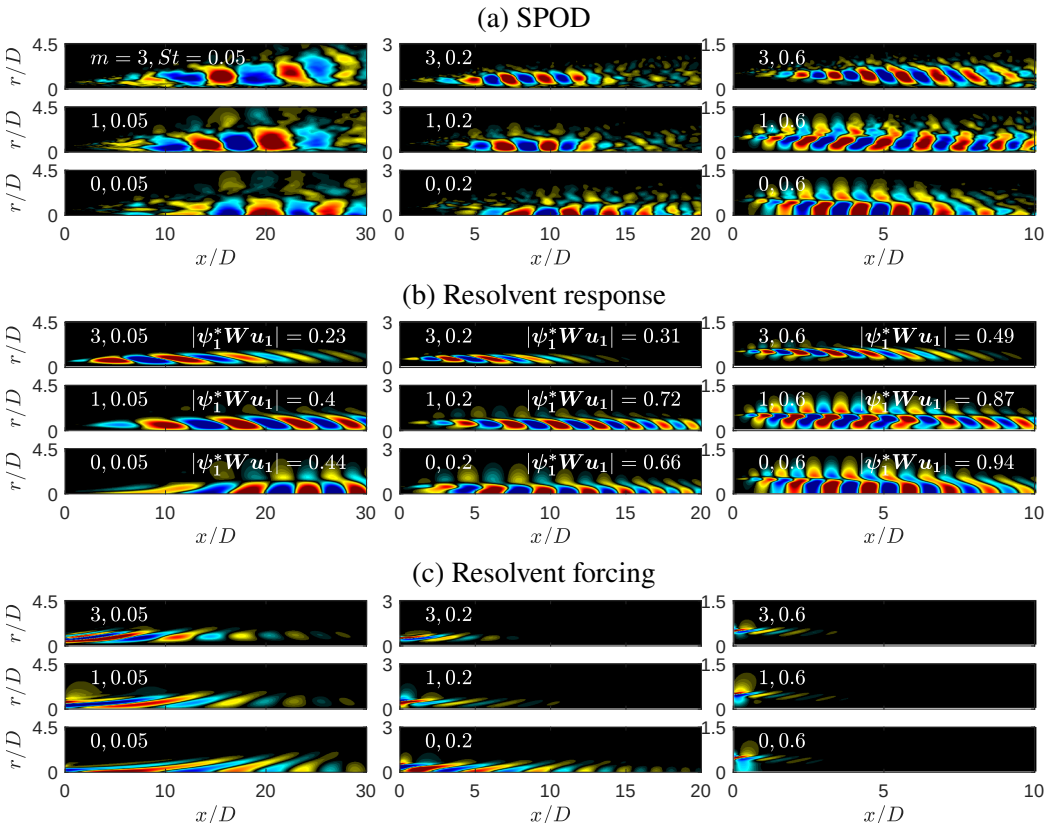

Figure 3.9: (a) Most energetic SPOD, (b) resolvent response, (c) and resolvent forcing modes for azimuthal wavenumbers $m = [0, 1, 3]$ and frequencies $St = [0.05, 0.2, 0.6]$. Streamwise velocity perturbation, u_x, component is shown with contours corresponding to $\pm 0.5 \|u_x\|_\infty$, with projection coefficients, $|\boldsymbol{\psi}_1^* \boldsymbol{W} \boldsymbol{u}_1|$, between the full SPOD responses, $\boldsymbol{\psi}_1$, and resolvent responses, $\boldsymbol{u}_1$, provided in (b). Note the change in domain limits, $x/D \in [0, 30]$, $[0, 20]$, and $[0, 10]$ for $St = [0.05, 0.2, 0.6]$, respectively.

A detailed analysis of these plots is given in the following subsections. Overall, one can see that the resolvent and SPOD analyses show significant agreement between the mode shapes and their component-wise amplitude content, particularly for the moderate frequencies where KH low-rank behavior is expected. The resolvent modes (Figure 3.9 (b,c)) are similar to those presented in Schmidt et al. (2018), but there are two important differences. The first is that these modes were computed by including an eddy-viscosity model in the resolvent operator, greatly improving the agreement between SPOD and resolvent, particularly at low St (Pickering, Rigas, Sipp, et al., 2019). The second difference is that we plot streamwise velocity rather than pressure, which better allows us to isolate features associated with the differing mechanisms.

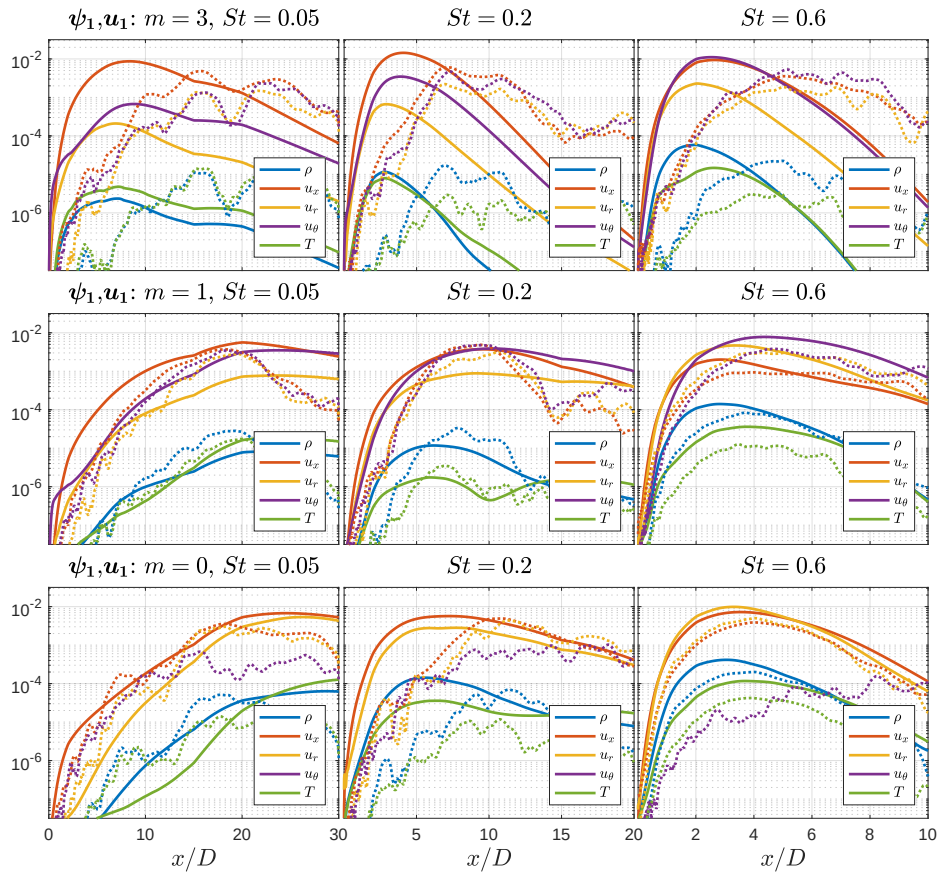

Figure 3.10: Streamwise evolution of component-wise amplitude curves for resolvent (solid lines) and SPOD (dotted lines) analyses. The layout of the Figure mirrors that of Figure 3.9 with $m = 3$ represented in the first row followed by $m = 1, 0$, and the first column displaying the lowest St increasing with columns to the right. Note that the truncated domains shown in Figure 3.9 are maintained for each $St - m$ pair.

KH-dominated response ($St = 0.6$**,** $m = 0, 1$**)**

At $[m, St] = [0, 0.6]$, the response is dominated by the KH mechanism (Schmidt et al., 2018) and displays the many characteristics described earlier. The SPOD and resolvent modes shown in 3.9 are almost indistinguishable, and similar to what has been previously reported using PSE. The associated forcing structures (Figure 3.9 (d)) are localized near the lip line of the nozzle and are tilted at an angle $\sim 45°$, representative of Orr-type forcing known to efficiently trigger the KH mechanism (Garnaud et al., 2013b; Tissot, Lajús Jr, et al., 2017; Tissot, Zhang, et al., 2017; Lesshafft et al., 2019). We also find an estimated phase speed of $c_{ph} \approx 0.8$ and a $90°$ phase shift at the critical layer where the apparent phase speed is equal to the mean flow speed (Cavalieri, Rodríguez, et al., 2013) (phase speed is estimated by

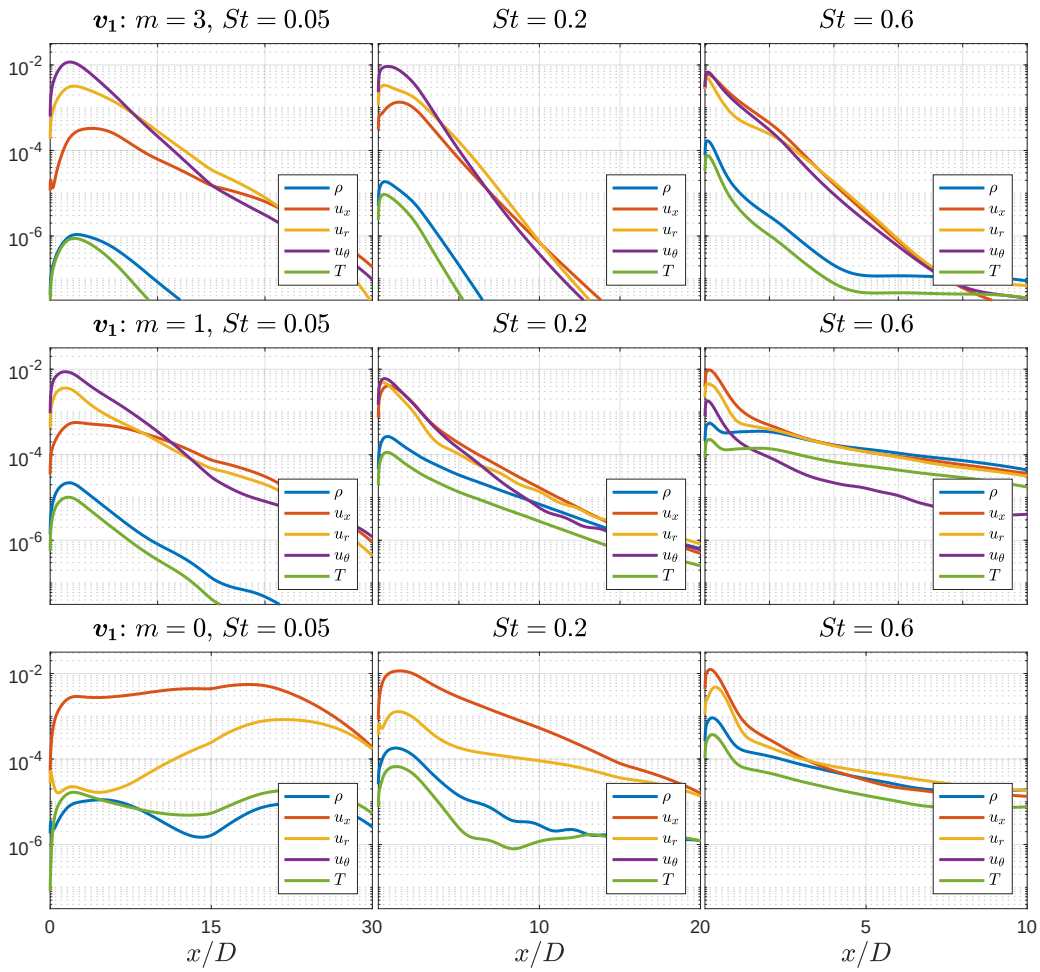

Figure 3.11: Streamwise evolution of component-wise amplitude curves for resolvent forcing modes. The layout and streamwise extent of each plot is identical to Figure 3.10.

taking the Fourier transform in the streamwise direction of the LES pressure along the lip line). Similar behavior is observed for $m = 1$ wavenumbers at $St = 0.6$, for which the KH response is also dominant.

The component-wise amplitude curves for $m \in [0, 3]$ and $St = 0.6$ in Figure 3.10 also support the KH interpretation with an initially rapid (exponential) growth followed by saturation and decay by $x/D \approx 5$. By contrast with what will be shown for the lowest frequency, the velocity components (streamwise, radial, and azimuthal) have similar amplitudes, apart from the absence of azimuthal velocity when $m = 0$. Forcing modes in Figure 3.11 for all azimuthal wavenumbers are concentrated upstream with the maximum forcing amplitude occurring within $x/D \leq 0.1$ and along

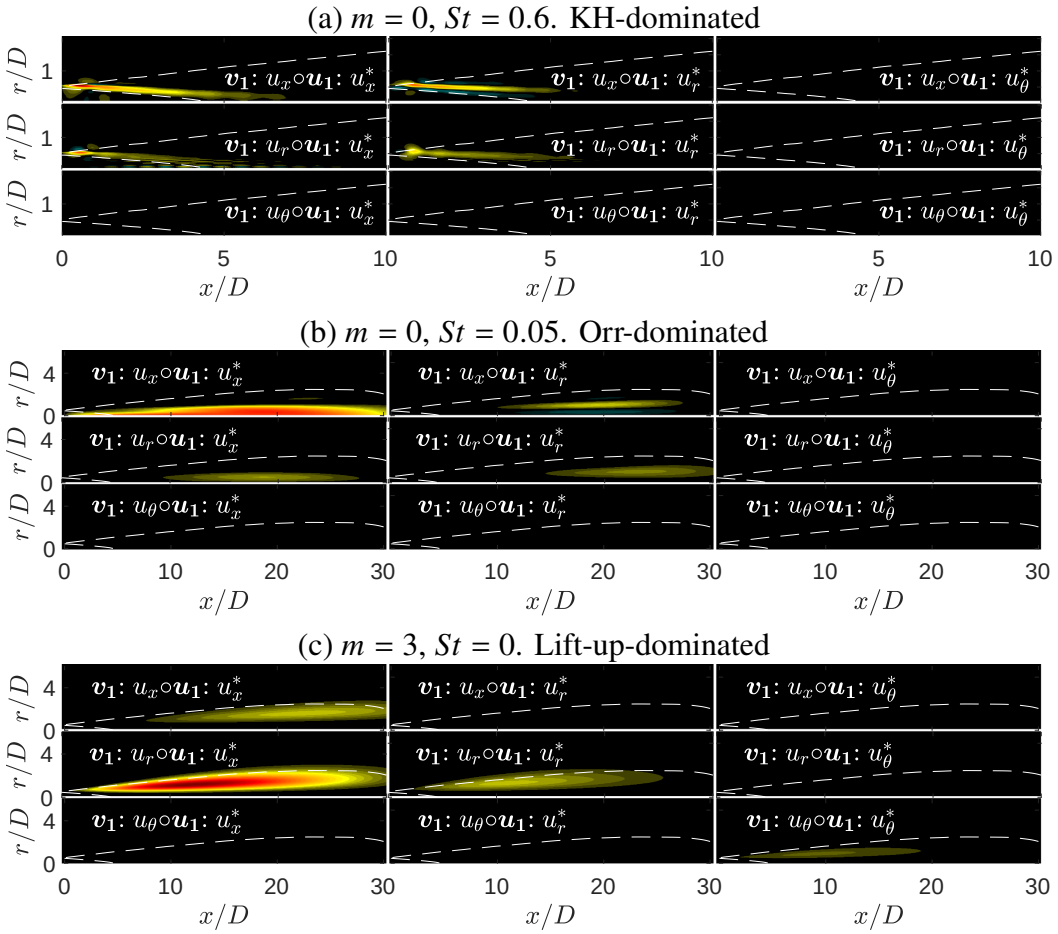

Figure 3.12: Resolvent-based spatial sensitivity plots for all nine velocity combinations for $[m, St] = [0, 0.6]$ (a), $[m, St] = [0, 0.05]$ (b), and $[m, St] = [3, 0]$ (c). Contours are set for each of the three plots by the maximum sensitivity, $\pm\|\boldsymbol{v_1} \circ \boldsymbol{u_1^*}\|_\infty$, across all nine velocity pairs. Note for the KH case, the domain is reduced to $x/D = [0, 10]$ and $r/D = [0, 2]$ to highlight the upstream behavior, as no sensitivity is observed outside this domain. The white, dotted lines provide reference to the envelope of the jet that is $> 10\%$ of the maximum turbulent kinetic energy.

the lip line. The forcing decays by at least two orders of magnitude within the first two jet diameters. This observation is also apparent from the gain sensitivity analysis (Figure 3.12 (a)), showing sensitivity localized to the inner edge of the shear layer terminating around the end of the potential core, with similar component-wise sensitivity found active for all velocity components (i.e. $\boldsymbol{v_1} : u_x, \boldsymbol{v_1} : u_r$ and $\boldsymbol{u_1} : u_x, \boldsymbol{u_1} : u_r$ pairs). This localized sensitivity is in stark contrast with the sensitivity contours associated with the Orr and lift-up mechanisms discussed next.

Orr-dominated response ($St \to 0$, $m = 0$)

At $[m, St] = [0, 0.05 - 0.2]$, the Orr mechanism dominates the response as shown previously by Schmidt et al. (2018). The upstream region of the forcing modes (Figure 3.9 (d)) is inclined at $-45°$ against the mean shear, and the response (Figure 3.9 (c)) turns from $-45°$ to $+45°$ throughout their envelope. The response modes possess a phase speed of approximately 0.4, and although we still observe a phase change across the critical layer, this behavior is rather weak when comparing to the KH-dominated modes described in § 3.4 ($St = 0.6$). In contrast to KH, the response grows gradually with x/D, peaking some 20 diameters downstream and is only weakly damped thereafter. We also find both forcing and response modes to peak near the jet centerline, similar to Orr-type modes found by Garnaud et al. (2013b) and Lesshafft et al. (2019), rather than at the region of maximum shear in the jets. Although this seems counter-intuitive for the Orr mechanism, by $x/D = 15$, well beyond the close of the potential core, the profile is diffuse, and the "critical layer" for this phase speed would be relatively close to the jet axis.

Finally, the sensitivity contours (Figure 3.12 (b)) provide contrast with what was observed for the KH response. First, the sensitivity is high over a spatially distributed region commensurate with the response region, and reaching far downstream where the flow no longer supports KH amplification. Secondly, there is a large component-wise sensitivity between the streamwise velocity forcing and the streamwise velocity response, a distinguishing characteristic when compared with the KH and lift-up mechanisms.

Lift-up-dominated response ($St \to 0$, $m > 0$)

For $m \neq 0$, and approaching zero frequency, the wavepackets in Figure 3.9 (a,b) show a different structure from the KH-dominated regimes. Although the response and forcing mode structures are inclined at 45° (this response behavior in jets was also observed by Bradshaw, Ferriss, and Johnson (1964)), and seem to indicate

Orr mechanism behavior (again, likely present), it is the component-wise amplitude curves that provide evidence of lift-up. For $[m, St] = [3, 0.05]$ in Figure 3.10, the streamwise velocity is approximately an order of magnitude larger than the other components, whereas for $[m, St] = [0, 0.05]$ (i.e. Orr only) both streamwise and radial velocities contribute similarly to the overall mode. The presence of streaks is directly responsible for this higher streamwise velocity. The forcing in Figure 3.11, by contrast, shows a dominance of radial and azimuthal forcing components, producing streamwise vortical forcing, $\boldsymbol{v_1} : \omega_x$. In tandem, the response and forcing amplitude curves describe the lifting of fluid, via cross-plane rolls, from high- and low-speed regions of the jet to the fluctuating streamwise velocity response. These results show that the lift-up mechanism, demonstrated at zero frequency in § 3.3, persists at small, non-zero frequencies. In this case the streaks are not stationary, and slowly rotate about the jet. We find evidence of streaks for all non-zero wavenumbers up to frequencies of $St \approx 0.2$.

The sensitivity analysis (Figure 3.12 (c)), after being described for KH and Orr, gives further evidence that the lift-up mechanism may be uniquely identified in turbulent jets. Unlike KH and Orr, we find the largest sensitivity in radial forcing to streamwise response, and unlike KH, but similar to Orr, the sensitivity is spatially distributed throughout the domain. The critical difference between Orr and lift-up is the shift of sensitivity to the radial forcing, streamwise response pair. We expect this for the lift-up mechanism as the radial forcing component lifts high- and low-speed regions of the jet to the streamwise response.

One puzzling aspect of the results is the lack of sensitivity of the streamwise velocity to the azimuthal velocity forcing (Figure 3.12 (c)). In general, streamwise vorticity is associated with either variation of azimuthal velocity with radius, or radial velocity with azimuth, and it seems surprising that the sensitivity identifies changes to the latter, but not the former, as a means to amplify the streaks. This is explained by the phase between radial/azimuthal forcing and the corresponding response. As is observed in Figure 3.6 (a,c) in § 3.3, the largest regions of radial forcing are coincident with the most energetic regions of the streaks (i.e. large sensitivity), but the largest azimuthal forcing occurs where streaks have low amplitude, resulting in low sensitivity. The above interpretation is limited to the sensitivity map as defined by Qadri and Schmid (2017), which examines the structural sensitivity to spatially localized (delta-function) changes to the structure of the linear system defining the resolvent. In reality, any finite-sized perturbation would convolve the response

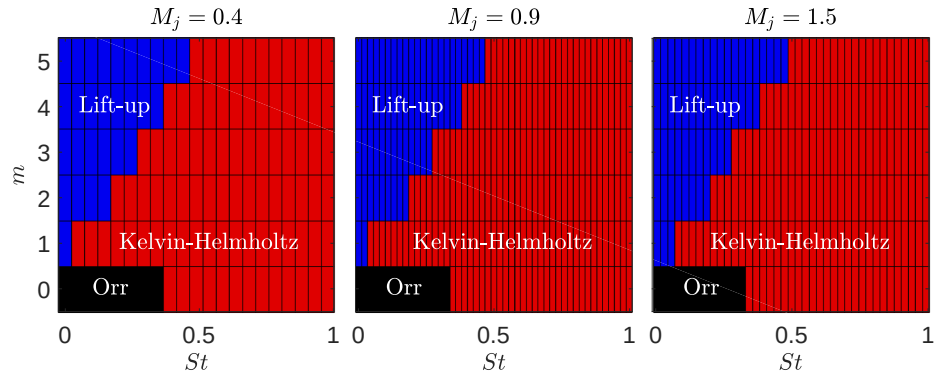

Figure 3.13: Linear mechanism map estimating the dominant linear mechanisms in the frequency-wavenumber space of the most amplified resolvent response for turbulent jets. Red, black, and blue represent the KH, Orr, and lift-up mechanisms, respectively.

and forcing (rather than multiply them), and likely lead to larger sensitivity to the azimuthal velocity than reported here.

Linear mechanism map

Following identification of the salient properties of each turbulent jet mechanism, we propose the mechanism map shown in Figure 3.13 estimating the regions of mechanism dominance in the frequency-wavenumber space for turbulent jets. We determine the mechanism map through inspection of individual frequency/azimuthal modes and identify the nature of the dominant mode by applying the criteria discussed earlier in this section. For $m = 0$, the map reflects the shift in dominance of the KH at moderate Strouhal numbers to Orr at low frequencies, with mechanism shifts occurring at $St \approx 0.3$ for $M_j = 0.4, 0.9, 1.5$. For the lift-up mechanism, the region of dominance may be estimated as $St/m \leq 0.1$ in Figure 3.13. Although, the lift-up mechanism continues to become more dominant as $St/m \to 0$, similar to the findings of Arratia, Caulfield, and Chomaz (2013) for a plane shear layer as lift-up dominates when $k_x/k_z \to 0$, where k_x, k_y are the streamwise and spanwise wavenumbers, respectively. It is important to stress that this map is an estimate of mechanism dominance, and mechanisms are simultaneously present at the boundaries of dominant mechanism regions.

3.5 Local analysis for higher azimuthal modes

Up until now, the SPOD and resolvent analyses have used the full computational domain extending 30 diameters downstream. The associated Chu compressible

energy norm, which is integrated over this entire region, is biased toward the lower azimuthal modes that have long wavelengths and dominate the jet far downstream. For example, the dominant azimuthal wavenumber for much of the frequency range is $m = 1$, and as $St \rightarrow 0$ the dominant azimuthal wavenumber is $m = 2$. When one inspects the results for the higher azimuthal modes in the global domain, large noise downstream prevents the identification of coherent structures likely near the nozzle. The question arises as to what is the dominant azimuthal wavenumber when smaller regions closer to the nozzle exit are considered, particularly as $St \rightarrow 0$.

To determine an overall picture of which azimuthal wavenumbers dominate at different streamwise positions in the jet, we first performed SPOD (using blocks of 256 snapshots and a 50% overlap) in 2-D cross-stream planes throughout the range $x/D = [0.5-30]$. The three azimuthal wavenumbers exhibiting the largest energy at each x/D are plotted in Figure 3.14. We see that the maximum energy for $x/D = 30$ is in line with the global analysis result, at azimuthal wavenumber $m = 2$. However, as the plane moves upstream, we see a trend towards higher azimuthal wavenumbers. In fact, this trend scales as $m_{max} \sim 1/x + 1$ (i.e. the maximum wavenumber approaches 1). This scaling is inversely proportional to the linear scaling of the shear layer of the jet, $\sim x$ (Schmidt et al., 2018), and has also been reported from experimental observations of Jung, Gamard, and George (2004) and Nogueira et al. (2019) for axial stations $x/D \leq 6$ and $x/D \leq 8$, respectively. This suggests that the width of the shear layer determines support for particular azimuthal wavenumbers as $St \rightarrow 0$.

Next, to better isolate streaks related to higher azimuthal wavenumbers, the truncated domains (including the 2-D cross-stream planes above) $x/D \in [0, 2], [0, 5], [0, 10]$ are examined for $m \in [0, 15]$ using SPOD and resolvent analyses. For these truncated domains, blocks of 256 snapshots and a 50% overlap suffice even at low frequencies and are used for this final analysis. Figure 3.15 shows the SPOD energy spectra and normalized azimuthal frequency-wavenumber maps similar to the ones reported in Figure 3.4 for the restricted domains, and Figure 3.16 shows the associated resolvent results.

The restricted SPOD and resolvent spectra and frequency-wavenumber maps are in striking agreement, and provide insight into both the total energy and the overall influence of each wavenumber as the domain is truncated towards the nozzle. The largest domain, $x/D \in [0, 10]$, shows energy peaking at low frequencies and dominated by low azimuthal wavenumbers, similar to the global spectrum in Figure

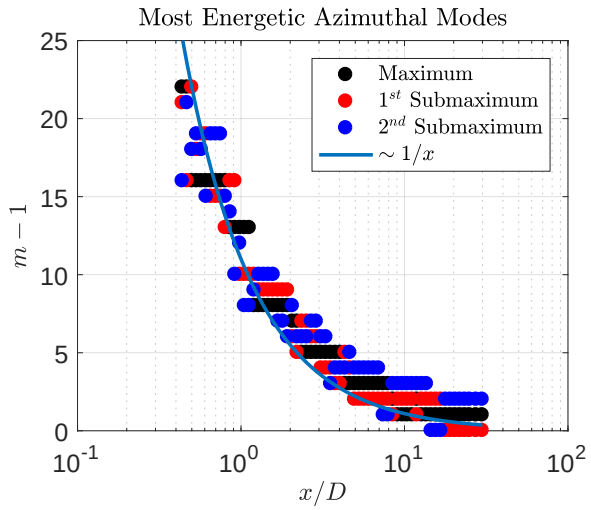

Figure 3.14: Wavenumbers of the three largest SPOD energies from the $St \to 0$ SPOD bin as a function of streamwise distance. Here SPOD was performed locally on 2-D streamwise cross sections, and we present a scaling of maximum azimuthal wavenumber as $\sim 1/x + 1$.

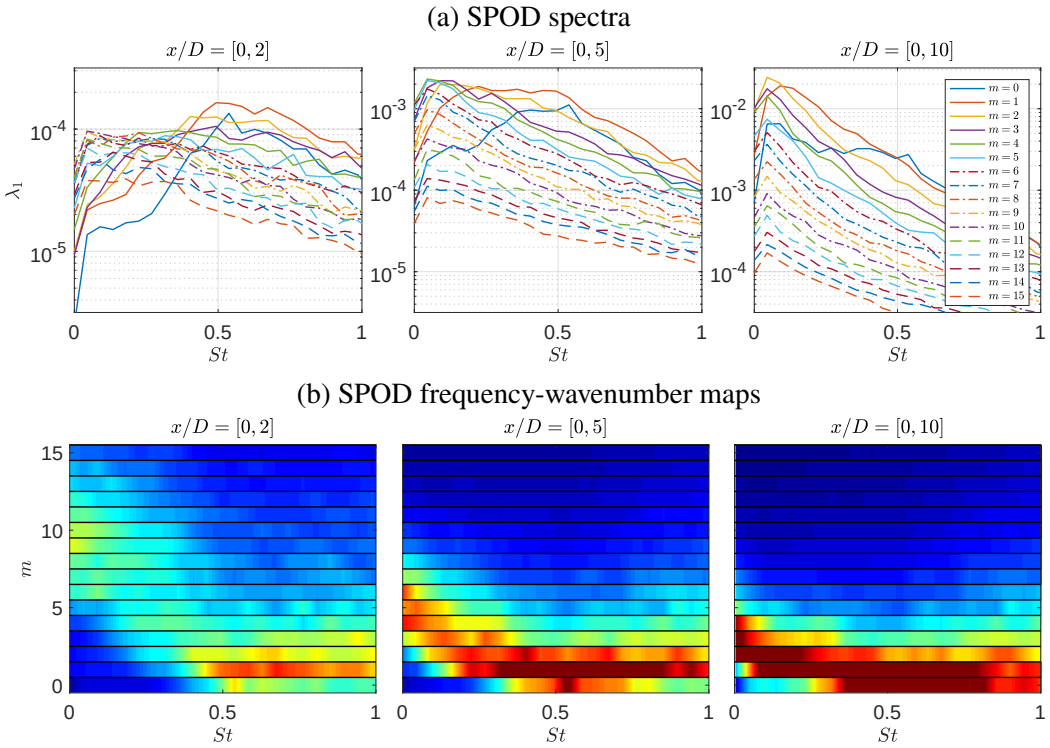

Figure 3.15: SPOD spectra, $\lambda_1(St, m)$, for truncated domains of $x/D \in [0, 2], [0, 5], [0, 10]$ left to right respectively, for azimuthal wavenumbers $m \in [0, 15]$. (a) SPOD spectrum curves for all wavenumbers. (b) Semi-discrete frequency-wavenumber maps showing the distribution of energy (as a percentage) among wavenumbers at each frequency with contour levels at 0-20%.

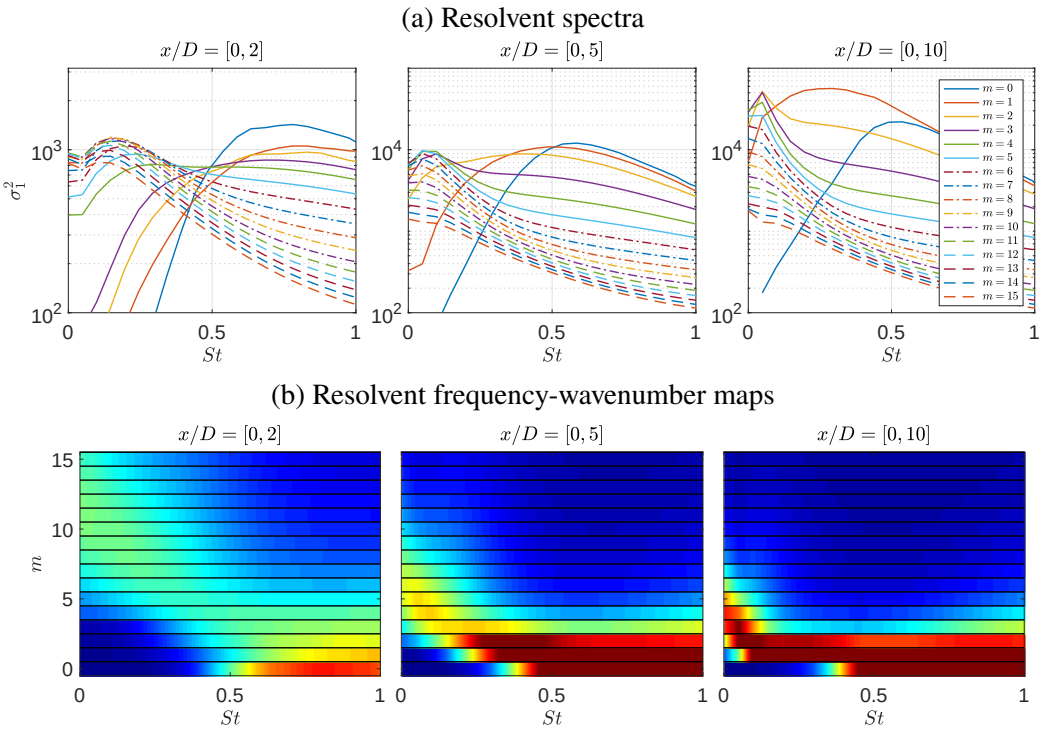

Figure 3.16: Resolvent spectra, $\sigma_1^2(St, m)$, for truncated domains of $x/D \in [0, 2], [0, 5], [0, 10]$ left to right respectively, for azimuthal wavenumbers $m \in [0, 15]$. (a) Resolvent spectrum curves for all wavenumbers. (b) Semi-discrete frequency-wavenumber maps showing the distribution of energy (as a percentage) among wavenumbers at each frequency with contour levels at 0-20%.

3.4. We also see that the peak azimuthal wavenumber at $St \to 0$ has increased, yet the moderate-frequency behavior associated with KH remains active for low azimuthal wavenumbers, similar to the full domain analysis. Truncating the domain to $x/D \in [0, 5]$ presents a relative shift in total energy towards higher frequencies and the KH content maintains its strong $m = [0, 1, 2]$ behavior at these frequencies, while the distribution of energy at low frequencies is now centered at $m = 6$. The final truncation, $x/D \in [0, 2]$, shows a significant drop in energy at low frequencies and higher frequencies dominate the energy spectrum, however, the peak maximum azimuthal wavenumber at low frequencies has shifted much higher, centered at $m = 10$ near zero frequency.

The Figures also show a clear separation between the lift-up mechanism's influence in the low-frequency portion of the energy map versus the KH mechanism's influence in moderate-frequency regions. Interestingly, both of these observations, despite truncation of the jet domain, still fall in line with the estimated mechanism map, Figure 3.13, with lift-up increasingly apparent as $St/m \to 0$.

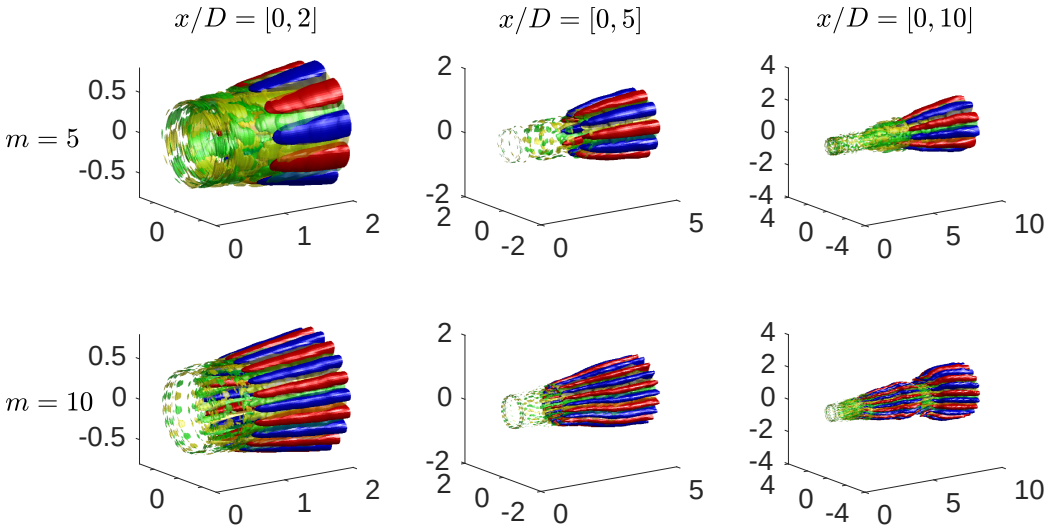

Figure 3.17: Three-dimensional reconstruction of the first SPOD mode for $m = [5, 10]$ (top and bottom, respectively) at three truncated domains $x/D \in [0, 2], [0, 5], [0, 10]$ (left to right, respectively) for $St \to 0$. Streamwise velocity, $\boldsymbol{\psi_1} : u_x$, is denoted as red-blue with isosurfaces ±25% the maximum streamwise velocity and streamwise vorticity, $\boldsymbol{\psi_1} : \omega_x$, is shown as yellow-green with isosurfaces as ±50% of the maximum streamwise vorticity.

To further show that the $St \to 0$ SPOD/resolvent energies/amplifications in this truncated domain analysis correspond to streaks, we show 3-D reconstructions of streamwise velocity and streamwise vorticity for $m = 5, 10$ for both SPOD and resolvent in Figures 3.17 and 3.18, respectively. The truncated SPOD and resolvent modes show close alignment with each plot for $m = 5$ and 10, presenting smooth streaks of streamwise velocity ($\boldsymbol{u_1} : u_x$), accompanied with streamwise rolls ($\boldsymbol{u_1} : \omega_x$) indicative of the lift-up mechanism, for all domains considered. Azimuthal wavenumber $m = 5$ presents a case in which streaks are present with significant energy for each truncated domain, and as such, give rise to well-defined streaks that occupy the entire domain. For $m = 10$, streamwise velocity streaks and streamwise vorticity rolls are easily identified in the truncated domains $x/D \in [0, 2]$ and $[0, 5]$. However, the $x/D \in [0, 10]$ domain gives a differing behavior for both SPOD and resolvent modes. In the resolvent case, highly amplified streaks are observed until $x/D \approx 5$, where response rolls disappear and the streaks begin to decay, showing that steady streaks are no longer supported downstream at this azimuthal wavenumber. This is also seen in the SPOD results as the original streaks decay at $x/D \approx 5$ and a low-frequency, slowly rotating streak enters towards the end of the domain. This can be attributed to the various domain and convergence issues described earlier, where

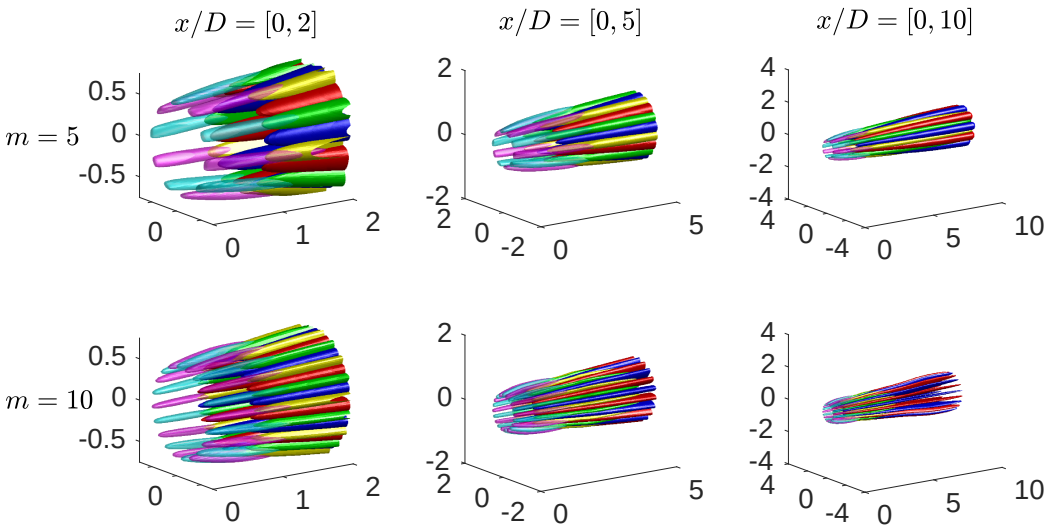

Figure 3.18: Three-dimensional reconstruction of the first resolvent mode for $m = [5, 10]$ (top and bottom, respectively) at three truncated domains $x/D \in [0, 2], [0, 5], [0, 10]$ (left to right, respectively) for $St = 0$. Streamwise velocity, $\boldsymbol{u_1} : u_x$, is denoted as red-blue with isosurfaces ±25% the maximum streamwise velocity, streamwise vorticity, $\boldsymbol{u_1} : \omega_x$, is shown as yellow-green with isosurfaces as ±50% of the maximum streamwise vorticity, and magenta-cyan represents isosurfaces of streamwise forcing vortices, $\boldsymbol{v_1} : \omega_x$, at ±50% of the maximum streamwise forcing vorticity.

a larger domain introduces additional energetic structures and noise which may be aliased into the $St \to 0$ bin. Again, for the global results presented earlier in the paper, this was averted by increasing the number of snapshots in the discrete Fourier transform (DFT) and reducing the bin sizes. Nevertheless, these results show that although high azimuthal wavenumbers do not appear to provide significant energy to the full flow field energy (e.g. Figure 3.4), their energetic impact is significant in the near nozzle region and is a result of the lift-up mechanism.

3.6 Conclusions & outlook

We have extended the linear resolvent and data-driven SPOD analyses of turbulent jet mean flow fields to the zero-frequency limit. The main result is a confirmation and extension of the local analysis of Nogueira et al. (2019), namely the identification of the lift-up mechanism as an important linear amplifier of disturbances in turbulent jets.

We found lift-up responsible for the generation of streamwise elongated structures, known as streaks, at low-frequency, non-zero azimuthal wavenumbers for turbulent

round jets at Mach numbers 0.4, 0.9, and 1.5. At moderate frequencies, KH becomes the globally dominant mechanism, and the Orr mechanism is active over all frequencies but plays a subdominant role at those frequencies and azimuthal wavenumbers where lift-up and KH are active. The behavior of the $m = 0$ response is unique, as axisymmetric streaks cannot exist; rather, the Orr response is dominant for low and high frequencies, with the KH response dominating over an intermediate-frequency regime centered on $St = 0.6$. For non-axisymmetric modes, the lift-up mechanism, and resulting streak response, is dominant as $St/m \to 0$, although with progressively higher wavenumber, lift-up responses are limited in spatial extent to nearer the nozzle exit. We find that the azimuthal wavenumber of dominant streak responses is inversely proportional to shear layer width and scales with $\sim 1/x$.

For all regimes, there is a reasonable agreement between the resolvent analysis and SPOD modes from the associated LES database, confirming that the theoretical mechanisms are active (and dominant) in the turbulent regime. This agreement is predicated on the addition of an eddy-viscosity model in the linear resolvent (Morra et al., 2019; Pickering, Rigas, Sipp, et al., 2019). While the simple model we employed suffices to establish the link between theory and observation, further refinements to the model would be required to establish a resolvent analysis that is *predictive* of turbulence structure.

Streaks observed using SPOD show similar structure to (space-only) POD modes reported by Freund and Colonius (2009) and SPOD modes with limited spatial extent by Citriniti and George (2000) and Jung, Gamard, and George (2004), and predicted by resolvent analyses for $m > 0$ at $St = 0$. Both SPOD and resolvent modes provide significant qualitative agreement in both streamwise vorticity and streamwise velocity, which are related to rolls and streaks, respectively. The resolvent results show optimal forcing in the form of streamwise vortices (rolls, $\boldsymbol{v_1} : \omega_x$) from the nozzle exit decaying slowly downstream, followed by a response of streamwise vortices ($\boldsymbol{u_1} : \omega_x$), and, finally, further downstream there appears a response of streamwise velocity ($\boldsymbol{u_1} : u_x$), or streaks. These characterizations of the flow, from both resolvent and SPOD, now link multiple previous experimental and numerical observations in transitional and turbulent jets of streamwise vortices (Bradshaw, Ferriss, and Johnson, 1964; Liepmann, 1991; Martin and Meiburg, 1991; Paschereit et al., 1992; Liepmann and Gharib, 1992; Arnette, Samimy, and Elliott, 1993) and streaks (Citriniti and George, 2000; Caraballo et al., 2003; Jung, Gamard, and George, 2004; Freund and Colonius, 2009; Cavalieri, Rodríguez, et al., 2013) to the lift-up

mechanism, forced upstream by a separate set of streamwise vortices.

Our results show that the lift-up mechanism, like the KH and Orr mechanisms, may be modeled as a direct amplification of disturbances to the turbulent jet mean flow. However, this work does not refute the idea, extrapolated from transitional free shear flows, that streaks arise via secondary instability of the KH rollers. The resolvent forcing that generates lift-up could involve, through triadic interactions, braid vortices. Indeed, the optimal forcing computed via the resolvent is non-zero in the region where the KH response is active. An explicit analysis of the triadic interactions involved in specific realizations of the turbulent flow would be needed to answer this question, a topic left for future research. Nevertheless, even though a nonlinear analysis would provide deeper insight into turbulence, the simplicity and ability of the linear resolvent framework to capture observed mode shapes and qualitatively capture their relative amplitudes across the wavenumber-frequency domain is remarkable.

The presence of the lift-up mechanism in turbulent jets also suggests further investigation of the resulting dynamics, and its potential impact for control of quantities such as jet noise. Considering streaks are highly energetic structures, it is likely that their behavior (i.e. breakdown and regeneration) have significant impact on the mean flow and other structures in turbulent jets, such as Orr and KH wavepackets and qualities associated with these structures' intermittency. In fact, noise reduction has been accomplished via the introduction of streamwise vortices at the nozzle exit using tabs (Samimy, Zaman, and Reeder, 1993; Zaman, Reeder, and Samimy, 1994; Zaman, 1999), chevrons (Bridges, Wernet, and Brown, 2003; Bridges and Brown, 2004; Saiyed, Mikkelsen, and Bridges, 2003; Callender, Gutmark, and Martens, 2005; Alkislar, Krothapalli, and Butler, 2007; Violato and Scarano, 2011), and microjets (Arakeri et al., 2003; Greska et al., 2005; Yang et al., 2016). However, these changes have, in certain configurations, increased noise, leaving fundamental questions regarding the dynamic impact of imposed streamwise vortices and streaks. Recently, Rigas et al. (2019) showed the presence of both chevron induced streamwise vortices and their accompanying streaks in the base flow of a turbulent, chevron jet, while Marant and Cossu (2018) have reported the ability of streaks, at particular wavenumbers, to stabilize the KH instability for a planar laminar shear flow. Considering past computational work of Sinha, Rajagopalan, and Singla (2016) (using PSE) demonstrated the ability of chevrons to "stabilize" (i.e. weaken) KH wavepackets, the dominant mechanism in jet noise (Jordan and Colonius, 2013), it

is likely that lift-up presents a fundamental mechanism of turbulent jet flow that may be tuned appropriately for optimal jet noise reduction techniques.

Acknowledgments

This research was supported by a grant from the Office of Naval Research (grant No. N00014-16-1-2445) with Dr. Steven Martens as program manager. E.P. was supported by the Department of Defense (DoD) through the National Defense Science & Engineering Graduate Fellowship (NDSEG) Program. The LES study was performed at Cascade Technologies, with support from ONR and NAVAIR SBIR project, under the supervision of Dr. John T. Spyropoulos. The main LES calculations were carried out on DoD HPC systems in ERDC DSRC.

Chapter 4

RESOLVENT-BASED MODELING OF TURBULENT JET NOISE

An adaptation of a proceeding of the *2020 AIAA Scitech Forum*

Chapter Abstract

Linear resolvent analysis has demonstrated encouraging results for modeling coherent structures in jets when compared against their data-educed counterparts from high-fidelity large-eddy simulations (LES). However, leveraging resolvent modes for predicting statistics of the far acoustic field remains elusive. In this study, we extend resolvent analysis to that of an acoustic analogy that relates the near-field forcing to the far-field acoustics 100 diameters from the nozzle. We use an LES database of round, isothermal, Mach 1.5 and 0.9 jets to produce an ensemble of realizations for the acoustic field, both in the near- and far-field, that we project on to a limited set of n resolvent modes. In the near-field, projections are done on a restricted acoustic output domain, $r/D = [5, 6]$, while the far-field projections are done upon a 100 diameter arc from the nozzle. In each case, this allows the LES realizations to be recast in the resolvent basis via a data-deduced, low-rank, $n \times n$ cross-spectral density matrix. We find substantial improvements to the acoustic field reconstructions with the addition of a RANS-derived eddy-viscosity model to the resolvent operator. The reconstructions quantitatively match the most energetic regions of the acoustic field across Strouhal numbers, $St = [0 - 1]$, and azimuthal wavenumbers, $m = [0, 2]$, using only *one* resolvent mode. We then present the necessary forcing amplitudes required for the associated resolvent modes and suggest avenues for modeling this forcing. Finally, we present a simple function, using only two fitting parameters, that results in a rank-1 resolvent model that agrees to within 2dB of the peak acoustic region for both jets.

4.1 Introduction

This thesis aims to further work on the development of accurate, reduced-order models for turbulent jet-noise prediction, control, and ultimately, reduction. Our goal is to develop a jet-noise model founded upon the underlying physics of turbulent flows that is both low-rank and provides direct insight into the mechanisms primarily responsible for noise generation. The resolvent analysis (McKeon and Sharma, 2010; Jovanović and Bamieh, 2005; Jeun, Nichols, and Jovanović, 2016; Schmidt et al., 2018), also known as input-output analysis, provides a useful framework for achieving these goals.

The central idea of the resolvent framework for jet noise modeling is similar to the acoustic analogy (Lighthill, 1952; Goldstein, 2003), whereby a forcing term, related to the statistics of the hydrodynamic near-field turbulence, gives rise, through a linear operator, to the observed far-field sound. The resolvent framework differs in

two important ways. First, the operator is decomposed into its singular components that represent the maximal amplification between the forcing and the output. This permits the resulting acoustic field to be described at low rank, and thus limiting the forcing statistics that must be modeled. Secondly, the full linearized Navier–Stokes equations are used as the propagator, and we seek a modal basis that represents *both* near and far-field coherent structures.

Before recent advances in computational power, the idea of modeling both the hydrodynamic component along with the acoustics would be seen as both unnecessary and computationally taxing. However, the ability to resolve both components of the flow is in fact a benefit. Starting with the experimental findings of Mollo-Christensen (1967) and Crow and Champagne (1971), it has become clear that coherent structures in the hydrodynamic near-field are directly responsible for far-field sound (Jordan and Colonius, 2013). These structures take the spatio-temporal form of wavepackets and have been found to be the dominant source for aft angle sound (Jordan and Colonius, 2013), as well as partial contributors to sideline noise (Papamoschou, 2018; Jeun and Nichols, 2018). These wavepackets may be linked to the early works of Crighton and Gaster (1976) (and Michalke (1977)) who hypothesized that coherent structures could be described as linear instability modes of the mean flow via modal analysis. However, it has now become apparent that the correct representation of wavepackets is that of a highly-amplified response to turbulent fluctuations, which is directly found via the resolvent framework.

Resolvent analysis uses the Singular Value Decomposition (SVD) to decompose the linear terms of the resolvent operator, identifying sets of mutually orthogonal *forcing/input* and *response/output* modes, and ranking them in terms of the corresponding energetic gain between the forcing and response. This is particularly important as it allows our model to select the most relevant amplification mechanisms for noise generation. We can then retain a limited set of the resolvent modes to produce a reduced-order model, or in other words, a reduced-rank acoustic analogy.

Several studies have applied resolvent analysis to develop low-rank jet models (Jeun, Nichols, and Jovanović, 2016; Cavalieri, Jordan, and Lesshafft, 2019; Lesshafft et al., 2019). The existence of relatively low-rank responses in round, turbulent jets was shown by Schmidt et al. (2018), with significant agreement between structures found through spectral proper orthogonal decomposition (Towne, Schmidt, and Colonius, 2018) (SPOD) of a high-fidelity experimentally-verified large-eddy simulations (LES) of jets (Brès, Jordan, et al., 2014; Brès, Jaunet, et al., 2015).

Of particular relevance to this study, are "acoustic resolvent modes" induced by performing resolvent analysis with an output domain defined over a region where fluctuations are purely acoustic. Through implementation of an acoustic output domain, resolvent analysis is able to filter out energetic, but acoustically irrelevant structures in the near-field. Jeun, Nichols, and Jovanović (2016) performed such an analysis and found that for a Mach 1.5 jet, at Strouhal number $St = 0.33$ and azimuthal wavenumber $m = 0$, that the first resolvent mode reconstructs 57% of the acoustic energy, but through inclusion of the next 23 resolvent modes, the reconstruction improved to 70% of the acoustic energy. This study looks to perform a similar analysis, in that we compute many acoustic resolvent modes and assess how well they reconstruct the acoustic energy. However, we also look to reduce the rank of the far-field significantly with the use of an eddy-viscosity model and generalize the performance of the resolvent framework across frequencies $St = 0-1$, azimuthal wavenumbers $m = [0-2]$, and for two turbulent jets at Mach numbers of 0.9 and 1.5.

For a resolvent jet model to fully reconstruct flow statistics, and in this case those of the acoustic field, a resolvent-based model must incorporate sub-optimal modes (Schmidt et al., 2018) and correctly describe correlations (i.e. covariance) between modes inherent to turbulent flow (Towne, Lozano-Durán, and Yang, 2020). The latter requirement can be shown via the statistical representation of the resolvent operator, (Towne, Schmidt, and Colonius, 2018)

$$\boldsymbol{S}_{yy} = \boldsymbol{R}\boldsymbol{S}_{ff}\boldsymbol{R}^{*} \tag{4.1}$$

where $\boldsymbol{S}_{yy}$ and $\boldsymbol{S}_{ff}$ are the cross-spectral density tensors of the responses and the forcing respectively and $\boldsymbol{R}$ is the resolvent operator. This equation shows that if the forcing CSD, describing spatial correlations or "color" (Zare, Jovanović, and Georgiou, 2017) can be modeled (Towne, Bres, and Lele, 2017), then the resolvent operator identically reconstructs the flow statistics, $\boldsymbol{S}_{yy}$. If the forcing were spatially uncorrelated, $\boldsymbol{S}_{ff} = \boldsymbol{\Lambda}$, where $\boldsymbol{\Lambda}$ is a diagonal matrix, then the eigenvectors of $\boldsymbol{S}_{yy}$, which are the SPOD modes of the outputs, are aligned with the eigenvectors of $\boldsymbol{R}\boldsymbol{R}^{*}$ (Towne, Schmidt, and Colonius, 2018), or the response modes of the resolvent operator, $\boldsymbol{R}$. Recent work incorporating classical eddy-viscosity models into the resolvent operator showed a significant improvement in the alignment between SPOD and resolvent modes in jets (Pickering, Rigas, Schmidt, et al., 2020), reducing the resulting effort required to model the effective $\boldsymbol{S}_{ff}$ by reducing the magnitude

of the off-diagonal terms. We utilize the same eddy-viscosity model in the present work.

This paper explores an approach to describe the coupling between resolvent modes that is necessary for reconstructing the acoustic field with a minimal set of resolvent modes. The coupling provides directional and energetic variability in acoustic radiation inherently important for noise prediction (Cavalieri, Jordan, Agarwal, et al., 2011). Determination of the coupling between modes is performed by leveraging an ensemble of LES realizations which are projected on to a limited set (i.e. low-rank) of acoustic resolvent modes. From these projections, we attain a (drastically) reduced-order cross-spectral density between the retained modes–a Hermitian, frequency-dependent matrix of size $n \times n$ that accurately represents the acoustic field.

Organization of the chapter is as follows. We first briefly describe the LES databases used, the main details pertaining to resolvent analysis, and present the statistical description of the resolvent framework for reconstructing the acoustic field and estimating the reduced order covariance matrix in § 4.2. In § 4.3 we present resolvent modes and LES reconstructions in the resolvent basis for one frequency-wavenumber pair for the Mach 1.5 jet before generalizing the approach to both jets over $St = [0, 1]$ and $m = [0, 2]$, and to both the near- and far-field acoustic regions. In the near-field section we compare the impact of including a RANS eddy viscosity to the resolvent operator and find it presents a significantly more efficient resolvent basis. We then present results for the far-field, along an arc at $100D$ from the nozzle, and show that reconstructions for both jets may be found using only the optimal resolvent mode. Finally, we conclude with a discussion on how the correct forcing coefficients may be estimated for a predictive jet noise model.

4.2 Methods

Large Eddy Simulation database

The LES database and resolvent analysis are described in Schmidt et al. (2018) and Towne, Schmidt, and Colonius (2018). For brevity, we summarize the main details here. The LES databases, transonic (Mach 0.9), and supersonic (Mach 1.5) cases, were computed using the flow solver "Charles" and details on numerical methods, meshing, and subgrid-models can be found in Brès, Ham, et al. (2017) and Brès, Bose, et al. (2018) along with validation cases conducted at PPRIME Institute, Poitiers, France for the Mach 0.9 jet (Brès, Jordan, et al., 2018). The Mach 1.5 round jet corresponds to a Reynolds number $Re_j = \rho_j U_j D/\mu_j = 1.76 \times 10^6$, and

for the Mach 0.9 jet $Re_j = 1.01 \times 10^6$, where subscript j gives the value at the center of the jet, ρ is density, μ is viscosity, and M_j is the Mach number $M_j = U_j/a_j$, with a_j as the speed of sound at the nozzle centerline.

Throughout the chapter, variables are non-dimensionalized by the mean jet velocity U_j, jet diameter D, and pressure $\rho_j U_j^2$, with the resulting equation of state $p = \frac{\rho T}{\gamma M_j^2}$, with T denoting temperature and γ the ratio of specific heats. Frequencies are reported in Strouhal number, $St = fD/U_j$, where f is the frequency. The database consists of 10,000 snapshots separated by $\Delta t c_\infty/D = 0.1$ and 0.2 for $M_j = 1.5$ and $M_j = 0.9$ jets, respectively, with c_∞ as the ambient speed of sound, and interpolated onto a structured cylindrical grid $x, r, \theta \in [0, 30] \times [0, 6] \times [0, 2\pi]$, where x, r, θ are streamwise, radial, and azimuthal coordinates, respectively. Variables are reported by the vector

$$\boldsymbol{q} = [\rho, u_x, u_r, u_\theta, T]^T, \tag{4.2}$$

where u_x, u_r, u_θ are the three velocity components.

For an ensemble approach, the LES database of 10,000 snapshots is segmented into bins of 256 snapshots, with an overlap of 75%, and under the implementation of a Hamming window, resulting in 153 independent realizations of the flow. Each realization is then decomposed in the azimuthal direction and in time. The temporal decomposition provides a resolution of $St = 0.026$ for the $M_j = 1.5$ jet and $St = 0.0217$ for $M_j = 0.9$ and the azimuthal decomposition is valid up to $m = 68$, however, the acoustically relevant azimuthal wavenumbers are much smaller, and only azimuthal wavenumbers $m = [0 - 2]$ are considered in this paper.

Considering the LES database only extends to $r/D = 6$, we implement a Kirchhoff surface (details provided in Appendix C.1), to the azimuthally and temporally transformed realizations of the flow. In doing so, we create an ensemble of far-field realizations located along an arc, with angle ϕ, of $100D$ from the nozzle at each frequency and azimuthal wavenumber. As done in Brès, Ham, et al. (2017), and associated experiments (Schlinker, Simonich, Reba, Colonius, and Ladeinde, 2008; Schlinker, Simonich, Reba, Colonius, Gudmundsson, et al., 2009), we specifically compute the acoustics for the aft-angle sound from $\phi = 100 - 160$ and find our acoustic far-field is in close agreement (within 2dB) with the far field computed via a Ffowcs Williams-Hawkings (FWH) surface in the LES calculation. Alternatively, we could have proceeded with the FWH data, however, doing so would provide an inconsistency between the LES and resolvent approach taken here for the near to

far-field propagation. Additionally, propagating the LES realizations with a Kirchhoff surface allows for a continuous computation of the arc, while the far-field data from the LES is rather coarse, with data located 5° apart.

Resolvent analysis

For the round, statistically-stationary, turbulent, jets considered in this thesis, the compressible Navier–Stokes, energy, and continuity equations are linearized via a standard Reynolds decomposition, and Fourier transformed both in time and azimuthally to the compact expression

$$(i\omega\mathbf{I} - \mathbf{A}_m)\boldsymbol{q}_{m,\omega} = \boldsymbol{L}_{m,\omega}\boldsymbol{q}_{m,\omega} = \boldsymbol{f}_{m,\omega}, \tag{4.3}$$

where $\boldsymbol{L}_{m,\omega}$ is the forward linear operator, $\boldsymbol{f}$ constitutes the nonlinear forcing in each variable, ω is the frequency, and m is the azimuthal wavenumber. For the purpose of suggesting resolvent analysis as a predictive modeling tool, mean-flow quantities used in the operator are derived from a RANS model, fitted closely to the LES mean flow. Although the mean flows are similar, the computation of a RANS model, using the standard $\kappa - \epsilon$ closure equations, also provides an eddy-viscosity field. With previous results of Pickering, Rigas, Sipp, et al. (2019) and Pickering, Rigas, Schmidt, et al. (2020) showing drastically improved agreement between SPOD and resolvent modes with the inclusion of an eddy-viscosity model, we incorporate the eddy-viscosity field from the RANS as $\mu_T = cC_\mu k^2/\epsilon$, where c and C_μ are scaling constants ($c = 0.2$, $C_\mu = 0.0554$ for $M_j = 1.5$ and $C_\mu = 0.0623$ for the $M_j = 0.9$ jet), k is the turbulent kinetic energy field, and ϵ is the turbulent dissipation field.

Continuing with the derivation of the resolvent operator, we rewrite Equation 4.3 by moving $\boldsymbol{L}_{m,\omega}$ to the right-hand side gives,

$$\boldsymbol{q}_{m,\omega} = \boldsymbol{L}^{-1}_{m,\omega}\boldsymbol{f}_{m,\omega}. \tag{4.4}$$

To specify particular domains for both the response and forcing, we may write the above as

$$\boldsymbol{q}_{m,\omega} = \boldsymbol{L}^{-1}_{m,\omega}\boldsymbol{B}\boldsymbol{f}_{m,\omega}, \tag{4.5}$$

and define the output variable

$$\boldsymbol{y}_{m,\omega} = \boldsymbol{C}\boldsymbol{q}_{m,\omega}, \tag{4.6}$$

where $\boldsymbol{B}$ and $\boldsymbol{C}$ are input and output matrices. Then by introducing the compressible energy norm of Chu (1965),

$$\langle \boldsymbol{q}_1, \boldsymbol{q}_2 \rangle_E = \int\int\int \boldsymbol{q}_1^* \mathrm{diag}\left(\frac{\bar{T}}{\gamma\bar{\rho}M^2}, \bar{\rho}, \bar{\rho}, \bar{\rho}, \frac{\bar{\rho}}{\gamma(\gamma-1)\bar{T}M^2}\right)\boldsymbol{q}_2 r\mathrm{d}x\mathrm{d}r\mathrm{d}\theta = \boldsymbol{q}_1^* \boldsymbol{W}\boldsymbol{q}_2, \tag{4.7}$$

(where superscript $*$ denotes the complex transpose) via the matrix $\boldsymbol{W}$ to the forcing and response, ($\boldsymbol{W}_f = \boldsymbol{W}_y = \boldsymbol{W}$) gives the weighted resolvent operator, $\hat{\boldsymbol{R}}_{m,\omega}$,

$$\hat{\boldsymbol{R}}_{m,\omega} = \boldsymbol{W}_y^{1/2}\boldsymbol{C}\boldsymbol{L}_{m,\omega}^{-1}\boldsymbol{B}\boldsymbol{W}_f^{-1/2}. \tag{4.8}$$

Resolvent modes may then be found by taking the singular value decomposition of the weighted resolvent operator giving

$$\hat{\boldsymbol{R}}_{m,\omega} = \hat{\boldsymbol{U}}_{m,\omega}\boldsymbol{\Sigma}\hat{\boldsymbol{V}}_{m,\omega}^* \tag{4.9}$$

where the optimal response and forcing modes are contained in the columns of $\boldsymbol{U}_{m,\omega} = \boldsymbol{W}_y^{-1/2}\hat{\boldsymbol{U}}_{m,\omega}$, with $\boldsymbol{U}_{m,\omega} = [\boldsymbol{u}_{m,\omega}^1, \boldsymbol{u}_{m,\omega}^2, ..., \boldsymbol{u}_{m,\omega}^N]$, $\boldsymbol{V}_{m,\omega} = \boldsymbol{W}_f^{-1/2}\hat{\boldsymbol{V}}_{m,\omega}$, $\boldsymbol{V}_{m,\omega} = [\boldsymbol{v}_{m,\omega}^1, \boldsymbol{v}_{m,\omega}^2, ..., \boldsymbol{v}_{m,\omega}^N]$, and $\boldsymbol{\Sigma} = \mathrm{diag}(\sigma_1, \sigma_2, ..., \sigma_N)$ as the optimal gains.

Near-field acoustic output

For analysis of the near-field acoustics, the output matrix $\boldsymbol{C}$ is chosen to only include pressure, $p' = \frac{\rho'\bar{T}+\bar{\rho}T'}{\gamma M_j^2}$, from x/D = [0, 30], and r/D = [5,20]. Ideally, the LES domain would extend from $r/D = [5, 20]$ so that the LES could be directly projected onto the resolvent basis, however, the LES database (i.e. the saved data from the LES) only extends to $r/D = 6$. Although one could define an output matrix $\boldsymbol{C}$ that only includes that surface at $r/D = 6$, the resolvent modes may still contain hydrodynamic behavior (unless allowed to propagate further from the jet), thus we use the larger domain to ensure the modes are clearly acoustic. Using the larger domain presents a clear loss of orthogonality in the space represented by the LES domain. This is alleviated by truncating the modes to $r/D = [5, 6]$ (after computing the resolvent SVD) and implementing a Moore-Penrose inverse such that a least square fit of the LES in the resolvent basis can be performed. Additionally, the input matrix, $\tilde{\boldsymbol{S}}_{\beta\beta}$, is chosen to be identity for the most general results, where other studies (Towne, Bres, and Lele, 2017) suggest the use of a filter based on the location and magnitude of turbulent kinetic energy in the jet.

Far-field acoustic output

To define an input-output relationship from the near-field forcing to the far-field acoustics, we introduce a Kirchhoff surface, applied as a linear operator and derived

in Appendix C.1, propagating a surface in the near-field to the far-field. We define three radii, R as the radial coordinate of the near-field cylindrical surface, r as the coordinate pertaining to the far-field cylindrical surface, and ρ representing the distance from the nozzle in spherical coordinates (e.g. $\rho/D = 100$ for this study). As described in § 4.2, the resolvent problem is defined as

$$\boldsymbol{q} = \boldsymbol{RBf} \tag{4.10}$$

$$\boldsymbol{y} = \boldsymbol{C}_{R,\rho}\boldsymbol{q} \tag{4.11}$$

where the output matrix $\boldsymbol{C}_{R,\rho}$ is the total Kirchhoff operator that maps the near-field cylindrical surface, R, to the far-field spherical surface, ρ. This operator is linearly composed of many Kirchhoff surfaces, $\boldsymbol{C}_{R,r}$, detailed next.

The cylindrical Kirchhoff operator is composed of a number of linear operations to ensure accurate results and is defined as,

$$\boldsymbol{C}_{R,r} = \boldsymbol{D}^{*}\boldsymbol{H}_{r}\boldsymbol{DPNTC}_{R}, \tag{4.12}$$

where $\boldsymbol{C}_R$ is a surface selection matrix ($\in \mathbb{R}^{N_{surface} \times N_r N_x N_v}$), $\boldsymbol{N}$ is an interpolation matrix from a non-uniform grid to a uniform grid with $\Delta x/D = 0.025$ ($\in \mathbb{R}^{N_{uniform} \times N_{surface}}$), $\boldsymbol{T}$ is a Tukey windowing matrix (using a taper value of 0.75) that extends over the Kirchhoff surface to reduce spectral leakage ($\in \mathbb{R}^{N_{uniform} \times N_{uniform}}$), $\boldsymbol{P}$ is a padding matrix extending the uniform grid with a total of 2^n points (n is set to 15) for computing the upstream and downstream wave propagation, as well as ensuring sufficient accuracy in the transform of the initial surface ($\in \mathbb{R}^{2^n \times N_{uniform}}$), $\boldsymbol{D}$ is the DFT matrix ($\in \mathbb{R}^{2^n \times 2^n}$), and $\boldsymbol{H}$ contains the derived Hankel functions of the Kirchhoff surface, with entries along the diagonal for each wavenumber, for a specified radial distance, r, from the surface at R ($\in \mathbb{R}^{2^n \times 2^n}$).

However, the above operator only supports one specified radial distance from the cylindrical surface at R, and thus a linear combination of $\boldsymbol{C}_{R,r}$ and proper selection of streamwise points are required to construct a spherical arc. Thus, the linear expression to construct the total Kirchhoff operator is then

$$\boldsymbol{C}_{R,\rho} = \sum_{i=1}^{N_C} \boldsymbol{C}_{x_i}\boldsymbol{C}_{R,r_i}, \tag{4.13}$$

where x_i represents the streamwise location in the $100/D$ arc and r_i represents the radial extent to which the Kirchhoff surface must propagate from surface R to the far-field arc for the respective streamwise location. Points are defined along the arc from $\phi = 100 - 160$ with a resolution of $\Delta\phi = 0.5$.

Statistics

The statistics we are interested in are contained within the cross-spectral density (CSD) tensor, which may be found for the desired output space by multiplying the resolvent equation by its complex conjugate and taking the expectation (Towne, Schmidt, and Colonius, 2018)

$$\langle \boldsymbol{y}\boldsymbol{y}^* \rangle = \langle \hat{\boldsymbol{R}}\boldsymbol{f}\boldsymbol{f}^*\hat{\boldsymbol{R}}^* \rangle \tag{4.14}$$

giving

$$\boldsymbol{S}_{yy} = \hat{\boldsymbol{R}}\boldsymbol{S}_{ff}\hat{\boldsymbol{R}}^* \tag{4.15}$$

where $\boldsymbol{S}_{yy}$ and $\boldsymbol{S}_{ff}$ are the CSD tensors of the response and the forcing respectively.

As mentioned earlier, this representation shows that if the forcing CSD tensor is known, then the resolvent operator reconstructs the response statistics. However, the forcing CSD is generally unknown. There are at least two potential avenues for modeling this. The first is to directly model $\boldsymbol{S}_{ff}$. To aid in such modeling efforts, $\boldsymbol{S}_{ff}$ may be computed directly from full LES data (Towne, Bres, and Lele, 2017), or estimated from limited flow statistics Towne, Lozano-Durán, and Yang (2020). A second approach is to modify the resolvent operator by supplementing the governing linearized equations with an appropriately linearized turbulence model. In Pickering, Rigas, Schmidt, et al. (2020), an eddy-viscosity model was considered, and LES data was used to determine an optimal eddy viscosity field that would align, insofar as possible, the modes of $\boldsymbol{S}_{yy}$ with those of $\boldsymbol{R}\boldsymbol{R}^*$. They found this to substantially reduce the magnitude of the off-diagonal terms of $\boldsymbol{S}_{ff}$, in so far as the near-field coherent structures were concerned, consequently simplifying the number of terms that must be modeled.

In this study, we look to take both modeling approaches. We first utilize the eddy-viscosity approximation of Pickering, Rigas, Schmidt, et al. (2020) and then estimating a low-order approximation of the forcing CSD for the acoustic field. To do the latter, we return to Equation 4.15 and expand the resolvent operator through its singular value decomposition:

$$\boldsymbol{S}_{yy} = \hat{\boldsymbol{U}}\boldsymbol{\Sigma}\hat{\boldsymbol{V}}^*\boldsymbol{S}_{ff}\hat{\boldsymbol{V}}\boldsymbol{\Sigma}\hat{\boldsymbol{U}}^* \tag{4.16}$$

and define a covariance matrix, $\boldsymbol{S}_{\beta\beta}$, as $\boldsymbol{S}_{\beta\beta} = \boldsymbol{V}^*\boldsymbol{W}_f\boldsymbol{S}_{ff}\boldsymbol{W}_f\boldsymbol{V}$, where $\boldsymbol{\beta}$ is the projection of the forcing upon the resolvent input modes, $\boldsymbol{\beta} = \boldsymbol{V}^*\boldsymbol{W}_f\boldsymbol{f}$. This gives

$$\boldsymbol{S}_{yy} = \hat{\boldsymbol{U}}\boldsymbol{\Sigma}\boldsymbol{S}_{\beta\beta}\boldsymbol{\Sigma}\hat{\boldsymbol{U}}^* \tag{4.17}$$

which can be rearranged to solve for the covariance matrix,

$$\boldsymbol{S}_{\beta\beta} = \boldsymbol{\Sigma}^{-1}\boldsymbol{U}^{*}\boldsymbol{W}_{y}\boldsymbol{S}_{yy}\boldsymbol{W}_{y}\boldsymbol{U}\boldsymbol{\Sigma}^{-1}. \tag{4.18}$$

In its current state, the covariance matrix is exact, maintaining a full size of the system and permitting approximately 10^{11} degrees of freedom (i.e. $\boldsymbol{S}_{\beta\beta} \in C^{5N_xN_r \times 5N_xN_r}$). To obtain a low-rank model of $\boldsymbol{S}_{\beta\beta}$ from the LES data, we compute $\boldsymbol{S}_{\beta\beta}$ with a truncated set of n resolvent modes, $\tilde{\boldsymbol{U}} \in C^{5N_xN_r \times n}$, as,

$$\tilde{\boldsymbol{S}}_{\beta\beta} = \tilde{\boldsymbol{\Sigma}}^{-1}\tilde{\boldsymbol{U}}^{*}\boldsymbol{W}_{y}\boldsymbol{S}_{yy}\boldsymbol{W}_{y}\tilde{\boldsymbol{U}}\tilde{\boldsymbol{\Sigma}}^{-1}. \tag{4.19}$$

Thereby reducing the size of the covariance matrix to $n \times n$, in that the degrees of freedom are now drastically reduced to $O(10^0 - 10^1)$.

With $\tilde{\boldsymbol{S}}_{\beta\beta}$, we may ask the following questions: (1) How well does $\tilde{\boldsymbol{S}}_{\beta\beta}$ reconstruct $\boldsymbol{S}_{yy}$ in the truncated resolvent basis? (2) May $\tilde{\boldsymbol{S}}_{\beta\beta}$ be further reduced (e.g. neglect off-diagonal terms)? (3) Can $\tilde{\boldsymbol{S}}_{\beta\beta}$ be modeled? (4) And can $\tilde{\boldsymbol{S}}_{\beta\beta}$ reconstruct a more general space (e.g. $\boldsymbol{C} = \boldsymbol{I}$)?

To address question (1), how well does $\tilde{\boldsymbol{S}}_{\beta\beta}$ reconstruct $\boldsymbol{S}_{yy}$, the estimated response CSD is computed by

$$\tilde{\boldsymbol{S}}_{yy} = \tilde{\boldsymbol{U}}_{y}\tilde{\boldsymbol{S}}_{\beta\beta}\tilde{\boldsymbol{U}}_{y}^{*}. \tag{4.20}$$

The error between $\boldsymbol{S}_{yy}$ and $\tilde{\boldsymbol{S}}_{yy}$ may be assessed in a number of ways. For our purposes, the quantity of utmost importance is the power spectral density (PSD) of the acoustic field, which are the diagonal terms of $\boldsymbol{S}_{yy}$. When considering such comparisons at individual frequencies and wavenumbers, a common comparison is through the difference in sound pressure level in decibels, dB, computed as

$$\Delta\text{dB} = 20\log\left(\sqrt{\frac{1}{k-1}\text{diag}(\tilde{\boldsymbol{S}}_{yy} - \boldsymbol{S}_{yy})^2}\right), \tag{4.21}$$

where k is the number of realizations. However, this comparison can be somewhat misleading as it does not take into account the regions of peak magnitude of acoustic field. From an engineering point of view, regions of the largest magnitude are of far greater importance for understanding how to reduce the peak noise of a turbulent jet. For example, underpredicting (or overpredicting) the acoustic field by 20dB in a region of the acoustic field that is measured to be 80dB, is of no consequence if the region associated with 120dB is closely predicted. Considering this, we opt to compare the PSD at distinct frequencies and wavenumbers visually, and only make

quantitative comparisons of the overall sounds pressure level (OASPL):

$$OASPL(\phi) = 10\log_{10}\left(\sum_{St_{min}}^{St_{max}} 2 \sum_{-m_{max}}^{m_{max}} \mathrm{diag}(\boldsymbol{S}_{yy}(\phi, m, St))\right). \tag{4.22}$$

To assess how well a more general space may be reconstructed with $\tilde{\boldsymbol{S}}_{\beta\beta}$, we use the original forcing modes computed from the resolvent and recalculate the responses with the response restriction matrix set to identity. This is computed as

$$\tilde{\boldsymbol{U}}_q = \boldsymbol{L}^{-1}\tilde{\boldsymbol{V}}_y \tag{4.23}$$

where $\boldsymbol{U}_q$ is the set of response modes of the full domain from the set of forcing modes $\boldsymbol{V}_y$ of the $\boldsymbol{C}_y$ restricted domain. We can then estimate the full state CSD,

$$\tilde{\boldsymbol{S}}_{qq} = \tilde{\boldsymbol{U}}_q \tilde{\boldsymbol{S}}_{\beta\beta} \tilde{\boldsymbol{U}}_q^*. \tag{4.24}$$

However, at present, we only provide the modes $\tilde{\boldsymbol{U}}_q$ associated in the near field, as they give insight into active physical mechanisms, while omitting the associated near-field statistics for future work.

Before advancing to the results, we must note that the above relations are valid when $\boldsymbol{U}$ and $\boldsymbol{V}$ are orthogonal bases in the same space as $\boldsymbol{y}$ and $\boldsymbol{f}$, respectively. However, in the case of the near-field calculations, $\boldsymbol{U}$ is defined over a larger space than $\boldsymbol{y}$ and a pseudo inverse must be constructed to find the least-square solution to above projections. First, we truncate the output modes $\boldsymbol{U}$ to the output space x/D = [0, 30] and r/D = [5,6] in the pressure field and define the associated output matrix as $\boldsymbol{C}_z$ where z denotes the new restricted space. Applying $\boldsymbol{C}_z$ to both the LES data and resolvent modes gives the ensemble of realizations $\boldsymbol{z}$ and resolvent modes $\boldsymbol{U}_z$. In addition to reducing the domain space, we also truncate the resolvent response basis to a limited set of n modes, as discussed above, represented as $\tilde{\boldsymbol{U}}_z$. There are now two important consequences of reducing the resolvent domain from $\boldsymbol{C}_y$ to $\boldsymbol{C}_z$. The first is a correction to the gain to the domain $\boldsymbol{C}_z$. Since both output domains share identical input modes we have,

$$\sigma_{i,y}^2 = \frac{\boldsymbol{u}_{i,y}^* \boldsymbol{W}_y \boldsymbol{u}_{i,y}^*}{\boldsymbol{v}_{i,f}^* \boldsymbol{W}_f \boldsymbol{v}_{i,f}^*}, \qquad \sigma_{i,z}^2 = \frac{\boldsymbol{u}_{i,z}^* \boldsymbol{W}_z \boldsymbol{u}_{i,z}^*}{\boldsymbol{v}_{i,f}^* \boldsymbol{W}_f \boldsymbol{v}_{i,f}^*}, \tag{4.25}$$

and the gain of the new domain is

$$\sigma_{i,z}^2 = \sigma_{i,y}^2 \frac{\boldsymbol{u}_{i,z}^* \boldsymbol{W}_z \boldsymbol{u}_{i,z}^*}{\boldsymbol{u}_{i,y}^* \boldsymbol{W}_y \boldsymbol{u}_{i,y}^*}. \tag{4.26}$$

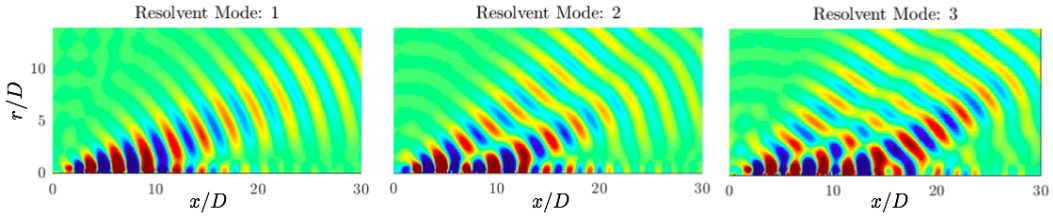

Figure 4.1: The first three resolvent modes of fluctuating pressure, $q_{p'}$. Red and blue contours vary from ± 50% of the maximum fluctuating pressure of each mode, $\pm 0.5||q_{p'}||_\infty$. $M_j = 1.5$, $St = 0.26$, $m = 0$.

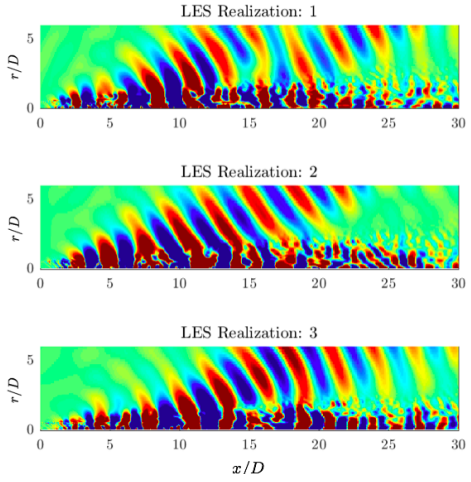

Figure 4.2: Three realizations of the LES pressure field at $M_j = 1.5$, $St = 0.26$, $m = 0$. Red and blue contours vary from ± 50% of the maximum fluctuating pressure of each mode, $\pm 0.5||q_{p'}||_\infty$.

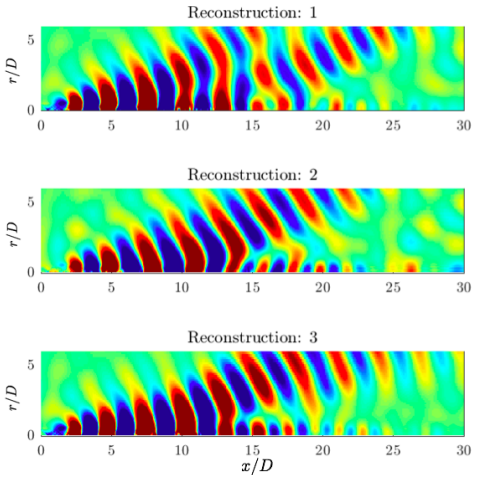

Figure 4.3: Reconstructions of the corresponding LES realizations using the 3-mode resolvent basis. Contour values are identical to Figure 4.2. $M_j = 1.5$, $St = 0.26$, $m = 0$.

The second is a loss of orthogonality, fortunately, we may still determine a least squares fit of the data by computing the Moore-Penrose inverse of $\boldsymbol{W}_z^{1/2}\tilde{\boldsymbol{U}}_z$, $(\boldsymbol{W}_z^{1/2}\tilde{\boldsymbol{U}}_z)^+ = (\tilde{\boldsymbol{U}}_z^*\boldsymbol{W}_z\tilde{\boldsymbol{U}}_z)^{-1}\tilde{\boldsymbol{U}}_z^*\boldsymbol{W}_z^{1/2}$, and projecting it onto the CSD of z to estimate $\tilde{\boldsymbol{S}}_{\beta\beta}$

$$\tilde{\boldsymbol{S}}_{\beta\beta} = \tilde{\boldsymbol{\Sigma}}_z^{-1}(\boldsymbol{W}_z^{1/2}\tilde{\boldsymbol{U}}_z)^{+*}\boldsymbol{W}_z^{1/2}\boldsymbol{S}_{zz}\boldsymbol{W}_z^{1/2}(\boldsymbol{W}_z^{1/2}\tilde{\boldsymbol{U}}_z)^{+}\tilde{\boldsymbol{\Sigma}}_z^{-1}. \tag{4.27}$$

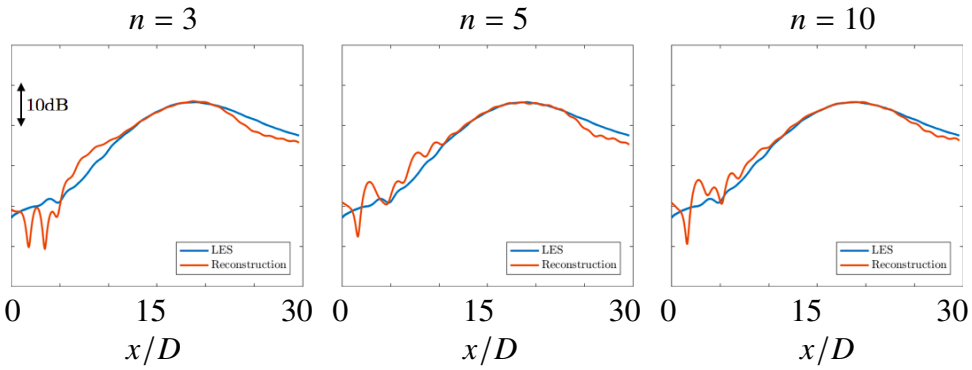

Figure 4.4: Comparison of pressure RMS values by dB at $r/D = 6$ for the LES ensemble and reconstructions in the resolvent basis using 3, 5, and 10 resolvent modes.

4.3 Results

Near-field

Resolvent analysis and LES reconstructions

We begin by providing detailed results for a single frequency and azimuthal wavenumber pair of the $M_j = 1.5$ jet using the RANS eddy-viscosity resolvent operator. Figure 4.1 presents the first three resolvent modes computed with a restricted acoustic output domain ($r/D = [5, 20]$ in the fluctuating pressure field) and recast in the full domain by $\boldsymbol{U}_q = \boldsymbol{L}^{-1}\boldsymbol{V}_y$ for $M_j = 1.5$, $St = 0.26$, and $m = 0$. The associated gain of these modes, normalized by the first resolvent gain, are $[1, 0.17, 0.15]$ (and slowly decreasing with higher modes), indicating the first resolvent mode has at least six times the amplification to its associated forcing than the following resolvent modes.

The resolvent response modes show a particular pattern of acoustic beams. For the first mode there is a single, energetic acoustic beam, propagating at a shallow angle to the jet axis. The first suboptimal mode consists of two acoustic beams, similar to what was found by Jeun, Nichols, and Jovanović (2016). This pattern continues to the next suboptimal mode, with three beams located at the perimeter of the first suboptimal. Although not shown, this behavior continues for further suboptimal modes.

The resolvent response modes are now be used to determine the covariance matrix $\tilde{\boldsymbol{S}}_{\beta\beta}$. However, before directly computing $\tilde{\boldsymbol{S}}_{\beta\beta}$, we first provide an example of individual reconstructions of the LES realizations. To do this we return to Equation 4.27

$$\tilde{\boldsymbol{S}}_{\beta\beta} = \tilde{\boldsymbol{\Sigma}}_z^{-1}\tilde{\boldsymbol{U}}_z^{+*}\boldsymbol{W}_z\boldsymbol{S}_{zz}\boldsymbol{W}_z\tilde{\boldsymbol{U}}_z^{+}\tilde{\boldsymbol{\Sigma}}_z^{-1}. \tag{4.28}$$

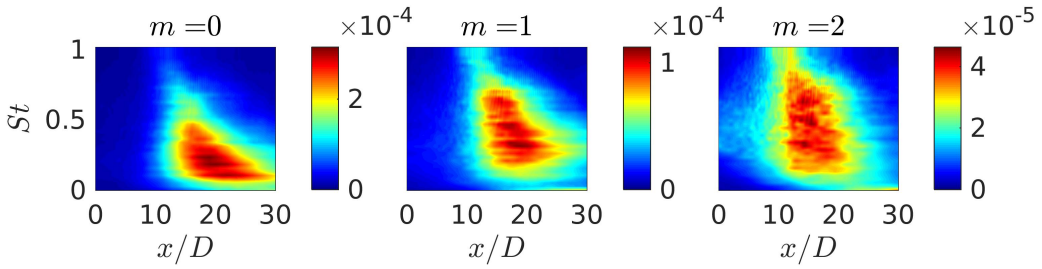

Figure 4.5: RMS of LES pressure fluctuations of the $M_j = 1.5$ jet at radial surface $r/D = 6$ from $St = [0, 1]$ and $x/D = [0, 30]$ for three azimuthal wavenumbers, $m = [0, 2]$.

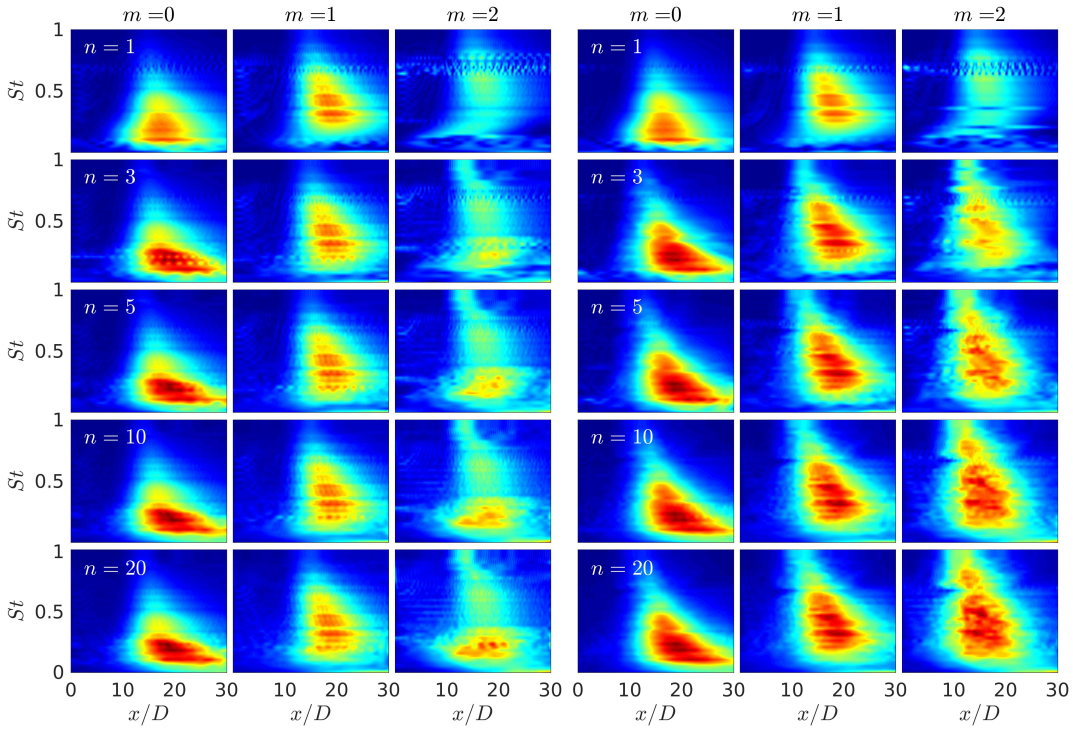

Figure 4.6: RMS of resolvent reconstructions of the $M_j = 1.5$ jet, without an eddy-viscosity model (left) and with a RANS eddy-viscosity model (right), at radial surface $r/D = 6$ from $St = [0, 1]$ and $x/D = [0, 30]$ for three azimuthal wavenumbers, $m = [0, 2]$, from left to right and using $n = 1, 3, 5, 10, 20$ modes from top to bottom. Contours and axes mirror those of Figure 4.5.

Expanding $\boldsymbol{S}_{zz}$ to $\boldsymbol{z}\boldsymbol{z}^*$ shows that $\tilde{\boldsymbol{S}}_{\beta\beta}$ is the scaled covariance of the ensemble of output projection coefficients, $\tilde{\boldsymbol{\alpha}} = \tilde{\boldsymbol{U}}_z^{+*}\boldsymbol{W}_z\boldsymbol{z}$ of the LES data in the resolvent basis. Figure 4.2 and 4.3 provide three independent LES realizations (i.e. $\boldsymbol{q}$) and their reconstructions (i.e. $\tilde{\boldsymbol{q}} = \tilde{\boldsymbol{U}}_q\tilde{\boldsymbol{\alpha}}$) in a 3-mode truncated resolvent basis.

While the resolvent gain is only optimal over the region $r/D = [5 - 20]$, the three

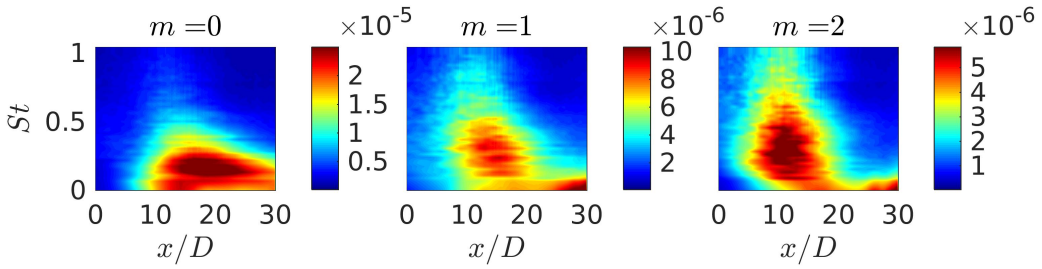

Figure 4.7: RMS of LES pressure fluctuations of the $M_j = 0.9$ jet at radial surface $r/D = 6$ from $St = [0, 1]$ and $x/D = [0, 30]$ for three azimuthal wavenumbers, $m = [0, 2]$.

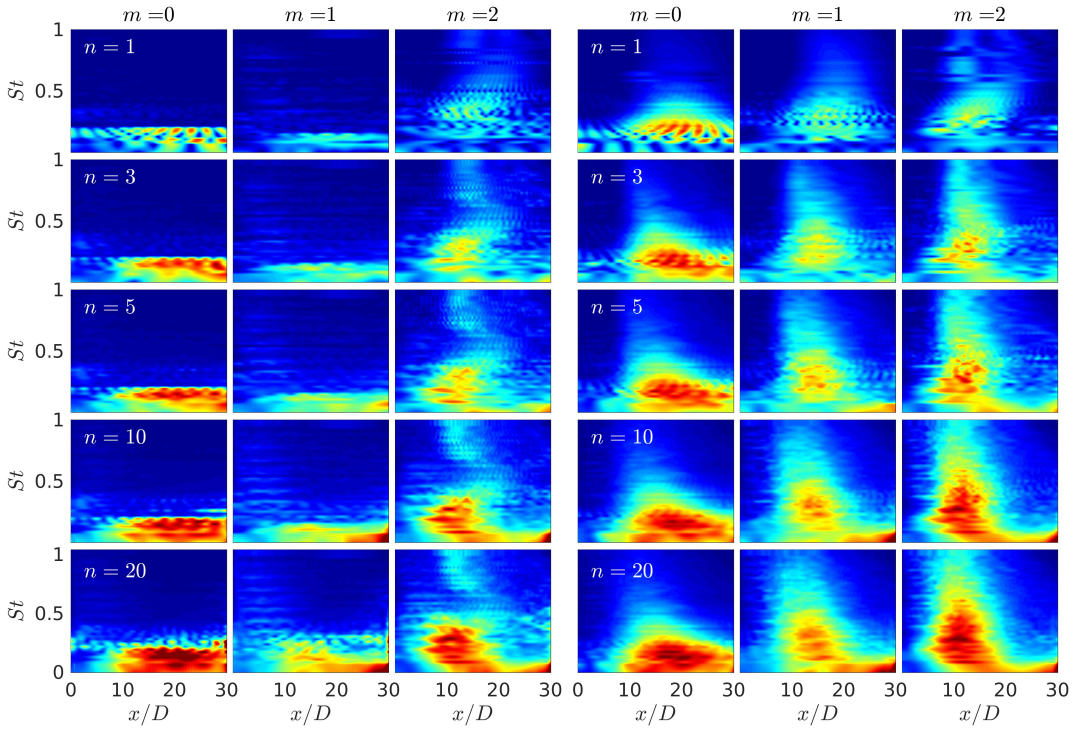

Figure 4.8: RMS of resolvent reconstructions of the $M_j = 0.9$ jet, without an eddy-viscosity model (left) and with a RANS eddy-viscosity model (right), at radial surface $r/D = 6$ from $St = [0, 1]$ and $x/D = [0, 30]$ for three azimuthal wavenumbers, $m = [0, 2]$, from left to right and using $n = 1, 3, 5, 10, 20$ modes from top to bottom. Contours and axes mirror those of Figure 4.7.

resolvent modes are able to accurately reconstruct the different radiation patterns evident in the realizations. Clearly there is constructive and destructive reinforcement amongst the three resolvent modes in order to produce the LES realizations.

To quantitatively assess how well the resolvent modes reconstruct the LES realizations, we compute and compare the RMS pressure values by relative dB at $r/D = 6$

in Figure 4.4, again for $St = 0.26$, $m = 0$ over all $k = 153$ realizations. In addition to the 3 resolvent mode set, results are also shown for 5 and 10 mode sets. With just three modes we see that the peak directivity is well captured, with minor improvements (and diminishing returns) in the off-peak directivity with increasing numbers of modes.

Eddy-viscosity model

We now expand our analysis to Strouhal numbers ranging from 0 to 1 and azimuthal wavenumbers 0-2 and assess the overall ability of the truncated resolvent basis to reconstruct the acoustic field, as well as determine the utility of implementing an eddy-viscosity model for noise modeling. We continue comparisons of the LES data and resolvent reconstructions by RMS pressure fluctuations at $r/D = 6$, which are now plotted over a range of frequencies ($St = [0, 1]$) and azimuthal modes ($m = [0 - 2]$) in Figure 4.5. In Figure 4.6, the resolvent-basis reconstructions of the pressure fluctuations are shown for rank 1, 3, 5, 10, and 20. The left and right columns show resolvent reconstructions without and with the eddy viscosity model, respectively. For the computations without eddy viscosity, a constant turbulent Reynolds number ($Re_T = 3 \times 10^4$) is used.

A visual comparison between these columns shows the clear advantage that the eddy-viscosity model provides, especially when two or more resolvent modes are retained. Interestingly, the rank-1 model appears to be quite similar both with and without eddy viscosity, which is likely due to the Kelvin-Helmholtz mechanism that dominates (i.e. as the leading resolvent mode) much of the frequency-wavenumber space considered (Pickering, Rigas, Nogueira, et al., 2020), and which is less sensitive to the eddy-viscosity model than the sub-optimal modes associated with the Orr-mechanism (Pickering, Rigas, Schmidt, et al., 2020). The rank-1 results are also similar to those of Sinha et al. (Sinha, Rodríguez, et al., 2014) who computed a rank-1 model via the parabolized stability equations and projected onto the first SPOD-mode at each $St - m$ pair. However, we show here that once additional modes are included, the reconstructions are substantially improved and the eddy-viscosity model shows superior performance; the 20-mode, eddy-viscosity model is indistinguishable from the LES for all frequencies and azimuthal modes, while even the 3-modes model is quantitatively accurate for $m = 0$ and $m = 1$.

In Figures 4.7 and 4.8, we plot the LES and reconstructed pressure fluctuations, respectively, for the $M_j = 0.9$ jet. We see many similar behaviors to the $M_j = 1.5$

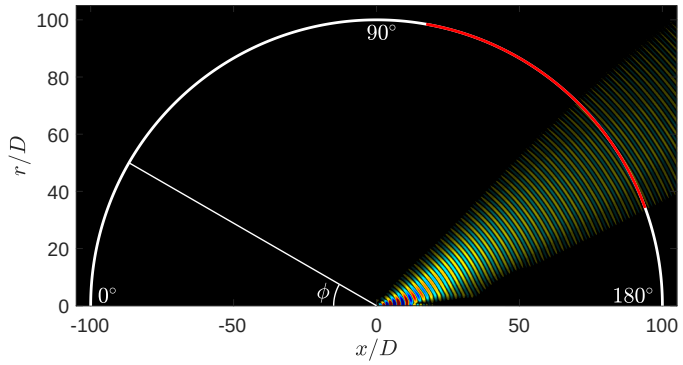

Figure 4.9: Schematic of the far-field arc at $100D$ from the nozzle exit. The angle along the arc is defined as ϕ, with 0 on the upstream axis and 180 on the downstream axis. The red portion of the arc denotes the region of interest, $\phi = 100 - 160$ and the acoustic beam presented is the first resolvent mode for $M_j = 1.5$, $St = 0.26$, $m = 0$, found for the far-field region.

case, most notably the superiority of the eddy-viscosity resolvent modes, which achieve nearly complete reconstruction of the full LES pressure with just 20 modes. However, it is also apparent that a larger number of modes is required to accurately reconstruct the modes compared to the $M_j = 1.5$ case. For example, about 10 modes are required to obtain a reasonable quantitative match (compared to just 3 modes at $M_j = 1.5$). This is consistent with multiple past observations where the $M_j = 0.9$ jet has been found to require many modes to reconstruct the acoustic field (Freund and Colonius, 2009; Towne, Colonius, et al., 2015).

4.4 Far-field Results

We now extend the analysis for both jets to the far-field at $100D$ from the nozzle (using the eddy-viscosity model), and aim to find the modes which are optimal in the far-field. The far-field is defined as an arc $100D$ from the nozzle, with locations on the arc defined by an angle, ϕ, where $\phi = 0$ lies on the axis upstream, and $\phi = 180$ lies on the axis downstream. For reference, Figure 4.9 presents a schematic of the far-field arc, including the region of interest denoted by red and an example of a the first resolvent mode, propagating throughout the domain, for $M_j = 1.5$ at $St = 0.26$ and $m = 0$.

We now proceed by investigating the first three resolvent modes for $M_j = 1.5$ and $M_j = 0.9$ at $St = 0.26$ and $m = 0$. Figure 4.10 (a) and (b) presents the magnitude of the first three resolvent modes as this representation provides a clear description of the acoustic beams. We observe for both jets, that mode 1 possesses one acoustic beam, peaking at about $\phi = 150$, while modes 2 and 3, possess

two and three acoustic beams, respectively, with the largest of the peaks located further upstream with increasing mode number (this progression in beam number and location continue in the higher mode numbers. One notable difference between the $M_j = 1.5$ and $M_j = 0.9$ is width and spacing of the modes. For the $M_j = 1.5$ jet, appreciable values of the modes are between $\phi = 110 - 160$, while the $M_j = 0.9$ jet has values in extending much further upstream and somewhat downstream as well. Additionally, Figure 4.10 (a) and (b) also presents the magnitude of modes found via spectral proper orthogonal decomposition (SPOD). Such modes are useful in determining the optimal decomposition of second-order, space-time statistics (Towne, Schmidt, and Colonius, 2018), and therefore, provide a useful comparison to resolvent modes. In fact, when the forcing CSD is uncorrelated, resolvent and SPOD modes are identical, however, this is generally not the case for turbulent flows. Comparing the SPOD and resolvent modes shows significant agreement amongst all three modes for both jets. The amplitudes and exact locations vary slightly, but such close agreement suggests that an uncorrelated model may suffice.

Just as computed in Figure 4.1, Figure 4.11 presents the near-field solution that gives rise to the far-field modes for the $M_j = 1.5$ case. In comparing Figures 4.1 and 4.11 we can see that they are nearly indistinguishable, with the greatest difference found near the axis. In Figure 4.1 there is energy along the axis after the beam detaches from the hydrodynamic wavepacket for approximately ten diameters downstream, while in Figure 4.11 there is no further energy after detaching from the axis. This shows that while solving for resolvent modes at closer locations (i.e. $r/D = 5$), portions of the hydrodynamic component may still affect the result, while computations at truly acoustic regions (i.e. $\rho/D = 100$) entirely eliminate any structures that do not carry acoustic significance.

We now investigate how well the computed resolvent modes can reconstruct the RMS of the far-field region across $St \in [0.1, 1]$ and $m = [0, 1, 2]$. Figure 4.12 presents the averaged RMS, over 153 Kirchhoff surface realizations, for the mentioned wavenumber and frequency space of the $M_j = 1.5$ jet. This Figure is, as expected, quite similar to that of 4.5, with a similar distribution amongst frequencies and wavenumbers. The greatest difference between the two is an order of magnitude drop after propagating nearly 100 diameters. We can observe that for all wavenumbers, and most frequencies, we find the peak values near angles ranging from $\phi = [140 - 155]$, indicating that this region is the largest, and therefore, most important region for modeling. We also find that the $m = 0$ wavenumber provides

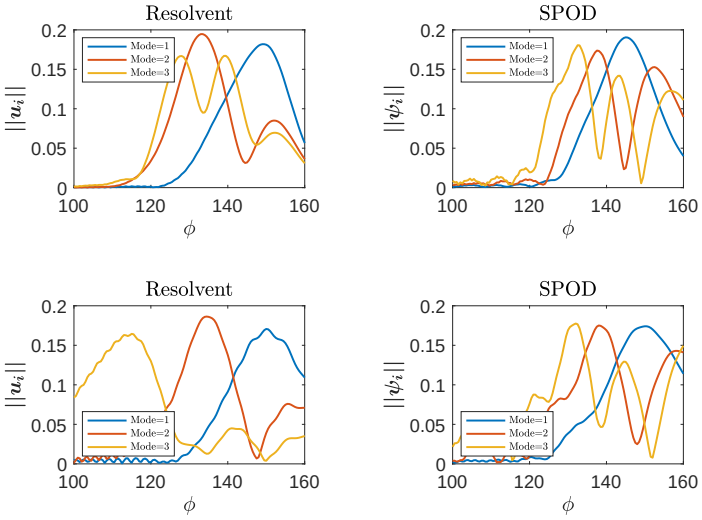

Figure 4.10: Magnitude of the first three resolvent (left) and SPOD (right) modes computed on the far-field arc for the $M_j = 1.5$ (top) and $M_j = 0.9$ (bottom) jet at $St = 0.26$ and $m = 0$.

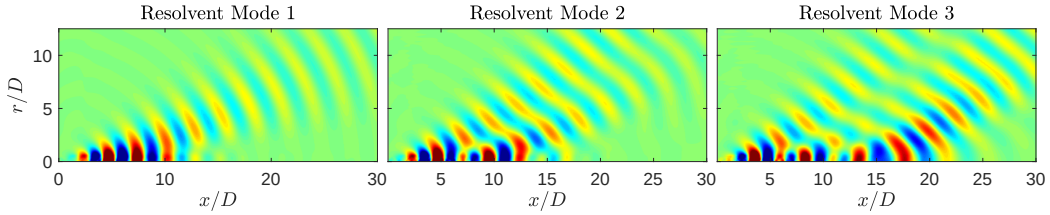

Figure 4.11: The near-field of three resolvent modes of fluctuating pressure, $q_{p'}$, computed considering the $100D$ are from $\phi = 100 - 160$. Red and blue contours vary from ± 50% of the maximum fluctuating pressure of each mode, $\pm 0.5||q_{p'}||_\infty$. $M_j = 1.5$, $St = 0.26$, $m = 0$.

amplitudes that are significantly larger as the contour for $m = 0$ is four and ten times larger than the contour levels of $m = 1$ and $m = 2$, respectively.

We present reconstructions using n resolvent modes, at each wavenumber and across frequencies, in Figure 4.13. For each of the wavenumbers, the rank-1 resolvent fit provides substantial agreement between the LES, reconstructing all the loudest features. Increasing the rank can capture nearly all the energy for each of the azimuthal wavenumbers, however, the increase in agreement with rank is rather gradual and serves largely to reconcile the quieter regions of the flow. Considering the loud regions are of greatest importance for reducing jet noise, we will proceed in the next section with a fit/model of the jet designed on the necessary forcing

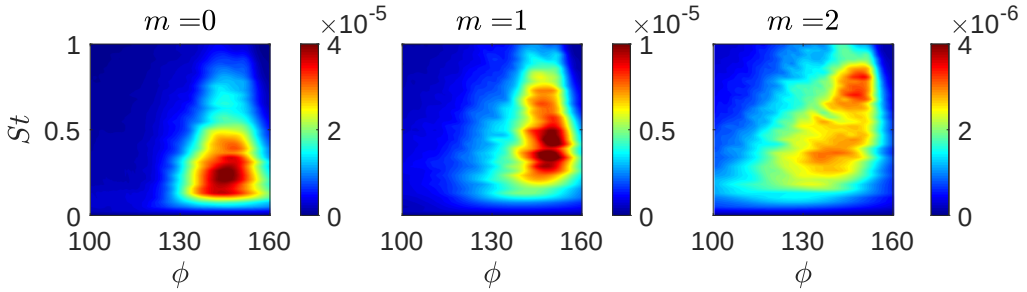

Figure 4.12: RMS of far-field from propagating the LES pressure fluctuations of the $M_j = 1.5$ jet at radial surface $r/D = 6$ from $St = [0, 1]$ and $x/D = [0, 30]$ via the Kirchhoff surface for three azimuthal wavenumbers, $m = [0, 2]$.

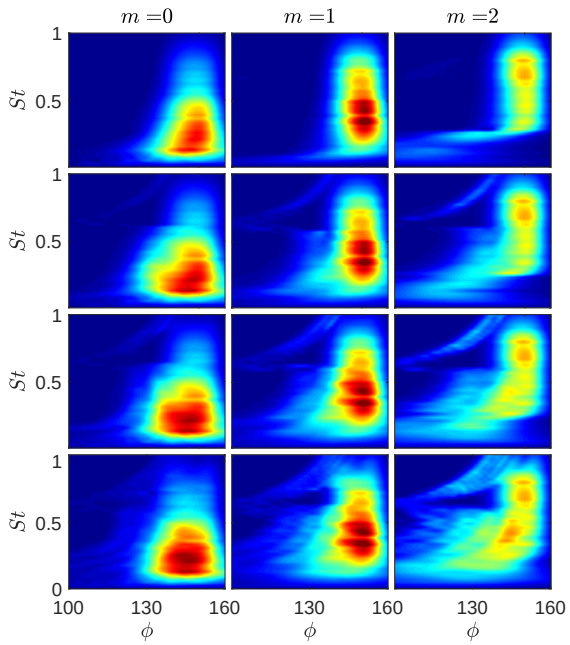

Figure 4.13: RMS of resolvent reconstructions of the $M_j = 1.5$ jet, at $\rho/D = 100$ from $\phi = [100-160]$, over frequencies, $St = [0, 1]$, azimuthal wavenumbers, $m = [0, 2]$, (from left to right) and using $n = 1, 2, 3, 5$ modes (from top to bottom). Contours and axes mirror those of Figure 4.12.

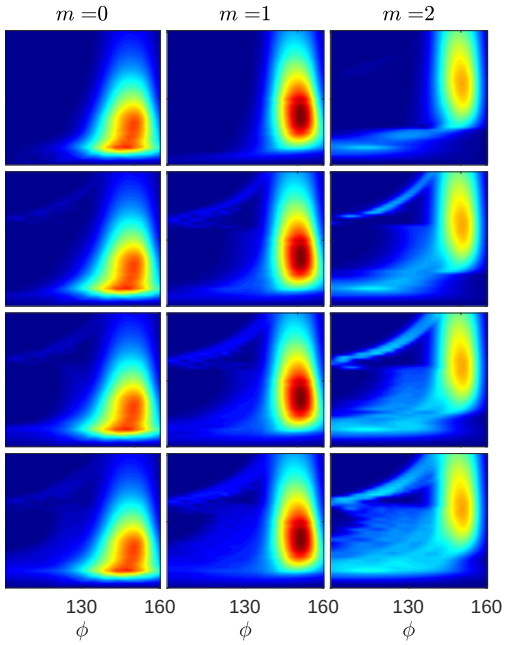

Figure 4.14: RMS of the simple resolvent model, presented in §4.4, of the $M_j = 1.5$ jet. The presentation mirrors that of Figure 4.13.

required to, at minimum, model the $n = 1$ reconstruction.

We now provide the same analysis of the far-field for the $M_j = 0.9$ case. Figure 4.15 provides the $100D$ far-field RMS found via the Kirchhoff realizations. Again,

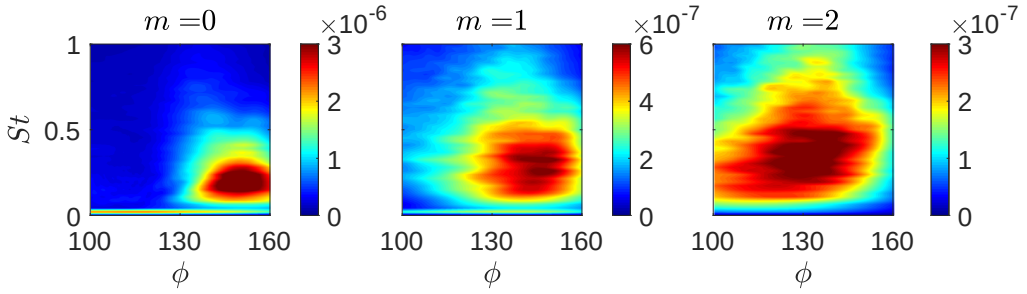

Figure 4.15: RMS of far-field from propagating the LES pressure fluctuations of the $M_j = 0.9$ jet at radial surface $r/D = 6$ from $St = [0, 1]$ and $x/D = [0, 30]$ via the Kirchhoff surface for three azimuthal wavenumbers, $m = [0, 2]$.

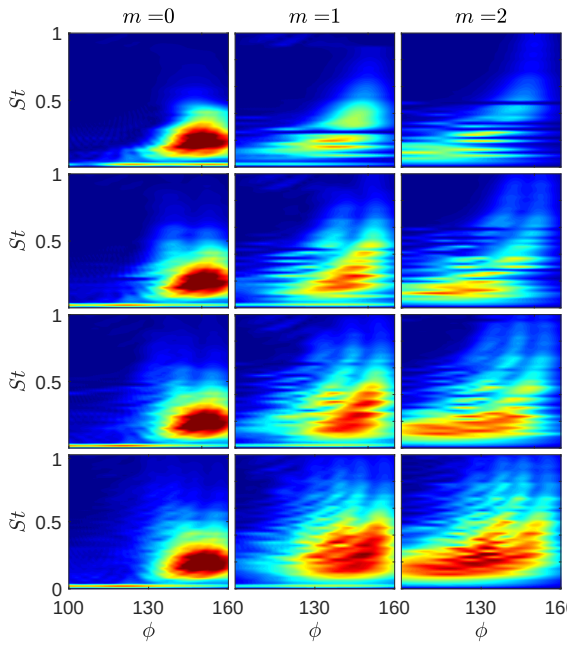

Figure 4.16: RMS of resolvent reconstructions of the $M_j = 0.9$ jet, at $\rho/D = 100$ from $\phi = [100-160]$, over frequencies, $St = [0, 1]$, azimuthal wavenumbers, $m = [0, 2]$, (from left to right) and using $n = 1, 2, 3, 5$ modes (from top to bottom). Contours and axes mirror those of Figure 4.15.

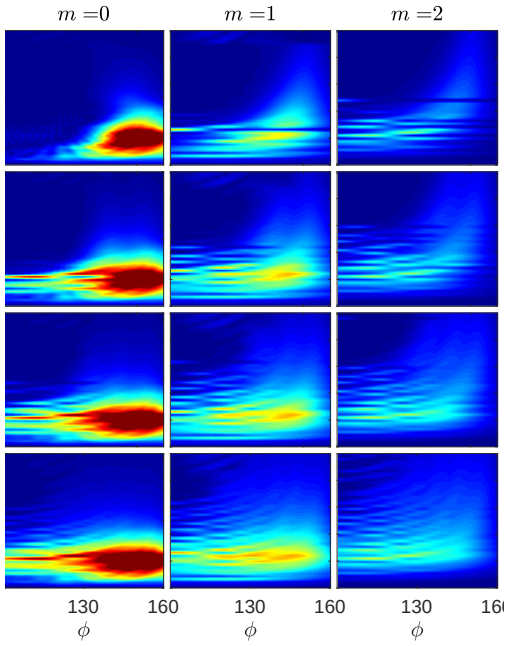

Figure 4.17: RMS of the simple resolvent model, presented in §4.4, of the $M_j = 0.9$ jet. The presentation mirrors that of Figure 4.16.

the Figure is relatively similar to that of the near-field RMS, shown in Figure 4.7, with values approximately an order of magnitude smaller. Relative to each jet's peak noise, the acoustic field appears to possess substantial noise at smaller angles of ϕ when compared with the $M_j = 1.5$ jet, particularly for the higher azimuthal

wavenumbers. Similar to the $M_j = 1.5$ jet, we also find the $m = 0$ component to be the loudest, about five-fold compared to the $m = 1$ case and an order of magnitude when compared to $m = 2$. Granted, the locations of the peaks are not identical, thus each wavenumber may have dominance at certain angles in terms of acoustic energy.

Figure 4.16 provides the reconstructions using n resolvent modes, at each wavenumber and across frequencies. Interestingly, when compared to our results in the near-field, the rank-1 resolvent model nearly reconstructs the $m = 0$ RMS, with only negligible improvements with increasing rank. The same is not true for the higher azimuthal wavenumbers. For both $m = 1$ and $m = 2$, the rank-1 reconstruction provides a foundation for the regions of highest acoustic energy, but additional modes are required to reconstruct the observed RMS. This higher-rank behavior is not entirely unexpected. From Figure 4.15, we can see that both $m = 1$ and $m = 2$ are noisy when compared to $m = 0$ and are not nearly as compact in space. Both of these observations suggest these azimuthal fields are of higher rank, requiring many modes to reconstruct them. This is further supported by the reconstructions of $m = 1$ and $m = 2$. The rank-1 reconstruction presents the "single-beam" solution, while the addition of subsequent modes shows a superposition of multi-beam structures that appear as sloping lines on the figure, and a complete jet model must consider these suboptimal modes. However, and similar to the $M_j = 1.5$ case, the loudest regions are of greatest importance for reducing jet noise, and we proceed with a simple model accounting for the forcing energy required to best fit the rank-1 reconstruction.

A simple fit/model

Considering we may reconstruct the far-field acoustics at low-rank, we ask whether we can now define a simple, yet sufficient, forcing model. One approach would be to propose a form of the forcing cross-spectral density tensor to which projecting this form onto the resolvent input modes would result in the reduced order matrix $\tilde{\boldsymbol{S}}_{\beta\beta}$. However, despite many efforts to define such a forcing CSD (Towne, Bres, and Lele, 2017), there does not yet exist a general form for estimating the forcing CSD $\boldsymbol{S}_{ff}$. Therefore, we continue by investigating the resulting structure of the estimated $\tilde{\boldsymbol{S}}_{\beta\beta}$ and attempt to determine simple forms of the associated values.

The estimated covariance matrix $\tilde{\boldsymbol{S}}_{\beta\beta}$ presents the least square reconstruction of the observed data and contains the amplitudes and correlations required to force

each resolvent mode. Where the forcings are uncorrelated, the estimated $\tilde{\boldsymbol{S}}_{\beta\beta}$ matrix becomes diagonal and only n coefficients (albeit at each wavenumber and frequency) require modeling. However, even if the forcing is uncorrelated, minor errors or discrepancies in the data, data-processing, computation of resolvent mode, etc., give a full $\tilde{\boldsymbol{S}}_{\beta\beta}$ matrix. Thus, we explore whether neglecting off-diagonal terms, but note that there are no guarantees for success. Further, as we increase rank, the statistical uncertainty in the fits becomes greater, reducing physical interpretability.

To limit uncertainty and prevent over-fitting, we take the assumption that the forcing is uncorrelated (i.e. diagonal) and that the projection of the data with the first resolvent mode,

$$\tilde{\boldsymbol{S}}_{\beta\beta} = \boldsymbol{\Sigma}_1^{-1}\boldsymbol{U}_1^*\boldsymbol{S}_{yy}\boldsymbol{U}_1\boldsymbol{\Sigma}_1^{-1} = \lambda_\beta, \tag{4.29}$$

possesses the lowest uncertainty. These values for the two jets and three azimuthal wavenumbers are shown in Figure 4.18. For the $M_j = 1.5$ jet, we see that the forcing amplitudes for $m = 0$ and $m = 1$ fall upon lines of constant slope for the most acoustically significant frequency ranges, $St = 0.1 - 0.8$. The $m = 2$ data similarly collapse to a line of constant slope, however, the trend is not nearly as clear. Similar observations also hold for the $M_j = 0.9$ jet. We also stress it that these curves are not only found via projections with the data but also through the resolvent gains, Σ. Including the gains is crucial to collapsing the observed trends.

We now look to fit the data with simple curves of the form,

$$\tilde{\lambda}_{m,\omega} = a_m St^{b_m}, \tag{4.30}$$

where a_m provides an amplitude of the curve and b_m provides the power of the curve. For the nonzero azimuthal wavenumbers, the data represent the sum of both the clockwise (m) and counter-clockwise ($-m$) about the round jet, such that a_m represents $a_{+m} + a_{-m}$, or $2a_{+m}$, since $a_{+m} = a_{-m}$, as either rotation about the jet is of equal probability. The power term, b_m is unaffected by this symmetry. Figure 4.18 provides the lines of best fit, where the fits are computed over the acoustically relevant region of $St = 0.13 - 0.7$ for the $M_j = 1.5$ and $St = 0.22 - 1$ for the $M_j = 0.9$. We find the difference in the frequency ranges by adjusting the Strouhal number by Mach number, $St_{0.9} = St_{1.5} * 1.5/0.9$, meaning each range is associated with the same range of acoustic Strouhal number, St_{c_∞}. The upper bound for the $M_j = 0.9$ case extends to $St = 1.17$, however, we cap the upper bound to $St = 1$ as done throughout this chapter.

	$M_j = 1.5$			$M_j = 0.9$		
Param.	$m = 0$	$m = 1$	$m = 2$	$m = 0$	$m = 1$	$m = 2$
a_m ($\times 10^{-11}$)	71.0	38.9	46.6	2.65	1.38	0.61
b_m	−2.58	−1.7	−1.76	−5.80	−3.77	−3.13

Table 4.1: Fit parameters used for the $M_j = 1.5$ and $M_j = 0.9$ jets shown in Figure 4.18. Parameters a_m are provided on the order of 10^{-11}.

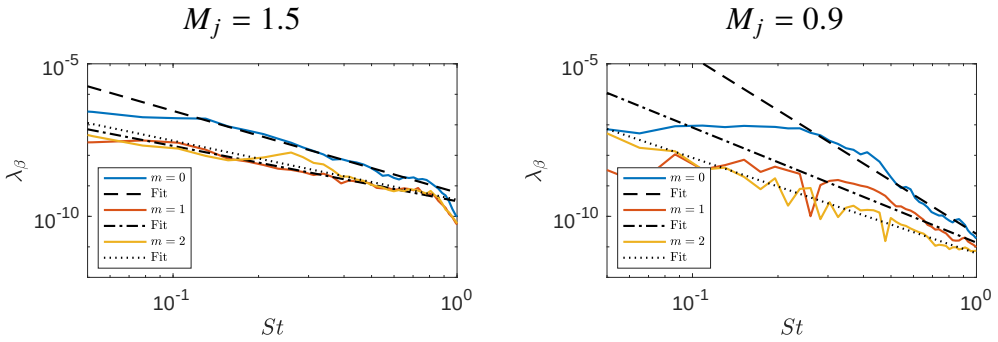

Figure 4.18: Values of the reconstruction projection coefficient, λ_β, of the first resolvent mode for the azimuthal wavenumbers $m = 0 - 2$ and their associated fits, the parameters of which are provided in Table 4.1.

Table 4.1 provides the determined coefficients for each jet and wavenumber. We do not have any physical meaning to suggest for these terms, other than the power terms show a steady decrease in energy as frequency increases (and thus the length scales of the structures decrease). We suspect we may find similar curves via projection of the resolvent forcing modes with the turbulent kinetic energy or other mean statistics, however, we leave this for future work.

To determine how well such curves predict the data, we use the fitted curves to compute,

$$\tilde{\boldsymbol{S}}_{yy}(\phi) = \tilde{\lambda}_{m,\omega}\tilde{\boldsymbol{U}}\Sigma^2\tilde{\boldsymbol{U}}^*, \tag{4.31}$$

where $\tilde{\boldsymbol{U}}$ represents the truncated resolvent basis to rank-n. Additionally, as the low-frequency regions are not acoustically important, nor can we expect our methods to have accurately captured such large structures in the finite domain used, we use the piece-wise function

$$\tilde{\lambda}_{m,\omega} = a_m St^{b_m} \quad \text{for} \quad St > St_{min} \tag{4.32}$$

$$\tilde{\lambda}_{m,\omega} = a_m St_{min}^{b_m} \quad \text{for} \quad St \leq St_{min}, \tag{4.33}$$

where $St_{min} = 0.13$ and 0.22 for $M_j = 1.5$ and $M_j = 0.9$, respectively. Figure

4.14 and 4.17 present the predicted RMS using $n = [1, 2, 3, 5]$ modes for the three azimuthal wavenumbers and two turbulent jets.

For the $M_j = 1.5$, the rank-1 approximation presents a close approximation of the reconstructions of 4.13, and, since these reconstructions closely agree with the overall RMS at rank-1, so too do the predictions represent similar features and magnitudes as the overall RMS at rank-1. We can say the same for the $M_j = 0.9$ case, except for the $m = 2$ case which does not agree at low-frequencies, however, we suspect such frequencies to be invalid for our approach.

Proceeding to the higher mode predictions of the $M_j = 1.5$ jet we see little difference, particularly at the loudest regions of the RMS plots, with increases only seen at smaller angles. This lack of change from the rank-1 prediction shows that the forcing amplitude is underpredicted for resolvent modes $n > 1$ by the model, meaning that the actual forcing is greater than $\tilde{\lambda}_{m,\omega}\sigma_n^2$ for $n > 1$. Physically, these observations aligns with differences found between two mechanisms in turbulent jets, the KH and Orr mechanisms (Pickering, Rigas, Nogueira, et al., 2020). The KH dominates the optimal resolvent modes at the wavenumbers and frequencies considered here, however, a family of Orr-type modes dominate the $n > 1$ region of the spectrum, and the main consequence, as far as we are concerned in this work, is a distinct change in the spatial location of the associated forcing modes. For KH modes, the forcing mode is found localized near the nozzle, while forcing modes associated with the Orr-mechanism are located much further downstream where the jet is significantly more energetic. Thus, this difference necessitates knowledge of the relative magnitudes associated with each forcing mechanism. In the very simple approach taken here, it would require a calibration of $n = 2$, however, the uncertainty in such a fit increases drastically, and due to the rather close fits of the rank-1 model, we leave this topic for future work and continue with the rank-1 model.

An analogous difficulty with $n > 1$ is also observed for the $M_j = 0.9$ jet. For $m = 0$, the forcing of the suboptimal, Orr-type modes is over predicted, contrary to the under prediction for the $M_j = 1.5$ jet. This could result from the acoustic efficiency of the KH mechanism drastically decreasing, while the Orr-type modes maintain their ubiquitous presence in the turbulent jet. Such a finding underscores the necessity to determine a forcing model that represents both KH and Orr modes, as their relative energies differ amongst varied flow conditions.

With the rank-1 prediction in hand, we conclude by computing the quantity that underpins our motivation in this work, the overall sound pressure level (OASPL).

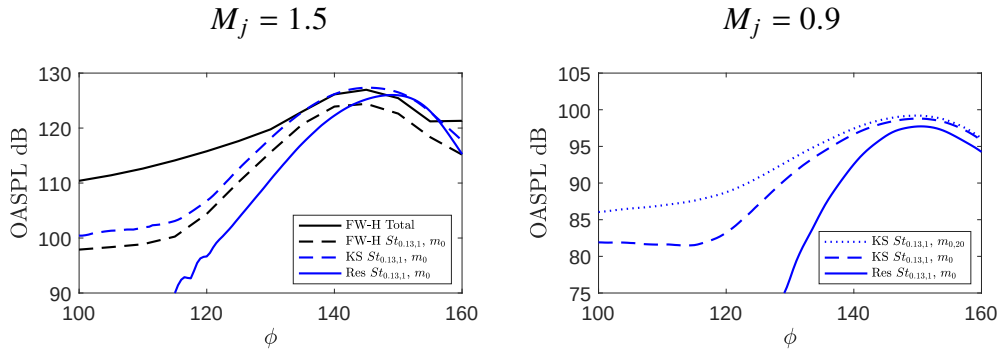

Figure 4.19: OASPL of the $M_j = 1.5$ (left) and $M_j = 0.9$ (right) turbulent jets at $100D$ from the nozzle over the arc ϕ. The solid black line denotes the total OASPL from the FW-H surface of the LES, while the dashed black line presents the contribution to the OASPL from only azimuthal wavenumber $m = 0$. Blue lines represent approximations, where the dotted line is the KS considering 20 azimuthal modes over $St = 0.1 - 1$, the dashed line considers only $m = 0$, and the solid line gives the $m = 0$ resolvent estimation.

Figure 4.19 presents multiple calculations of the OASPL from both jets. For the $M_j = 1.5$ case, data from a FW-H surface coupled directly with the LES simulation is available (data for the $M_j = 0.9$ case is not) for comparison, and the black lines represent this LES data, with the solid line denoting the total OASPL, at $100D$ from the nozzle, and the dashed line giving the contributions from only the $m = 0$ component. The latter component is what we wish to compare for the remainder of the paper for two reasons. First, the difference between the total and $m = 0$ FW-H OASPLs is 2dB at peak noise from $\phi = 130 - 160$. Second, the previous reconstructions and model show that the higher azimuthal wavenumbers require multiple modes to be accurate. Thus, we only compare the $m = 0$ component as it both represents most of the peak acoustic energy and may be reasonably represented at rank-1.

The blue lines in Figure 4.19 represent approximations of the KS surface and the resolvent model for both jets. Comparisons of the $m = 0$ component for the $M_j = 1.5$ jet show the KS surface consistently over predicting the FW-H values by 2dB. The rank-1, $m = 0$ resolvent model, trained on the KS surface, which alternatively could have been trained of the FW-H data, aligns fairly well with the KS curve at the loudest angles. The greatest difference is that the resolvent model peaks at about 5 degrees higher than the LES data. Interestingly, a similar experiment and simulation in Brès, Ham, et al. (2017) disagreed by the same angle. Although $100D$ data from the experiment is not available, projecting the resolvent modes onto this data would

likely result in much greater alignment, as shifting the LES data by 5 degrees results in a significantly improved estimation. However, since the latter is a loosely justified extrapolation of our methods, we do not present this result.

We see similar behavior between the KS surface and the resolvent model for the transonic case. The dashed line in Figure 4.19 represents the total OASPL computed by the KS surfaces for reference and the $m = 0$ only OASPL shows a minor difference of 0.5dB at peak angles. The rank-1 $m = 0$ resolvent model again presents agreement of the peak OASPL to within 2dB. We stress that this result for the $M_j = 0.9$ jet is rather surprising as many previous studies have found the acoustic field requires many modes to agree within 2dB (Freund and Colonius, 2009; Towne, Colonius, et al., 2015), showing that the eddy-viscosity model included in our resolvent analysis significantly reduces the rank of the acoustic jet problem. Further, we note that this transonic jet has been extensively verified by experimental data in the near-field and at $\rho = 50D$, and, although we extend the results to $100D$, the peak angles of the KS and the resolvent model are closely aligned when compared to the $M_j = 1.5$ case.

4.5 Conclusions

We extended resolvent analysis to that of an acoustic analogy relating the near-field forcing to both the near-field and far-field acoustics, the latter being 100 diameters from the nozzle. Leveraging the availability of a LES database, we examined resolvent-based reconstructions of the acoustic near- and far-field of round, turbulent $M_j = 1.5$ and $M_j = 0.9$ jets. We represented the forcing cross-spectral density matrix with a truncated set of resolvent modes and approximate the amplitudes of the modes with best-fit expansion coefficients of realizations from the LES acoustic field. We found that relatively low-rank models comprising as few as *one* resolvent mode can accurately reconstruct the acoustic field for the first two azimuthal modes for a $M_j = 1.5$ jet and the $m = 0$ azimuthal mode for the $M_j = 0.9$ jet, whereas about five modes were required for the higher azimuthal modes (i.e. $m = 2$ and $m = 1, 2$ for $M_j = 1.5$ and $M_j = 0.9$, respectively). Based on the relative increase in radiation efficiency of the (low-rank) Kelvin-Helmholtz response of the jet, it is perhaps not surprising that we can capture the higher Mach number case at lower rank. In both jets, the use of an eddy-viscosity model in the resolvent formulation led to (vastly) superior results compared to a fixed Reynolds number.

Based on the ability of the rank-1 reconstructions to describe much of the RMS energy, we investigated a simple model to collapse the forcing coefficients to one

scaling function per wavenumber (and Mach number). We found that a power law representation, with only a scaling and a power value, suffices for describing the forcing coefficients for the optimal resolvent mode. Fortunately, the first resolvent mode contains much of the acoustic energy, and reductions of the gain for this specific mode (related to the KH mechanism) are likely to provide the greatest reductions in the peak noise of the acoustic field. However, the model does not accurately account for the suboptimal modes, under predicting their role in the $M_j = 1.5$ jet and over predicting them for the $M_j = 0.9$ jet (for at least the $m = 0$ wavenumber).

Regardless of this difficulty, the rank-1 $m = 0$ resolvent models could estimate the peak noise to within 2dB for both the $M_j = 1.5$ and $M_j = 0.9$ jets. Further, the ability of the resolvent basis to describe much of the acoustic field with only a handful of modes across multiple Mach numbers, a large range of frequencies, and the acoustically dominant azimuthal wavenumbers is promising. This shows that the resolvent framework already contains the appropriate acoustic functions to describe jet noise. The next step must then be to generalize the forcing coefficients and tie them to other known statistics from RANS calculations, such as the turbulent kinetic energy or the Reynolds stresses.

Acknowledgments

The authors would like to thank André Cavalieri, Oliver Schmidt, and Georgios Rigas for many productive discussions on topics related to this paper. This research was supported by a grant from the Office of Naval Research (grant No. N00014-16-1-2445) with Dr. Steven Martens as program manager. E.P. was supported by the Department of Defense (DoD) through the National Defense Science & Engineering Graduate Fellowship (NDSEG) Program. The LES study was performed at Cascade Technologies, with support from ONR and NAVAIR SBIR project, under the supervision of Dr. John T. Spyropoulos. The main LES calculations were carried out on DoD HPC systems in ERDC DSRC.

Chapter 5

CONCLUSIONS

We made advancements on several components of the resolvent-based modeling framework of turbulent flow design and jet noise prediction as displayed in Figure 1.1. Detailed conclusions on each of these areas can be found in the previous sections of this report. We provide some highlights below.

In Chapter 2 we proposed and validated an extension of the resolvent approach that includes an eddy-viscosity model. The eddy viscosity models a portion of the stochastic forcing associated with the effect of nonlinear interactions on coherent structures. We developed a novel data-driven technique to determine an optimal eddy-viscosity field, defined by attempting to match the theoretical highest-gain resolvent response to the corresponding largest SPOD mode observed from the LES data. Through a corresponding theoretical connection between SPOD and resolvent, we show that matching these structures corresponds to removing complexity (i.e. correlations) from the required stochastic forcing model. This implies that the resulting eddy-viscosity-amended resolvent computation could predict the dominant turbulent structure based only on the mean flow field, the eddy-viscosity model, and a frequency-dependent amplitude of forcing. We showed that the eddy-viscosity fields substantially improve the agreement between resolvent-predicted and SPOD-observed structures. Most surprisingly, we found predictions based on an a priori prediction of the eddy-viscosity fields from RANS was nearly as effective as the optimal eddy-viscosity model.

In Chapter 3, we used SPOD and global, linear resolvent analysis to distill coherent turbulent structures for round jets over a range of Mach numbers from subsonic to supersonic and investigate, in detail, three turbulent jet mechanisms. Both techniques revealed that three dominant amplification mechanisms exist in the turbulent jet: the well known Kelvin-Helmholtz (KH) instability, an Orr-type response (associated with the tilting of wavefronts against mean shear) and the lift-up mechanism (associated with streaks). The KH-type instability is of low-rank type, meaning that the leading, highest gain mode is well separated from sub-optimal, lower gain modes, and is readily forced by disturbances near the nozzle exit. It is active, over a range of frequencies and azimuthal wavenumbers, in the initial shear-layer, whereas

Orr-type waves dominate the region downstream of the potential core. The Orr response is not low rank and relies on distributed forcing from turbulence throughout the jet. In the initial shear layer region, Orr-type waves are also present but not readily observed as they are swamped by the high-gain KH waves. An exception is the axisymmetric response at low frequencies where the Orr modes again become the dominant mechanism. The lift-up mechanism becomes apparent when investigating the lower-frequency limits for nonzero azimuthal wavenumbers, where the lift-up effect generates elongated streaks at a variety of azimuthal wavenumbers. The lift-up mechanism has long been understood as an instability mechanism in boundary layers, but has only recently received attention in jets. Our global analysis is the first to clearly identify it both as a fundamental linear amplification mechanism and through its presence, as coherent structures, in the LES data. The analysis serves to unify many past observations of streaky structures in jets, and to provide a mechanistic understanding of their formation and use for future noise control.

In Chapter 4 we extended resolvent analysis to that of an acoustic analogy that relates the near-field forcing to the far-field acoustics 100 diameters from the nozzle. Leveraging the availability of a LES database, we produce resolvent-based reconstructions of the acoustic field of round, turbulent $M_j = 1.5$ and $M_j = 0.9$ jets. We represent the forcing cross-spectral density matrix with a truncated set of resolvent modes and approximated the amplitudes of the modes with best-fit expansion coefficients of realizations from the observed LES acoustic field. We found that low-rank models comprising as few as *one* resolvent mode can accurately reconstruct the acoustic far-field for the first two azimuthal modes for the $M_j = 1.5$ jet, whereas about five modes were required for the higher azimuthal mode ($m = 2$). For the transonic jet, $M_j = 0.9$, a rank-1 model was sufficient for $m = 0$, while $m = 1, 2$ required significantly more modes to reconstruct. We then find the necessary forcing amplitudes required for reconstructing the acoustic field and suggest avenues for modeling this forcing. Finally, we present a simple function, using only two fitting parameters, that results in a rank-1 resolvent model that agrees to withing 2dB of the peak acoustic region for both jets. The ability of the resolvent basis to describe much of the acoustic field with a substantially limited set of modes across multiple Mach numbers, frequencies, and azimuthal wavenumbers is promising. This shows that the resolvent framework already contains the appropriate acoustic functions to describe jet noise. The next step must then be to generalize the correlations between modes such that they represent the complete effect of turbulence on noise generation.

Overall, the research shows that the resolvent-based framework is a viable approach for RANS-based prediction of turbulent jets, but not limited to jets, and their associated noise. We showed that the resolvent approach accurately predicts the observed structures across a range of jet operating conditions. As a predictive tool, the stochastic forcing of these structures remains a pacing item. While promising results were obtained for the $M = 1.5$ and $M_j = 0.9$ circular jet by retaining only a few acoustic resolvent modes, much work remains to fit model coefficients to a range of jet operating conditions and nozzles, and to assess the universality of the resulting noise predictions - and application to other flow fields. Besides prediction, the modeling framework will be essential for future design efforts. Indeed, RANS-based noise models would enable drag, noise, and mixing efficiency control studies at a computational cost far lower than corresponding LES techniques.

5.1 Future work

Although the eddy-viscosity approach provided useful results, there remains an open question "What exact turbulence model should be used for resolvent analysis?" For example, the eddy-viscosity model used here is based on the Boussinesq hypothesis, which for almost all turbulent flows can not be verified (Schmitt, 2007). Therefore, there may be a better, or more rigorously defined, model that exists. One approach to find such a model would be to use the presented optimization framework, but assume no form of the eddy-viscosity model and learn the partial differential equation best suited to represent the turbulence quantities. Additionally, the optimization presented here is general for altering any mean-flow quantity, thus use of the same optimization framework requires only changes to the gradient and cost function.

The identification of the lift-up mechanism in jets provides an exciting opportunity as a mechanism for noise control and work into its potential, either actively or passively, appears promising. Although streaks have only recently been characterized in turbulent jets, their presence is now much clearer while reviewing the literature. Considering past experiments (Citriniti and George, 2000) and simulations (Freund and Colonius, 2009) show signatures of streaks in the natural jet and experiments imposing streak-like disturbances that give rise to acoustic bursts (Wu and Huerre, 2009), it is now clear, more or less, that current jet noise reduction techniques, such as chevrons, unknowingly leverage the lift-up mechanism to induced streaks that increase mean-flow spreading and reduce noise (Rigas et al. (2019) specifically identified streaks in the mean-flow of LES data of a chevron jet). Further, past experimental studies in chevrons (Bridges and Brown, 2004) found that not all

azimuthal configurations lead to the reduction (or increases) of noise, while other work in mixing layers has similarly found that the relationship between streaks and the KH mechanism depends on each mechanism's respective wavenumbers (Marant and Cossu, 2018). Therefore, establishing connections between these mechanisms may prove fruitful for noise reduction. One data-driven approach could lie in performing higher-order statistics to identify energetically relevant triadic interactions between these mechanisms via a cross-bispectral analysis of the flow as described by Schmidt (2020).

To make resolvent models truly predictive, the amplitudes of the resolvent modes and their correlations need to be determined independent of verified "truth" statistics. Therefore, it is imperative that we pursue general strategies and models of the forcing coefficients. As insinuated by Figure 1.1, one approach could be that of a RANS data-driven optimization that couples linear theory with RANS data (that is independent of verified data) to learn the resolvent forcing coefficients. This could be done by matching the first-order statistics available from RANS computations, such as the turbulent kinetic energy (TKE) field, with structures found from resolvent analysis. If successful, such an approach could produce consistent estimates for other RANS computed statistics like the Reynolds stresses but can also predict quantities that are not directly available from RANS such as near-field pressure fluctuations and far-field sound. Further, this approach not only would provide averaged statistics but also give information about all the relevant coherent structures and their relative effects in the flow.

One could also see this future work as another approach for improving RANS with Machine learning techniques (Duraisamy, Iaccarino, and Xiao, 2019), yet is unique in leveraging resolvent analysis in such a large parameter space. An iterative coupling of RANS and accurate representations of the fluctuating fields (i.e. resolvent modes) may allow for an improved and self-consistent RANS model. Further, given that linear models are ideal for posing optimizations and controlling engineering quantities, such a coupling is attractive for a truly predictive reduced order-model with a capacity for informing design. Previous studies have coupled RANS with linear models, however, its generality and application to flows with broadband response or high-rank behavior is lacking. Moarref and Jovanović (2012) coupled RANS and linear modeling to propagate the influence of linear responses to RANS via the turbulent viscosity hypothesis. In a similar vein, Yim, Meliga, and Gallaire (2019) coupled a harmonically forced, quasi-linear resolvent analysis

with RANS equations, using an eddy viscosity model, determined from resolvent modes, to link coherent and incoherent perturbation dynamics. Presenting a similar approach for flows with broadband responses would likely have a substantial impact in the field.

BIBLIOGRAPHY

Abreu, L. I., A. V. G. Cavalieri, P. Schlatter, R. Vinuesa, and D. Henningson (2019). "Reduced-order models to analyse coherent structures in turbulent pipe flow". In: *11th International Symposium on Turbulence and Shear Flow Phenomena*. University of Southampton, 2019.

Agüí, J. C. and L. Hesselink (1988). "Flow visualization and numerical analysis of a coflowing jet: a three-dimensional approach". In: *J. Fluid Mech.* 191 (1988), pp. 19–45.

Åkervik, E., U. Ehrenstein, F. Gallaire, and D. S. Henningson (2008). "Global two-dimensional stability measures of the flat plate boundary-layer flow". In: *European Journal of Mechanics-B/Fluids* 27.5 (2008), pp. 501–513.

Alkislar, M. B., A. Krothapalli, and G. W. Butler (2007). "The effect of streamwise vortices on the aeroacoustics of a Mach 0.9 jet". In: *J. Fluid Mech.* 578 (2007), pp. 139–169.

Arakeri, V. H., A. Krothapalli, V. Siddavaram, M. B. Alkislar, and L. M. Lourenco (2003). "On the use of microjets to suppress turbulence in a Mach 0.9 axisymmetric jet". In: *J. Fluid Mech.* 490 (2003), pp. 75–98.

Arnette, S. A., M. Samimy, and G. S. Elliott (1993). "On streamwise vortices in high Reynolds number supersonic axisymmetric jets". In: *Physics of Fluids A: Fluid Dynamics* 5.1 (1993), pp. 187–202.

Arratia, C., C. P. Caulfield, and J. M. Chomaz (2013). "Transient perturbation growth in time-dependent mixing layers". In: *J. Fluid Mech.* 717 (2013), pp. 90–133.

Bagheri, S., P. Schlatter, P. J. Schmid, and D. S. Henningson (2009). "Global stability of a jet in crossflow". In: *J. Fluid Mech.* 624 (2009), pp. 33–44.

Bechara, W., C. Bailly, P. Lafon, and S. M. Candel (1994). "Stochastic approach to noise modeling for free turbulent flows". In: *AIAA journal* 32.3 (1994), pp. 455–463.

Becker, H. A. and T. A. Massaro (1968). "Vortex evolution in a round jet". In: *J. Fluid Mech.* 31.3 (1968), pp. 435–448.

Benney, D. J. (1961). "A non-linear theory for oscillations in a parallel flow". In: *J. Fluid Mech.* 10.2 (1961), pp. 209–236.

Benney, D. J. and C. C. Lin (1960). "On the Secondary Motion Induced by Oscillations in a Shear Flow". In: *The Physics of Fluids* 3.4 (1960), pp. 656–657. DOI: 10.1063/1.1706101.

Bernal, L. P. (1981). "The coherent structure of turbulent mixing layers". PhD thesis. Ph.D. Thesis, California Institute of Technology, 1981.

Bernal, L. P., R. E. Breidenthal, G. L. Brown, J. H. Konrad, and A. Roshko (1979). "On the development of three dimensional small scales in turbulent mixing layers". In: *Proc. 2nd Int. Symp. on Turbulent Shear Flows, Imperial College, London*. 1979, pp. 8.1–8.6.

Bernal, L. P. and A. Roshko (1986). "Streamwise vortex structure in plane mixing layers". In: *J. Fluid Mech.* 170 (1986), pp. 499–525.

Boronin, S. A., J. J. Healey, and S. S. Sazhin (2013). "Non-modal stability of round viscous jets". In: *J. Fluid Mech.* 716 (2013), pp. 96–119.

Bradshaw, P. (1972). "The understanding and prediction of turbulent flow". In: *Aeronaut. J* 76.739 (1972), pp. 403–418.

Bradshaw, P., D. H. Ferriss, and R. F. Johnson (1964). "Turbulence in the noise-producing region of a circular jet". In: *J. Fluid Mech.* 19.4 (1964), pp. 591–624.

Brandt, L. (2014). "The lift-up effect: the linear mechanism behind transition and turbulence in shear flows". In: *European Journal of Mechanics-B/Fluids* 47 (2014), pp. 80–96.

Brandt, L., D. Sipp, J. O. Pralits, and O. Marquet (2011). "Effect of base-flow variation in noise amplifiers: the flat-plate boundary layer". In: *J. Fluid Mech.* 687.503-528 (2011), p. 15.

Breidenthal, R. (1981). "Structure in turbulent mixing layers and wakes using a chemical reaction". In: *J. Fluid Mech.* 109 (1981), pp. 1–24.

Breidenthal, R. E. (1978). "A chemically reacting shear layer". PhD thesis. Ph.D. Thesis, California Institute of Technology, 1978.

Brès, G. .A, V. Jaunet, M. Le Rallic, P. Jordan, T. Colonius, and S. K. Lele (2015). *Large eddy simulation for jet noise: the importance of getting the boundary layer right*. AIAA paper 2015-2535. 2015.

Brès, G. A., S. T. Bose, M. Emory, F. E. Ham, O. T. Schmidt, G. Rigas, and T. Colonius (2018). *Large eddy simulations of co-annular turbulent jet using a Voronoi-based mesh generation framework*. AIAA paper 2018-3302. 2018.

Brès, G. A., F. E. Ham, J. W. Nichols, and S. K. Lele (2017). "Unstructured large-eddy simulations of supersonic jets". In: *AIAA Journal* 55.4 (2017), pp. 1164–1184.

Brès, G. A., P. Jordan, T. Colonius, M. Le Rallic, V. Jaunet, and S. K. Lele (2014). "Large eddy simulation of a Mach 0.9 turbulent jet". In: *Proceedings of the Summer Program*. Center for Turbulence Research, Stanford University, 2014.

Brès, G. A., P. Jordan, V. Jaunet, M. Le Rallic, A. V. G. Cavalieri, A. Towne, S. K. Lele, T. Colonius, and O. T. Schmidt (2018). "Importance of the nozzle-exit boundary-layer state in subsonic turbulent jets". In: *J. Fluid Mech.* 851 (2018), pp. 83–124.

Brès, G. A. and S. K. Lele (2019). "Modelling of jet noise: a perspective from large-eddy simulations". In: *Philosophical Transactions of the Royal Society A* 377.2159 (2019), p. 20190081.

Bridges, J. and C. Brown (2004). "Parametric testing of chevrons on single flow hot jets". In: *10th AIAA/CEAS Aeroacoustics Conference*. 2004, p. 2824.

Bridges, J., M. Wernet, and C. Brown (2003). "Control of jet noise through mixing enhancement". In: *NASA Rep. No. NASA/TM 2003-212335* (2003).

Browand, F. K. and J. Laufer (1975). "The Roles of large scale structures in the initial development of circular Jets". In: *Symposia on Turbulence in Liquids*. University of Missouri–Rolla, 1975, p. 35.

Brown, G. L. and A. Roshko (1974). "On density effects and large structure in turbulent mixing layers". In: *J. Fluid Mech.* 64.4 (1974), pp. 775–816.

Butler, K. M. and B. F. Farrell (1992). "Three-dimensional optimal perturbations in viscous shear flow". In: *Physics of Fluids A: Fluid Dynamics* 4.8 (1992), pp. 1637–1650.

Callender, B., E. J. Gutmark, and S. Martens (2005). "Far-field acoustic investigation into chevron nozzle mechanisms and trends". In: *AIAA journal* 43.1 (2005), pp. 87–95.

Caraballo, E., M. Samimy, J. Scott, S. Narayanan, and J. DeBonis (2003). "Application of proper orthogonal decomposition to a supersonic axisymmetric jet". In: *AIAA journal* 41.5 (2003), pp. 866–877.

Cavalieri, A. V. G. and A. Agarwal (2014). "Coherence decay and its impact on sound radiation by wavepackets". In: *J. Fluid Mech.* 748 (2014), pp. 399–415.

Cavalieri, A. V. G., P. Jordan, A. Agarwal, and Y. Gervais (2011). "Jittering wave-packet models for subsonic jet noise". In: *Journal of Sound and Vibration* 330.18-19 (2011), pp. 4474–4492.

Cavalieri, A. V. G., P. Jordan, and L. Lesshafft (2019). "Wave-packet models for jet dynamics and sound radiation". In: *Applied Mechanics Reviews* 71.2 (2019), p. 020802.

Cavalieri, A. V. G., D. Rodríguez, P. Jordan, T. Colonius, and Y. Gervais (2013). "Wavepackets in the velocity field of turbulent jets". In: *J. Fluid Mech.* 730 (2013), pp. 559–592.

Cess, R. D. (1958). "A survey of the literature on heat transfer in turbulent tube flow." In: *Tech. Rep.* (1958), 8-0529–R24.

Chantry, M., L. S. Tuckerman, and D. Barkley (2016). "Turbulent–laminar patterns in shear flows without walls". In: *J. Fluid Mech.* 791 (2016), R8.

Cho, M., Y. Hwang, and H. Choi (2018). "Scale interactions and spectral energy transfer in turbulent channel flow". In: *Journal of Fluid Mechanics* 854 (2018), pp. 474–504.

Chu, B.-T. (1965). “On the energy transfer to small disturbances in fluid flow (Part I)”. In: *Acta Mechanica* 1.3 (1965), pp. 215–234.

Citriniti, J. H. and W. K. George (2000). “Reconstruction of the global velocity field in the axisymmetric mixing layer utilizing the proper orthogonal decomposition”. In: *J. Fluid Mech.* 418 (2000), pp. 137–166.

Committee, Naval Research Advisory et al. (2009). “Report on jet engine noise reduction”. In: (2009).

Cossu, C., G. Pujals, and S. Depardon (2009). “Optimal transient growth and very large–scale structures in turbulent boundary layers”. In: *J. Fluid Mech.* 619 (2009), pp. 79–94.

Crighton, D. G. and M. Gaster (1976). “Stability of slowly diverging jet flow”. In: *J. Fluid Mech.* 77.2 (1976), pp. 397–413.

Crouch, J. D., A. Garbaruk, and D. Magidov (2007). “Predicting the onset of flow unsteadiness based on global instability”. In: *Journal of Computational Physics* 224.2 (2007), pp. 924–940.

Crow, S. C. and F. H. Champagne (1971). “Orderly structure in jet turbulence”. In: *J. Fluid Mech.* 48.3 (1971), pp. 547–591.

Davoust, S., L. Jacquin, and B. Leclaire (2012). “Dynamics of m= 0 and m= 1 modes and of streamwise vortices in a turbulent axisymmetric mixing layer”. In: *J. Fluid Mech.* 709 (2012), pp. 408–444.

Del Alamo, J. C. and J. Jimenez (2006). “Linear energy amplification in turbulent channels”. In: *J. Fluid Mech.* 559 (2006), pp. 205–213.

Dergham, G., D. Sipp, and J. C. Robinet (2013). “Stochastic dynamics and model reduction of amplifier flows: the backward facing step flow”. In: *J. Fluid Mech.* 719 (2013), pp. 406–430.

Dimotakis, P. E., R. C. Miake-Lye, and D. A. Papantoniou (1983). “Structure and dynamics of round turbulent jets”. In: *The Physics of fluids* 26.11 (1983), pp. 3185–3192.

Duraisamy, K., G. Iaccarino, and H. Xiao (2019). “Turbulence modeling in the age of data”. In: *Ann. Rev. Fluid Mech.* 51 (2019).

Eitel-Amor, G., R. Örlü, and P. Schlatter (2014). “Simulation and validation of a spatially evolving turbulent boundary layer up to Reθ= 8300”. In: *International Journal of Heat and Fluid Flow* 47 (2014), pp. 57–69.

Ellingsen, T. and E. Palm (1975). “Stability of linear flow”. In: *Phys. Fluids* 18.4 (1975), pp. 487–488.

Farrell, B. F. (1988). “Optimal excitation of perturbations in viscous shear flow”. In: *The Physics of fluids* 31.8 (1988), pp. 2093–2102.

Farrell, B. F. and P. J. Ioannou (1993). “Optimal excitation of three-dimensional perturbations in viscous constant shear flow”. In: *Physics of Fluids A: Fluid Dynamics* 5.6 (1993), pp. 1390–1400.

– (2001). “Accurate low-dimensional approximation of the linear dynamics of fluid flow”. In: *Journal of the atmospheric sciences* 58.18 (2001), pp. 2771–2789.

Foures, D. P. G, N. Dovetta, D. Sipp, and P. J. Schmid (2014). “A data-assimilation method for Reynolds-averaged Navier–Stokes-driven mean flow reconstruction”. In: *Journal of fluid mechanics* 759 (2014), pp. 404–431.

Freund, J. B. (2001). “Noise sources in a low-Reynolds-number turbulent jet at Mach 0.9”. In: *Journal of Fluid Mechanics* 438 (2001), p. 277.

Freund, J. B. and T. Colonius (2009). “Turbulence and sound-field POD analysis of a turbulent jet”. In: *Int. J. Aeroacoust.* 8.4 (2009), pp. 337–354.

Garnaud, X., L. Lesshafft, P. J. Schmid, and P. Huerre (2013a). “Modal and transient dynamics of jet flows”. In: *Physics of Fluids* 25.4 (2013), p. 044103.

– (2013b). “The preferred mode of incompressible jets: linear frequency response analysis”. In: *J. Fluid Mech.* 716 (2013), pp. 189–202.

Georgiadis, N. J., D. A. Yoder, and W. A. Engblom (2006). “Evaluation of modified two-equation turbulence models for jet flow predictions”. In: *AIAA journal* 44.12 (2006), pp. 3107–3114.

Ghosal, S., T. S. Lund, P. Moin, and K. Akselvoll (1995). “A dynamic localization model for large-eddy simulation of turbulent flows”. In: *J. Fluid Mech.* 286 (1995), pp. 229–255.

Giovanetti, M. de, H. J. Sung, and Y. Hwang (2017). “Streak instability in turbulent channel flow: the seeding mechanism of large-scale motions”. In: *Journal of Fluid Mechanics* 832 (2017), pp. 483–513.

Goldstein, M. E. (2003). “A generalized acoustic analogy”. In: *J. Fluid Mech.* 488 (2003), pp. 315–333.

Greska, B., A. Krothapalli, J. Seiner, B. Jansen, and L. Ukeiley (2005). “The effects of microjet injection on an F404 jet engine”. In: *11th AIAA/CEAS Aeroacoustics Conference*. 2005, p. 3047.

Gudmundsson, K. and T. Colonius (2011). “Instability wave models for the near-field fluctuations of turbulent jets”. In: *J. Fluid Mech.* 689 (2011), pp. 97–128.

Hack, M. J. P. and P. Moin (2017). “Algebraic disturbance growth by interaction of Orr and lift-up mechanisms”. In: *J. Fluid Mech.* 829 (2017), pp. 112–126.

Hamilton, J. M., J. Kim, and F. Waleffe (1995). “Regeneration mechanisms of near-wall turbulence structures”. In: *J. Fluid Mech.* 287 (1995), pp. 317–348.

Hansen, P. C. and D. P. O’Leary (1993). “The Use of the L-Curve in the Regularization of Discrete Ill-Posed Problems”. In: *SIAM Journal on Scientific Computing* 14.6 (1993), pp. 1487–1503.

Hellström, L. H. O., A. Sinha, and A. J. Smits (2011). "Visualizing the very-large-scale motions in turbulent pipe flow". In: *Phys. Fluids* 23.1 (2011), p. 011703.

Hinze, J. O. (1959). *Turbulence*. McGraw-Hill, New York, 1959.

Ho, C.-M. and P. Huerre (1984). "Perturbed free shear layers". In: *Annual review of fluid mechanics* 16.1 (1984), pp. 365–422.

Hultgren, L. S. and L. H. Gustavsson (1981). "Algebraic growth of disturbances in a laminar boundary layer". In: *The Physics of Fluids* 24.6 (1981), pp. 1000–1004.

Hutchins, N. and I. Marusic (2007). "Evidence of very long meandering features in the logarithmic region of turbulent boundary layers". In: *J. Fluid Mech.* 579 (2007), pp. 1–28.

Hwang, Y. (2016). "Mesolayer of attached eddies in turbulent channel flow". In: *Physical Review Fluids* 1.6 (2016), p. 064401.

Hwang, Y. and C. Cossu (2010a). "Amplification of coherent streaks in the turbulent Couette flow: an input–output analysis at low Reynolds number". In: *J. Fluid Mech.* 643 (2010), pp. 333–348.

– (2010b). "Linear non-normal energy amplification of harmonic and stochastic forcing in the turbulent channel flow". In: *J. Fluid Mech.* 664 (2010), pp. 51–73.

Hwang, Y. and B. Eckhardt (2020). "Attached eddy model revisited using a minimal quasi-linear approximation". In: *J. Fluid Mech* 894.A23 (2020).

Illingworth, S. J., J. P. Monty, and I. Marusic (2018). "Estimating large-scale structures in wall turbulence using linear models". In: *J. Fluid Mech.* 842 (2018), pp. 146–162.

Jaunet, V., P. Jordan, and A. V. G. Cavalieri (2017). "Two-point coherence of wave packets in turbulent jets". In: *Physical Review Fluids* 2.2 (2017), p. 024604.

Jeun, J. and J. W. Nichols (2018). "Input-output analysis of Mach 0.9 jet noise". In: *arXiv preprint arXiv:1806.09280* (2018).

Jeun, J., J. W. Nichols, and M. R. Jovanović (2016). "Input-output analysis of high-speed axisymmetric isothermal jet noise". In: *Phys. Fluids* 28.4 (2016), p. 047101.

Jimenez, J., M. Cogollos, and L. P. Bernal (1985). "A perspective view of the plane mixing layer". In: *J. Fluid Mech.* 152 (1985), pp. 125–143.

Jiménez, J. (2013). "How linear is wall-bounded turbulence?" In: *Physics of Fluids* 25.11 (2013), p. 110814.

– (2018). "Coherent structures in wall-bounded turbulence". In: *J. Fluid Mech.* 842 (2018), P1.

Jiménez, J. and A. Pinelli (1999). "The autonomous cycle of near-wall turbulence". In: *J. Fluid Mech.* 389 (1999), pp. 335–359.

Jimenez-Gonzalez, J. I. and P. Brancher (2017). “Transient energy growth of optimal streaks in parallel round jets”. In: *Physics of Fluids* 29.11 (2017), p. 114101.

Jordan, P. and T. Colonius (2013). “Wave packets and turbulent jet noise”. In: *Annu. Rev. Fluid Mech.* 45 (2013), pp. 173–195.

Jovanović, M. R. (2004). *Modeling, analysis, and control of spatially distributed systems*. University of California at Santa Barbara, Dept. of Mechanical Engineering, 2004.

– (2021). “From Bypass Transition to Flow Control and Data-Driven Turbulence Modeling: An Input–Output Viewpoint”. In: *Annual Review of Fluid Mechanics* 53.1 (2021), null. DOI: 10.1146/annurev-fluid-010719-060244.

Jovanović, M. R. and B. Bamieh (2005). “Componentwise energy amplification in channel flows”. In: *J. Fluid Mech.* 534 (2005), pp. 145–183.

Jung, D., S. Gamard, and W. K. George (2004). “Downstream evolution of the most energetic modes in a turbulent axisymmetric jet at high Reynolds number. Part 1. The near-field region”. In: *J. Fluid Mech.* 514 (2004), pp. 173–204.

Kantharaju, J., R. Courtier, B. Leclaire, and L. Jacquin (2020). “Interactions of large-scale structures in the near field of round jets at high Reynolds numbers”. In: *J. Fluid Mech.* 888 (2020), A8. DOI: 10.1017/jfm.2020.34.

Karban, U., B. Bugeat, E. Martini, A. Towne, A. V. G. Cavalieri, L. Lesshafft, A. Agarwal, P. Jordan, and T. Colonius (2020). “Ambiguity in mean-flow-based linear analysis”. In: *J. Fluid Mech.* 900 (2020), R5. DOI: 10.1017/jfm.2020.566.

Karman, T. von (1938). “Some remarks on the statistical theory of turbulence”. In: *Proc. 5th Int. Congr. Appl. Mech., Cambridge, MA* (1938), p. 347.

Kim, H. T., S. J. Kline, and W. C. Reynolds (1971). “The production of turbulence near a smooth wall in a turbulent boundary layer”. In: *J. Fluid Mech.* 50.1 (1971), pp. 133–160.

Klebanoff, P. S. (1971). “Effect of freestream turbulence on the laminar boundary layer”. In: *Bulletin of the American Physical Society* 16 (1971), p. 1321.

Kline, S. J., W. C. Reynolds, F. A. Schraub, and P. W. Runstadler (1967). “The structure of turbulent boundary layers”. In: *J. Fluid Mech.* 30.4 (1967), pp. 741–773.

Konrad, J. H. (1976). “An Experimental Investigation of Mixing in Two-Dimensional Turbulent Shear Flows with Applications to Diffusion-Limited Chemical Reactions”. PhD thesis. Ph.D. Thesis, California Institute of Technology, 1976.

Landahl, M. T. (1980). “A note on an algebraic instability of inviscid parallel shear flows”. In: *J. Fluid Mech.* 98.2 (1980), pp. 243–251.

Launder, B. E. and D. B. Spalding (1983). “The numerical computation of turbulent flows”. In: *Numerical prediction of flow, heat transfer, turbulence and combustion*. Elsevier, 1983, pp. 96–116.

Lesieur, M. and O. Metais (1996). “New trends in large-eddy simulations of turbulence”. In: *Annual review of fluid mechanics* 28.1 (1996), pp. 45–82.

Lesshafft, L., O. Semeraro, V. Jaunet, A. V. G. Cavalieri, and P. Jordan (2019). “Resolvent-based modelling of coherent wavepackets in a turbulent jet”. In: *Phys. Rev. Fluids* 4.6 (2019), p. 063901.

Liepmann, D. (1991). “Streamwise vorticity and entrainment in the near field of a round jet”. In: *Physics of Fluids A: Fluid Dynamics* 3.5 (1991), pp. 1179–1185.

Liepmann, D. and M. Gharib (1992). “The role of streamwise vorticity in the near-field entrainment of round jets”. In: *J. Fluid Mech.* 245 (1992), pp. 643–668.

Lighthill, M. J. (1952). “On sound generated aerodynamically I. General theory”. In: *Proc. R. Soc. Lond. A* 211.1107 (1952), pp. 564–587.

– (1954). “On sound generated aerodynamically. II. Turbulence as a source of sound”. In: *Proc. R. Soc. Lond. A* 222.1148 (1954), pp. 1–32.

Lin, C. C. (1981). “The evolution of streamwise vorticity in the free shear layer”. PhD thesis. Ph.D. Thesis, Univ. Calif., Berkeley, 1981.

Lin, S. J. and G. M. Corcos (1984). “The mixing layer: deterministic models of a turbulent flow. Part 3. The effect of plane strain on the dynamics of streamwise vortices”. In: *J. Fluid Mech.* 141 (1984), pp. 139–178.

Lumley, J. L. (1967). “The structure of inhomogeneous turbulent flows”. In: *Atmospheric turbulence and radio propagation* (1967), pp. 166–178.

– (1970). *Stochastic tools in turbulence*. New York: Academic Press, 1970.

– (1981). “Coherent structures in turbulence”. In: *Transition and turbulence*. Elsevier, 1981, pp. 215–242.

Malik, M. and C. L. Chang (1997). “PSE applied to supersonic jet instability”. In: *35th Aerospace Sciences Meeting and Exhibit*. 1997, p. 758.

Malkus, W. V. R. (1956). “Outline of a theory of turbulent shear flow”. In: *J. Fluid Mech.* 1.5 (1956), pp. 521–539.

Mantič-Lugo, V., C. Arratia, and F. Gallaire (2014). “Self-consistent mean flow description of the nonlinear saturation of the vortex shedding in the cylinder wake”. In: *Physical review letters* 113.8 (2014), p. 084501.

Marant, M. and C. Cossu (2018). “Influence of optimally amplified streamwise streaks on the Kelvin–Helmholtz instability”. In: *J. Fluid Mech.* 838 (2018), pp. 478–500.

Martin, J. E. and E. Meiburg (1991). “Numerical investigation of three-dimensionally evolving jets subject to axisymmetric and azimuthal perturbations”. In: *J. Fluid Mech.* 230 (1991), pp. 271–318.

Martini, E., A. V. G. Cavalieri, P. Jordan, A. Towne, and L. Lesshafft (2020). “Resolvent-based optimal estimation of transitional and turbulent flows”. In: *J. Fluid Mech.* 900 (2020), A2.

Mattsson, K. and J. Nordström (2004). “Summation by parts operators for finite difference approximations of second derivatives”. In: *J. Computat. Phys.* 199.2 (2004), pp. 503–540.

Maulik, R., O. San, J.D. Jacob, and Ch. Crick (2019). “Sub-grid scale model classification and blending through deep learning”. In: *J. Fluid Mech.* 870 (2019).

McKeon, B. J. (2017). “The engine behind (wall) turbulence: perspectives on scale interactions”. In: *Journal of Fluid Mechanics* 817 (2017).

McKeon, B. J. and A. S. Sharma (2010). “A critical-layer framework for turbulent pipe flow”. In: *J. Fluid Mech.* 658 (2010), pp. 336–382.

Meliga, P., G. Pujals, and E. Serre (2012). “Sensitivity of 2-D turbulent flow past a D-shaped cylinder using global stability”. In: *Physics of Fluids* 24.6 (2012), p. 061701.

Metcalfe, R. W., S. A. Orszag, M. E. Brachet, S. Menon, and J. J. Riley (1987). “Secondary instability of a temporally growing mixing layer”. In: *J. Fluid Mech.* 184 (1987), pp. 207–243.

Mettot, C., D. Sipp, and H. Bézard (2014). “Quasi-laminar stability and sensitivity analyses for turbulent flows: prediction of low-frequency unsteadiness and passive control”. In: *Physics of Fluids* 26.4 (2014), p. 061701.

Michalke, A. (1971). “Instability of a compressible circular free jet with consideration of the influence of the jet boundary layer thickness”. In: *Z. für Flugwissenschaften* 19.8 (1971), pp. 319–328.

– (1977). “Instability of a compressible circular free jet with consideration of the influence of the jet boundary layer thickness”. In: (1977).

– (1984). “Survey on jet instability theory”. In: *Progress in Aerospace Sciences* 21 (1984), pp. 159–199.

Miksad, R. W. (1972). “Experiments on the nonlinear stages of free-shear-layer transition”. In: *J. Fluid Mech.* 56.4 (1972), pp. 695–719.

Mizuno, Y. and J. Jiménez (2013). “Wall turbulence without walls”. In: *J. Fluid Mech.* 723 (2013), pp. 429–455.

Moarref, R. and M. R. Jovanović (2012). “Model-based design of transverse wall oscillations for turbulent drag reduction”. In: *J. Fluid Mech.* 707 (2012), pp. 205–240.

Moarref, R., A. S. Sharma, J. A. Tropp, and B. J. McKeon (2013). "Model-based scaling of the streamwise energy density in high-Reynolds-number turbulent channels". In: *J. Fluid Mech.* 734 (2013), pp. 275–316.

Moffatt, H. K. (1965). "The interaction of turbulence with strong wind shear". In: *Atmospheric Turbulence and Radio Waves Propagation, Proc. Intern. Collq. Moscow, 1965* (1965), pp. 139–156.

Mohseni, K. and T. Colonius (2000). "Numerical treatment of polar coordinate singularities". In: *J. Computat. Phys.* 157.2 (2000), pp. 787–795.

Moin, P. and K. Mahesh (1998). "Direct numerical simulation: a tool in turbulence research". In: *Annual review of fluid mechanics* 30.1 (1998), pp. 539–578.

Mollo-Christensen, E. (1967). "Jet noise and shear flow instability seen from an experimenter's viewpoint". In: *J. Appl. Mech.* 34 (1967), pp. 1–7.

Monokrousos, A., E. Åkervik, L. Brandt, and D. S. Henningson (2010). "Global three-dimensional optimal disturbances in the Blasius boundary-layer flow using time-steppers". In: *J. Fluid Mech.* 650 (2010), pp. 181–214.

Monty, J. P., J. A. Stewart, R. C. Williams, and M. S. Chong (2007). "Large-scale features in turbulent pipe and channel flows". In: *J. Fluid Mech.* 589 (2007), pp. 147–156.

Morra, P., O. Semeraro, D. S. Henningson, and C. Cossu (2019). "On the relevance of Reynolds stresses in resolvent analyses of turbulent wall-bounded flows". In: *J. Fluid Mech.* 867 (2019), pp. 969–984.

Morris, P. J. (1976). "The spatial viscous instability of axisymmetric jets". In: *J. Fluid Mech.* 77.3 (1976), pp. 511–529.

Neu, J. C. (1984). "The dynamics of stretched vortices". In: *J. Fluid Mech.* 143 (1984), pp. 253–276.

Nichols, J. W. and S. K. Lele (2011). "Global modes and transient response of a cold supersonic jet". In: *J. Fluid Mech.* 669 (2011), pp. 225–241.

Nogueira, P. A. S., A. V. G. Cavalieri, P. Jordan, and V. Jaunet (2019). "Large-scale, streaky structures in turbulent jets". In: *J. Fluid Mech.* 873 (2019), pp. 211–237.

Oberleithner, K., C. O. Paschereit, and I. Wygnanski (2014). "On the impact of swirl on the growth of coherent structures". In: *J. Fluid Mech.* 741 (2014), pp. 156–199.

Papamoschou, D. (2018). "Wavepacket modeling of the jet noise source". In: *International Journal of Aeroacoustics* 17.1-2 (2018), pp. 52–69.

Parish, E. and K. Duraisamy (2016). "A paradigm for data-driven predictive modeling using field inversion and machine learning". In: *Journal of Computational Physics* 305 (2016), pp. 758–774.

Paschereit, C. O., D. Oster, T. A. Long, H. E. Fiedler, and I. Wygnanski (1992). "Flow visualization of interactions among large coherent structures in an axisymmetric jet". In: *Experiments in Fluids* 12.3 (1992), pp. 189–199.

Pickering, E., G. Rigas, P. A. S. Nogueira, A. V. G. Cavalieri, O. T. Schmidt, and T. Colonius (2020). "Lift-up, Kelvin–Helmholtz and Orr mechanisms in turbulent jets". In: *Journal of Fluid Mechanics* 896 (2020), A2. DOI: 10.1017/jfm.2020.301.

Pickering, E., G. Rigas, O. T. Schmidt, D. Sipp, and T. Colonius (2020). "Optimal eddy viscosity for resolvent-based models of coherent structures in turbulent jets". In: *arXiv preprint arXiv:2005.10964* (2020).

Pickering, E., G. Rigas, D. Sipp, O. T. Schmidt, and T. Colonius (2019). "Eddy viscosity for resolvent-based jet noise models". In: *25th AIAA/CEAS Aeroacoustics Conference*. 2019, p. 2454. DOI: 10.2514/6.2019-2454.

Pickering, E., A. Towne, P. Jordan, and T. Colonius (2020). "Resolvent-based jet noise models: a projection approach". In: *AIAA Scitech 2020 Forum*. 2020, p. 0999. DOI: 10.2514/6.2020-0999.

Pierrehumbert, R. T. and S. E. Widnall (1982). "The two-and three-dimensional instabilities of a spatially periodic shear layer". In: *J. Fluid Mech.* 114 (1982), pp. 59–82.

Pope, S. B. (1978). "An explanation of the turbulent round-jet/plane-jet anomaly". In: *AIAA journal* 16.3 (1978), pp. 279–281.

– (2001). *Turbulent flows*. IOP Publishing, 2001.

Pujals, G., M. García-Villalba, C. Cossu, and S. Depardon (2009). "A note on optimal transient growth in turbulent channel flows". In: *Physics of Fluids* 21.1 (2009), p. 015109.

Qadri, U. A. and P. J. Schmid (2017). "Frequency selection mechanisms in the flow of a laminar boundary layer over a shallow cavity". In: *Phys. Rev. Fluids* 2 (1 2017), p. 013902. DOI: 10.1103/PhysRevFluids.2.013902.

Reynolds, W. C. and A. K. M. F. Hussain (1972). "The mechanics of an organized wave in turbulent shear flow. Part 3. Theoretical models and comparisons with experiments". In: *J. Fluid Mech.* 54.2 (1972), pp. 263–288.

Reynolds, W. C. and W. G. Tiederman (1967). "Stability of turbulent channel flow, with application to Malkus's theory". In: *J. Fluid Mech.* 27.2 (1967), pp. 253–272.

Rigas, G., E. Pickering, O. T. Schmidt, P. A. Nogueira, A. V. Cavalieri, G. A. Brès, and T. Colonius (2019). "Streaks and coherent structures in jets from round and serrated nozzles". In: *25th AIAA/CEAS Aeroacoustics Conference*. 2019, p. 2597.

Rodríguez, D., A. V. G. Cavalieri, T. Colonius, and P. Jordan (2015). "A study of linear wavepacket models for subsonic turbulent jets using local eigenmode decomposition of PIV data". In: *European Journal of Mechanics-B/Fluids* 49 (2015), pp. 308–321.

Rogers, M. M. and R. D. Moser (1992). “The three-dimensional evolution of a plane mixing layer: the Kelvin–Helmholtz rollup”. In: *J. Fluid Mech.* 243 (1992), pp. 183–226.

Rosenberg, K. and B. J. McKeon (2019). “Computing exact coherent states in channels starting from the laminar profile: A resolvent-based approach”. In: *Physical Review E* 100.2 (2019), p. 021101.

Rukes, L., C. O. Paschereit, and K. Oberleithner (2016). “An assessment of turbulence models for linear hydrodynamic stability analysis of strongly swirling jets”. In: *European Journal of Mechanics-B/Fluids* 59 (2016), pp. 205–218.

Saiyed, N. H., K. L. Mikkelsen, and J. E. Bridges (2003). “Acoustics and thrust of quiet separate-flow high-bypass-ratio nozzles”. In: *AIAA journal* 41.3 (2003), pp. 372–378.

Samimy, M., K. Zaman, and M.F. Reeder (1993). “Effect of tabs on the flow and noise field of an axisymmetric jet”. In: *AIAA journal* 31.4 (1993), pp. 609–619.

Sarkar, S., G. Erlebacher, M. Y. Hussaini, and H. Otto. Kreiss (1991). “The analysis and modelling of dilatational terms in compressible turbulence”. In: *J. Fluid Mech.* 227 (1991), pp. 473–493.

Sartor, F., C. Mettot, and D. Sipp (2014). “Stability, receptivity, and sensitivity analyses of buffeting transonic flow over a profile”. In: *AIAA Journal* 53.7 (2014), pp. 1980–1993.

Sasaki, K., A. V. G. Cavalieri, P. Jordan, O. T. Schmidt, T. Colonius, and G. A. Brès (2017). “High-frequency wavepackets in turbulent jets”. In: *J. Fluid Mech.* 830 (2017).

Schlinker, R. H., J. C. Simonich, R. A. Reba, T. Colonius, K. Gudmundsson, and F. Ladeinde (2009). *Supersonic Jet Noise from Round and Chevron Nozzles: Experimental Studies*. AIAA Paper 2009-3257. 2009.

Schlinker, R. H., J. C. Simonich, R. A. Reba, T. Colonius, and F. Ladeinde (2008). *Decomposition of High Speed Jet Noise: Source Characteristics and Propagation Effects*. AIAA paper 2008-2890. 2008.

Schmid, P. J., D. S. Henningson, and D. F. Jankowski (2002). “Stability and transition in shear flows”. In: *Appl. Mech. Rev.* 55.3 (2002), B57–B59.

Schmidt, O. T. (2020). “Bispectral mode decomposition of nonlinear flows”. In: *Nonlinear Dynamics* 102.4 (2020), pp. 2479–2501.

Schmidt, O. T., A. Towne, G. Rigas, T. Colonius, and G. A. Brès (2018). “Spectral analysis of jet turbulence”. In: *J. Fluid Mech.* 855 (2018), pp. 953–982.

Schmitt, F. G. (2007). “About Boussinesq’s turbulent viscosity hypothesis: historical remarks and a direct evaluation of its validity”. In: *Comptes Rendus Mécanique* 335.9-10 (2007), pp. 617–627.

Semeraro, O., V. Jaunet, P. Jordan, A. V. Cavalieri, and L. Lesshafft (2016). "Stochastic and harmonic optimal forcing in subsonic jets". In: *22nd AIAA/CEAS Aeroacoustics Conference*. 2016, p. 2935.

Semeraro, O., L. Lesshafft, V. Jaunet, and P. Jordan (2016). "Modeling of coherent structures in a turbulent jet as global linear instability wavepackets: theory and experiment". In: *International Journal of Heat and Fluid Flow* 62 (2016), pp. 24–32.

Sharma, A. S. and B. J. McKeon (2013). "On coherent structure in wall turbulence". In: *J. Fluid Mech.* 728 (2013), pp. 196–238.

Sharma, A. S., R. Moarref, B. J. McKeon, J. S. Park, M. D. Graham, and A. P. Willis (2016). "Low-dimensional representations of exact coherent states of the Navier-Stokes equations from the resolvent model of wall turbulence". In: *Physical Review E* 93.2 (2016), p. 021102.

Sinha, A., A. Rajagopalan, and S. Singla (2016). "Linear stability implications of chevron geometry modifications for turbulent jets". In: *22nd AIAA/CEAS Aeroacoustics Conference*. 2016, p. 3053.

Sinha, A., D. Rodríguez, G. A. Brès, and T. Colonius (2014). "Wavepacket models for supersonic jet noise". In: *J. Fluid Mech.* 742 (2014), pp. 71–95.

Sipp, D. and O. Marquet (2013). "Characterization of noise amplifiers with global singular modes: the case of the leading-edge flat-plate boundary layer". In: *Theoretical and Computational Fluid Dynamics* 27.5 (2013), pp. 617–635.

Sipp, D., O. Marquet, P. Meliga, and A. Barbagallo (2010). "Dynamics and control of global instabilities in open-flows: a linearized approach". In: *Applied Mechanics Reviews* 63.3 (2010).

Smagorinsky, J. (1963). "General circulation experiments with the primitive equations: I. The basic experiment". In: *Monthly weather review* 91.3 (1963), pp. 99–164.

Stansfeld, S. A. and M. P. Matheson (2003). "Noise pollution: non-auditory effects on health". In: *British medical bulletin* 68.1 (2003), pp. 243–257.

Swearingen, J. D. and R. F. Blackwelder (1987). "The growth and breakdown of streamwise vortices in the presence of a wall". In: *J. Fluid Mech.* 182 (1987), pp. 255–290.

Tam, C. K. W. and L. Auriault (1999). "Jet mixing noise from fine-scale turbulence". In: *AIAA journal* 37.2 (1999), pp. 145–153.

Tam, C. K. W. and F. Q. Hu (1989). "On the three families of instability waves of high-speed jets". In: *J. Fluid Mech.* 201 (1989), pp. 447–483.

Tammisola, O. and M. P. Juniper (2016). "Coherent structures in a swirl injector at $Re = 4800$ by nonlinear simulations and linear global modes". In: *J. Fluid Mech.* 792 (2016), pp. 620–657.

Thies, A. T. and C. K. W. Tam (1996). "Computation of turbulent axisymmetric and nonaxisymmetric jet flows using the k-ϵ model". In: *AIAA journal* 34.2 (1996), pp. 309–316.

Tissot, G., F. C. Lajús Jr, A. V. G. Cavalieri, and P. Jordan (2017). "Wave packets and Orr mechanism in turbulent jets". In: *Phys. Rev. Fluids* 2.9 (2017), p. 093901.

Tissot, G., M. Zhang, F. C. Lajús, A. V. G. Cavalieri, and P. Jordan (2017). "Sensitivity of wavepackets in jets to nonlinear effects: the role of the critical layer". In: *J. Fluid Mech.* 811 (2017), pp. 95–137.

Toedtli, S. S., M. Luhar, and B. J. McKeon (2019). "Predicting the response of turbulent channel flow to varying-phase opposition control: Resolvent analysis as a tool for flow control design". In: *Physical Review Fluids* 4.7 (2019), p. 073905.

Towne, A., G. A. Bres, and S. K. Lele (2017). "A statistical jet-noise model based on the resolvent framework". In: *23rd AIAA/CEAS Aeroacoustics Conference*. 2017, p. 3706.

Towne, A., T. Colonius, P. Jordan, A. V. Cavalieri, and G. A. Bres (2015). "Stochastic and nonlinear forcing of wavepackets in a Mach 0.9 jet". In: *21st AIAA/CEAS Aeroacoustics Conference*. 2015, p. 2217.

Towne, A., A. Lozano-Durán, and X. Yang (2020). "Resolvent-based estimation of space–time flow statistics". In: *J. Fluid Mech.* 883 (2020).

Towne, A., O. T. Schmidt, and T. Colonius (2018). "Spectral proper orthogonal decomposition and its relationship to dynamic mode decomposition and resolvent analysis". In: *J. Fluid Mech.* 847 (2018), pp. 821–867.

Trefethen, L. N., A. E. Trefethen, S. C. Reddy, and T. A. Driscoll (1993). "Hydrodynamic stability without eigenvalues". In: *Science* 261.5121 (1993), pp. 578–584.

Vadarevu, S. B., S. Symon, S. J. Illingworth, and I. Marusic (2019). "Coherent structures in the linearized impulse response of turbulent channel flow". In: *J. Fluid Mech.* 863 (2019), pp. 1190–1203.

Violato, D. and F. Scarano (2011). "Three-dimensional evolution of flow structures in transitional circular and chevron jets". In: *Physics of Fluids* 23.12 (2011), p. 124104.

Vreman, A. W. (2004). "An eddy-viscosity subgrid-scale model for turbulent shear flow: Algebraic theory and applications". In: *Phys. Fluids* 16.10 (2004), pp. 3670–3681.

Wang, Z., K. Luo, D. Li, J. Tan, and J. Fan (2018). "Investigations of data-driven closure for subgrid-scale stress in large-eddy simulation". In: *Phys. Fluids* 30 (2018), p. 125101.

Widnall, S. E., D. B. Bliss, and C.-Y. Tsai (1974). "The instability of short waves on a vortex ring". In: *J. Fluid Mech.* 66.1 (1974), pp. 35–47.

Wu, X. and P. Huerre (2009). “Low-frequency sound radiated by a nonlinearly modulated wavepacket of helical modes on a subsonic circular jet”. In: *Journal of Fluid Mechanics* 637 (2009), pp. 173–211.

Yang, H., Y. Zhou, R. M. C. So, and Y. Liu (2016). “Turbulent jet manipulation using two unsteady azimuthally separated radial minijets”. In: *Proceedings of the Royal Society A: Mathematical, Physical and Engineering Sciences* 472.2191 (2016), p. 20160417.

Yankaskas, K. (2013). “Prelude: noise-induced tinnitus and hearing loss in the military”. In: *Hearing research* 295 (2013), pp. 3–8.

Yeh, C.-A. and K. Taira (2019). “Resolvent-analysis-based design of airfoil separation control”. In: *J. Fluid Mech.* 867 (2019), pp. 572–610.

Yim, E., P. Meliga, and F. Gallaire (2019). “Self-consistent triple decomposition of the turbulent flow over a backward-facing step under finite amplitude harmonic forcing”. In: *Proceedings of the Royal Society A* 475.2225 (2019), p. 20190018.

Yule, A. J. (1978). “Large-scale structure in the mixing layer of a round jet”. In: *J. Fluid Mech.* 89.3 (1978), pp. 413–432.

Zaman, K. (1999). “Spreading characteristics of compressible jets from nozzles of various geometries”. In: *J. Fluid Mech.* 383 (1999), pp. 197–228.

Zaman, K., M. F. Reeder, and M. Samimy (1994). “Control of an axisymmetric jet using vortex generators”. In: *Physics of Fluids* 6.2 (1994), pp. 778–793.

Zare, A., M. R. Jovanović, and T. T. Georgiou (2017). “Colour of turbulence”. In: *J. Fluid Mech.* 812 (2017), pp. 636–680.

Zhiyin, Y. (2015). “Large-eddy simulation: Past, present and the future”. In: *Chinese journal of Aeronautics* 28.1 (2015), pp. 11–24.

Appendix A

OPTIMAL EDDY VISCOSITY FOR RESOLVENT-BASED MODELS OF COHERENT STRUCTURES IN TURBULENT JETS

A.1 Linear damping term

Besides the studied eddy-viscosity models, we also investigated the impact of a linear damping term, which is equivalent to a finite-time-horizon resolvent analysis introduced by Jovanović (2004), recently studied by Yeh and Taira (2019) to localize the resolvent forcing and response modes on an airfoil. For this model, we modify the operator so that,

$$\boldsymbol{L}_\beta = \boldsymbol{L} - \beta \boldsymbol{I}, \tag{A.1}$$

where $\beta = 1/\tau > 0$, and τ is the desired temporal decay rate. We then find the value of β that best aligns the dominant resolvent and SPOD modes.

Figure A.1 presents the alignments for the linear damping case. Although linear damping improves alignments, the performance is significantly inferior to the eddy-viscosity models, likely because of its monolithic damping effect over all wavenumbers, whereas the eddy-viscosity methods directly address the effect of the Reynolds stresses. Considering its suboptimal performance when compared to eddy-viscosity models, we only present results for the $M_j = 0.4$, $m = 0$, and $St \in [0.05, 1]$ cases.

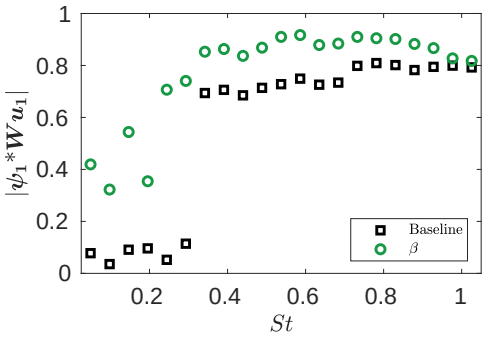

Figure A.1: Optimal alignments for the linear damping term and the baseline case, $\mathrm{Re}_T = 3 \times 10^4$.

.

A.2 Governing equations

Conservation of mass, momentum, and energy for a compressible, Newtonian fluid are written as,

$$\frac{D\rho}{Dt} = -\rho\Theta \tag{A.2}$$

$$\rho\frac{D\boldsymbol{u}}{Dt} = -\frac{1}{\gamma M_j^2}\nabla(\rho T) + \nabla\cdot\left[\mu\left((\nabla\boldsymbol{u}) + (\nabla\boldsymbol{u})^T - \frac{2}{3}\Theta\mathbb{I}\right)\right] \tag{A.3}$$

$$\begin{aligned}\rho\frac{DT}{Dt} = &-\frac{1}{\gamma M_j^2}\rho T\Theta + \frac{\mu}{(\gamma-1)M_j^2 Pr_\infty}\nabla^2 T \\ &+ \gamma M_j^2\mu\left[\frac{1}{2}\left\{(\nabla\boldsymbol{u}) + (\nabla\boldsymbol{u})^T\right\} : \left\{(\nabla\boldsymbol{u}) + (\nabla\boldsymbol{u})^T\right\} - \frac{2}{3}\Theta^2\right],\end{aligned} \tag{A.4}$$

respectively, where $\Theta = \nabla\cdot\boldsymbol{u}$ is the dilatation. We take $Pr_\infty = 0.7$ and $\gamma = 1.4$ as constants. The equations have been made nondimensional with the jet density (ρ_j), speed (U_j) , and diameter, D. The nondimensional viscosity, $\mu = \frac{1}{Re_j}$, is also a constant.

Applying the Reynolds decomposition (i.e. $\boldsymbol{q}(\boldsymbol{x},t) = \bar{\boldsymbol{q}}(\boldsymbol{x}) + \boldsymbol{q}'(\boldsymbol{x},t)$) to the above equations and separating terms that are linear and nonlinear in the fluctuations to the left- and right-hand side, respectively, gives

$$\frac{\bar{D}\rho'}{Dt} + \boldsymbol{u}'\cdot\nabla\bar{\rho} + \rho'\bar{\Theta} + \bar{\rho}\Theta' = f_\rho \tag{A.5}$$

$$\begin{aligned}&\bar{\rho}\frac{\bar{D}\boldsymbol{u}'}{Dt} + \bar{\rho}\boldsymbol{u}'\cdot\nabla\overline{\boldsymbol{u}} + \rho'\overline{\boldsymbol{u}}\cdot\nabla\overline{\boldsymbol{u}} \\ &+\frac{1}{\gamma M_j^2}\left(\bar{\rho}\nabla T' + \rho'\nabla\bar{T} + \bar{T}\nabla\rho' + T'\nabla\bar{\rho}\right) \\ &-\nabla\cdot\left[\mu\left((\nabla\boldsymbol{u}') + (\nabla\boldsymbol{u}')^T - \frac{2}{3}\Theta'\mathbb{I}\right)\right] = \boldsymbol{f_u}\end{aligned} \tag{A.6}$$

$$\begin{aligned}&\bar{\rho}\frac{\bar{D}T'}{Dt}\bar{\rho}\mathbf{u}'\cdot\nabla\bar{T} + \frac{1}{\gamma M_j^2}\left(\bar{T}\Theta' + T'\bar{\Theta}\right) \\ &+\rho'\{\overline{\mathbf{u}}\cdot\nabla\bar{T} + \frac{\bar{\rho}}{\gamma M_j^2}\bar{T}\bar{\Theta}\} - \frac{\mu}{(\gamma-1)M_j^2 Pr_\infty}\nabla^2 T' \\ &-\gamma M_j^2\mu\left[\left\{(\nabla\overline{\mathbf{u}}) + (\nabla\overline{\mathbf{u}})^{\mathrm{T}}\right\} : \left\{(\nabla\mathbf{u}') + (\nabla\mathbf{u}')^{\mathrm{T}}\right\} - \frac{4}{3}\bar{\Theta}\Theta'\right] = f_T.\end{aligned} \tag{A.7}$$

with $\frac{\bar{D}}{Dt} = \frac{\partial}{\partial t} + \overline{\boldsymbol{u}}\cdot\nabla$, and where we have grouped all the nonlinear terms as forcing terms on the right-hand side.

The left-hand side is then transformed to a cylindrical coordinate frame and Fourier transformed in time (ω) and azimuth (m). The resulting equations are discretized as discussed in § 2.2.

The eddy-viscosity model we use, discussed in § 2.2, simply replaces μ in Equations (A.5) to (A.7) with $\mu + \mu_T(x, r)$.

A.3 Optimizing in an input and output framework

In resolvent analysis, it is often useful to restrict the input and output spaces by writing

$$\boldsymbol{L}_T \boldsymbol{q} = \boldsymbol{B} \boldsymbol{f} \tag{A.8}$$

$$\boldsymbol{y} = \boldsymbol{C} \boldsymbol{q}$$

$$\boldsymbol{y} = \boldsymbol{C} \boldsymbol{L}_T^{-1} \boldsymbol{B} \boldsymbol{f} \tag{A.9}$$

where $\boldsymbol{C}$ transforms the state vector to a desired output space $\boldsymbol{y}$ and $\boldsymbol{B}$ maps a smaller dimensional input space to the state space. Here we show that such additions do not hinder the generality of the optimization presented in this thesis.

The structure of the cost function does not change,

$$\mathcal{J} = \boldsymbol{u}_1^* \boldsymbol{W}_{\boldsymbol{y}} \boldsymbol{\psi}_1 \boldsymbol{\psi}_1^* \boldsymbol{W}_{\boldsymbol{y}} \boldsymbol{u}_1 - l^2 \boldsymbol{\mu}_T^* \boldsymbol{M} \boldsymbol{\mu}_T + c.c, \tag{A.10}$$

but the SPOD modes, $\boldsymbol{\psi}$, and the resolvent modes, $\boldsymbol{u}$, are now computed considering the observable $\boldsymbol{y}$ and the appropriate norms for the input and output space are defined by including weighting matrices $\boldsymbol{W}_{\boldsymbol{y}}$ and$\boldsymbol{W}_f$, respectively. The Lagrangian functional also takes a similar form as § 2.3,

$$\begin{aligned} \mathcal{L} = {} & \boldsymbol{u}_1^* \boldsymbol{W}_{\boldsymbol{y}} \boldsymbol{\psi}_1 \boldsymbol{\psi}_1^* \boldsymbol{W}_{\boldsymbol{y}} \boldsymbol{u}_1 - l^2 \boldsymbol{\mu}_T^* \boldsymbol{M} \boldsymbol{\mu}_T - \tilde{\boldsymbol{u}}_1^* \left(\boldsymbol{u}_1 - \boldsymbol{C} \boldsymbol{L}_T^{-1} \boldsymbol{B} \boldsymbol{v}_1 \right) \\ & - \tilde{\boldsymbol{v}}_1^* \left(\boldsymbol{B}^* \boldsymbol{L}_T^{-*} \boldsymbol{C}^* \boldsymbol{W}_{\boldsymbol{y}} \boldsymbol{u}_1 - \sigma_1^2 \boldsymbol{W}_{\boldsymbol{f}} \boldsymbol{v}_1 \right) - \tilde{\sigma}_1 \left(\boldsymbol{u}_1^* \boldsymbol{W}_{\boldsymbol{y}} \boldsymbol{u}_1 - 1 \right) + c.c, \end{aligned} \tag{A.11}$$

where, $\tilde{\boldsymbol{u}}_1, \tilde{\boldsymbol{v}}_1, \tilde{\boldsymbol{\sigma}}_1$ are the Lagrange multipliers. The effective composition of the functional is identical to that of the full-state optimization as it is composed of the cost function, the forward solution, the resolvent eigenvalue problem, and a normalization constraint. Taking variations with respect to each variable, with exception to the eddy-viscosity term, results in the following system of equations,

$$\begin{bmatrix} \boldsymbol{I} & \boldsymbol{W}_{\boldsymbol{y}}^* \boldsymbol{C} \boldsymbol{L}_T^{-1} \boldsymbol{B} & \boldsymbol{W}_{\boldsymbol{y}} \boldsymbol{u}_1 \\ \boldsymbol{B}^* \boldsymbol{L}_T^{-*} \boldsymbol{C}^* & \sigma_1^2 \boldsymbol{W}_{\boldsymbol{f}}^* & 0 \\ 0 & \boldsymbol{v}_1^* \boldsymbol{W}_{\boldsymbol{f}} & 0 \end{bmatrix} \begin{bmatrix} \tilde{\boldsymbol{u}}_1 \\ \tilde{\boldsymbol{v}}_1 \\ \tilde{\sigma}_1 \end{bmatrix} = \begin{bmatrix} 2 \boldsymbol{W}_{\boldsymbol{y}} \boldsymbol{\Psi}_1 \boldsymbol{W}_{\boldsymbol{y}} \boldsymbol{u}_1 \\ 0 \\ 0 \end{bmatrix}, \tag{A.12}$$

whose solution provides the Lagrange multipliers, $\tilde{\boldsymbol{u}}_1, \tilde{\boldsymbol{v}}_1, \tilde{\sigma}_1$.

A difficulty that arises in building Equation A.12 is that the term $\boldsymbol{L}_T^{-1}$ is a large, dense matrix. When $\boldsymbol{L}$, $\boldsymbol{B}$, $\boldsymbol{C}$, and the weighting matrices are sparse, we may

instead introduce auxiliary variables through

$$\boldsymbol{L}_T\tilde{\boldsymbol{\eta}}_1 = \boldsymbol{B}\tilde{\boldsymbol{u}}_1$$
$$\boldsymbol{L}_T^*\tilde{\boldsymbol{\zeta}}_1 = \boldsymbol{C}^*\tilde{\boldsymbol{v}}_1,$$

whereupon Equation A.12 may be written as a larger, but now sparse, system of equations

$$\begin{bmatrix} \boldsymbol{L}_T^* & 0 & -\boldsymbol{C}^* & 0 & 0 \\ 0 & \boldsymbol{L}_T & 0 & -\boldsymbol{B} & 0 \\ 0 & \boldsymbol{W}_{\boldsymbol{y}}^*\boldsymbol{C} & \boldsymbol{I} & 0 & \boldsymbol{W}_{\boldsymbol{y}}\boldsymbol{u}_1 \\ \boldsymbol{B}^* & 0 & 0 & \sigma_1^2\boldsymbol{W}_{\boldsymbol{f}}^* & 0 \\ 0 & 0 & 0 & \boldsymbol{v}_1^*\boldsymbol{W}_{\boldsymbol{f}} & 0 \end{bmatrix} \begin{bmatrix} \tilde{\boldsymbol{\zeta}}_1 \\ \tilde{\boldsymbol{\eta}}_1 \\ \tilde{\boldsymbol{u}}_1 \\ \tilde{\boldsymbol{v}}_1 \\ \tilde{\sigma}_1 \end{bmatrix} = \begin{bmatrix} 0 \\ 0 \\ 2\boldsymbol{W}_{\boldsymbol{y}}\boldsymbol{\Psi}_1\boldsymbol{W}_{\boldsymbol{y}}\boldsymbol{u}_1 \\ 0 \\ 0 \end{bmatrix}. \tag{A.13}$$

The above presents a general optimization framework for aligning any input-output resolvent analysis to data (i.e. here we use SPOD modes, but $\boldsymbol{\Psi}$ need not be restricted to SPOD modes). Variations with respect to any parameter of the resolvent operator may now be made to investigate their effect on modeling (or assimilating) known quantities.

Appendix B

LIFT-UP, KELVIN-HELMHOLTZ AND ORR MECHANISMS IN TURBULENT JETS

B.1 Transonic and supersonic jets

This section presents similar results supporting the presence of the lift-up mechanisms and streaks for $M_j = 0.9$ and $M_j = 1.5$ turbulent round jets. We first show the azimuthal frequency-wavenumber maps for each of the jets in Figure B.1 and Figure B.2. For both Figures, there is significant qualitative agreement between the SPOD energies and the resolvent gains.

In the $M_j = 0.9$ jet, we see a small spike at $St \sim 0.4$ for the resolvent analysis, due to trapped acoustic modes, that is slightly over predicted when compared to the SPOD energies. Another small discrepancy between SPOD and resolvent is the additional influence of the $m = 0$ mode in the resolvent analysis when compared to SPOD. However, both show large energies for $m = 1$ and at low frequencies, displaying

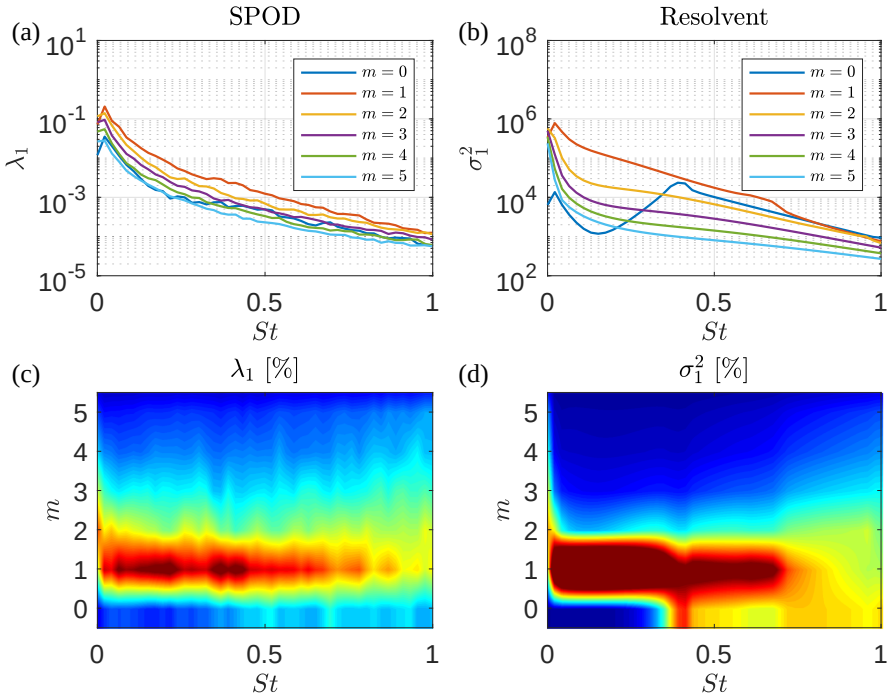

Figure B.1: Modal energy from SPOD and resolvent analyses of the $M_j = 0.9$ round jet.

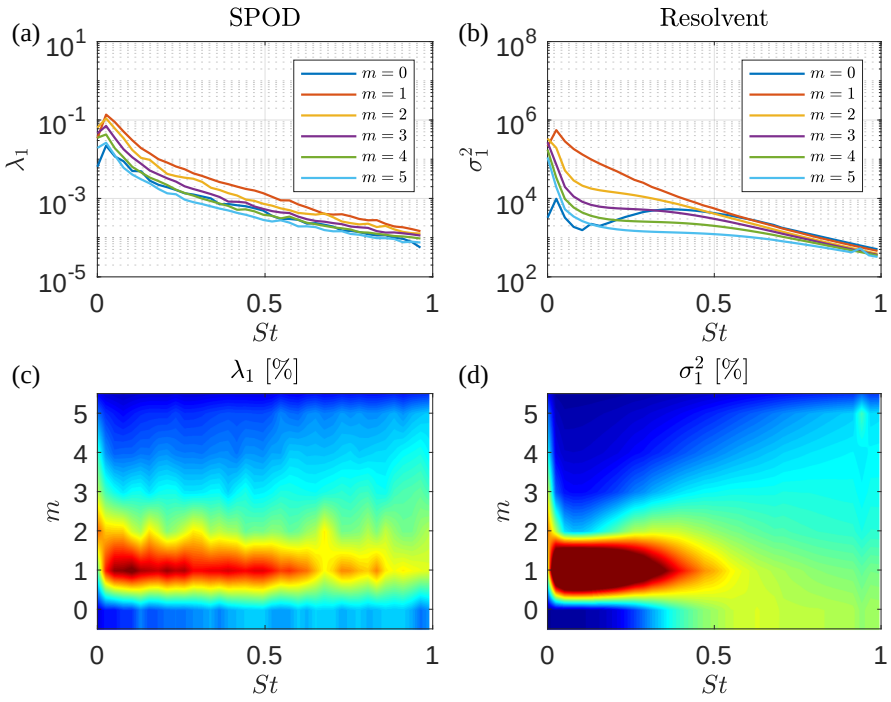

Figure B.2: Modal energy from SPOD and resolvent analyses of the $M_j = 1.5$ round jet.

behavior similar to the $M_j = 0.4$ jet with energy peaking at $m = 2$ as $St \to 0$.

For the $M_j = 1.5$, jet there is a similar over-prediction by resolvent analysis for $m = 0$ when compared to SPOD. Despite this, the remainder of the resolvent map follows SPOD characteristics quite well. For higher frequencies, energy is distributed across multiple azimuthal wavenumbers, and at low frequencies both analyses display high-energy behavior similar to the $M_j = 0.4$ jet with energy peaking at $m = 2$ as $St \to 0$.

We also show the 3-D reconstructions of both the $M_j = 0.9$ and 1.5 jet SPOD modes at $St = 0$ and $m = 1, 3$ shown in Figure B.3 using 1024 snapshots and 75% overlap. All four plots show streaks of streamwise velocity response along with the associated streamwise vorticity, with the clearest descriptions shown for the $m = 3$ cases. The $m = 3$ case for both jets presents streaky structures paired with streamwise vorticity rolls placed perfectly between each streak. The $m = 1$ plots are not quite as appealing, but both plots present streaks in streamwise velocity and are also paired with streamwise vorticity placed between each streak.

Finally, we show the resolvent analysis at $St = 0$ for both jets and wavenumbers $m = 1, 3$ in Figure B.4. Here, we show the same behavior as previously described

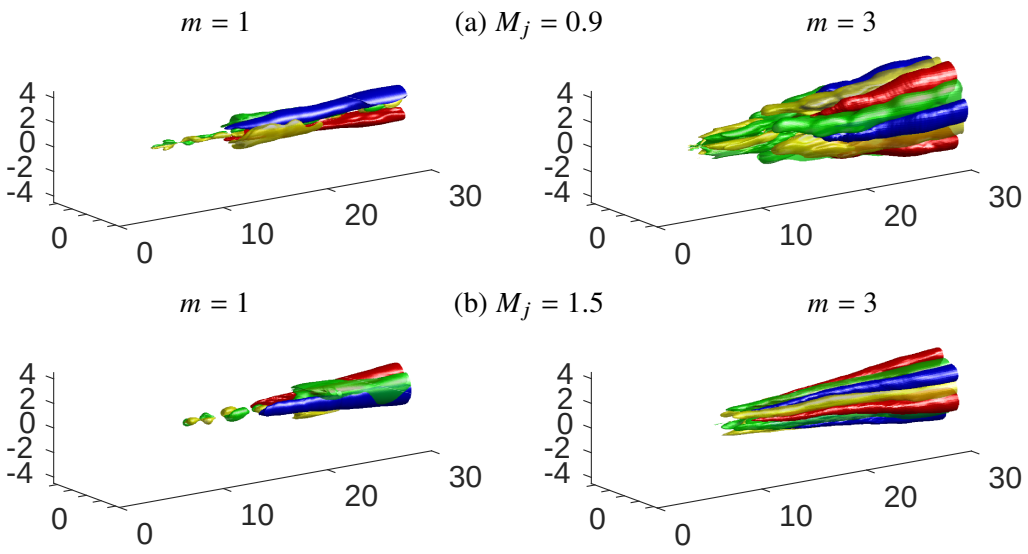

Figure B.3: Three-dimensional reconstruction of the first SPOD mode (streamwise velocity, $\boldsymbol{\psi_1} : u_x$, red-blue, streamwise vorticity, $\boldsymbol{\psi_1} : \omega_x$, yellow-green) as $St \to 0$ for $m = 1$ (left column) and $m = 3$ (right column) using isosurfaces of ±50% of the maximum streamwise velocity and isosurfaces of ±25% of the maximum streamwise vorticity, with the exception of the $M_j = 1.5$, $m = 1$, case where red-blue isosurfaces are instead ±30% of the maximum streamwise velocity.

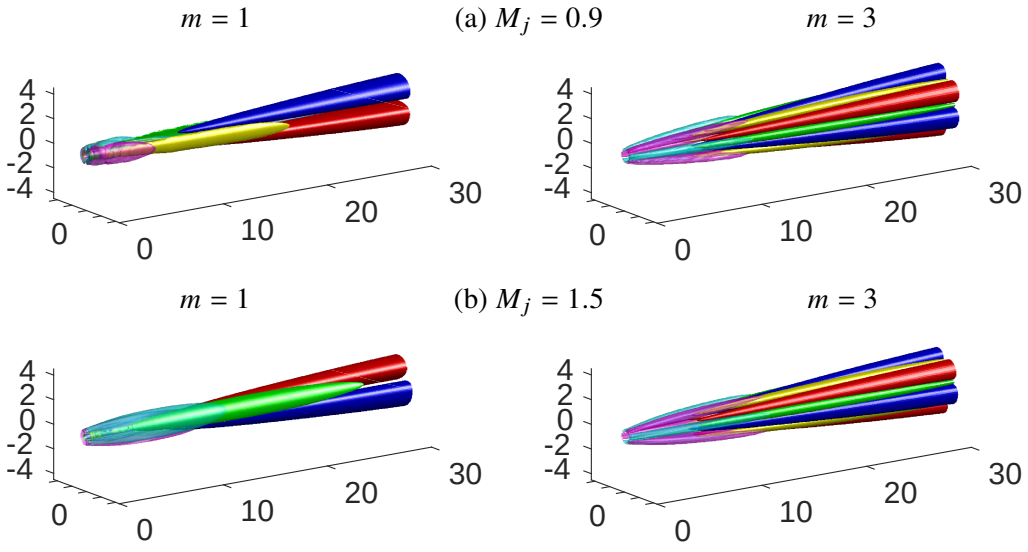

Figure B.4: Global resolvent forcing and response for $m = 1$ (left) and $m = 3$, (right) at $St = 0$. The streamwise forcing vorticity is shown in magenta-cyan with isosurfaces $\pm 0.05\|\boldsymbol{v_1} : \omega_x\|_\infty$ for $m = 1$ and $\pm 0.2\|\boldsymbol{v_1} : \omega_x\|_\infty$ for $m = 3$, streamwise response vorticity is shown in yellow-green with isosurfaces $\pm 0.5\|\boldsymbol{u_1} : \omega_x\|_\infty$, and streamwise response velocity is shown in red-blue with isosurfaces $\pm 0.25\|\boldsymbol{u_1} : u_x\|_\infty$.

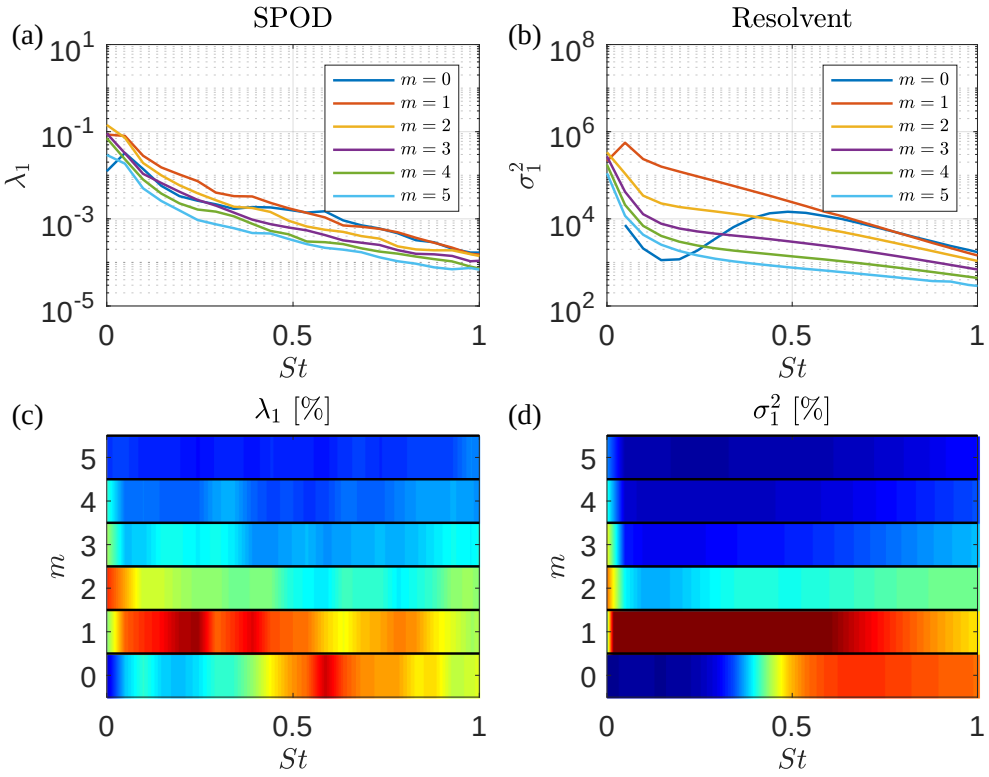

Figure B.5: Modal energy from SPOD and resolvent analyses of a Mach 0.4 round jet, shown here in semi-discrete form.

for the $M_j = 0.4$ jet. Forcing in the form of streamwise vorticity begins upstream near the nozzle, followed by responses of streamwise rolls, that then lead to lift-up and large streamwise velocity responses. Considering all of the presented evidence for $M_j = 0.9$ and 1.5 jets, we conclude that the lift-up mechanism is present in all turbulent jets.

B.2 SPOD and resolvent semi-discrete energy maps for Mach 0.4

Figure B.5 gives the semi-discrete, continuous in frequency and discrete in azimuthal wavenumber, representation of Figure 3.4. Through both representations of SPOD and resolvent analyses, we can make similar conclusions as the interpolated results of Figure 3.4. We can clearly see the shift from the KH-dominated space at $m = 0$ as frequency is decreased to the Orr dominated region. For non-zero azimuthal wavenumbers we see significant energy for frequencies approaching 0 and find $m = 2$ has the largest energetic contribution for $St \approx 0$.

Appendix C

RESOLVENT-BASED MODELING OF TURBULENT JET NOISE

C.1 Derivation of the Kirchhoff Surface

We begin with the homogeneous wave equation:

$$\frac{\partial^2 p'}{\partial t^2} - \nabla^2 p' = 0 \tag{C.1}$$

where p' is a function of x, r, θ, t and can be expressed, due to stationarity in time and homogeneity in the azimuthal and streamwise direction, as $p\prime(x, r, \theta, t) = \hat{p}(r)e^{-i\omega t + -im\theta - ikx}$. Applying this definition of the pressure the wave equation gives

$$\frac{\partial^2 \hat{p}}{\partial r^2} + \frac{1}{r}\frac{\partial \hat{p}}{\partial r} + \left(\omega^2 - \frac{m^2}{r^2} - k^2\right)\hat{p} = 0, \tag{C.2}$$

and with a general solution of

$$\hat{p}_m(r, k, \omega) = c_1 J_m(\sqrt{\omega^2 - k^2}r) + c_2 Y_m(\sqrt{\omega^2 - k^2}r), \tag{C.3}$$

and by satisfying the Sommerfeld radiation condition reduces the expression to

$$\hat{p}_m(r, k, \omega) = c(k, \omega) H_m(\sqrt{\omega^2 - k^2}r). \tag{C.4}$$

This leaves one to solve for the unknown coefficients by using the surface at the edge of the boundary, $r = R$

$$c(k, \omega) = \hat{p}_m(R, k, \omega)/H_m(\sqrt{\omega^2 - k^2}R) \tag{C.5}$$

Therefore the particular solution is thus (as reported by Freund (2001)),

$$\hat{p}_m(r, k, \omega) = \hat{p}_m(R, k, \omega) H_m(\sqrt{\omega^2 - k^2}r)/H_m(\sqrt{\omega^2 - k^2}R). \tag{C.6}$$